Sulphur isotopes in Permian-Triassic evaporites: A tool for stratigraphy and correlation

SALISBURY, JACK

Sulphur isotopes in Permian-Triassic evaporites: A tool for stratigraphy and correlation

Jack Salisbury

A thesis submitted in partial fulfilment of the requirements for the degree of Doctor of Philosophy at Durham University

Department of Earth Sciences

Durham University

2024

Abstract

The latest Permian-Triassic time interval is associated with major perturbations in the global sulphur cycle, expressed as variability in the sulphur isotopic composition ($\delta^{34}S$) of seawater sulphate and recorded in sedimentary sulphates of marine origin. Recent efforts have applied sulphur isotope stratigraphy for the correlation of evaporitic strata in central Europe and Spain. However, despite the abundance of evaporitic material, sulphur isotope stratigraphy has yet to see widespread application to the UK late Permian-Triassic. This thesis presents evaporite-based sulphur isotope ($\delta^{34}S_{evap}$) records from multiple UK sub-basins, the Larne, East Irish Sea, Wessex, Cleveland, and UK Southern North Sea (SNS) basins. The data herein expands the geospatial coverage of the Permian-Triassic sulphur isotope age curve and provides further age-calibration for sedimentary evaporites with limited biostratigraphic constraint.

$\delta^{34}S_{evap}$ data from drillcore of the Staithes S-20 borehole, Cleveland Basin, provides coverage of the uppermost Zechstein, through to the uppermost Mercia Mudstone Group (MMG) and forms the basis from which to correlate other UK latest Permian-Triassic $\delta^{34}S_{evap}$ records. The Staithes S-20 profile is correlated with the global $\delta^{34}S_{evap}$ curve to form a composite record, which is assimilated into a sulphur biogeochemical box model, producing the most complete record of pyrite burial rates for the latest Permian-Triassic.

An equivalent $\delta^{34}S_{evap}$ profile is presented from drill cuttings of well 42/28-2 in the UK SNS and correlated with the Staithes S-20 record. The successful correlation demonstrates the potential suitability of drill cuttings for sulphur isotope stratigraphy of evaporitic lithologies, greatly increasing the number of sites available for sampling, presenting the potential to expand the geospatial coverage of the Triassic $\delta^{34}S_{evap}$ age curve. In addition, $\delta^{34}S_{evap}$ data from the Bunter Shale and Bunter Sandstone (Sherwood Sandstone Group – SSG) in both Staithes S-20 and 42/28-2 are within the range for late Permian seawater. Additional $\delta^{34}S_{evap}$ data from nodular calcium sulphates of drillcore GT-01 Kilroot, Larne Basin, within an evaporitic siltstone interval at the base of the Ormskirk Sandstone (SSG), also fall within the range established for Permian seawater. $\delta^{34}S_{evap}$ data from the uppermost SSG in another core within the Larne Basin, Cairncastle-2, compare well to the $\delta^{34}S$ of latest Early Triassic seawater sulphate.

Together, these data suggest that in the locations sampled, the position of the Permian-Triassic boundary should be placed at a currently unconfirmed position within the SSG. However, uncertainties persist regarding the precise degree of marine vs. terrestrial influence and additional sampling is necessary to confirm the reproducibility of these $\delta^{34}S_{evap}$ data.

Further $\delta^{34}S_{evap}$ data were generated from Middle to Late Triassic strata of 110/13-8, East Irish Sea Basin (EISB). Although the $\delta^{34}S_{evap}$ profile exhibits a greater degree of scatter than the equivalent records of Staithes S-20 and 42/28-2, the broad, general declining trend established for the Middle-Late Triassic is clearly replicated, enabling correlation. These data constitute the highest resolution $\delta^{34}S_{evap}$ profile generated for Triassic strata of the EISB and assist in providing tighter age constraint beyond that which can be achieved with sparse biostratigraphy alone. Further sampling of the EISB is required to better confirm the trends observed in the $\delta^{34}S_{evap}$ profile of 110/13-8.

It can be difficult to confidently distinguish between marine and nonmarine evaporite systems in the geologic record, due to sedimentological and mineralogical ambiguities. The $\delta^{34}S_{evap}$ profiles for the MMG of Carnduff-02 (Larne Basin) and Burton Row (Wessex Basin) are largely offset from the global composite $\delta^{34}S_{evap}$ age curve, which are interpreted here as evidence for terrestrial deposition and hydrologic restriction from the seawater sulphate reservoir. When compared with the $\delta^{34}S_{evap}$ profiles of 110/13-8, Staithes S-20, and 42/28-2, the data imply a spatial distinction in the degree of marine influence during of the UK Triassic, helping to reconcile apparent disagreements between sedimentological, mineralogical, and palaeontological data.

A suite of stable isotopic ($\delta^{34}S_{evap}$, $\delta^{34}S_{CRS}$, $\delta^{15}N_{tot}$, $\delta^{13}C_{org}$) and organic geochemical data were generated from the late Permian Eden Shales, Vale of Eden, Cumbria. Two stages defined by distinct biogeochemistry can be defined, with Stage 1 spanning evaporite bed A and Stage 2 evaporite beds B and C. The data for Stage 1 is particularly speculative and requires further refinement. In Stage 2, isotopic and lipid biomarker data possibly indicate photic zone euxinia. In addition, extreme $\delta^{13}C_{org}$ enrichments (>0 ‰), along with the detection of β-carotane, potentially reflect a combination of hypersalinity and enhanced primary productivity. The interpretations

put forth here remain speculative, and the generation of additional geochemical data and further sampling of the Eden Shales should be pursued to further constrain the palaeoenvironmental conditions during deposition.

Table of contents

Declaration

I declare that this thesis, which I submit for the degree of Doctor of Philosophy at Durham University, is my own work and unlike any other submitted here or at any other institution.

Jack Salisbury

Department of Earth Sciences, Durham University, September 2024

Acknowledgments

Firstly, I would like to thank my supervisor Darren Gröcke for his careful supervision over the last four years. Darren has been an excellent supervisor for the duration of my PhD. He, with great patience, taught me everything I currently know regarding the operation of a stable isotope mass spectrometry laboratory, equipping me with skills that will prove useful for the remainder of my career. In addition, Darren was always willing to discuss scientific concepts, and this thesis would not have been possible without his support and involvement. I would also like to thank my secondary supervisor, Tom McKie at Shell, UK. Over the past four years I have regularly inundated Tom's inbox with questions about the Triassic, and he has always taken the time to answer my questions and share with me his encyclopaedic knowledge of Permian-Triassic stratigraphy. Without his involvement, this thesis would also no have been possible.

During the duration of my PhD, I have been fortunate to work as a visiting student in different institutions, enabling me to gain experience in the application of a wide range of geochemical methodologies. I would like to thank Vincent Grossi for being kind enough to host me for a month in his lab at the Université de Lyon. Through Vincent' tutelage, I gained experience in generating organic geochemical data. Much of this data forms a major component of Chapter 5 of this thesis, which benefitted greatly from Vincent's involvement. In addition, I would like to thank Eva Stüeken for hosting me at the University of St Andrews. This visit enabled me to complete pyrite extraction, and the resulting data formed a major part of Chapter 5.

I would also like to thank the staff at the British Geological Survey core store for assisting us with sampling on several different visits. In particular, I would like to thank Scott Renshaw for taking samples for us while we could not visit in person during COVID. I would also like to thank Robert Raine at the Geological Survey of Northern Ireland for sampling multiple cores for us, as well as the logging of Cairncastle-2. Without his efforts, the spatial coverage of our sulphur isotope data presented in Chapter 4 would have been far more limited.

Finally, I would like to thank my family for their continuous support over the last four years. In addition, I would like to thank the many friends I have met during my time

in Durham. Their willingness to accompany me to the pub on Friday nights kept me sane over the past four years.

Chapter 1: Introduction

1. Thesis rationale

The late Permian and Triassic time intervals are associated with major environmental and climatic perturbations (Sun et al., 2012; Cui and Kump, 2015; Trotter et al., 2015; Wu, et al., 2021), associated with severe shifts within the Earth's biosphere, including the End Permian Mass Extinction (EPME) and the End Triassic Extinction (ETE), two of the 'Big Five' mass extinction events (Raup and Sepkowski, 1982; Sepkowski, 1996). Both extinctions have been linked to major and abrupt volcanic outgassing related to the emplacement of large igneous provinces (LIPs); the Siberian Traps of the late Permian (Burgess and Bowring, 2012) and the Central Atlantic Magmatic Province (CAMP) of the Late Triassic (Wignall, 2001; Ruhl et al., 2011; Davies et al., 2017).

The EPME and the ETE are associated with perturbations in the cycling of various redox-sensitive elements (e.g., Ruhl et al., 2011; Rothman et al., 2014; Stüeken et al., 2015a; Newby et al., 2021; Bond et al., 2023). Of particular note is the sulphur isotopic composition ($\delta^{34}S$) of seawater sulphate, which exhibits major variability, especially across the Early Triassic (e.g., Claypool et al., 1980; Bernasconi et al., 2017; Crockford et al., 2019). Despite this, understanding of the Triassic sulphur cycle has been impeded by the diagenesis of carbonate associated sulphate (Bernasconi et al., 2017; Johnson et al., 2021) and the lack of high-resolution long-term $\delta^{34}S$ records between the EPME and the ETE. It has been common for work to focus primarily on specific short intervals of time, such as the Permian-Triassic boundary (PTB) (e.g., Korte et al., 2004; Newton et al., 2004; Kaiho et al., 2006; Riccardi et al., 2006; Schobben et al., 2015), Early Triassic (e.g., Lyu et

al., 2019; Song et al., 2019) and the Triassic-Jurassic boundary (TJB) (e.g., He et al., 2020; Tang et al., 2023).

Recent efforts have expanded the coverage of the sulphur isotope record during the Triassic, with sulphur isotope data from carbonate-associated sulphate ($\delta^{34}S_{CAS}$) generated from the Late Permian through to the Middle Triassic (Song et al., 2014). Despite the relatively good chronostratigraphic coverage of this data, concerns exist regarding the susceptibility of $\delta^{34}S_{CAS}$ records to diagenetic overprinting (e.g., Present et al. 2019). Bernasconi et al. (2017) and Ortí et al. (2022) compiled composite $\delta^{34}S$ records from sedimentary evaporites ($\delta^{34}S_{evap}$) of central Europe and eastern Iberia, respectively. While successful in expanding the resolution of the Triassic $\delta^{34}S_{evap}$ age curve, a lack of chronostratigraphic coverage persists for certain intervals. Despite this, these $\delta^{34}S_{evap}$ records can provide the basis for the development of further $\delta^{34}S_{evap}$-based correlations.

During the late Permian-Triassic, the UK was located within the eastern part of Panagaean supercontinent, at a palaeolatitude of ~20 °N (Newell et al., 2018). Deposition occurred under a warm and arid to semi-arid climate (McKie and Williams, 2009; Sun et al., 2012; Trotter et al., 2015). The vast expanse of continental landscape ensured a high degree of continentality and a scarcity of open water sources, maintaining aridity within the continental interior (Parrish, 1993). Punctuated rifting episodes through the late Permian and Early Triassic generated a complex network of interconnected rift basins that propagated through the warm and arid continental interior (Coward, 1995; Hounslow et al., 2012; McKie, 2014). These rift basins were often sub-sea level, enabling accommodation space for sediment and the periodic ingress of marine waters (McKie, 2017). This tectonic setting, in combination with the warm and

arid climate, facilitated the widespread deposition of sedimentary evaporites, which provide relatively consistent chronostratigraphic coverage of the Late Permian and Middle-Late Triassic (Hounslow and Ruffell., 2006; McKie, 2017).

Thus, the UK late Permian-Triassic provides the opportunity to generate additional $\delta^{34}S_{evap}$ data and build upon the efforts of previous work (Bernasconi et al., 2017; Ortí et al., 2022), improving the chronostratigraphic coverage of the global $\delta^{34}S_{evap}$ curve. This thesis focusses on the establishment of robust $\delta^{34}S_{evap}$ records from the late Permian uppermost Zechstein, and Triassic Sherwood Sandstone and Mercia Mudstone groups of the UK, for which the currently available $\delta^{34}S_{evap}$ data are limited, lacking spatial and chronostratigraphic coverage (e.g., Taylor, 1983).

In doing so, I aim to establish further chronostratigraphic constraint to the evaporitic stratigraphy of the UK Permian-Triassic, via the establishment of correlation schemes between UK $\delta^{34}S_{evap}$ records and the global composite $\delta^{34}S_{evap}$ curve. Due to the arid and often hypersaline nature of the depositional environment, the UK Triassic is generally impoverished in fossils suitable for biostratigraphy (Warrington et al., 1980; Hounslow and Ruffell, 2006), and thus a lack of chronostratigraphic constraint persists (McKie and Williams, 2009). Much of the established correlation schemes for the UK are based upon lithostratigraphy (e.g., Jackson et al., 1997) and sparse biostratigraphic data (e.g., Warrington, 1974; Warrington et al., 1980). Thus, the development of high-resolution $\delta^{34}S_{evap}$ records presents the opportunity to constrain and corroborate established lithostratigraphic correlation schemes between different UK basins, and between the UK sector and continental Europe.

In addition, through correlation with the global composite $\delta^{34}S_{evap}$ curve and the application of biogeochemical box modelling, I further refine understanding regarding the biogeochemical evolution of the Triassic. Long-term $\delta^{34}S_{evap}$ records from the Middle-Late Triassic Mercia Mudstone Group have the potential to provide valuable insight regarding the broader trends in biogeochemical change between the EPME and ETE, particularly for time intervals for which the established $\delta^{34}S_{evap}$ curve currently lacks chronostratigraphic resolution, such as the Late Triassic (see Bernasconi et al., 2017).

Finally, although there exist clear geochemical distinctions between marine and nonmarine evaporite systems (Warren, 2010) (see below), it can be difficult to confidently distinguish between evaporites of marine and terrestrial origin in the geologic record, due to ambiguities in their sedimentology and mineralogy (e.g., Hardie, 1984; Lowenstein et al., 1989; Chivas, 2007; Warren, 2010; Leitner et al., 2023). Accordingly, much debate persists regarding the degree of marine influence during deposition of UK Triassic evaporites (e.g., Taylor, 1983; Andeskie et al., 2018). $\delta^{34}S_{evap}$ data exhibit sensitivity to marine 'vs' terrestrial sulphate inputs. Thus, through comparison with the global composite $\delta^{34}S_{evap}$ curve, the $\delta^{34}S_{evap}$ data presented herein, provide further constraint to the extent of marine influence during evaporite deposition. This has the potential to further our understanding of the depositional environment of UK Triassic evaporites, providing insight valuable for the refinement of Triassic palaeogeographic reconstruction.

2. Evaporites

Evaporites are ionic salts that form via physicochemical precipitation from supersaturated saline brines (Hardie, 1991). A state of supersaturation is generally

achieved through evaporative concentration by solar heating, which causes water loss through vapourisation as water in the brine undergoes transition to a gaseous phase, concentrating the residual brine and increasing its' salinity (Warren, 2021). Under certain circumstances, saturation can also result from temperature changes (cooling or non-solar heating), degassing and the mixing or brines in diagenetic and hydrothermal settings (Hardie, 1991; Warren, 2021). The parent brines from which evaporites precipitate can be fed by marine or nonmarine waters (fluvial runoff, terrestrial groundwaters, hydrothermal fluids) (Hardie, 1984, 1991; Warren, 2010, 2021), with many evaporites likely occupying a position between these two end member extremes.

Evaporite minerals contain the major ions Na, Ca, Mg, K, Cl, SO_4, CO_3 in varying proportions, depending on the exact evaporite mineral species, and certain evaporitic precipitates also contain structurally bound H_2O, as well as B, Ba, Sr, Br, Li, and I (Warren, 2010). The mineralogy of ancient evaporite systems generally includes alkaline earth carbonates, calcium-sulphates (gypsum and anhydrite), halite and potash salts, including sylvite, carnallite, polyhalite and epsomite (Warren, 2021), with halite and calcium-sulphates being the most common (Chivas, 2007). The relative proportions of course vary between distinct evaporite systems, however these four evaporite mineral groupings constitute approximately 95 % of Neoproterozoic and Phanerozoic evaporites globally (Warren, 2010). The remaining 5 % consist largely of sodium carbonate, sodium sulphate and sodium borate salts, which ordinarily form in continental playa settings (Chivas, 2007; Warren, 2010).

Due to the important role of solar heating, evaporites are generally associated with warm and arid climates, providing sufficient heat and aridity to maintain

evaporative conditions (Hardie, 1991). In addition, evaporite deposits generally form within basins that maintain hydrographic restriction and are unable to form in settings with a consistent open surface connection to seawater (Warren, 2010). Large voluminous marine evaporite systems require hydrologically restricted sub-sea level basins, which in combination with heat and aridity, enable conditions of hypersalinity to be maintained, while also providing access to fresh brine material (Sloss, 1953; Warren, 2010) (see below). Only certain terrestrial evaporites can form in supra-sea level settings, however these evaporite systems are far less voluminous, as is the case for terrestrial evaporites in general (Warren, 2010). Thus, evaporite systems require a combination of specific climatic, environmental, and tectonic conditions favourable for their formation (Sloss, 1953; Krijgsman et al., 2006; Warren, 2010).

2.1. Marine evaporites

Marine evaporites are ionic salts that precipitate via the evaporative concentration of marine-fed saline brines sourced from the inflow of seawater into sub-sealevel basins (Warren, 2010). The largest ancient evaporites are of marine origin, with such large evaporite deposits requiring access to a large NaCl pool, which only the ocean reservoir can provide (Warren, 2010). It should of course be noted that the largest evaporites in the geologic record (e.g., the Permian Zechstein and Khuff Formation) not only required a marine mother brine, but also certain climate and tectonic settings. In the case of Permian evaporites, the continentality of Pangaea (Parrish, 1993), extremes in temperatures and aridity (Parrish, 1993; Chumakov and Zharkov, 2003), and an abundance of sub-sealevel rift basins (McKie, 2017) facilitated the formation of evaporite deposits on such a large scale. In contrast, the modern Earth is characterised

by far smaller marine-fed evaporite systems, as it does not possess the climate conditions and tectonic configuration favourable to the formation of marine evaporite deposits on the scale of those observed in the geologic record (Warren, 2010).

In a modern marine evaporite system, assuming the ionic proportions and composition of Quaternary seawater, precipitation proceeds from calcium carbonate, to gypsum, then halite, and finally the bittern salts, with this sequential precipitation progressing with increasing salinity (Babel and Schreiber, 2014; Warren, 2021) (Fig. 1). Carbonates form at 1.5-3 times the salinity of the original seawater, leaving a residual brine with excess Ca. This subsequently reacts with sulphate to precipitate gypsum/anhydrite, which commences at 5-6 times the original salinity, consuming available Ca and leaving excess sulphate. The onset of halite precipitation begins at 10-11 times the salinity, and bittern salts subsequently precipitate once the brine reaches 60-70 times the original salinity. Residual sulphate combines with magnesium to form $MgSO_4$ salts, and eventually KCl salts as Mg concentrations decline (Warren, 2010) (Fig. 1). Halite continues to precipitate during the bittern stage, up to a salinity 90 times that of the original seawater (Warren, 2021). An evaporite system attains equilibrium when solute loss via evaporation equals rates of brine influx. Theoretically, this can occur at any stage along the precipitative sequence, with the point at which this equilibrium is achieved controlling the dominant evaporite mineral composition of the basin fill (Warren, 2010).

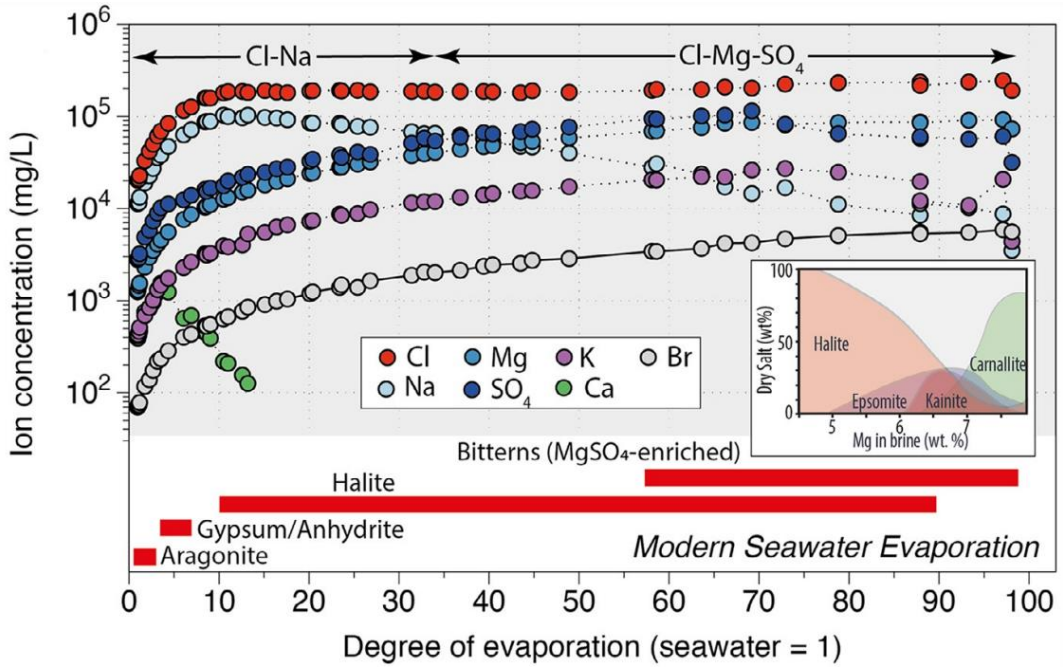

Figure 1: *Changes in the ionic proportions of a modern seawater brine during the sequential precipitation of evaporite minerals. The inset displays the sequential precipitation of potash salts against Mg content within a brine (sourced from Warren, 2021).*

The ionic proportions of seawater have of course evolved with time (e.g, Lowenstein et al., 2001, 2003), and thus assuming Quaternary compositions may be misleading when attempting to understand ancient evaporite deposits for certain intervals in the geologic past. For example, the initial ratio of magnesium to calcium (Mg/Ca) of the original brine material acts to control the carbonate mineral species that precipitates at the beginning of the reaction series (Warren, 2021). In this way, the Mg/Ca ratio forms a chemical divide known as the carbonate divide, separating subsequent possible precipitation pathways according to the initial composition of the evaporite brine (Babel and Schreiber, 2014). During equilibrium precipitation, the concentrations of ions for a particular salt (e.g., Ca^{2+} and CO_3^{2-} for calcite) must vary inversely, with the ion exhibiting the greatest initial abundance undergoing progressive

enrichment, whilst the least abundant ion is depleted until it is consumed beyond detection (Eugster, 1980; Babel and Schreiber, 2014). Thus, calcium carbonate minerals precipitate during the initial stages of the precipitative series and will continue to form until the least abundant ionic component is depleted (Babel and Schreiber, 2014; Warren, 2021). Modern seawater is rich in Ca, and thus carbonate mineral precipitation ceases once HCO_3 is consumed. However, if Ca is consumed, a Type 1 (alkaline) brine forms (Fig. 2), preventing the subsequent precipitation of gypsum, and promoting the formation of bittern salts (Eugster, et al., 1980; Warren, 2021). Type 1 brines may have been prevalent within the hypothesised soda ocean (Kempe and Degens, 1984) or soda lakes (Stüeken et al., 2015b) of the Archaean.

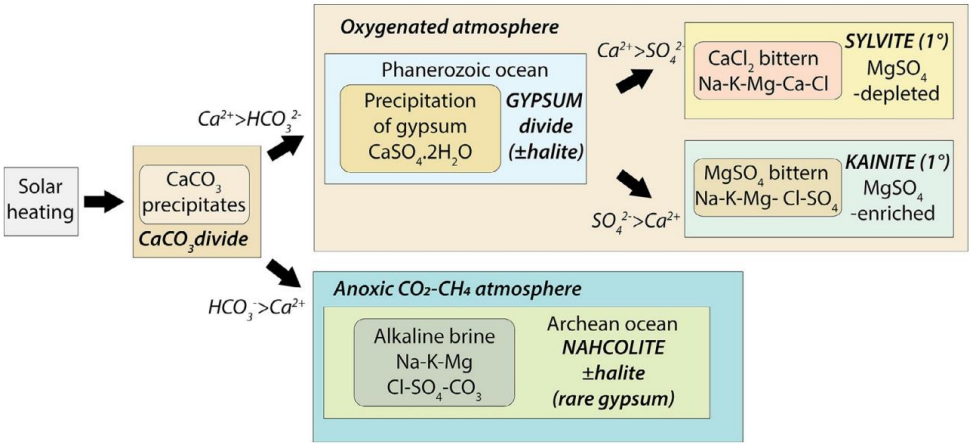

Figure 2: *The chemical divides that control the evaporation pathway of seawater brines (sourced from Warren, 2021).*

Thus, a chemical divide exists at each precipitation step, controlled by the ionic proportions of the brine prior to saturation (Harvie et al., 1982). Another chemical divide, the 'gypsum divide', occurs during the precipitation of gypsum (Fig. 2) (Eugster et al., 1980; Babel and Schreiber, 2014). This is far more relevant to the post-Archaean Earth (Warren, 2021), due to higher levels of atmospheric oxygen (Lyons et al., 2014).

Assuming HCO_3 was depleted during the earlier precipitation of calcium carbonates, the residual brine experiences an enrichment in Ca or Mg, characterised by a neutral pH balance (Warren, 2021). Once gypsum precipitation initiates, either Ca or SO_4 is consumed until depletion, depending upon the relative ionic proportions at the beginning of gypsum formation. If Ca is the first to be consumed, a bittern enriched in Na, K, Mg, Cl and SO_4 will result, facilitating the precipitation of magnesium sulphates (Fig. 2). In contrast, if SO_4 reaches depletion before Ca, the brine will become enriched in Na, K, Mg, Ca, and Cl, promoting the development of calcium chloride brines and facilitating the precipitation of potassium chloride and calcium chloride minerals (Warren, 2021).

While $MgSO_4$-rich bitterns characterise modern saline systems (Warren, 2010), it is thought that during the Phanerozoic, seawater fluctuated between a state of $Ca > SO_4$ and $SO_4 < Ca$ (Fig. 3) (Lowenstein et al., 2001, 2003). During depletions in seawater $MgSO_4$, the Earth's oceans were enriched in Ca (i.e., $Ca > SO_4$), and were thus calcitic, correlating with high seafloor spreading rates, a heightened influx of Ca-rich mid-ocean ridge hydrothermal brines and high sea levels (Hardie, 1996; Lowenstein et al., 2001). This of course contrasts with $MgSO_4$-rich aragonitic seas, which characterise the Permian-Triassic, as well as Quaternary seawater (Warren, 2010).

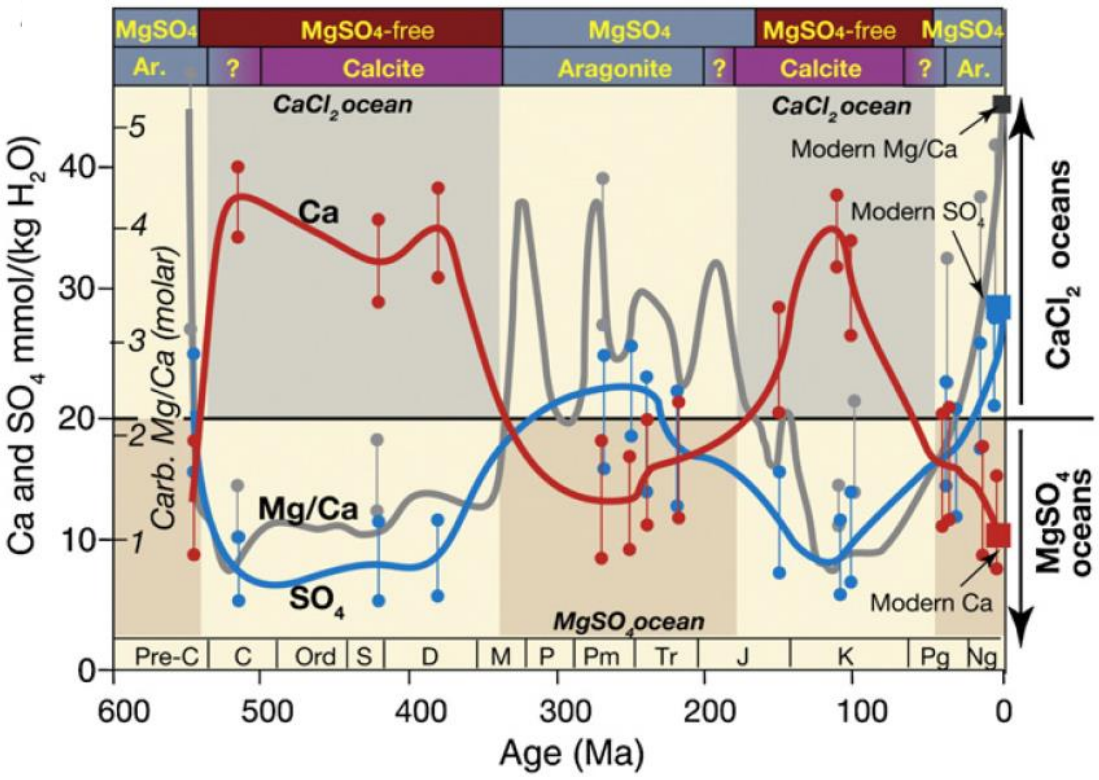

Figure 3: *Temporal evolution in the relative concentrations of seawater Ca and SO_4 over the past 600 million years (sourced from Warren, 2010).*

2.2. Nonmarine evaporites

Nonmarine evaporites are generally less voluminous, forming within hydrologically closed continental depressions, and do not source brine material from the ocean reservoir (Warren, 2010, 2021). Instead, the ions required for evaporite precipitation are sourced from fluvial systems and groundwaters (Warren, 2021). As a result, the ionic proportions of nonmarine evaporite brines are far less predictable than those of marine brines and are controlled by the composition of the inflowing waters, which in turn depend upon the labile lithologies exposed to weathering in the local drainage basin (Hardie and Eugster, 1970; Eugster, 1980). The weathering reactions involved are diverse and varied between different settings. Broadly speaking, these reactions include the dissolution of soluble mineral species, such as gypsum and halite, calcite and silicate

dissolution, as well as redox reactions involved in the oxidation of sulphides and iron-silicate dissolution (see Eugster, 1980). The majority of sodium carbonate, sodium sulphate and sodium borate accumulations are derived from non-marine brines (Warren, 2021).

Five major brine types can be defined for nonmarine evaporite systems (Hardie and Eugster, 1970; Warren, 2010):

- Na-CO_3-Cl
- Na-CO_3-SO_4-Cl
- Na-(Ca)-SO_4-Cl
- Mg-Na-(Ca)-SO_4-Cl
- Ca-Mg-Na-(K)-Cl

All evaporation pathways begin with the precipitation of alkaline earth carbonates, including aragonite, low-magnesian calcite, high-magnesian calcite and dolomite, with the Mg/Ca ratio of the initial brine inflow controlling the specific carbonate mineralogy (Warren, 2010). This constitutes the first chemical divide during the precipitative series of nonmarine carbonates, constraining the direction of the subsequent evaporation pathway by determining whether the residual brine will experience Ca enrichment relative to carbonate, or vice versa (Eugster, 1980). If the brine inflow is enriched in HCO_3 relative to Mg and Ca, then carbonate precipitation will generate depletions in Mg and Ca, leaving excess HCO_3 within the residual brine. As a result, the precipitative series will progress according to pathway 1 in Fig. 4, as HCO_3 reacts with Na to precipitate sodium carbonate minerals. Note that almost no gypsum can form during this pathway, as the Ca is consumed during initial carbonate precipitation (Warren, 2010).

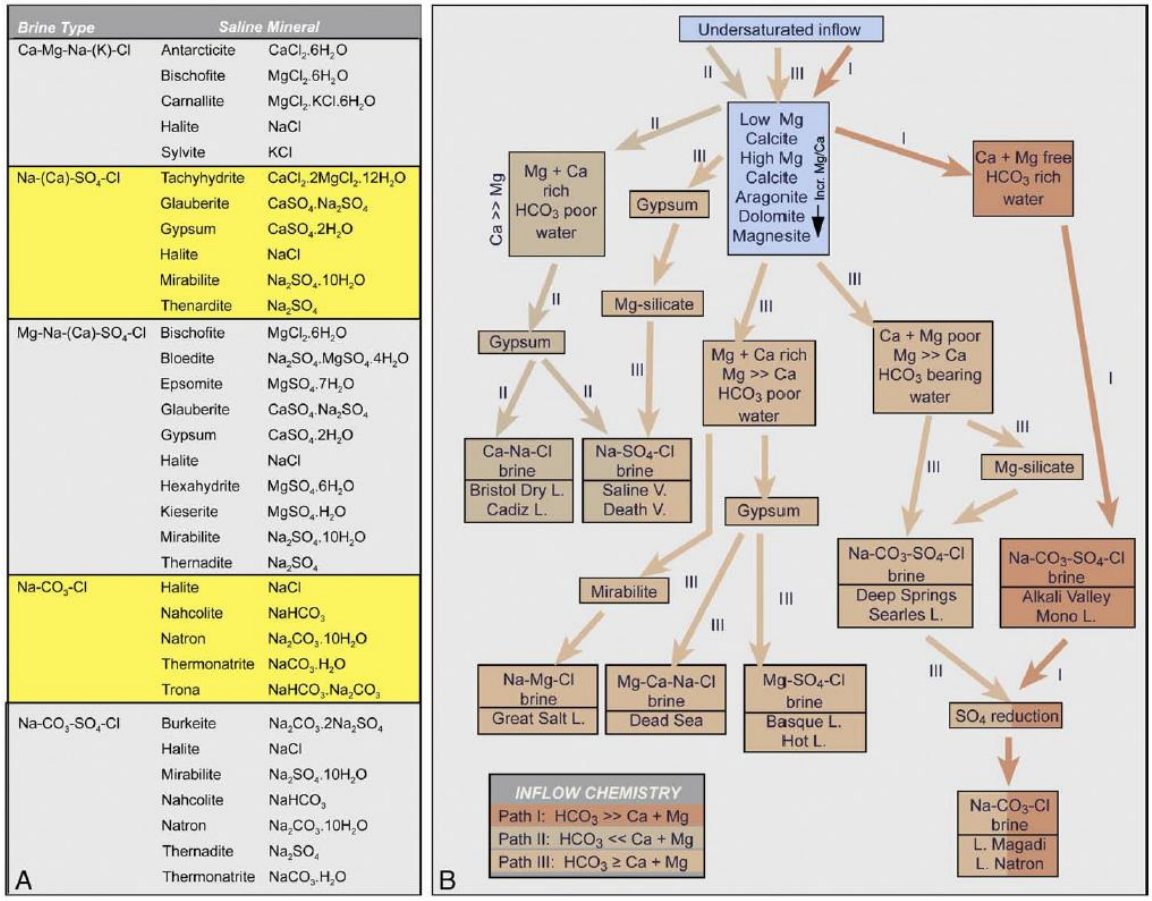

Figure 4: *(A) The five major brine types associated with nonmarine evaporite systems; (B) The three evaporation pathways for nonmarine evaporites (pathways I to III) (sourced from Warren, 2010).*

If the initial brine is enriched in Mg and Ca relative to HCO_3, then the reaction series follows pathway 2 in Fig. 4. Once the initial carbonate precipitation step is complete, the residual brine is left enriched in Mg and Ca, promoting the precipitation of abundant sulphates (e.g., gypsum) (Eugster, 1980; Warren, 2010). Gypsum precipitation of course acts as a chemical divide for Ca and SO_4, with pathway 2 subsequently dividing based upon the relative ionic proportions of Ca and SO_4 remaining after gypsum formation (Fig. 4) (Eugster, 1980).

An initial brine with approximately equivalent concentrations of Mg and Ca relative to HCO_3 will follow pathway 3 in Fig. 4. The formation of abundant alkaline earth

carbonates constitutes the first step in this reaction pathway, inciting a progressive enrichment in Mg relative to Ca, which in turn drives the precipitation of high-Mg calcite, dolomite and magnesite (Eugster, 1980; Warren, 2010, 2021). The brines are subsequently depleted in either HCO_3 or Mg + Ca and can experience gypsum saturation (Eugster, 1980). The subsequent direction of pathway 3 depends upon the concentration of Mg + Ca within the residual brine (Fig. 4) (Warren, 2010).

3. The sulphur cycle and isotope system

3.1. The sulphur cycle

The sulphur cycle in Earth's surface environment is controlled by redox-driven microbial processes and is intimately linked to the cycles of carbon and oxygen (Habicht et al., 2002; Gill et al., 2007). On the modern Earth, the marine sulphate reservoir is relatively large, with a concentration of 28 mM (1.3×10^{21} g) (Canfield, 2004; Fike et al., 2015) and a residence time of ~10 million years (Paytan et al., 2012). The major input of sulphur into the ocean reservoir is the weathering of Ca-sulphate minerals, and the oxidative weathering of sedimentary sulphide minerals, especially pyrite (see Fig. 1) (Faure and Mensing, 2005), the latter of which are unstable in an oxygenated environment (Bottrell and Newton, 2006). Under neutral pH, pyrite weathering occurs most efficiently in the presence of molecular oxygen:

$$2FeS_2 + 4H_2O + 6O_2 \rightarrow 2Fe^{2+} + 4H_2SO_4 \qquad [1]$$

This reaction consumes oxygen, and in conjunction with the oxidation of organic carbon, imparts a control on atmospheric pO_2 (Bottrell and Newton, 2006). Upon the release of sulphur-bearing phases, sulphur is transported by fluvial systems to the

marine reservoir as sulphate. Riverine sulphur is the primary input flux of sulphate into the Earth's oceans, with an estimated magnitude of 1.5 x 10^{14} g/yr (Burke et al., 2018). Anthropogenic sulphur contributes to approximately 30-50 % of the modern input flux (Ivanov, 1981; Burke et al., 2018). In addition to fluvial weathering, seawater sulphate is sourced from volcanic outgassing from terrestrial volcanism and hydrothermal vent systems at mid-ocean ridges, atmospheric dust, biogenic gases, and the biological and inorganic oxidation of sulphide to sulphate (Fig. 5) (Canfield, 2004; Fike et al., 2015).

The major sinks of marine sulphur include the biological production and burial of sulphides (f_{pyrite} = 4 x 10^{13} g/yr) (Fike et al., 2015) (Fig. 5), as well as the incorporation of sulphate into evaporite, and to a lesser extent, carbonate minerals (f_{SO4} = 6 x 10^{13} g/yr) (Canfield and Farquhar, 2009; Fike et al., 2015). The difference between the burial of reduced (sulphide) and oxidised (sulphate) sulphur-bearing species imparts an additional control on surface redox chemistry (Fike et al., 2015).

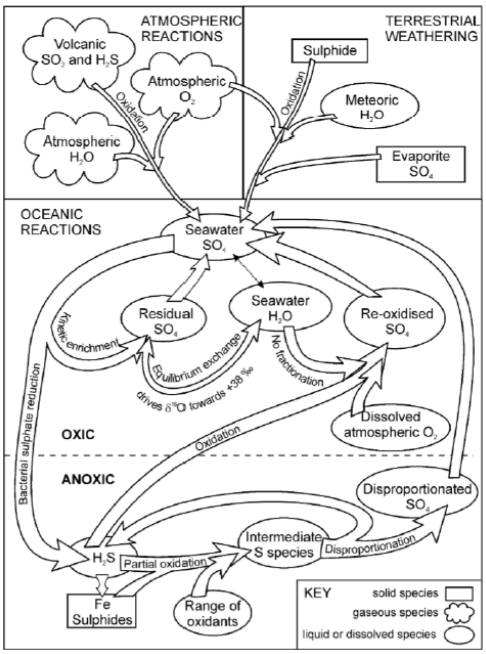

Figure 5: *Diagram depicting the sulphur cycle and its biogeochemical relationship with oxygen (sourced from Bottrell and Newton, 2006).*

In nature, the redox state of sulphur is transformed by microbial processes for metabolic energy conservation (Fike et al., 2015). These metabolic reactions mediate the transfer of sulphur between oxic and reduced reservoirs (Strauss, 1997), and thus contribute to the regulation of Earth's surface chemistry (Faure and Mensing, 2005; Fike et al., 2015). One such process is dissimilatory microbial sulphate reduction (MSR):

$$CH_3CO_2^- + SO_4^{2-} + 3H^+ \rightarrow 2CO_2 + H_2S + 2H_2O \qquad [2]$$

Occurring primarily in anoxic marine sediments, it serves as a major link between the sulphur cycle and the oxygen and carbon cycles (Fike et al., 2015). It involves organic carbon remineralization, whereby organic carbon is oxidised to CO_2 (Jørgensen et al., 2019), and is coupled to the anaerobic oxidation of methane (Knittel and Boetius, 2009). The organic carbon, sourced largely from primary producers, serves as the electron donor, whilst sulphate is reduced, serving as the electron acceptor (Fike et al., 2015). During MSR, the internal enzymatic machinery of anaerobic microorganisms reduces sulphate to sulphide via several intermediate species (Fig. 6) (Fike et al., 2015). Initially, sulphate is actively transported into the cell by membrane-bound sulphate transporter proteins. Upon entry into the cell, the reduction of sulphate can follow the APS (adenosine-5 – phosphosulphate) pathway, whereby sulphate combines with the enzyme ATP sulfurylase to form APS (Canfield, 2001). The subsequent reduction of APS to sulphite is facilitated by APS reductase, after which sulphite is reduced to hydrogen sulphide (H_2S) through several biochemical reactions involving the DsrABC complex (Fike et al., 2015).

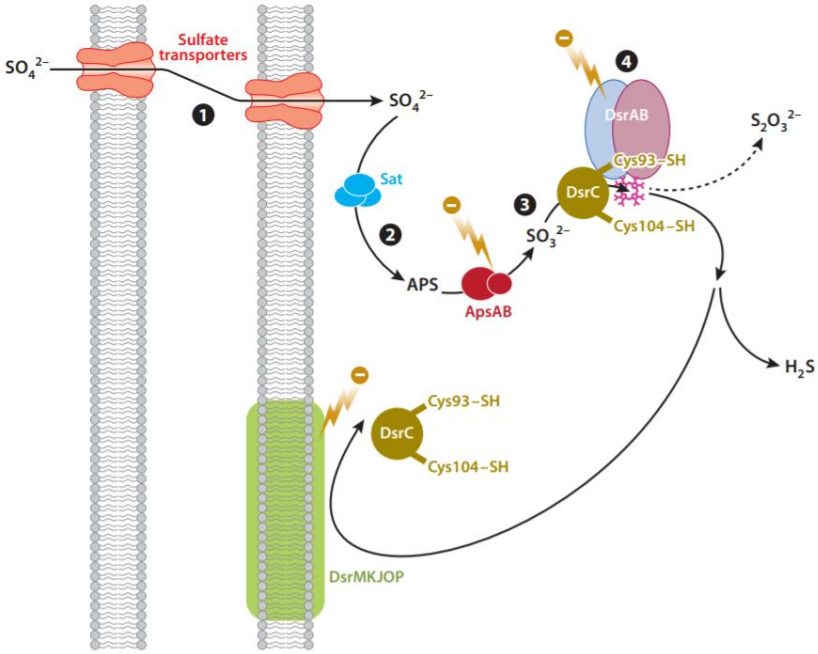

Figure 6: *A depiction of the biochemical process of microbial sulphate reduction, including the major steps and enzymes involved. (1) The transportation of sulphate through the cell wall into the cytoplasm. (2) Sulphate converted to APS by ATP. (3) APS reduced to sulphite by the enzyme APS reductase. (4) The reduction of sulphite to sulphide through reactions involving the DsrABC complex (sourced from Fike et al., 2015).*

Assuming sufficient iron availability, the hydrogen sulphide produced is scavenged for the formation of sedimentary iron sulphide minerals, such as pyrite (Strauss, 1997). Due to its stability over geologic time under conditions of anoxia, pyrite burial represents the most significant sink of sulphur in marine sediments (Jørgensen et al., 2019). The initial reaction between hydrogen sulphide and ferric iron yields a number of different chemical species, including polysulphides, elemental sulphur and pyrite. Several mechanisms for the formation of pyrite in sediments have been discussed. These include the H_2S pathway (Eq. 3), whereby FeS_{aq} reacts with H_2S (Thiel et al., 2019), and the polysulphide pathway (Eq. 4) (Fig. 7), involving reaction between FeS_{aq} and

nucleophilic polysulphide (Rickard and Luther, 2007; Thiel et al., 2019) and the elemental sulphur pathway, where FeS_{aq} reacts with elemental sulphur (S^0) (Liseroudi et al., 2021):

$$FeS + H_2S \rightarrow FeS_2 + H_2 \qquad [3]$$

$$FeS + S_x^{2-} \rightarrow FeS_2 + S_{x-1}^{2-} \qquad [4]$$

The supply of FeS and polysulphide are rate limiting (Yücel et al., 2010; Jørgensen et al., 2019) and local environmental conditions are likely to influence the relative importance of each pathway (Jørgensen et al., 2019). For example, the speciation of sulphide is controlled by pH and redox chemistry, and thus, under acidic and /or anoxic conditions, the H_2S pathway is thought to be more important. Consequently, the H_2S pathway is the dominant mechanisms of pyrite formation in anoxic environments (including many diagenetic settings) where concentrations of HS^- and H_2S are relatively high (Liseroudi et al., 2021). Reactions 4 and 5 occur only in oxic settings under a range of pH values, with some research suggesting that reaction 5 is most common in oxic settings (Liseroudi et al., 2021). However, according to the modelling of pyrite formation in oxidised turbidites, under neutral pH and, the polysulphide pathway dominates assuming FeS and polysulphide are available in sufficient concentrations (Yücel et al., 2010). This remains the case until elemental sulphur (necessary for the formation of polysulphide) is consumed. The H_2S pathway then becomes the dominant mechanism for pyrite formation once elemental sulphur has been exhausted (Jørgensen et al., 2019).

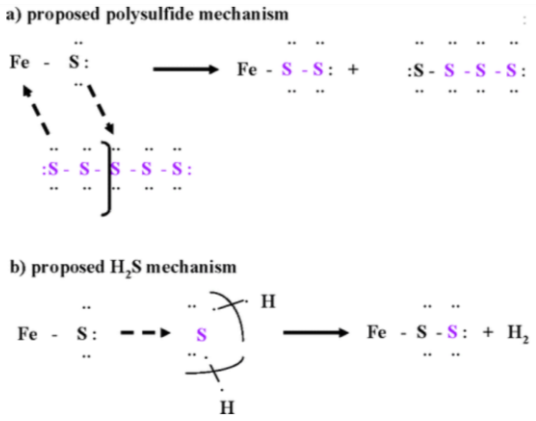

Figure 7: *Mechanisms proposed for the formation of pyrite (sourced from Rickard and Luther, 2007).*

The process of sulphate reduction can be reversed via sulphide oxidation, whereby sulphide minerals (including pyrite) and other reduced sulphur species are oxidised (Fike et al., 2015). This can be pervasive in modern environments (Canfield, 2001), with only a small fraction (1-2%) of biologically synthesised H_2S converted to and buried as pyrite (Finster, 2008). Natural mechanisms are varied and poorly understood, including inorganic oxidation, as well as biological phototrophic and nonphototrophic pathways (Canfield, 2001; Zopfi et al., 2004), with some of the relevant microorganisms coupling this process to metabolic energy conservation (Fike et al., 2015). For sulphide oxidation to occur, electron acceptors (oxic species), such as O_2, are required to balance the oxidation of the reduced sulphur species (Canfield, 2001). Notably, during pathways, the reduced species serve as electron donors necessary for carbon fixation from CO_2, which balances the oxidation process (Canfield, 2001; Fike et al., 2015), demonstrating yet another link between the sulphur, oxygen and carbon cycles.

A number of complex enzymatic systems are involved in the oxidation of reduced sulphur, with the most studied pathways utilising the Sox proteins (Friedrich et al., 2001; Fike et al., 2015). However, chemotrophic and acidophilic bacteria employ different

enzymatic systems (Friedrich, et al., 2005). Depending on the biological and geochemical pathways involved, the sulphide may be oxidised directly or through a variety of reactive S-bearing species of intermediate oxidation states, (Fike et al., 2015), including polysulphides, thiosulphate, elemental sulphur, sulphite and tetrathionate (Canfield, 2001; Fike et al., 2015; Jørgensen et al., 2019). The concentrations of oxyanaions in marine sediments are generally far lower - micromolar or lower (Zopfi et al., 2004).

Elemental sulphur (S^0) is a particularly important intermediary, as its' concentrations in marine sediments is relatively high (Jørgensen et al., 2019), being prominent in a number of sedimentary, aqueous and hydrothermal systems. When the concentrations of oxidants are low relative to sulphide, elemental sulphur can be produced via abiotic pathways, as well as an intermediate during the two-step oxidising of sulphide by phototrophic bacteria (Findlay and Kamyshny, 2017). Importantly, reaction between elemental sulphur and sulphide can yield polysulphide (see Equation 5; Findlay and Kamsyshny, 2017), which is important in a variety of processes of biogeochemical significance, especially pyrite burial (see above) (Jørgensen et al., 2019).

$$x\mathrm{S}^0 + \mathrm{HS}^- \leftrightarrow \mathrm{S}_x^{2-} \qquad [5]$$

$x\mathrm{S}^0$ is elemental sulphur and $\mathrm{S_x}^{2-}$ represents polysulphide species with a range of chain lengths, in a state of chemical equilibrium. Although the above reaction is important for the formation of polysulphides, they can also be formed directly via microbial metabolic processes (Findlay and Kamyshny, 2017).

Sulphide oxidation by chemotrophic bacteria and incomplete MSR can yield thiosulfate, as can a number of abiotic sulphide oxidation pathways when the oxidant to sulphide ratio increases. Thiosulfate can be oxidised through abiotic pathways by Fe(III)

and MnO_2, yielding tetrathionate (Findlay and Kamyshny, 2017). It is consumed by a range of microbial communities (Jørgensen et al., 2019), including chemotrophic and phototrophic bacteria (Findlay and Kamyshny, 2017).

If the ratio of oxidants to sulphide is high, then sulphite, the most oxidised intermediate species, can form. It is more reactive than thiosulfate (Jørgensen et al., 2019), and is quickly converted to sulphate (Findlay and Kamyshny, 2017). It is also consumed by a variety of microorganisms, and thus, due to its' reactivity, rarely accumulates in natural environments (Findlay and Kamyshny, 2017).

Every intermediate species mentioned above can be reduced, oxidised or disproportionated (Findlay and Kamyshny, 2017). As discussed above, sulphide can be oxidised directly to sulphate through a number of intermediate species (Fike et al., 2015; Jørgensen et al., 2019). However, a number of metabolisms have evolved to consume these intermediates. Sulphur disproportionation is a microbiologically driven process that does not require an external electron donor or acceptor, instead certain strains of bacteria consume these intermediate sulphur-bearing species, which simultaneously serve as electron donors and acceptors, yielding hydrogen sulphide and sulphate (Zopfi et al., 2004; Finster, 2008; Fike et al., 2015). The work of Bak and Cypionka (1987) demonstrated that thiosulfate can be disproportionated under anoxic conditions:

$$S_2O_3^{2-} + H_2O \rightarrow SO_4^{2-} + HS^- + H^+ \qquad [6]$$

It was found that a group of sulphate reducing microorganisms, *Desulfovibrio sulfodismutans*, were responsible for the above reaction. Interestingly, they are also capable of disproportionating sulphite:

$$4SO_3^{2-} + H^+ \rightarrow 3SO_4^{2-} + HS^- \qquad [7]$$

Thermodynamic calculations suggest the above reactions can occur under standard conditions, in which the pH is neutral and the concentrations of reactants and products are around 1 M (Fike et al., 2015). It was determined that a relatively large number of strains of sulphur-reducing bacteria conduct these processes (Krämer and Cypionka, 1989). In addition to thiosulfate and sulphite, elemental sulphur can also be disproportionated (Fike et al., 2015):

$$4S^0 + 4H_2O \rightarrow 3H_2S + SO_4^{2-} + 2H^+ \qquad [8]$$

Unlike the disproportionation of thiosulfate and sulphite, the disproportionation of elemental sulphur is endogenic (Finster et al., 2008). Thus, thermodynamic constraints ensure the sulphide produced must remain below 1 mM for elemental sulphur disproportionation, requiring it to be scavenged by iron (Eq. 9) or manganese (Finster et al., 2008; Fike et al., 2015):

$$3S^0 + 2Fe(OH)_3 \rightarrow 2FeS + 2H_2O + SO_4^{2-} + 2H^+ \qquad [9]$$

The biochemistry involved in sulphur disproportionation is complex and poorly understood (Fike et al., 2015). There is some evidence to suggest that enzymes associated with sulphate reduction are involved with the disproportionation of sulphite and thiosulfate (Fike et al., 2015), with some suggesting that APS reductase and APS sulfurylase are utilised to form sulphate via the disproportionation of sulphite and thiosulfate (Krämer and Cypionka, 1989).

The intermediate species necessary for sulphur disproportionation are produced via sulphide oxidation. Although this can occur in anoxic settings, heightened levels of

sulphide common in anoxic water masses limits the growth of some microbes capable of S-disproportionation (see above) (Canfield and Teske, 1996). These factors ensure sulphur disproportionation likely postdates the onset of the oxidative sulphur cycle (Canfield and Thamdrup, 1994; Fike et al., 2015). However, it is interesting to note that Philippot et al. (2007) found evidence suggesting the activity of elemental sulphur disproportionating bacteria in rocks dating to 3.5 Ga. Due to the fact that the disproportionation of elemental sulphur is theoretically limited at high sulphide concentrations, it is hard to assess the role of this process before the widespread oxygenation of Earth's atmosphere ocean system (Finster, 2008). It is likely that sulphur disproportionation did not become globally significant until the Ediacaran (Kunzmann et al, 2017).

3.2. The sulphur isotope system

High-resolution sulphur isotope records can be applied to further elucidate the geochemical history of the ocean-atmosphere system. There exist four stable isotopes of sulphur. ^{32}S is the most abundant, accounting for 95% of the sulphur on Earth. In descending order of abundance, the following most abundant isotopes are ^{34}S, ^{33}S, and ^{36}S (Canfield, 2001). ^{34}S is 6.2 % greater in mass than ^{32}S, facilitating mass-dependent fractionation (Faure and Mensing, 2005). The ratio of ^{34}S to ^{32}S is most commonly used for palaeoredox reconstruction, and the degree of fractionation between two substances, the fractionation factor (α), can be represented mathematically (Marini et al., 2011):

$$\alpha_{x-y} = \frac{(^{34}S/^{32}S)_x}{(^{34}S/^{32}S)_y} \qquad [10]$$

To facilitate inter-laboratory comparison, sulphur stable isotope ratios are expressed in delta notation (δ) in per mil (‰) as deviations from Vienna Canyon Diablo Triolite (VCDT):

$$\delta^{34}S_{sample} = \left[\frac{((^{34}S/^{32}S)_{sample} - (^{34}S/^{32}S)_{standard})}{(^{34}S/^{32}S)_{standard}}\right] * 1000 \qquad [11]$$

The $\delta^{34}S$ of seawater sulphate exhibits a modern value of +21 ‰ (Rees et al., 1978) and is thought to be isotopically homogenous at any given time (Paytan et al., 2012), as the large size and long residence time of seawater sulphate prevents isotopic change at rates >0.5 ‰/Myr (Kah et al., 2004). It is controlled by the respective contributions and the isotopic composition of the fluxes of sulphur entering and exiting the ocean reservoir (Paytan et al., 2012, 2020; Bernasconi et al., 2017). The isotopic composition ($\delta^{34}S$) of fluxes is controlled by the relative contribution of the sources and sinks, each having their own isotopic signature (Bernasconi et al., 2017).

On the modern Earth, the fluvial input flux of sulphate has an average $\delta^{34}S$ value of +4.8 ‰, exhibiting a high degree of spatial variability (Burke et al., 2018), depending upon the isopotic composition of sulphur-bearing phases exposed to the weathering environment within a drainage basin (Paytan et al., 2012). Volcanism is also a minor source of sulphur, however due to its' insignificance relative to other sources and sinks, it generally has a negligible impact on the $\delta^{34}S$ of seawater sulphate (Bernasconi et al., 2017). The incorporation of carbonate associated sulphate (CAS) into carbonate minerals has little impact on the isotopic composition of sulphate (Burdett et al., 1989; Lyons et al, 2004). In addition, the evaporation of seawater and the subsequent crystallisation of gypsum and halite is associated with only a minor degree of fractionation (see below).

The most significant catalyst for the fractionation of sulphur species is the sulphur metabolism of anaerobic bacteria (Fike et al., 2015), such as *Desulfovibrio desulfuricans* (Faure and Mensing, 2005). This includes microbial processes that transform the oxidation state of sulphur to provide energy for growth, especially, but not restricted to, microbial sulphate reduction (Canfield, 2001). The isotopic fractionation that occurs during this metabolic process is poorly understood (Fike et al., 2015). Research findings by Rees (1973) suggest the reduction of APS to sulphite, and sulphite to sulphide yields a fractionation of 25 ‰ against ^{34}S, whilst the cellular uptake of sulphate is accompanied by an inverse fractionation of 3 ‰, in favour of ^{34}S (Johnston, 2010).

Overall, the bacterial reduction of sulphate yields a sulphide product depleted in ^{34}S, preferentially selecting the light isotope (^{32}S) due to its marginally weaker bond when present in the sulphate molecule (Bottrell and Newton, 2006). Canfield and Teske (1996) measured a maximum fractionation of 46 ‰ in pure cultures, however, a later study of pure cultures measured a maximum fractionation of 66 ‰ (Sim et al., 2011a), and a study focusing on natural cultures measured fractionations of 60-70 ‰ (Canfield et al., 2010). It appears that several parameters primarily influence the degree of fractionation during MSR. An association exists between sulphur isotope fractionation during MSR and a range of environmental factors (Habicht et al., 2002; Pasqiuer et al., 2017; Rennie et al., 2018), including seawater sulphate concentrations, with greater sulphate concentrations facilitating higher degrees of fractionation (Habicht et al., 2002). Another significant factor is the cell-specific sulphate reduction rates (csSRR) associated with the microorganisms conducting MSR (Fike et al., 2015). Experimental work with sulphur reducing bacteria have found an inverse relationship between csSRR and sulphur isotope fractionation (Sim et al., 2011b; Sim et al., 2012; Bradley et al., 2016).

Due to the relatively minor fractionation associated with the formation of CAS and evaporitic sulphates, MSR and the burial of pyrite primarily determine the $\delta^{34}S$ of marine sulphate (Bottrell and Newton, 2006). As stated previously, much of the sulphide produced through MSR is reoxidised. When this process is driven by biological systems, it is associated with negligible sulphur isotope fractionations (Canfield, 2001), between 1 and 2 ‰ (Fike et al., 2015). It should be noted, however, that under circumstances of repeated oxidative reworking of sediments, potentially by benthic organisms, oxidative processes may help to regulate the $\delta^{34}S$ of marine sediments (Fike et al., 2015).

Sulphur disproportionation can impart a significant fractionation effect, generating sulphide and sulphate products with distinct isotopic compositions (Fike et al., 2015; Crockford et al., 2019). The ^{34}S-depleted sulphide produced by MSR can be oxidised to S^0 with negligible fractionation, and subsequent disproportionation of S^0 yields sulphate and sulphide, the latter experiencing a 4-9 ‰ ^{34}S depletions relative to S^0 (Fike et al., 2015). Accordingly, repeated cycles of sulphide oxidation and sulphur disproportionation can generate sulphide products that are progressively depleted in ^{34}S (Fig. 8) (Canfield et al., 1998; Fike et al., 2015; Kunzmann et al., 2017). However, it should be noted that under certain conditions, large fractionations up to ~70 ‰ can be produced by sulphate reduction alone (Canfield et al., 2010; Sim et al., 2011a; Wing and Halevy, 2014). Thus, large fractionations in the geological record could be interpreted to reflect either MSR, or the combined influence of MSR and bacterial sulphur disproportionation (Fike et al., 2015).

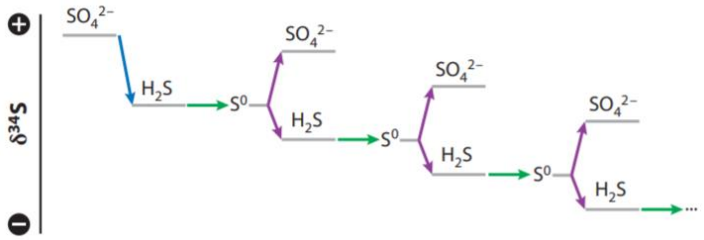

Figure 8: *The impact of sulphate reduction and subsequent sulphide oxidation, followed by the disproportionation of sulphur intermediaries on the $\delta^{34}S$ of sedimentary sulphides. Blue represents sulphate reduction, green represents sulphide oxidation and purple represents sulphur disproportionation (sourced from Fike et al., 2015).*

3.3. Sulphur isotope effects of evaporite crystallisation

The equilibrium fractionation of sulphur isotopes during evaporite precipitation is generally considered negligible (see Bernasconi et al., 2017). The available data is relatively limited; however, it is thought that gypsum and halite formation yield a precipitate with a minor $\delta^{34}S$ enrichment when compared to the $\delta^{34}S$ of sulphate within the parent brine. Studies focusing on gypsum naturally precipitated from seawater report a range of fractionation factors ($\Delta^{34}S_{precipitate\text{-}SW}$) between +0.5 and +4.2 ‰ (Ault and Kulp, 1959; Thode et al., 1961; Thode, 1964; Thode and Monster, 1965; Holser and Kaplan, 1966). Experimental data derived from the artificial precipitation of gypsum under laboratory conditions exhibit a lower range of values, between +1.59 and +2.0 ‰ (Thode and Monster, 1965; Holser and Kaplan, 1966; Nielsen, 1978; Raab and Spiro, 1991; Van Driessche et al., 2016).

Thode and Monster (1965) measured the sulphur isotope fractionation during gypsum precipitation from a solution saturated with $CaSO_4$. Conducted at room temperature, and under reduced pressure for a duration of 24 months, the experiment determined a fractionation of +1.65‰. In an experiment using natural seawater and a

fixed temperature of 30 °C, Holser and Kaplan (1966) determined a $\Delta^{34}S_{precipitate\text{-}brine}$ value of +1.7 ‰ for gypsum, comparable to the value of +1.65 ‰ derived by Nielsen (1978). Also using filtered natural seawater, Raab and Spiro (1991) conducted a stepwise evaporation experiment at room temperature (23.5 °C), establishing a mean $\Delta^{34}S_{precipitate\text{-}brine}$ value of +1.59 ‰ for gypsum. Due to a Rayleigh distillation effect under closed system conditions, the $\delta^{34}S$ of both the brine and precipitate decrease with progressive evaporation, however a comparable $\Delta^{34}S_{precipitate\text{-}brine}$ value is maintained until the middle of the halite stability field (Fig. 9).

Interestingly, the sulphur isotopic effect associated with precipitation within the K- and K-Mg sulphate fields (i.e., at higher salinities) appears distinct (Fig. 9). Unlike for gypsum and halite, the $\delta^{34}S$ of the precipitate is lighter than the $\delta^{34}S$ of the brine (i.e., a negative $\Delta^{34}S_{precipitate\text{-}brine}$ value), and as a result, Rayleigh distillation yields a progressive $\delta^{34}S$ enrichment in both the precipitate and the brine with continued evaporation. In addition, the $\delta^{34}S$ of the brine exhibits an abrupt increase immediately following the halite stability field (Fig. 9) (Raab and Spiro, 1991). The authors interpret these data to suggest a cross-over point at the beginning of the Mg-sulphates field, whereby the $\delta^{34}S$ of the precipitate and the $\delta^{34}S$ of the brine are equal (i.e., a $\Delta^{34}S_{precipitate\text{-}brine}$ value of 0 ‰). In addition, the negative $\Delta^{34}S_{precipitate\text{-}brine}$ value suggests a distinct fractionation factor for the Mg-sulphates and K- Mg-sulphates (Raab and Spiro, 1991).

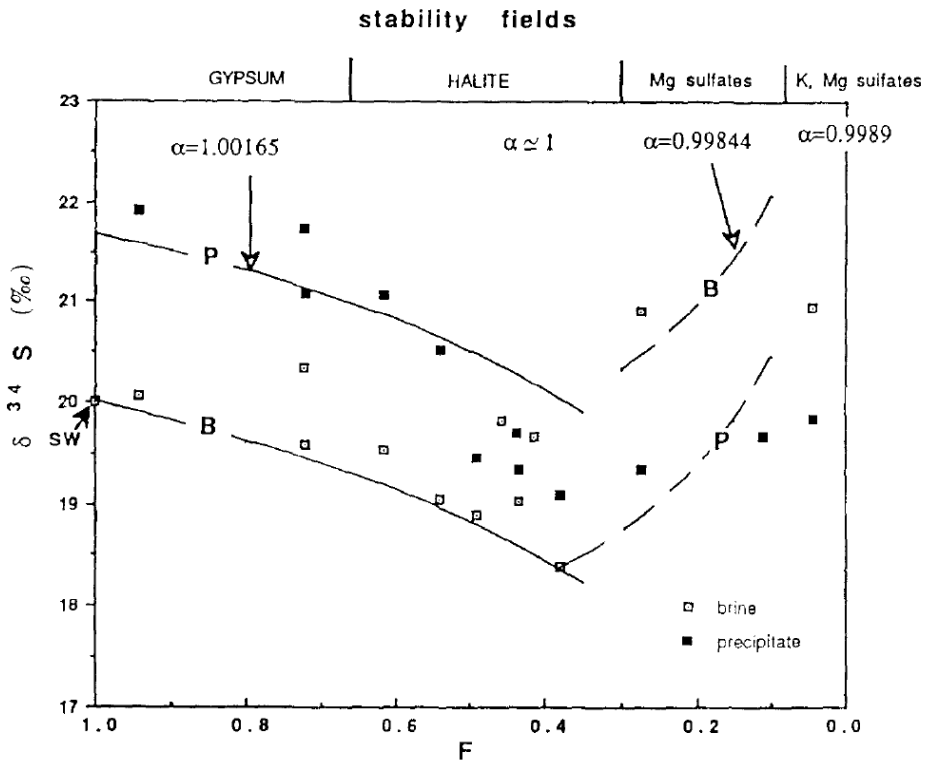

Figure 9: *The sulphur isotope composition ($\delta^{34}S$) of precipitates and parent brines during a stepwise evaporation experiment of natural seawater, plotted against the fraction of sulphate remaining in the solute (F). Rayleigh fractionation curves are included and were calculated using experimentally determined fractionation factors (α) (sourced from Raab and Spiro, 1991).*

The authors suggest the abrupt increase in $\delta^{34}S$ brine at the beginning of the Mg-sulphate stability field simply reflects the small volume of solute remaining at this stage of evaporation, compared to the amount of precipitate formed, and is thus a consequence of the analytical procedure (Raab and Spiro, 1991). In addition, it should be noted that while a distinct fractionation factor for the Mg- and K-, Mg-sulphate fields is intriguing, the precipitates in these fields contained multiple evaporite mineral species. Thus, the fractionation factors estimated for these fields are only rough approximations (Raab and Spiro, 1991). Furthermore, the data resolution is lower from the Mg-sulphate field onwards (Fig. 9), limiting confidence of interpretation.

The experimental work yielded comparable results for sulphur isotope fractionation during gypsum precipitation, however each experiment was conducted at a fixed temperature and thus did not provide insight into the relationship between temperature and sulphur isotope fractionation (Thode and Monster, 1965; Holser and Kaplan, 1966; Nielsen, 1978; Raab and Spiro, 1991). In a more recent effort, Van Driessche et al (2016) conducted an experimental study to determine the influence of temperature, salinity and saturation index on the fractionation factor for sulphur isotopes between aqueous sulphate and gypsum. This work derived a $\Delta^{34}S_{precipitate\text{-}brine}$ value of +2 ‰, which is slightly higher than previous studies, yet small enough to still be considered negligible in natural evaporitic settings. Interestingly, the data suggests a weak relationship between temperature and sulphur isotope fractionation, in that with decreasing temperature the precipitate becomes progressively more depleted relative to the parent brine. However, no temperature dependence was measured under high salinity (4.5 M NaCl) (Van Driessche et al., 2016). Thus, despite the fact temperature is a control on the rate of gypsum precipitation (Van Driessche et al., 2011), no clear relationship between temperature and fractionation factor was measured.

Considering the above discussion, the available data indeed suggest that the degree of sulphur isotopic discrimination during evaporite mineral crystallisation is negligible, at least within the gypsum and halite stability fields. The distinct fractionation factor calculated for the Mg-sulphate and K-, Mg-sulphate stability fields (Raab ad Spiro, 1991) could have implications for interpreting $\delta^{34}S_{evap}$ records in deep time. Caution should be maintained when interpreting $\delta^{34}S_{evap}$ data from evaporites containing highly evaporated minerals, as their precipitation may be associated with a distinct sulphur isotopic discrimination when compared to the precipitation of gypsum and halite.

3.4. Sulphur isotope stratigraphy

It is generally assumed that for much of the Phanerozoic, the relatively long residence time of seawater sulphate has enabled it to maintain $\delta^{34}S$ homogeneity at any given point in geologic time (Paytan et al., 2012). Thus, time equivalent sedimentary sulphates of marine origin will exhibit comparable sulphur isotopic compositions. The abundance of seawater sulphate can prove problematic for isotope stratigraphy, as a large reservoir is less susceptible to isotopic perturbation, with relatively stable $\delta^{34}S$ records precluding high-resolution correlation (Yao et al., 2019; Paytan et al., 2020). However, intervals of variability in the $\delta^{34}S$ seawater sulphate are frequent within the geologic record (Crockford et al., 2019; Present et al., 2020), enabling stratigraphic correlation between sedimentary basins, particularly during periods of substantial $\delta^{34}S$ variability (Yao et al., 2019), such as the Early and Middle Triassic (Claypool et al., 1980; Bernasconi et al., 2017; Crockford et al., 2019; Present et al., 2020).

Sulphur isotope stratigraphy has been widely employed for stratigraphic correlation using marine evaporites, barite and carbonate associated sulphate ($\delta^{34}S_{evap}$, $\delta^{34}S_{barite}$ and $\delta^{34}S_{CAS}$, respectively; see review by Yao et al., 2019). The abundance of barite within pelagic sediments and its' relative resistance to diagenesis (Paytan et al., 1993, 2002, Yao et al., 2019) has enabled the generation of $\delta^{34}S_{barite}$ age curves at high resolution (Fig. 10) (e.g., Paytan et al., 1998, 2004, 2012, 2020; Turchyn et al., 2009; Markovic et al., 2015; Yao et al., 2018, 2020; Toyama et al., 2020). However, barite can generally only provide $\delta^{34}S$ records suitable for stratigraphic correlation across the previous 130 million years, as it is predominantly acquired form pelagic marine sediments (Yao et al., 2019).

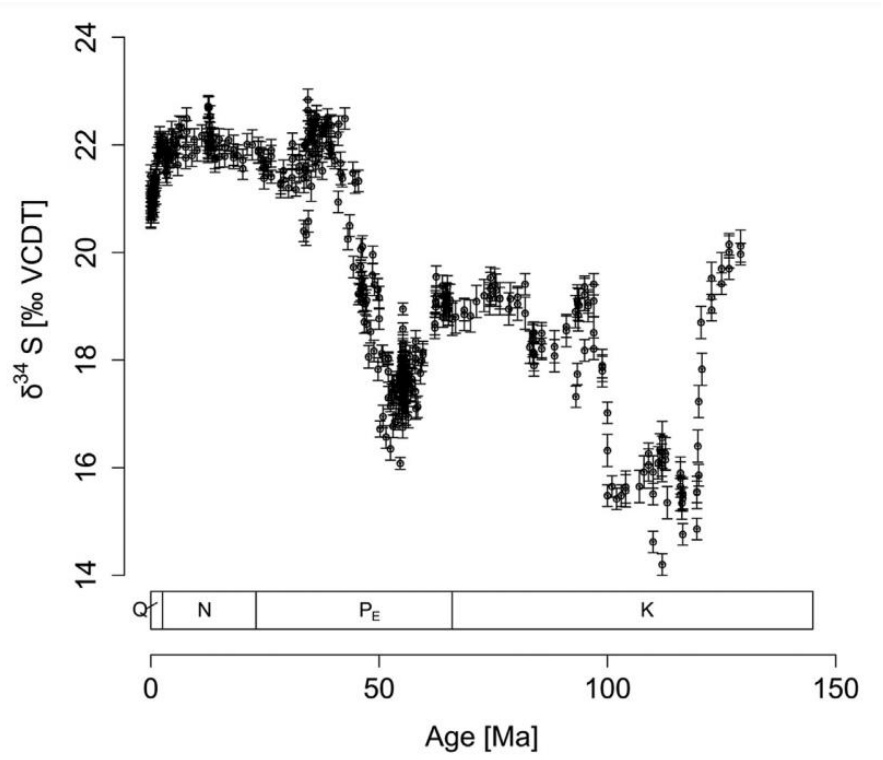

Figure 10: *Sulphur isotope age curve for the previous 130 million years from marine barite (sourced from Paytan et al., 2020).*

$\delta^{34}S_{CAS}$ records have seen widespread use in reconstructing the ancient sulphur cycle (e.g., Newton et al., 2004; Luo et al., 2010; He et al., 2019; 2020), providing chronostratigraphic coverage for time intervals with little evaporite deposition (Kampschulte and Strauss, 2004). However, recent work has emphasised the susceptibility of $\delta^{34}S_{CAS}$ to local diagenetic effects (Rennie and Turchyn, 2014; Present et al., 2015; 2019; Richardson et al., 2019, 2021; Murray et al., 2021; Bryant et al., 2022). Additionally, analytical errors associated with the incomplete separation of CAS from isotopically distinct non-CAS phases can contribute to scatter in $\delta^{34}S_{CAS}$ records (Wotte et al., 2012). In some instances, comparisons between coeval $\delta^{34}S_{barite}$, $\delta^{34}S_{evap}$ and $\delta^{34}S_{CAS}$ suggest the latter can preserve a primary seawater signal (Rennie et al., 2018; Toyama et al., 2020; Edward et al., 2024). However, in the case of the Permian-Triassic boundary (PTB), $\delta^{34}S_{CAS}$ exhibits greater variability than $\delta^{34}S_{evap}$ (Fig. 11), attributed to

the effects of diagenetic overprinting of CAS, whilst evaporitic sulphate appears to provide a primary seawater signal more consistently (Bernasconi et al., 2017; Johnson et al., 2021).

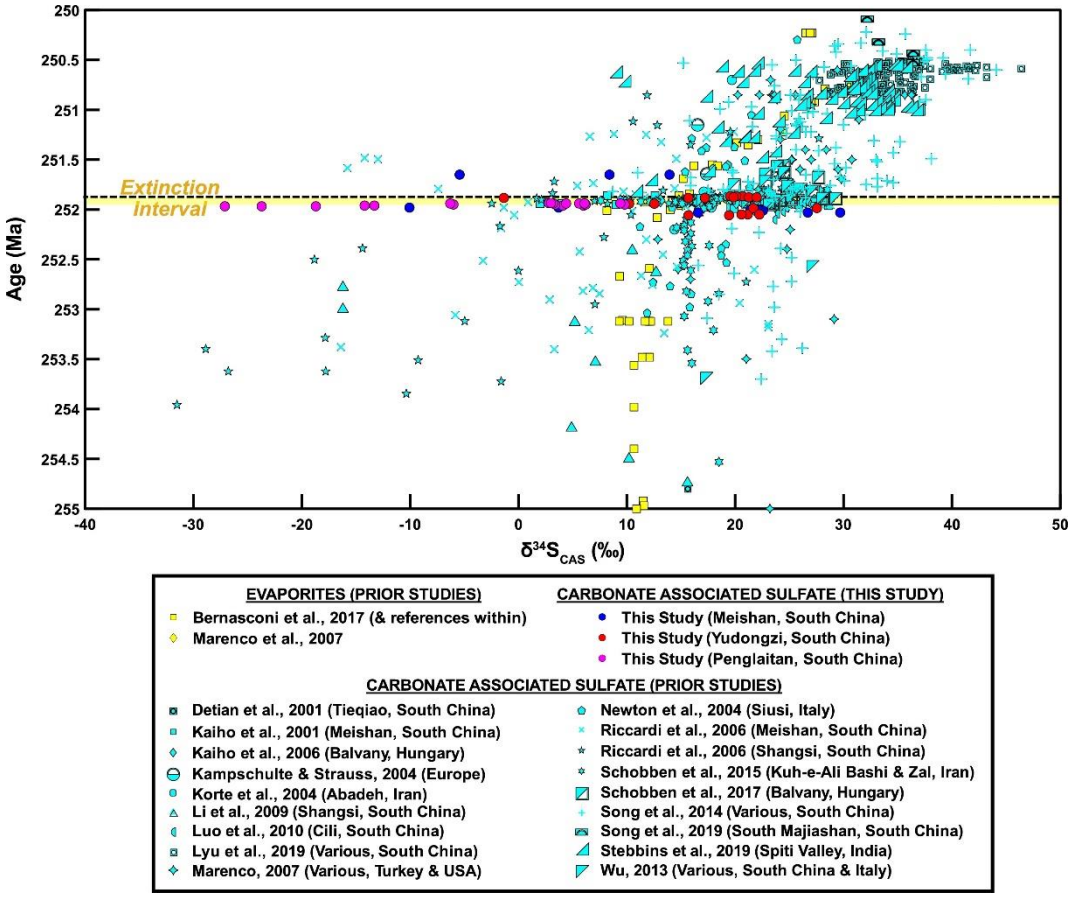

Figure 11: *A comparison between the $\delta^{34}S_{evap}$ and $\delta^{34}S_{CAS}$ data across the Permian-Triassic boundary (sourced from Johnson et al., 2021).*

One of the major issues with the use of evaporites for the development of seawater sulphate $\delta^{34}S$ curves is the discontinuous nature of evaporite deposits within the geologic record (Bernasconi et al., 2017). Large scale marine evaporite deposition is dependent upon specific climatic, environmental, and tectonic conditions (Hardie, 1991; Warren, 2010), and thus their occurrence within the sedimentary record is often sporadic. As a result, $\delta^{34}S_{evap}$ records commonly lack temporal coverage for some geologic time intervals (Yao et al., 2019). The first attempts to derive long-term $\delta^{34}S$

seawater sulphate ($\delta^{34}S_{SO4}$) records from marine evaporites utilised discrete $\delta^{34}S_{evap}$ datasets to produce composite $\delta^{34}S_{evap}$ age curves (Holser and Kaplan, 1966; Claypool et al., 1980). These efforts presented a view of the broad, long-term evolution of seawater $\delta^{34}S_{SO4}$ during the Phanerozoic, but lacked the chronostratigraphic coverage necessary for high-resolution correlation (Fig. 12). Subsequent studies have built upon this, utilising $\delta^{34}S_{evap}$ datasets available since the publication of the original records, but issues with temporal coverage persist for certain time intervals (see Crockford et al., 2019; Present et al., 2020).

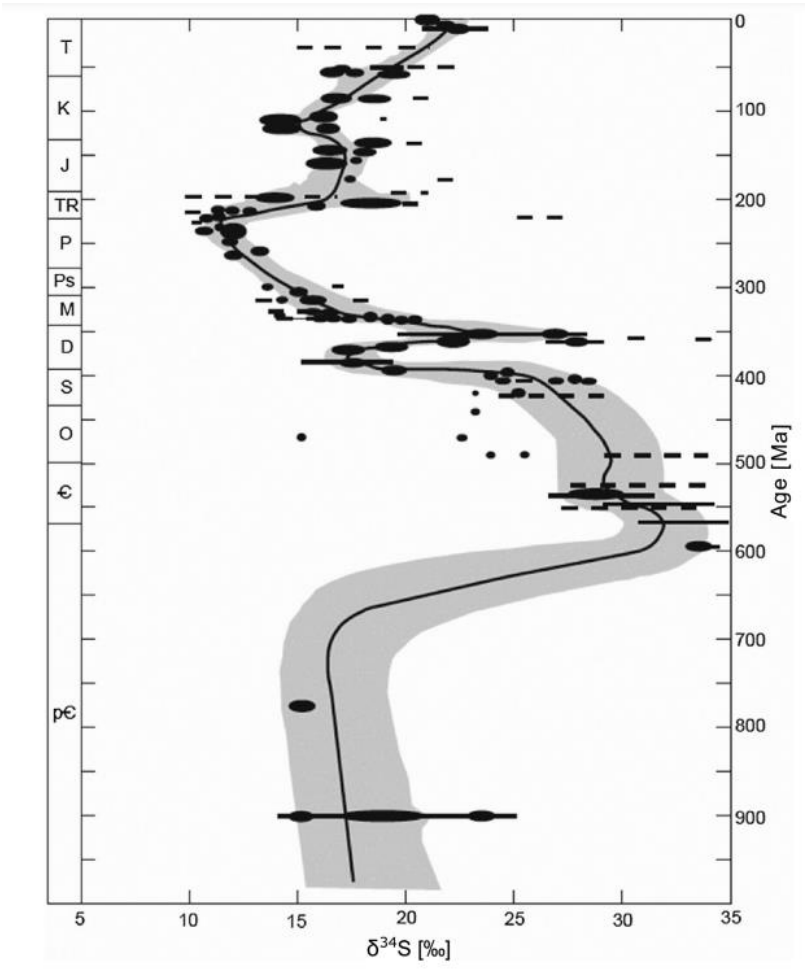

Figure 12: *$\delta^{34}S_{evap}$ age curve for the previous 1 Ga. Solid vertical lines represent the data of Claypool et al. (1980) and data the authors compiled from published literature plotted against their most likely age. Dashed vertical lines represent the $\delta^{34}S_{evap}$ range*

based upon a small number of analyses. The solid black line is the author's best estimate for the $\delta^{34}S$ of seawater sulphate based upon the evaporite data and the grey shading represents the uncertainty associated to the seawater sulphate $\delta^{34}S$ curve. (Sourced from Paytan et al., 2020).

An exception to this is the European Permian-Triassic. The sedimentary environment was largely arid and continental (with episodic marine influence) (Parrish, 1993), facilitating widespread evaporite deposition, with marine evaporites providing relatively consistent coverage of the Triassic time interval (McKie, 2017). Thus, the abundance of evaporites within European Triassic strata and their apparent ability to preserve a primary $\delta^{34}S$ seawater signal, at least for the PTB (Bernasconi et al., 2017; Johnson et al., 2021), have motivated the use of $\delta^{34}S_{evap}$ records for high-resolution correlation of the European Permian-Triassic (Bernasconi et al., 2017; Ortí et al., 2014, 2022).

3.5. The Permian-Triassic $\delta^{34}S_{evap}$ record

The late Permian-Triassic time interval is associated with several major perturbations in the sulphur cycle, recorded as variability in $\delta^{34}S_{evap}$ (Claypool et al., 1980; Bernasconi et al., 2017). The rate and magnitude of observed $\delta^{34}S_{evap}$ variability permits the development of Triassic $\delta^{34}S_{evap}$ records suitable for high-resolution stratigraphic correlation. This is of particular value to the European Triassic, as evaporites typically lack fossils for biostratigraphy, ensuring much of the European late Permian-Triassic commonly lacks chronostratigraphic constraint (McKie, 2017). Bernasconi et al. (2017) produced and compiled $\delta^{34}S_{evap}$ data from multiple sedimentary basins, creating a composite $\delta^{34}S_{evap}$ curve spanning the latest Permian through to the Norian of the Late Triassic from sulphates of northern Switzerland and the western Tethys (Fig. 13). Their

efforts greatly expanded the coverage of the $\delta^{34}S_{evap}$ record across the Anisian, Ladinian and Carnian (Bernasconi et al., 2017), and demonstrated the suitability of $\delta^{34}S_{evap}$ records for high-resolution correlation of the European Triassic.

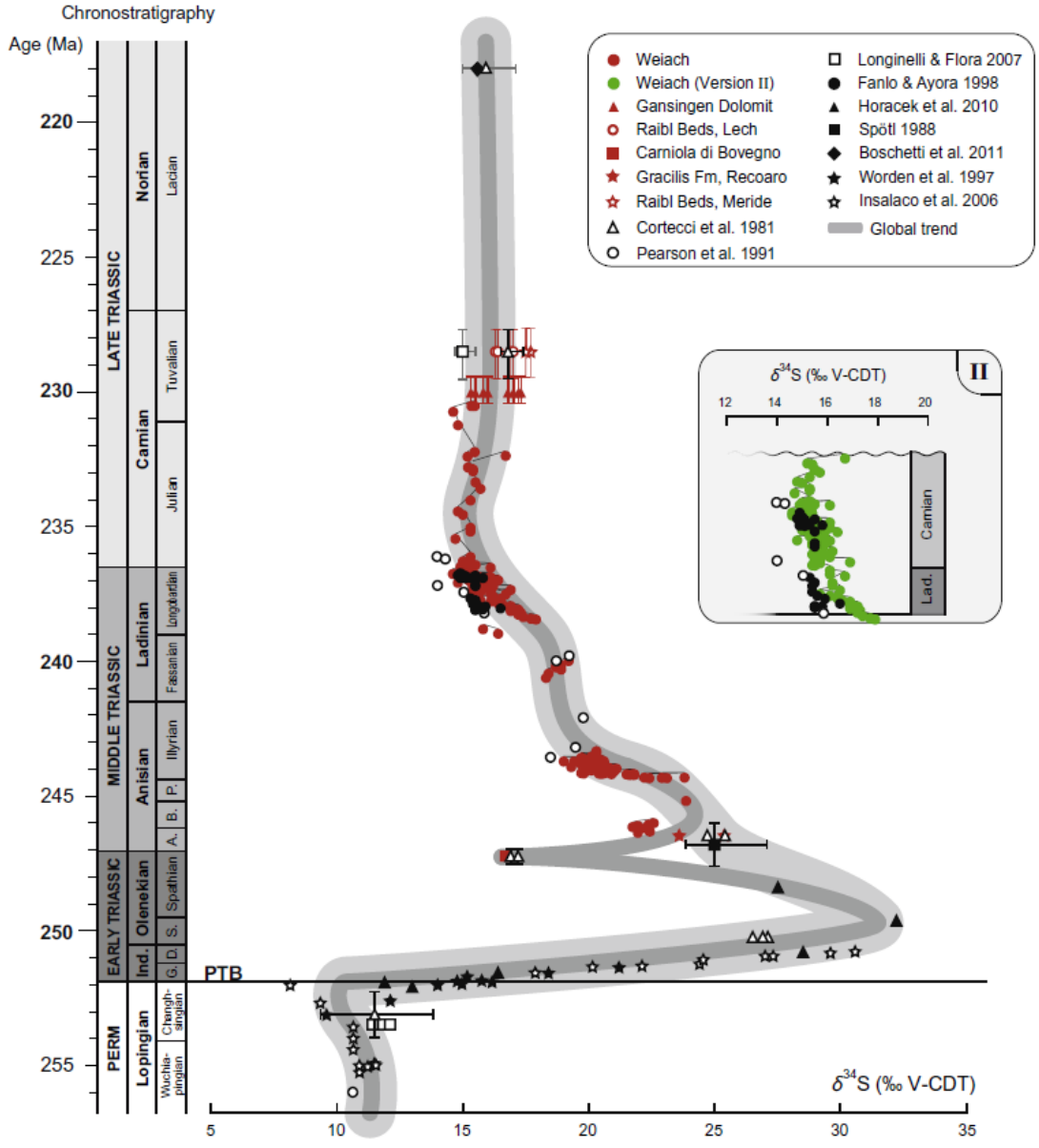

Figure 13: *Global composite $\delta^{34}S_{evap}$ age curve from the Lopingian (Late Permian) through to the late Norian (Late Triassic). The red points represent the original data of Bernasconi et al. (2017), while the black and grey symbols are from previously published literature. The thick light grey line is a visual fit of the data, without including the depleted $\delta^{34}S_{evap}$ values at the Olenekian-Anisian boundary (OAB). The thin dark*

grey line is a fit of the data assuming the depleted values at the OAB are a global seawater signal. The inset displays an alternative chronostratigraphy for the Gipskeuper. (Sourced from Bernasconi et al., 2017).

The PTB and Early Triassic exhibits a major positive $\delta^{34}S_{evap}$ excursion, recording an abrupt rise in the $\delta^{34}S$ of seawater sulphate from values around +12 ‰ that had been maintained in a state of relative stability for much of the latest Permian (Claypool et al., 1980; Crockford et al., 2019; Present et al., 2020), to >+30 ‰ in the earliest Triassic (Fig. 13) (Bernasconi et al., 2017). The current consensus attributes the primary driver of this isotopic shift to an enhancement of the pyrite burial flux, as a response to heightened weather rates and the expansion of anoxia related to the emplacement of the Siberian Traps Large Igneous Province (Newton et al., 2004; Bernasconi et al., 2017). Although environmental and climatic change associated with Siberian Traps volcanism was the likely trigger for the observed positive $\delta^{34}S_{evap}$ excursion, it has been suggested that the large magnitude of the isotopic shift was facilitated by low seawater sulphate concentrations (Newton et al., 2004; Bernasconi et al., 2017), possibly related to the deposition of the sulphate-rich Zechstein evaporites during the late Permian (Hay et al., 2006).

The $\delta^{34}S_{evap}$ record of Bernasconi et al. (2017) suggested two possible scenarios for the cessation of the Early Triassic $\delta^{34}S_{evap}$ positive excursion. A gradual decline that continues into the Middle Triassic, or an abrupt negative $\delta^{34}S_{evap}$ excursion at the Early-Middle Triassic boundary that interrupts the otherwise gradual declining trend in $\delta^{34}S_{evap}$ (Fig. 13). It is currently unclear which of these two scenarios is most likely. However, it should be emphasised that the low $\delta^{34}S_{evap}$ values (~+17 ‰) at the Early-Middle Triassic boundary reported by Cortecci et al. (1981) and Bernasconi et al. (2017)

are all from the Carniola di Bovegno Formation, western Southern Alps. As a result, it is difficult to confidently distinguish between a signal reflecting local depositional processes and one that records a global signal of seawater sulphate.

If the negative excursion is a primary global signal, then the observed isotopic depletion was only a transient feature, as $\delta^{34}S_{evap}$ values abruptly recover to ~+25 ‰ (Fig. 13) (Bernasconi et al., 2017). Such substantial variability in $\delta^{34}S_{evap}$ would suggest seawater sulphate concentrations remained low throughout the Early Triassic. However, if the negative $\delta^{34}S_{evap}$ excursion reported is a local signal, then a more gradual decline in $\delta^{34}S_{evap}$ could be evidence to suggest seawater sulphate concentrations recovered more quickly from a minimum at the PTB, with the recovery beginning before the onset of the Middle Triassic (Bernasconi et al., 2017). Further work should endeavour to construct additional $\delta^{34}S_{evap}$ records across the Early-Middle Triassic boundary. If the abrupt decline in $\delta^{34}S_{evap}$ reported by Cortecci et al. (1981) and Bernasconi et al. (2017) can be reproduced through the analysis of time equivalent evaporites in geographically distinct sedimentary basins, then this would suggest the negative $\delta^{34}S_{evap}$ excursion in the Carniola di Bovegno Formation is a primary seawater signal useful for stratigraphic correlation across OAB sections globally.

The $\delta^{34}S_{evap}$ record exhibits a more gradual decline through the Middle Triassic, until achieving relative stability around +15 ‰ in the early Carnian, Late Triassic (Fig. 13) (Bernasconi et al., 2017); potentially reflecting an end to the climatic extremes of the Early Triassic (Sun et al., 2012; Trotter et al., 2015). In addition, modelling efforts suggest seawater sulphate concentrations were higher by the Middle Triassic (Bernasconi et al.,

2017; Stebbins et al., 2019), making the sulphate reservoir less susceptible to isotopic perturbation.

The $\delta^{34}S_{evap}$ record of Bernasconi et al. (2017) lacks resolution beyond the Carnian-Norian boundary. Recently, Ortí et al. (2022) produced and compiled $\delta^{34}S_{evap}$ data to create a composite curve for eastern Iberia, spanning the Middle Triassic through to the Early Jurassic. The authors successfully correlate Iberian sulphates to those of central Europe through comparison with the record of Bernasconi et al. (2017) and established a low resolution $\delta^{34}S_{evap}$ record across the Triassic-Jurassic boundary (TJB). However, this record lacks resolution. The reason for this is the fragmented nature of the Iberian Triassic stratigraphy, which underwent remobilisation and deformation during rifting in the Jurassic and Cretaceous, followed by orogenesis in the Miocene (Pérez-López, 1998). As a result, the authors sampled distinct outcrops, constructing a composite sulphur isotope curve by calculating an average $\delta^{34}S_{evap}$ value for each geologic unit (Ortí et al., 2022). This extended the time coverage of the Triassic $\delta^{34}S_{evap}$ record, however the averaging of $\delta^{34}S_{evap}$ values for each unit ensured the data resolution was lower than that of Bernasconi et al. (2017), preventing the establishment of high-resolution $\delta^{34}S_{evap}$ correlation schemes.

Currently, high-resolution $\delta^{34}S_{evap}$ records are lacking for the Rhaetian-Hettangian, including sparse, low-resolution $\delta^{34}S_{evap}$ data from halites of onshore Morocco (Clement and Holser, 1988), Ca-sulphates of the Anhydrite Zone, Spain (Ortí et al., 2014; 2022) and halites of offshore northeast Canada (Holser et al., 1988). At each site, the precise position of these data relative to the TJB is poorly understood, due to a scarcity of fossils for biostratigraphy and an absence of complementary organic carbon

isotope ($\delta^{13}C_{org}$) data. Interestingly, the $\delta^{34}S_{evap}$ records broadly assigned to the TJB exhibit relative stability (Clement and Holser, 1988; Holser et al., 1988; Ortí et al., 2014; 2022), which is intriguing considering the geochemical (Ruhl et al., 2011; He et al., 2020, 2022; Bond et al., 2023) and biotic (Sepkowski, 1996; Wignall and Atkinson, 2020) perturbations recorded across this time interval. Better age constraint and higher resolution $\delta^{34}S_{evap}$ records are required before confidant inferences can be made regarding the sulphur cycle across the Rhaetian and TJB.

Thus, while the established $\delta^{34}S_{evap}$ records for the late Permian-Triassic provide an excellent basis from which to establish further global correlation schemes, it is clear in light of the above discussion that gaps in the spatial and temporal resolution still persist. The UK Triassic is characterised by abundant evaporites, with intervals of bedded halites commonly interspersed with nodular and bedded gypsum/anhydrite throughout the latest Permian, as well as the Middle and Late Triassic (e.g., Tucker, 1991; Jackson and Johnson, 1996; Howard et al., 2008). Episodic marine flooding is evidenced by marine fossils in various locations (Warrington, 1974; Warrington, 1995; Ambrose and Wakefield, 2015; Warrington and Pollard, 2021). This and the abundance of evaporitic material, would suggest the UK Triassic is ideal for the application of sulphur isotope stratigraphy, providing a clear opportunity to expand the spatial and temporal coverage of the Triassic $\delta^{34}S_{evap}$ age curve.

4. Thesis outline

The research in this thesis is presented in paper format, with chapters 2 through 5 being manuscripts for publication, each representing a complete study. Thus, they include a standalone abstract, introduction, methodology, results, discussion, and conclusion.

These chapters either have, or will be, submitted for publication, and I have noted the relevant co-authors at the beginning of each. Overall conclusions and suggestions for future work are presented in Chapter 6. The following section of this introductory chapter provides a brief synopsis of chapters 2 through 5.

4.1. Chapter 2: An 80-million-year sulphur isotope record of pyrite burial over the Permian-Triassic

This chapter was published in *Scientific Reports,* ***12, 17370, 2022***. Co-authors include Darren R. Gröcke, H.D.R. Ashleigh Cheung, Lee R. Kump, Tom McKie and Alastair Ruffell.

In this chapter, I present a $\delta^{34}S_{evap}$ record from drillcore Staithes S-20, Yorkshire northeast, England. The record spans the uppermost Zechstein, the Bunter Shale and Bunter Sandstone (Sherwood Sandstone Group), and the Mercia Mudstone Group (MMG). At the time of publication, these data represent the most complete $\delta^{34}S_{evap}$ record for the UK Triassic. In addition, a refined global composite $\delta^{34}S_{evap}$ curve is established, incorporating multiple composite Triassic $\delta^{34}S_{evap}$ age curves as well as additional $\delta^{34}S_{evap}$ data from Triassic evaporites globally. An unconformity, likely the Hardegsen Unconformity, ensures the record of Staithes S-20 fails to capture the positive $\delta^{34}S_{evap}$ excursion characteristic of the Early Triassic. Otherwise, the data from Staithes S-20 compare well with the global $\delta^{34}S_{evap}$ age curve, enabling correlation and providing additional chronostratigraphic calibration beyond that which is achievable based upon sparse biostratigraphy alone.

The establishment of a correlation scheme between Staithes S-20 and the global composite sulphur isotope age curve enabled the generation of a composite $\delta^{34}S_{evap}$, incorporating the global data and that of Staithes S-20. This composite dataset was

assimilated into the biogeochemical box model of Kurtz et al. (2003), enabling reconstruction of the pyrite burial flux across the Triassic time interval based upon our $\delta^{34}S_{evap}$ data.

4.2. Chapter 3: Sulphur isotope stratigraphy of drill cuttings and stratigraphic correlation of Permian-Triassic evaporites

This chapter was published in *Frontiers in Earth Science,* ***11, 1216365, 2023***. Co-authors include Darren R. Gröcke and Tom McKie.

The chapter presents a $\delta^{34}S_{evap}$ record generated from well 42/28-2, of the southern North Sea, UK sector. The $\delta^{34}S_{evap}$ data span from the uppermost Zechstein, the Bunter shale and sandstone and through to the uppermost Mercia Mudstone Group. The $\delta^{34}S_{evap}$ record of 42/28-2 compares well with the $\delta^{34}S_{evap}$ record of Staithes S-20, enabling stratigraphic correlation. Equivalent gamma ray logs were used for correlation and compared with the $\delta^{34}S_{evap}$-based correlation scheme. Not only does this further confirm the applicability of sulphur isotope stratigraphy for correlating the UK Triassic, but it is also particularly significant as the sampled interval in 42/28-2 is composed entirely of drill cuttings. Due to the ubiquity of drill cuttings, their apparent suitability for evaporite-based sulphur isotope stratigraphy substantially increases the number of sites available for sampling and sulphur isotope analysis, presenting the potential to greatly expand the geospatial coverage of the Triassic $\delta^{34}S_{evap}$ age curve.

Finally, $\delta^{34}S_{evap}$ data from the Bunter Shale and Bunter Sandstone of both Staithes S-20 and 42/28-2 appear to agree well with $\delta^{34}S$ range established for late Permian seawater sulphate. As a result, we propose that the Bunter Shale and lower Bunter Sandstone could be assigned to the latest Permian towards the basin margins in

the western Southern North Sea, UK sector. This would of course imply that, in this location, the Permian-Triassic boundary (PTB) should be shifted vertically to a position likely within the Sherwood Sandstone Group (SSG). Although due to erosion associated with the Hardegsen Unconformity, we are unable to establish the precise placement of the PTB.

4.3. Chapter 4: Sulphur isotope stratigraphy of the Triassic Sherwood Sandstone and Mercia Mudstone groups, United Kingdom

This chapter is not yet published. However, we intend to submit it for publication in *Depositional Record*. Co-authors include Darren R. Gröcke, Tom McKie, H.D.R. Ashleigh Cheung, and Robert Raine.

In this chapter, we further report $\delta^{34}S_{evap}$ data from the SSG of the Larne Basin, Northern Ireland, as well as the Mercia Mudstone Group of the Larne Basin, East Irish Sea Basin (EISB) and Wessex Basin. In the case of the $\delta^{34}S_{evap}$ data from the SSG of the Larne Basin, $\delta^{34}S_{evap}$ values from the lowermost SSG of drillcore GT-01 Kilroot appear to compare well with values for Permian seawater sulphate, whilst $\delta^{34}S_{evap}$ data from the uppermost SSG from drillcore Cairncastle-2 appear to compare well with the composite $\delta^{34}S_{evap}$ curve across the Early-Middle Triassic boundary, the established chronostratigraphic position of the SSG-MMG lithostratigraphic boundary in this location. These data would appear to confirm the possible preservation of marine $\delta^{34}S_{evap}$ values in the SSG.

For the MMG in the EISB, our $\delta^{34}S_{evap}$ record of 110/13-8 appears to correlate relatively well with the global composite and the equivalent $\delta^{34}S_{evap}$ records of Staithes S-20 and 42/28-2 and presents the first $\delta^{34}S_{evap}$ curve from the EISB at this resolution.

Using our $\delta^{34}S_{evap}$ records, and the available biostratigraphic data, we establish a correlation scheme between Staithes S-20, 42/28-2, 110/13-8, GT-01 Kilroot, Cairncastle-2 and the global composite age curve, presenting the highest resolution $\delta^{34}S_{evap}$-based correlation scheme for the UK Triassic.

The $\delta^{34}S_{evap}$ data from the MMG of Carnduff-02, Larne Basin, and Burton Row, Wessex Basin, fail to correlate with the global composite. We suggest this may reflect hydrologic isolation from the seawater sulphate reservoir during evaporite deposition, with the $\delta^{34}S_{evap}$ signal being overwhelmed by isotopically distinct terrestrial sulphate inputs. Although far more research is required, our data suggest a state of spatial and temporal variability in the degree of marine influence during evaporite deposition across the UK Triassic.

4.4. Chapter 5: Biogeochemical changes within a hypersaline sabkha of the late Permian Eden Shales, UK: Stable isotopes and organic geochemistry

This chapter is not yet published. However, we intend to submit it for publication in *Organic Geochemistry*. Co-authors include Vincent Grossi, Eva E. Stüeken, Balkis Eddhif, Arnauld Vinçon-Laugier, Ross Collin, Tom McKie, and Darren R. Gröcke.

The chapter presents a suite of stable isotopic and organic geochemical data from the late Permian Eden Shales (evaporite beds A, B and C), Vale of Eden, Cumbria, UK. Two biogeochemically distinct stages can be identified within the stratigraphy. Stage 1 (A Bed) is interpreted to represent deposition within a hydrologically isolated playa lake system, in line with previous sedimentological and lithostratigraphic interpretations. Partial denitrification likely generated an enrichment in $\delta^{15}N_{tot}$, while inputs of terrestrial plant biomass, possibly derived from the stratigraphically equivalent

Hilton Plant Beds, was transported into the paya lake system, inciting an increase in C/N ratios. The $\delta^{34}S_{evap}$ record during Stage 1 exhibits a negative excursion to values < 0 ‰. While we cannot rule out the possibility that this reflects microbially mediated sulphur cycling during deposition, we suggest the most likely explanation is the late-stage diagenetic remobilisation of sulphate. This would have formed gypsum veins, which are rather abundant in A Bed, and may have incorporated isotopically light sulphate derived from the oxidation of sedimentary sulphides.

We suggest that Stage 2 (beds B and C) may reflect an interval of greater marine influence, due to the $\delta^{34}S_{evap}$ data comparing well with late Permian seawater sulphate. Variability in the $\delta^{34}S$ of pyrite sulphide is broadly concomitant with isorenieratane and okenane, which together may suggest the expansion and photic zone euxinia. In addition, highly enriched $\delta^{13}C_{org}$ values (> 0 ‰) are broadly concomitant with the detection of β-carotane and a low Pr/Ph ratio. Together, these data may suggest an ^{13}C-enrichment in the bulk organic carbon pool due to heightened levels of salinity and cyanobacterial productivity.

5. References

Ambrose, K., and Wakefield, O. (2015). Permo-Triassic rocks of Nottingham. *Mercian Geol.* 18, 260–263.

Andeskie, A.S., Benison, K.C., Eichenlaub, L.A., Raine, R., 2018. Acid-saline-lake systems of the Triassic Mercia Mudstone Group, County Antrim, Northern Ireland. *J. Sediment. Res.* 88, 385-398. DOI: 10.2110/jsr.2018.14

Ault, W.U., Kulp, J.L., 1959. Isotopic geochemistry of sulphur. *Geochim. Cosmochim. Acta*, 16, 201-235. DOI: 10.1016/0016-7037(59)90112-7

Babel, M., Schreiber, B.C., 2014. "Geochemistry of evaporites and evolution of seawater", in *Treatise on geochemistry, second edition*. Editors: Holland, H.D., Turekian, K.K., (Oxford: Elsevier) 9, 483-560. DOI: 10.1016/B978-0-08-095975-7.00718-X

Bak, F., Cypionka, H., 1987. A novel type of energy metabolism involving fermentation of inorganic sulphur compounds. *Nature*, 326, 891-892. DOI: 10.1038/326891a0

Bernasconi, S.M., Meier, I., Wohlwend, S., Brack, P., Hochuli, P.A., Bläsi, H., Wortmann, U.G., Ramseyer, K., 2017. An evaporite-based high-resolution sulfur isotope record of Late Permian and Triassic seawater sulfate. *Geochim. Cosmochim. Acta*, 204, 331-349. DOI: 10.1016/j.gca.2017.01.047

Bond, A.D., Dickson, A.J., Ruhl, M., Bos, R., van de Schootbrugge, B., 2023. Globally limited but severe shallow-shelf euxinia during the end-Triassic extinction. *Nat. Geosci.* 16, 1181-1187. DOI: 10.1038/s41561-023-01303-2

Bottrell, S.H., Newton, R.J., 2006. Reconstruction of changes in global sulfur cycling from marine sulfate isotopes. *Earth-Sci. Rev.* 75, 59-83. DOI: 10.1016/j.earscirev.2005.10.004

Bradley, A.S., Leavitt, W.D., Schmidt, M., Knoll, A.H., Girguis, P.R., Johnston, D.T., 2016. Patterns of sulfur isotope fractionation during microbial sulfate reduction. *Geobiology*, 14, 91-101. DOI: 10.1111/gbi.12149

Bryant, R.N., Present, T.M., Ahm, A-S.C., McClelland, H-L.O., Razionale, D., Blättler, C.L., 2022. Early diagenetic constraints on Permian seawater chemistry from the Capitan Reef. *Geochim. Cosmochim. Acta*, 328, 1-18. DOI:10.1016/j.gca.2022.04.027

Burdett, J.W., Arthur, M.A., Richardson, M., 1989. A Neogene seawater sulfur isotope age curve from calcareous pelagic microfossils. *Earth Planet. Sci. Lett.* 94, 189-198. DOI: 10.1016/0012-821X(89)90138-6

Burgess, S.D., Bowring, S.A., 2012. A high-precision geochronology confirms voluminous magmatism before, during, and after Earth's most severe extinction. *Sci. Adv.* 1, 1-14. DOI: 10.1126/sciadv.1500470

Burke, A., Present, T.M., Paris, G., Rae, E.C.M., Sandilands, B.H., Gaillardet, J., Peucker-Ehrenbrink, Fischer, W.W., McClelland, J.W., Spencer, R.G.M., Voss, B.M., Adkins, J.F., 2018. Sulfur isotopes in rivers: Insights into global weathering budgets, pyrite oxidation, and the modern sulfur cycle. *Earth Planet. Sci. Lett.* 496, 168-177. DOI: 10.1016/j.epsl.2018.05.022

Canfield, D.E., 2001. Biogeochemistry of sulfur isotopes. *Rev. Mineral. Geochem.* 43, 607-636. DOI: 10.2138/gsrmg.43.1.607

Canfield, D.E., 2004. The evolution of the Earth surface sulfur reservoir. *Am. J. Sci.* 304, 839-861. DOI: 10.2475/ajs.304.10.839

Canfield, D.E., Farquhar, J., 2009. Animal evolution, bioturbation, and the sulfate concentration of the oceans. *Proc. Natl. Acad. Sci.* 106, 8123-8127. DOI: 10.1073/pnas.0902037106

Canfield, D.E., Farquhar, J., Zerkle, A.L., 2010. High isotope fractionations during sulfate reduction in a low-sulfate euxinic ocean analog. *Geology*, 38, 415-418. DOI: 10.1130/G30723.1

Canfield, D.E., Teske, A., 1996. Late Proterozoic rise in atmospheric oxygen concentration inferred from phylogenetic and sulphur-isotope studies. *Nature*, 382, 127-132. DOI: 10.1038/382127a0

Canfield, D.E., Thamdrup, B., 1994. The production of ^{34}S-depleted sulfide during bacterial disproportionation of elemental sulfur. *Science*, 266, 1973-1975. DOI: 10.1126/science.11540246

Canfield, D.E., Thamdrup, B., Fleisher, S., 1998. Isotope fractionation and sulfur metabolism by pure and enrichment cultures of elemental sulfur-disproportionating bacteria. *Limnol. Oceanogr.* 43, 253-264. DOI: 10.4319/lo.1998.43.2.0253

Chivas, A.R., 2007. "Chapter 10 Terrestrial evaporites", in *Geochemical sediments and landscapes*. Editors: Nash, D.J., McLaren, S.J., (Oxford: Blackwell Publishing Ltd) 330-364. DOI: 10.1002/9780470712917.ch10

Chumakov, N.M., Zharkov, M.A., 2003. Climate during the Permian-Triassic biosphere reorganizations. Article 2. Climate of the Late Permian and Early Triassic: General inferences. *Stratigr. Geol. Correl.* 11, 361-375.

Claypool, G.E., Holser, W.T., Kaplan, I.R., Sakai, H., Zak, I., 1980. The age curves of sulfur and oxygen isotopes in marine sulfate and their mutual interpretation. *Chem. Geol.* 28, 199-260. DOI: 10.1016/0009-2541(80)90047-9

Clement, G.P., Holser, W.T., 1988. Geochemistry of Moroccan evaporites in the setting of the North Atlantic Rift. *J. Afr. Earth Sci.* 7, 375-383. DOI: 10.1016/0899-5362(88)90082-6

Cortecci, G., Reyes, E., Berti, G., Casati, P., 1981. Sulfur and oxygen isotopes in Italian marine sulfates of Permian and Triassic ages. *Chem. Geol.* 34, 65–79. DOI: 10.1016/0009-2541(81)90072-3

Coward, M.P., 1995. "Structural and tectonic setting of the Permo-Triassic basins of north-west Europe", in *Permian and Triassic rifting in north-west Europe*. Editor: Boldy, S.A.R. (London: Geological Society of London, Special Publications) 91, 7-39. DOI: 10.1144/GSL.SP.1995.091.01.02

Crockford, P.W., Kunzmann, M., Bekker, A., Hayles, J., Bao, H., Halverson, G.P., Peng, Y., Bui, T.H., Cox, G.M., Gibson, T.M., Wörndle, S., Rainbird, R., Lepland, A., Swanson-Hysell, N.L., Master, S., Sreenivas, B, Kuznetsov, A., Krupernik, V., Wing, B.A., 2019. Claypool continued: Extending the isotopic record of sedimentary sulfate. *Chem. Geol.* 513, 200-225. DOI: 10.1016/j.chemgeo.2019.02.030

Cui, Y., Kump, L.R., 2015. Global warming and the end-Permian extinction event: Proxy and modelling perspectives. *Earth Sci. Rev.* 149, 5-22. DOI: 10.1016/j.earscirev.2014.04.007

Davies, J.H.F.L., Marzoli, A., Bertrand, H., Youbi, N, Ernesto, M., Schaltegger, U., 2017. End-Triassic mass extinction started by intrusive CAMP activity. *Nat. Commun.* 8, 15596. DOI: 10.1038/ncomms15596

Edward, O., Spangenberg, J.E., Leu, M., Ragon, C., Houedec, S.L., Baud, A., Bucher, H., Vennemann, T., 2024. Olenekian sulfur isotope records: Deciphering global trends, linking to marine redox changes and faunal evolution. *Chem. Geol.* 649, 121984. DOI: 10.1016/j.chemgeo.2024.121984

Eugster, H.P., 1980. Geochemistry of evaporitic lacustrine deposits. *Annu. Rev. Earth Planet. Sci.* 8, 35-63. DOI: 10.1146/annurev.ea.08.050180.000343

Faure, G., Mensing, T.M., 2005. *Isotopes: Principles and applications*. 4th Ed. Hoboken: Wiley

Findlay, A.J., Kamyshny, A., 2017. Turnover rates of intermediate sulphur species (S_x^{2-}, S^0, $S_2O_3^{2-}$, $S_4O_6^{2-}$, SO_3^{2-}) in anoxic freshwater and sediments. *Front. Microbiol.* 8, 1-15. DOI: 10.3389/fmicb.2017.02551

Finster, K., 2008. Microbial disproportionation of inorganic sulfur compounds. *J. Sulfur Chem.* 29, 281-292. DOI: 10.1080/17415990802105770

Friedrich, C.G., Bardischewsky, F., Rother, D., Quentmeier, A., Fischer, J., 2005. Prokaryotic sulphur oxidation. *Curr. Opin. Microbiol.* 8, 253-259. DOI: 10.1016/j.mib.2005.04.005

Friedrich, C.G., Rother, D., Bardischewsky, F., Quentmeier, A., Fischer, J., 2001. Oxidation of reduced inorganic sulfur compounds by bacteria: emergence of a common mechanism. *Appl. Environ. Microbiol.* 67, 2873-2882. DOI: 10.1128/AEM.67.7.2873-2882.2001

Gill, B.C., Lyons, T.W., Saltzman, M.R., 2007. Parallel, high-resolution carbon and sulfur isotope records of the evolving Paleozoic marine sulfur reservoir. *Palaeogeogr. Palaeoclimatol. Palaeoecol.* 256, 156-173. DOI: 10.1016/j.palaeo.2007.02.030

Habicht, K.S., Gade, M., Thamdrup, B., Berg, P., Canfield, D.E., 2002. Calibration of sulfate levels in the Archean ocean. *Science*, 298, 2372-2374. DOI: 10.1126/science.1078265

Hardie, L.A., 1984. Evaporites: Marine or non-marine? *Am. J. Sci.* 284, 193-240. DOI: 10.2475/ajs.284.3.193

Hardie, L.A., 1991. On the significance of evaporites. *Annu. Rev. Earth Planet. Sci.* 19, 131-168. DOI: 10.1146/annurev.ea.19.050191.001023

Hardie, L.A., 1996. Secular variation in seawater chemistry: An explanation for the coupled secular variation in the mineralogies of marine limestones and potash evaporites over the past 600 m.y. *Geology*, 24, 279-283. DOI: 10.1130/0091-7613(1996)024<0279:SVISCA>2.3.CO;2

Hardie, LA., Eugster, H.P., 1970. The evolution of closed-basin brines. *Mineral. Soc. Amer. Spec. Pap.* 3, 273-290.

Harvie, C.E., Eugster, H.P., Weare, J.H., 1982. Mineral equilibria in the six-component seawater system, Na-K-Mg-Ca-SO_4-Cl-H_2O at 25°C. II: Compositions of the saturated solutions. *Geochim. Cosmochim. Acta*, 46, 1603-1618. DOI: 10.1016/0016-7037(82)90317-9

Hay, W.W., Migdisov, A., Balukhovsky, A.N., Wold, C.N., Flögel, S., Söding, E., 2006. Evaporites and the salinity of the ocean during the Phanerozoic: Implications for climate, ocean circulation and life. *Palaeogeogr. Palaeoclimatol. Palaeoecol.* 240, 3-46. DOI: 10.1016/j.palaeo.2006.03.044

He, T., Dal Corso, J., Newton, R.J., Wignall, P.B., Mills, B.J.W., Todaro, S., Stefano, P.D., Turner, E.C., Jamieson, R.A., Randazzo, V., Rigo, M., Jones, R.E., Dunhill, A.M., 2020. An enormous sulfur isotope excursion indicates marine anoxia during the end-Triassic mass extinction. *Sci. Adv.* 6, eabb6704. DOI: 10.1126/sciadv.abb6704

He, T., Newton, R.J., Wignall, P.B., Reid, S., Dal Corso, J., Takahashi, S., Wu, H., Todaro, S., Di Stefano, P., Randazzo, V. and Rigo, M., 2022. Shallow ocean oxygen decline during the end-Triassic mass extinction. *Glob. Planet. Change*, 210, 103770. DOI: 10.1016/j.gloplacha.2022.103770

He, T., Zhu, M., Mills, B.J.W., Wynn, P.M., Zhuravlev, A.Y., Tostevin, R., Pogge von Strandmann, P.A.E., Yang, A., Poulton, S.W., Shields, G.A., 2019. Possible links between extreme oxygen perturbations and the Cambrian radiation of animals. *Nat. Geosci.* 12, 468-474. DOI: 10.1038/s41561-019-0357-z

Holser, W.T., Kaplan, I.R., 1966. Isotope geochemistry of sedimentary sulfates. *Chem. Geol.* 1, 93-135. DOI: 10.1016/0009-2541(66)90011-8

Hounslow, M.W., McKie, T., Ruffell, A.H., 2012. "Permian to Late Triassic post-orogenic collapse and rifting, arid deserts, evaporating seas and mass extinctions" in *The geological history of Britain and Ireland*. Editors Woodcock, N.H., Strachan, R.A., (Wiley: Chichester) 2, 301-321.

Hounslow, M.W., Ruffell, A.H., 2006. "Triassic: Seasonal rivers, dusty deserts and saline lakes", in *The geology of England and Wales*. Editors Rawson, P.F., Brenchley, P., (London: Geological Society of London) 295-325. DOI: 10.1144/GOEWP.13

Howard, A.S., Warrington, G., Ambrose, K., Rees, J.G., 2008. A formational framework for the Mercia Mudstone Group (Triassic) of England and Wales. British Geological Survey Research Report, RR/08/004

Ivanov, M.V., 1981. "The global biogeochemical sulphur cycle", in *Some perspectives of the major biogeochemical cycles*. Editor: Likens, G.E., (Chichester, UK: John Wiley), 175

Jackson, D.I., Johnson, H., 1996. Lithostratigraphic nomenclature of the Triassic, Permian and Carboniferous of the UK offshore East Irish Sea Basin. British Geological Survey, Nottingham

Jackson, D.I., Johnson, H., Smith, N.J.P., 1997. "Stratigraphical relationships and a revised lithostratigraphical nomenclature for the Carboniferous, Permian and Triassic rocks of the offshore East Irish Sea Basin", in *Petroleum geology of the Irish Sea and adjacent areas*. Editors: Meadows, N.S., Trueblood, S.P., Hardman, M., Cowan, G. Geological Society of London Special Publication, 124, 11-32. DOI: 10.1144/GSL.SP.1997.124.01.02

Johnson, D.I., Present, T.M., Li, M., Shen, Y., Adkins, J.F., 2021. Carbonate associated sulfate (CAS) $\delta^{34}S$ heterogeneity across the End-Permian Mass Extinction in South China. *Earth Planet. Sci. Lett.* 574, 117172. DOI: 10.1016/j.epsl.2021.117172

Johnston, D.T., 2010. Touring the biogeochemical landscape of a sulfur-fueled world. *Elements*, 6, 101-106. DOI: 10.2113/gselements.6.2.101

Jørgensen, B.B., Findlay, A.J., Pellerin, A., 2019. The biogeochemical sulfur cycle of marine sediments. *Front. Microbiol.* 10, 849. DOI: 10.3389/fmicb.2019.00849

Kah, L.C., Lyons, T.W., Frank, T.D., 2004. Low marine sulphate and protracted oxygenation of the Proterozoic biosphere. *Nature*, 431, 834-838. DOI: 10.1038/nature02974

Kaiho, K., Kajiwara, Y., Chen, Z-Q., Gorjan, P., 2006. A sulfur isotope event at the end of the Permian. *Chem. Geol.* 235, 33-47. DOI: 10.1016/j.chemgeo.2006.06.001

Kampschulte, A., Strauss, H., 2004. The sulfur isotopic evolution of Phanerozoic seawater based on the analysis structurally substituted sulfate in carbonates. *Chem. Geol.* 204, 255-286. DOI: 10.1016/j.chemgeo.2003.11.013

Kempe, S., Degens, E.T., 1985. An early soda ocean? *Chem. Geol.* 53, 95-108. DOI: 10.1016/0009%2D2541(85)90023%2D3

Knittel, K, Boetius, A., 2009. Anaerobic oxidation of methane: Progress with an unknown process. *Annu. Rev. Microbiol.* 63, 311-334. DOI: 10.1146/annurev.micro.61.080706.093130

Korte, C., Kozur, H.W., Joachimski, M.M., Strauss, H., Veizer, J., Schwark, L., 2004. Carbon, sulfur, oxygen and strontium isotope records, organic geochemistry and biostratigraphy across the Permian/Triassic boundary in Abadeh, Iran. *Int. J. Earth Sci.* 93, 565-581. DOI: 10.1007/s00531-004-0406-7

Krämer, M., Cypionka, H., 1989. Sulfate formation via ATP sulfurylase in thiosulfate- and sulphite-disproportionating bacteria. *Arch. Microbiol.* 151, 232-237. DOI: 10.1007/BF00413135

Krijgsman, W., Leewis, M.E., Garcés, M., Kouwenhoven, T.J., Kuiper, K.F., Sierro, F.J, 2006. Tectonic control for evaporite formation in the Eastern Betics (Tortonian, Spain). *Sediment. Geol.* 188-189, 155-170. DOI: 10.1016/j.sedgeo.2006.03.003

Kunzmann, M., Bui, T.H., Crockford, P.W., Halverson, G.P., Scott, C., Lyons, T.W., Wing, B.A., 2017. Bacterial sulfur disproportionation constrains timing of Neoproterozoic oxygenation. *Geology*, 45, 207-210. DOI: 10.1130/G38602.1

Kurtz, A.C., Kump, L.R., Arthur, M.A., Zachos, J.C., Paytan, A., 2003. Early Cenozoic decoupling of the global carbon and sulfur cycles. *Paleoceanography*, 18, 1090. DOI: 10.1029/2003PA000908

Leitner, C., Köster, M., Finger, F., 2023. Saltern, mudflat, and dry playa: playa basin types of a retreating epeiric sea (Keuper, Germany). *J. Sediment. Res.* 93, 840-856. DOI: 10.2110/jsr.2023.013

Liseroudi, M.H., Ardakani, O.H., Pedersen, P.K., Stern, R.A., Wood, J.M., Sanei, H., 2021. Microbial and thermochemical controlled sulfur cycle in the Early Tiassic sediments of the Western Canadian sedimentary basin. *J. Geol. Soc.* 178, 1-20. DOI: 10.1144/jgs2020-175

Lowenstein, T.K., Hardie, L.A., Timofeeff, M.N., Demicco, R.V., 2003. Secular variation in seawater chemistry and the origin of calcium chloride basinal brines. *Geology*, 31, 857-860. DOI: 10.1130/G19728R.1

Lowenstein, T.K., Spencer, R.J., Pengxi, Z., 1989. Origin of ancient potash evaporites: Clues from the modern nonmarine Qiadam Basin of western China. *Science*, 245, 1090-1092. DOI: 10.1126/science.245.4922.1090

Lowenstein, T.K., Timofeff, M.N., Brennan, S.T., Hardie, L.A., Demicco, R.V., 2001. Oscillations in Phanerozoic seawater chemistry: Evidence from fluid inclusions. *Science*, 294, 1086-1088. DOI: 10.1126/science.1064280

Luo, G., Kump, L.R., Wang, Y., Tong, J., Arthur, M.A., Yang, H., Huang, J., Yin, H., Xia, S., 2010. Isotopic evidence for an anomalously low oceanic sulfate concentration following

end-Permian mass extinction. *Earth Planet. Sci. Lett.* 300, 101-111. DOI: 10.1016/j.epsl.2010.09.041

Lyons, T.M., Reinhard, C.T., Planavsky, N.J., 2014. The rise of oxygen in the Earth's early ocean and atmosphere. *Nature*, 506, 307-315. DOI: 10.1038/nature13068

Lyons, T.W., Walter, L.M., Gellatly, A.M., Martini, A.M., Blake, R.E., 2004. "Sites of anomalous organic remineralization in the carbonate sediments of South Florida, USA: The sulfur cycle and carbonate associated sulfate", in *Sulfur biogeochemistry – past and present*. Editors: Amend, J.P., Edwards, K.J., Lyons, T.W., (Boulder, CO: Geological Society of America) 161-176. DOI: 10.1130/0-8137-2379-5.161

Lyu, Z., Zhang, L., Algeo, T. J., Zhao, L., Chen, Z-Q., Li, C., Ma, B., Ye, F., 2019. Global ocean circulation changes during the Smithian-Spathian transition inferred from carbon sulfur-cycle records. *Earth Sci. Rev.* 195, 114–132. DOI: 10.1016/j.earscirev.2019.01.010

Marini, L., Moretti, R., Accornero, M., 2011. Sulfur isotopes in magmatic-hydrothermal systems, melts, and magmas. *Rev. Mineral. Geochem.* 73, 423-492. DOI: 10.2138/rmg.2011.73.14

Markovic, S., Paytan, A., Wortmann, U.G., 2015. Pleistocene sediment offloading and the global sulfur cycle. *Biogeosciences*, 12, 3043-3060. DOI: 10.5194/bg-12-3043-2015

McKie, T., 2014. Climatic and tectonic controls on Triassic dryland terminal fluvial system architecture, central North Sea. *Int. Assoc. Sedimentol. Spec. Publ.* 46, 19-58. DOI: 10.1002/9781118920435.ch2

McKie, T., 2017. "Palaeogeographic evolution of latest Permian and Triassic salt basins in northwest Europe", in *Permo-Triassic salt provinces of Europe, North Africa and the*

Atlantic margins, tectonics and hydrocarbon potential. Editors Soto, J.J., Flinch, J.F., Tari, G. (Amsterdam Netherlands: Elsevier), 159-173. DOI: 10.1016/B978-0-12-809417-4.00008-2

McKie, T., Williams, B., 2009. Triassic palaeogeography and fluvial dispersal across the northwest European basins. *Geol. J.* 44, 711-741. DOI: 10.1002/gj.1201

Murray, S.T., Higgins, J.A., Holmden, C., Lu, C., Swart, P.K., 2021. Geochemical fingerprints of dolomitization in Bahamian carbonates: Evidence from sulphur, calcium, magnesium and clumped isotopes. *Sedimentology*, 68, 1-29. DOI: 10.1111/sed.12775

Newby, S.M., Owens, J.D., Schoepfer, S.D., Algeo, T.J., 2021. Transient oxygenation at end-Permian mass extinction onset shown by thallium isotopes. *Nat. Geosci.* 14, 678-683. DOI: 10.1038/s41561-021-00802-4

Newell, A., 2018. Rifts, rivers and climate recovery: A new model for the Triassic of England. *Proc. Geol. Assoc.* 129, 352-371. DOI: 10.1016/j.pgeola.2017.04.001

Newton, R.J., Pevitt E.L., Wignall, P.B., Bottrell, S.H., 2004. Large shifts in the isotopic composition of seawater sulphate across the Permo-Triassic boundary in northern Italy. *Earth Planet. Sci. Lett.* 218, 331-345. DOI: 10.1016/S0012-821X(03)00676-9

Nielsen, H., 1978. "Sulfur isotopes in nature", in *Handbook of Geochemistry. Sect. 16-B.* Editor: Wedepohl, K.K., (Berlin: Springer)

Ortí, F., Peréz-López, A., García-Veigas, J., Rosell, L., Cendón, D.I., Pérez-Valera, F., 2014. Sulfate isotope compositions ($\delta^{34}S$, $\delta^{18}O$) and strontium isotopic ratios ($^{87}Sr/^{86}Sr$) of Triassic evaporites in the Betic Cordillera (SE Spain). *Revista de la Sociedad Geológica de España*, 27, 79–89.

Ortí, F., Peréz-López, A., Pérez-Valera, F., Benedicto, C., 2022. Isotope composition ($\delta^{34}S$, $\delta^{18}O$) of the Middle Triassic-Early Jurassic sulfates in eastern Iberia. *Sediment. Geol.* 431, 106104. DOI: 10.1016/j.sedgeo.2022.106104

Parrish, J.T., 1993. Climate of the supercontinent Pangea. *J. Geol.* 101, 215-233. DOI: 10.1086/648217

Pasqiuer, V., Sansjofre, P., Rabineau, M., Revillon, S., Houghton, J., Fike, D.A., 2017. Pyrite sulfur isotopes reveal glacial-interglacial environmental changes. *Proc. Natl. Acad. Sci.* 114, 5941-5945. DOI: 10.1073/pnas.1618245114

Paytan, A, Gray, E.T., Ma, Z., Erhardt, E., Faul, K., 2012. Application of sulfur isotopes for stratigraphic correlation. *Isot. Environ. Health Stud.* 48, 195-206. DOI: 10.1080/10256016.2011.625423

Paytan, A., Kastner, M., Campbell, D., Thiemens, M.H., 1998. Sulfur isotopic composition of Cenozoic seawater sulfate. *Science*, 282, 1459-1462. DOI: 10.1126/science.282.5393.1459

Paytan, A., Kastner, M., Campbell, D., Thiemens, M.H., 2004. Seawater sulfur isotope fluctuations in the Cretaceous. *Science*, 304, 1663-1665. DOI: 10.1126/science.1095258

Paytan, A., Kastner, M., Martin E.E., Macdougall, J.D., Hervert, T., 1993. Marine barite as a monitor of seawater strontium isotope composition. *Nature*, 366, 445-449. DOI: 10.1038/366445a0

Paytan, A., Mearon, S., Cobb, K., Kastner, M., 2002. Origin of marine barite deposits: Sr and S isotope characterization. *Geology*, 30, 747-750. DOI: 10.1130/0091-7613(2002)030<0747:OOMBDS>2.0.CO;2

Paytan, A., Yao, W., Faul, K.L., Gray, E.T., 2020. “Sulfur isotope stratigraphy”, in *Geologic time scale 2020*. Editors Gradstein F.M., Ogg, J.G., Schmitz, M.D., Ogg, G.M., (Amsterdam, Netherlands: Elsevier) 1, 259-278. DOI: 10.1016/B978-0-12-824360-2.00009-7

Pérez-López, A., 1998. “Epicontinental Triassic of the southern Iberian continental margin (Betic Cordillera, Spain)”. In *Epicontinental Triassic*. Editors Bachman, G.H., Lerche, I., (Stuttgart: Zentralblatt für Geologie und Paläontologie1) 1009-1031.

Philippot, P., Zuilen, M.V., Lepot, K., Thomazo, C., Farquhar, J., Van Kranendonk, M.J., 2007. Early Archean microorganisms preferred elemental sulfur, not sulfate. *Science*, 317, 1534-1537. DOI: 10.1126/science.1145861

Present, T.M., Adkins, J.F., Fischer, W.W., 2020. Variability in sulfur isotope records of Phanerozoic seawater sulfate. *Geophys. Res. Lett.* 47, e2020GL088766. DOI:10.1029/2020GL088766

Present, T.M., Gutierrez, M., Paris, G., Kerans, C., Grotzinger, J.P., Adkins, J.F., 2019. Diagenetic controls on the isotopic composition of carbonate-associated sulphate in the Permian Capitan Reef Complex, West Texas. *Sedimentology*, 66, 2605–2626. DOI: 10.1111/sed.12615

Present, T.M., Paris, G., Burke, A., Fischer, W.W., Adkins, J.F., 2015. Large carbonate associated sulfate isotopic variability between brachiopods, micrite, and other sedimentary components in Late Ordovician strata. *Earth Planet. Sci. Lett.* 432, 187-198. DOI: 10.1016/j.epsl.2015.10.005

Raab, M., Spiro, B., 1991. Sulfur isotopic variations during seawater evaporation with fractional crystallization. *Chem. Geol.* 86, 323-333. DOI: 10.1016/0168-9622(91)90014-N

Raup, D.M., Sepkoski, J.J., 1989. Mass extinctions in the marine fossil record. *Science*, 215, 1501-1503. DOI: 10.1126/science.215.4539.1501

Rees, C.E., 1973. Steady-state model for sulfur isotope fractionation in bacterial reduction processes. *Geochim. Cosmochim. Acta*, 37, 1141-1162. DOI: 10.1016/0016-7037(73)90052-5

Rees, C.E., Jenkins, W.J., Monster, J., 1978. The sulphur isotopic composition of ocean water sulphate. *Geochim. Cosmochim. Acta*, vol., 42, 377-381. DOI: 10.1016/0016-7037(78)90268-5

Rennie, V.C.F., Paris, G., Sessions, A.L., Abramovich, S., Turchyn, A.V., Adkins, J.F., 2018. Cenozoic record of $\delta^{34}S$ in foraminiferal calcite implies an early Eocene shift to deep-ocean sulfide burial. *Nat. Geosci.* 11, 761-765. DOI: 10.1038/s41561-018-0200-y.

Rennie, V.C.F., Turchyn, A.V., 2014. The preservation of $\delta^{34}S_{SO4}$ and $\delta^{18}O_{SO4}$ in carbonate-associated sulfate during marine diagenesis: A 25 Myr test case using marine sediments. *Earth Planet. Sci. Lett.* 395, 13-23. DOI: 10.1016/j.epsl.2014.03.025

Riccardi, A.L., Arthur, M.A., Kump, L.R., 2006. Sulfur isotopic evidence for chemocline upward excursions during the end-Permian mass extinction. *Geochim. Cosmochim. Acta*, 70, 5740-5752. DOI: 10.1016/j.gca.2006.08.005

Richardson, J.A., Keating, C., Lepland, A., Hints, O., Bradley, A.S., Fike, D.A., 2019. Silurian records of carbon and sulfur cycling from Estonia: The importance of depositional

environment on isotopic trends. *Earth Planet. Sci. Lett.* 512, 71-82. DOI: 10.1016/j.epsl.2019.01.055

Richardson, J.A., Lepland, A., Hints, O., Prave, A.R., Gilhooly III, W.P., Bradley, A.S., Fike, D.A., 2021. Effects of early marine diagenesis and site-specific depositional controls on carbonate-associated sulfate: Insights from paired S and O isotopic analyses. *Chem. Geol.* 584, 120525. DOI: 10.1016/j.chemgeo.2021.120525

Rickard, D., Luther, G.W., 2007. Chemistry of iron sulfides. *Chem. Rev.* 107, 514-562. DOI: 10.1021/cr0503658

Rothman, D.H., Fournier, G.P., French, K.L., Summons, R.E., 2014. Methanogenic burst in the end-Permian carbon cycle. *Proc. Natl. Acad. Sci.* 111, 5462-5467. DOI: 10.1073/pnas.1318106111

Ruhl, M., Bonis, N.R., Reichart, G-J., Sinninghe Damsté, J.S., Kürschner, W.M., 2011. Atmospheric carbon injection linked to End-Triassic Mass Extinction. *Science*, 333, 430-434. DOI: 10.1126/science.1204255

Schobben, M., Stebbins, A., Ghaderi, A., Strauss, H., Korn, D., and Korte, C., (2015). Flourishing ocean drives the end-Permian marine mass extinction. *Proc. Natl. Acad. Sci.* 112, 10298–10303. DOI: 10.1073/pnas.1503755112

Sepkoski, J.J., 1996. “Patterns of Phanerozoic extinction: A perspective from global databases”, in *Global events and event stratigraphy in the Phanerozoic*. Editor: Walliser, O.H., (Berlin: Springer) 35-51. DOI: 10.1007/978-3-642-79634-0_4

Sim, M.S., Bosak, T., Ono, S., 2011a. Large sulfur isotope fractionation does not require disproportionation. *Science*, 333, 74-77. DOI: 10.1126/science.1205103

Sim, M.S., Ono, S., Bosak, T., 2012. Effects of iron and nitrogen limitation on sulfur isotope fractionation during microbial sulfate reduction. *Appl. Environ. Microbiol.* 78, 8368-8376. DOI: 10.1128/AEM.01842-12

Sim, M.S., Ono, S., Donovan, K., Templer, S.P., Bosak, T., 2011b. Effect of electron donors on the fractionation of sulfur isotopes by a marine Desulfovibrio sp. *Geochim. Cosmochim. Acta*, 75, 4244-4259. DOI: 10.1016/j.gca.2011.05.021

Sloss, L.L., 1953. The significance of evaporites. *J. Sediment. Petrol.* 23, 143-161. DOI: 10.1306/D42695F3-2B26-11D7-8648000102C1865D

Song, H., Du, Y., Algeo, T. J., Tong, J., Owens, J. D., Song, H., Tian, L., Qiu, H., Zhu, Y., Lyons, T.W., 2019. Cooling-driven oceanic anoxia across the Smithian/Spathian boundary (mid-Early Triassic). *Earth Sci. Rev.* 195, 133–146. DOI: 10.1016/j.earscirev.2019.01.009

Song, H., Tong, J., Algeo, T.J., Song, H., Qui, H., Zhu, Y., Tian, L., Bates, S., Lyons, T.W., Luo, G., Kump, L.R., 2014. Early Triassic seawater sulfate drawdown. *Geochim. Cosmochim. Acta*, 128, 95-113. DOI: 10.1016/j.gca.2013.12.009

Stebbins, A., Algeo, T.J., Olsen, C., Sano, H, Rowe, H., Hannigan, R., 2019. Sulfur-isotope evidence for recovery of seawater sulfate concentrations from a PTB minimum by the Smithian-Spathian transition. *Earth Sci. Rev.* 195, 83-95. DOI: 10.1016/j.earscirev.2018.08.010

Strauss, H., 1997. The isotopic composition of sedimentary sulfur through time. *Palaeogeogr. Palaeoclimatol. Palaeoecol.* 132, 97-118. DOI: 10.1016/S0031-0182(97)00067-9

Stüeken, E.E., Buick, R., Schauer, A.J., 2015b. Nitrogen isotope evidence for alkaline lakes on late Archean continents. *Earth Planet. Sci. Lett.* 411, 1-10. DOI: 10.1016/j.epsl.2014.11.037

Stüeken, E.E., Foriel, J., Buick, R., Schoepfer, S.D., 2015a. Selenium isotope ratios, redox changes and biological productivity across the end-Permian mass extinction. *Chem. Geol.* 410, 28-39. DOI: 10.1016/j.chemgeo.2015.05.021

Sun, Y., Joachimski, M.M., Wignall, P.B., Yan, C., Chen, Y., Jiang, H., Wang, L., Lai, X., 2012. Lethally hot temperatures during the Early Triassic greenhouse. *Science*, 338, 366-370. DOI: 10.1126/science.1224126

Tang, W., Wang, J., Wei, H., Fu, X., Ke, P., 2023. Sulfur isotopic evidence for global marine anoxia and low seawater sulfate concentration during the Late Triassic. *J. Asian Earth Sci.* 251, 105659. DOI: 10.1016/j.jseaes.2023.105659

Taylor, S.R., 1983. A stable isotope study of the Mercia Mudstone Group (Keuper Marl) and associated sulphate horizons in the English Midlands. *Sedimentology*, 30, 11-31. DOI: 10.1111/j.1365-3091.1983.tb00647.x

Thiel, J., Byrne, J.M., Kappler, A., Schink, B., Pester, M., 2019. Pyrite formation from FeS and H_2S is mediated through microbial redox activity. *Proc. Natl. Acad. Sci.* 116, 6897-6902. DOI: 10.1073/pnas.1814412116

Thode, H.G., 1964. Stable isotopes: A key to our understanding of natural processes. *Bull. Can. Pet. Geol.* 12, 246-262

Thode, H.G., Monster, J., 1965. Sulfur isotope geochemistry of petroleum, evaporites, and ancient seas. *Am. Assoc. Pet. Geol. Mem.* 4, 367-377.

Thode, H.G., Monster, J., Dunford, H.B., 1961. Sulphur isotope geochemistry. *Geochim. Cosmochim. Acta*, 25, 159-174. DOI: 10.1016/0016-7037(61)90074-6

Toyama, K., Paytan, A., Sawada, K., Hasegawa, T., 2020. Sulfur isotope ratios in co-occurring barite and carbonate from Eocene sediments: A comparison study. *Chem. Geol.* 535, 119454. DOI: 10.1016/j.chemgeo.2019.119454

Trotter, J.A., Williams, I.S., Nicora, A., Mazza, M., Rigo, M., 2015. Long-term cycles of Triassic climate change: A new $\delta^{18}O$ record from conodont apatite. *Earth Planet. Sci. Lett.* 415, 165-174. DOI: 10.1016/j.epsl.2015.01.038

Tucker, M.E., 1991. Sequence stratigraphy of carbonate-evaporite basins: Models and applications to the Upper Permian Zechstein of northeast England and adjoining North Sea. *J. Geol. Soc. Lond.* 148, 1019-1036. DOI: 10.1144/gsjgs.148.6.1019

Turchyn, A.V., Schrag, D.P., Coccioni, R., Montanari, A., 2009. Stable isotope analysis of the Cretaceous sulfur cycle. *Earth Planet. Sci. Lett.* 285, 115-123. DOI: 10.1016/j.epsl.2009.06.002

Van Driessche, A.E.S., Canals, A., Ossorio, M., Reyes, R.C., García-Ruiz, J.M., 2016. Unraveling the sulfate sources of (giant) gypsum crystals using gypsum isotope fractionation factors. *J. Geol.* 124, 235-245. DOI: 10.1086/684832

Van Driessche, A.E.S., García-Ruíz, J.M., Tsukamoto, K., Patiño-Lopez, L.D., Satoh, H., 2011. Ultraslow growth rates of giant gypsum crystals. *Proc. Natl. Acad. Sci.* 108, 15721-15726. DOI: 10.1073/pnas.1105233108

Warren, J.K., 2010. Evaporites through time: Tectonic, climatic and eustatic controls in marine and nonmarine deposits. *Earth-Sci. Rev.* 98, 217-268. DOI: 10.1016/j.earscirev.2009.11.004

Warren, J.K., 2021. "Evaporite deposits", in *Encyclopaedia of geology (second edition)*. Editors: Alderton, D., Elias, S.A., (Oxford: Academic Press) 945-977. DOI: 10.1016/B978-0-08-102908-4.00165-X

Warrington, G., 1974. Studies in the palynological biostratigraphy of the British Trias. 1. Reference sections in west Lancashire and north Somerset. *Rev. Palaeobot. Palynol.* 17, 133-147. DOI: 10.1016/0034-6667(74)90095-5

Warrington, G., 1995. The Permian, Triassic and Jurassic in Northern Ireland: A palynological study with special reference to the hydrocarbon prospectivity of the Larne – Lough Neagh Basin. Geological Survey of Northern Ireland. Technical Report GSNI/95/7

Warrington, G., Audley-Charles, M.G., Elliott, R.E., Evans, W.B., Ivimey-Cook, H.C., Kent, P., Robinson, P.L., Shotton, F.W., Taylor, F.M., 1980. A correlation of Triassic rocks in the British Isles. *Geol. Soc. Lond.,* Special Report No. 13

Warrington, G., and Pollard, J. E. (2021). On the records of the brachiopod 'Lingula' and associated fossils in Mid-Triassic deposits in England. *Proc. Yorks. Geol. Soc.* 63, 1–9. DOI: 10.1144/pygs2020-015

Wignall, P.B., 2001. Large igneous provinces and mass extinctions. *Earth Sci. Rev.* 53, 1-33. DOI: 10.1016/S0012-8252(00)00037-4

Wignall, P.B., Atkinson, J.W., 2020. A two-phase end-Triassic mass extinction. *Earth-Sci. Rev.* 208, 103282. DOI: 10.1016/j.earscirev.2020.103282

Wing, B.A., Halevy, I., 2014. Intracellular metabolite levels shape sulfur isotope fractionation during microbial sulfate respiration. *Proc. Natl. Acad. Sci.* 111, 18116-18125. DOI: 10.1073/pnas.1407502111

Wotte, T., Shields-Zhou, G.A., Strauss, H., 2012. Carbonate-associated sulfate: Experimental comparisons of common extraction methods and recommendations toward a standard analytical protocol. *Chem. Geol.* 326-327, 132-144. DOI: 10.1016/j.chemgeo.2012.07.020

Wu, Y., Chu, D., Tong, J., Song, H., Dal Corso, J., Wignall, P.B., Song, H., Du, Y., Cui, Y., 2021. Six-fold increase of atmospheric pCO_2 during the Permian-Triassic mass extinction. *Nat. Commun.* 12, 2137. DOI: 10.1038/s41467-021-22298-7

Yao, W., Paytan, A., 2020. Possible triggers of the seawater sulfate S-isotope increase between 55 and 40 million years ago. *Chem. Geol.* vol., 552, pp., 1-11. DOI: 10.1016/j.chemgeo.2020.119788

Yao, W. Q., Paytan, A., Wortmann, U. G., 2018. Large-scale ocean deoxygenation during the Paleocene-Eocene Thermal Maximum. *Science*, 361, 804–806. DOI: 10.1126/science.aar8658

Yao, W., Wortmann, U.G., Paytan, A., 2019. "Sulfur isotopes — Use for stratigraphy during times of rapid perturbations", in *Stratigraphy and timescales*. Editor Montenari, M., (Amsterdam: Elsevier Academic Press) 4, 1-33. DOI: 10.1016/bs.sats.2019.08.004

Yücel, M., Konovalov, S.K., Moore, T.S., Janzen, C.P., Luther III, G.W., 2010. Sulfur speciation in the upper Black Sea sediments. *Chem. Geol.* 269, 364-375 DOI: 10.1016/j.chemgeo.2009.10.010

Zopfi, J., Ferdelman, T.G., Fossing, H., 2004. “Distribution and fate of sulfur intermediates – sulfite, tetrathionate, thiosulfate, and elemental sulfur – in marine sediments”, in *Sulfur biogeochemistry – past and present*. Editors: Amend, J.P., Edwards, K.J., Lyons, T.W., (Boulder, CO: Geological Society of America) 97-116. DOI: 10.1130/0-8137-2379-5.97

Chapter 2

Citation: Salisbury, J., Gröcke, D.R., Cheung, H.D.R.A., Kump, L.R., McKie, T., Ruffell, A., An 80-millio-year sulphur isotope record of pyrite burial over the Permian-Triassic. *Sci. Rep.* 12, 17370. DOI: 10.1038/s41598-022-21542-4

An 80-million-year sulphur isotope record of pyrite burial over the Permian–Triassic

Jack Salisbury[1*], Darren R. Gröcke[1*], H.D.R. Ashleigh Cheung[1], Lee R. Kump[2], Tom McKie[3], Alastair Ruffell[4]

1. Department of Earth Sciences, Durham University, South Road, Durham, DH1 3LE, UK

2. College of Earth and Mineral Sciences, Pennsylvania State University, University Park, PA 16802, USA

3. Shell UK Exploration and Production, 1 Altens Farm Road, Nigg, Aberdeen, AB12 3FY, UK

4. School of Natural and Built Environment (Elmwood Building), Queen's University, Belfast, BT7 1NN, UK

** = corresponding authors: jack.salisbury@durham.ac.uk, d.r.grocke@durham.ac.uk*

Despite the extensive use of sulphur isotope ratios ($\delta^{34}S$) for understanding ancient biogeochemical cycles, many studies focus on specific time-points of interest, such as the end-Permian mass extinction (EPME). We have generated an 80 million-year Permian–Triassic $\delta^{34}S_{evap}$ curve from the Staithes S-20 borehole, Yorkshire, England. The Staithes $\delta^{34}S_{evap}$ record replicates the major features of the global curve, while confirming a new excursion at the Olenekian/Anisian boundary at ~247 million years ago (~247 Ma). We incorporate the resultant $\delta^{34}S_{evap}$ curve into a sulphur isotope box model. Our modelling approach reveals three significant pyrite burial events (PBEs) in the Triassic. In particular, it predicts a significant biogeochemical response across the EPME, resulting in a substantial increase in pyrite burial, possibly driven by Siberian Traps volcanism. Our model suggests that after ~10 million years pyrite burial achieves relative long-term stability until the latest Triassic.

The Permian–Triassic interval has attracted much attention due to significant biological and geochemical events, including the end-Permian mass extinction (EPME) — the most catastrophic extinction event of the Phanerozoic (Alroy et al., 2008). The EPME is associated with a reduction in marine species biodiversity on the order of 80–90% (Payne and Clapham, 2012), extinction amongst tetrapods, and a possible dieback of terrestrial vegetation (Benton and Newell, 2014). Driven by volcanism from the Siberian Traps (Burgess and Bowring, 2015), the EPME is intimately linked with increased CO_2, CH_4 and SO_2 fluxes (Rothman et al., 2014; Cui and Kump, 2015; Wu et al., 2021), heightened global atmospheric and sea surface temperatures (SST) (Sun et al., 2012), intensified chemical weathering (Sun et al., 2018), ozone depletion (Broadley et al., 2018), a reduction in marine pH (Jurikova et al., 2020) and an expansion of anoxic, and possibly euxinic, oceanic water masses (Newby et al., 2021; Zhang et al., 2021). It has been

proposed that the Early Triassic represents a period of climatic, geochemical, and biological instability, delaying the recovery from the EPME (Payne et al., 2004; Song et al., 2014; Lyu et al., 2019; Stebbins et al., 2019). Multiple SST changes (Sun et al., 2012; Trotter et al., 2015) likely coincided with major fluctuations in ocean chemistry expressed as excursions in the carbon and sulphur isotope geochemistry of marine carbonates and evaporites (Payne et al., 2004; Bernasconi et al., 2017; Lyu et al., 2019; Stebbins et al., 2019), followed by conditions of relative stability in the Middle Triassic (Song et al., 2014).

Despite the biogeochemical significance of the Triassic, robust sulphur isotope data are sparse, with most studies focusing on specific, short periods of time, such as the EPME (Kaiho et al., 2012) and the Smithian/Spathian boundary (Lyu et al., 2019; Stebbins et al., 2019). These records lack temporal coverage and fail to capture long-term biogeochemical conditions for the Triassic at high resolutions. One exception is by Song et al. (2014), who compiled a $\delta^{34}S$ record of carbonate-associated sulphate (CAS) from the late Permian to Middle Triassic from sections in south China. However, CAS is prone to diagenetic alteration (Richardson et al., 2019; 2021), with much of the isotopic heterogeneity of $\delta^{34}S_{CAS}$ records across the EPME attributed to post-depositional alteration (Bernasconi et al., 2017; Johnson et al., 2021). Bernasconi et al. (2017) compiled a $\delta^{34}S_{evap}$ record from sedimentary evaporites from the late Permian to Middle Triassic, from multiple sections across several countries in Europe. Although evaporites are less prone to diagenetic alteration (Bernasconi et al., 2017), their coverage in the sedimentary record is often sparse and not continuous, thus resulting in a lack of high-resolution $\delta^{34}S_{evap}$ curves.

Constructing a high-resolution $\delta^{34}S$ record

To address the lack of a single geographic and stratigraphic record, we have generated a high-resolution $\delta^{34}S_{evap}$ curve from the Staithes S-20 borehole (NZ71NE/14; grid reference, NZ 476034E 518000N), Yorkshire, England (Fig. 1). The Staithes S-20 borehole was chosen due to its stratigraphic coverage (~668 meters) of evaporite-bearing strata that are lithostratigraphically dated between the late Permian to Late Triassic. The Hardegsen unconformity has removed much of the Early Triassic in the Staithes S-20 borehole, although a palynological age constraint acquired from immediately above the unconformity is determined to be earliest Anisian in age (Warrington, *pers. comm.*, 2019; see Supplementary for more information).

A total of 364 individual evaporite samples (e.g., gypsum, anhydrite, and halite) were collected at regular intervals. For gypsum and anhydrite, a drill was used to produce a fine powder for isotopic analysis, whilst for halite the sulphate was obtained through barium sulphate precipitation (see Supplementary for Methodology).

We compiled and recalibrated the global $\delta^{34}S_{evap}$ curve for the Permian and Triassic, consisting of ~1000 $\delta^{34}S_{evap}$ results (see Supplementary); our new, continuous record from a single site adds 38% more data to the global curve. All results were double-checked for their age assignment against a standardised geological timescale (Cohen et al., 2013). Based upon trends and inflection points in the global $\delta^{34}S_{evap}$ record, we correlated the Staithes S-20 curve to generate a more robust global $\delta^{34}S_{evap}$ record of the late Permian–Late Triassic; especially the Middle and Late Triassic (Fig. 2; see Appendix 1).

Late Permian – Early Triassic sulphur isotope instability

The composite late Permian – Early Triassic $\delta^{34}S_{evap}$ record exhibits substantial variability (Fig. 2), interpreted as a product of environmental changes possibly induced by Siberian Traps volcanism (Burgess and Bowring, 2015). The late Permian Zechstein evaporites have an average $\delta^{34}S_{evap}$ of ~10.9 ‰, before lowering to ~8.2 ‰ at the PTB. Immediately following this, $\delta^{34}S_{evap}$ values exhibit a sharp increase, reaching a maximum of ~32 ‰ at ~250 Ma in the Early Triassic (Fig. 2). Possibly facilitated by low sulphate concentrations (Bernasconi et al., 2017; Stebbins et al., 2019) due to deposition of the late Permian Zechstein evaporites (Bernasconi et al., 2017), this positive excursion reflects a major perturbation in the Early Triassic sulphur cycle. In addition, with the assistance of a palynological age constraint for the Hardegsen unconformity (see Supplementary), and stratigraphic correlation with the composite $\delta^{34}S_{evap}$ curve, a new rapid negative $\delta^{34}S_{evap}$ excursion (on the order of 15 ‰) is recorded at the Olenekian/Anisian boundary (OAB) (~247 Ma). Following this, the $\delta^{34}S_{evap}$ record exhibits an abrupt recovery to pre-excursion values of 29 ‰ at ~246 Ma.

Middle – Late Triassic sulphur isotope stability

The extreme environmental conditions that persisted during the late Permian and Early Triassic were more subdued in the Middle Triassic (Song et al., 2014; Bernasconi et al., 2017; Stebbins et al., 2019). Accordingly, our $\delta^{34}S_{evap}$ record exhibits a gradual and persistent decline from ~246 Ma in the early Anisian, before stabilising at ~236 Ma in the early Carnian (Fig. 2). Relative stability is maintained throughout the Carnian and the majority of the Norian.

Interestingly, we see no evidence for a substantial change in $\delta^{34}S_{evap}$ during the Carnian Pluvial Event (CPE), potentially suggesting the environmental changes during the CPE had little impact on the global sulphur cycle. This is of interest, as the CPE is associated with major carbon cycle perturbations, the emplacement of the Wrangellian LIP and a mass extinction event (followed by biotic radiation) (Dal Corso et al., 2020, 2022). It is thus intriguing that our $\delta^{34}S_{evap}$ record maintains relative stability across this time interval. Higher resolution $\delta^{34}S_{evap}$ records spanning the CPE, accompanied by further biogeochemical modelling, are required to confirm the apparent disconnect between the carbon and sulphur cycles during the CPE.

Our new $\delta^{34}S_{evap}$ record also highlights the presence of a small positive $\delta^{34}S_{evap}$ excursion (~4 ‰) prior to the Norian/Rhaetian boundary (Fig. 2), which potentially coincides with the emplacement of the Angayucham Complex (see below). Additional data are required to confirm the precise age and magnitude of this $\delta^{34}S_{evap}$ excursion.

Sulphur isotope box model and pyrite burial

To explore the mechanisms responsible for the observed trends in the $\delta^{34}S_{evap}$ curve, we incorporated our $\delta^{34}S_{evap}$ data (compiled global dataset and the Staithes S-20 borehole data) into a sulphur isotope box model (Kurtz et al., 2003) (see Supplementary). The model outputs predict three pyrite burial events (PBEs) during the time interval of this study, at ~251 Ma, ~246 Ma, and ~213 Ma (Fig. 3).

It should be noted however, that the fractionation factor ($\Delta^{34}S$) associated with microbial reduction of sulphate to sulphide (and subsequent pyrite formation/burial) has been shown to vary according to a range of biological and environmental factors (Canfield et al., 2010; Pasqiuer et al., 2017; Bryant et al., 2018). Recent biogeochemical

modelling approaches suggest that variability in the $\delta^{34}S$ of seawater sulphate during the Cenozoic can be accounted for by a shift in $\Delta^{34}S$, reflecting a change in the locus of pyrite burial to deeper more oxygen-sparse water masses, rather than a simple change in pyrite burial rates (Rennie et al., 2018). Unfortunately, previous work (Bernasconi et al., 2017) did not consider a possible change in $\Delta^{34}S$ when interpreting variability in the $\delta^{34}S$ of seawater sulphate observed for the Early Triassic.

We completed a range of sensitivity tests to determine how shifts in the $\Delta^{34}S$ affected predicted pyrite burial rates (see Supplementary for details). We explored a range of values for $\Delta^{34}S$ between -35 ‰ and -50 ‰ for the Early Triassic (Fig. 3). Our results suggest that changing $\Delta^{34}S$ to more negative values supress the magnitude of the pyrite burial flux inferred for the PTB and earliest Triassic but does not eliminate it entirely from the model outputs (Fig. 3). Thus, an increase in the magnitude of sulphur isotopic fractionation associated with pyrite formation is certainly possible, which is in line with evidence for an expansion of ocean anoxia during the PTB and Early Triassic time interval (Algeo et al., 2013; Grasby et al., 2021; Muto, 2021; Newby et al., 2021). This may have contributed to the positive isotope excursion reported for the Early Triassic. However, our model outputs also predict that a change in $\Delta^{34}S$ within the range tested here would have been insufficient by itself to account for the positive shift in $\delta^{34}S_{evap}$ during the Early Triassic. Thus, the Early Triassic $\delta^{34}S_{evap}$ excursion must require an accompanying and substantial increase in the pyrite burial flux; a prediction in line with previous work (Newton et al., 2004; Bernasconi et al., 2017).

It has been suggested that elevated CO_2 and CH_4 emissions associated with the Siberian Traps (Cui and Kump, 2015; Wu et al., 2021) increased Earth's surface

temperature (Sun et al., 2012; Trotter et al., 2015). Along with the possible dieback of terrestrial vegetation (Benton and Newell, 2014) and environmental acidity (Algeo and Twitchett, 2010), this likely increased continental weathering in the latest Permian and Early Triassic (Korte et al., 2003; Algeo and Twitchett, 2010; Sun et al., 2018; Xie et al., 2019). Weathering liberates bio-essential nutrients and may have heightened the supply of nitrogen and phosphorus to the surface oceans (Algeo et al., 2013), stimulating primary productivity (Shen et al., 2015; Muto, 2021), and hence the flux of organic matter to the seafloor (Muto, 2021). Oceanic oxygen solubility would have been low in a warm ocean, and combined with increased organic marine snow, this would have fuelled the expansion of anoxia/euxinia in the late Permian and Early Triassic (Algeo et al., 2013; Lyu et al., 2019; Newby et al., 2021). Microbial sulphate reduction, encouraged by heightened nutrient fluxes and low oxygen concentrations would have driven the conversion of sulphate to sulphide and promote pyrite formation (Wignall et al., 2010) (and a "pyrite burial event", PBE) in the presence of reduced iron. With the expansion of anoxia, pyrite formation may have occurred more readily within the water column (Wignall et al., 2010; Grasby et al., 2021; Muto, 2021), heightening the magnitude of isotopic fractionation (Owens et al., 2013; Bryant et al., 2018). As suggested by our model results, this process would have sequestered isotopically light sulphur (^{32}S) from the ocean reservoir, contributing to the major positive $\delta^{34}S_{evap}$ excursion in the Early Triassic (Fig. 4).

Our modelling outputs predict the subsequent negative $\delta^{34}S_{evap}$ excursion at the OAB was preceded by a reduction in pyrite burial to a minimum of ~–0.02 Tmol/yr at 248 Ma (Fig. 4) (assuming a $\Delta^{34}S$ value of -40 ‰). As before, it was necessary to test for the sensitivity of inferred pyrite burial rates to changes in $\Delta^{34}S$, and we thus completed

several sensitivity tests with a range of values between -25 and -40 ‰ for the time interval 249 to 247 Ma (Fig. 3). For the above range of $\Delta^{34}S$ values, estimates for the pyrite burial flux minima at ~248 Ma varies between -0.03 and -0.02 Tmol/yr, respectively. Thus, our modelling procedure suggests that the fractionation factor for sulphate reduction and pyrite formation had little control over the reduction in the pyrite burial flux across the OAB. The isotopic composition of pyrite ($\delta^{34}S_{pyr}$) has been demonstrated to correlate with sea level fluctuations (Pasqiuer et al., 2017), and is of interest considering the OAB coincides with a general fall in eustatic sea level (Haq, 2018) (Fig. 4). It is intriguing that our modelling output suggests that changes in $\Delta^{34}S$ provide a relatively minor contribution to the decline in $\delta^{34}S_{evap}$ values we report for the OAB. Therefore, this time interval may reflect the expansion of anoxia and shallowing of the chemocline (Leavitt et al., 2013) inferred for much of the Early Triassic.

The available geochemical and sedimentological data fail to highlight any single mechanism for driving the observed negative $\delta^{34}S_{evap}$ excursion, and therefore we propose several mechanisms.

Oxygen isotope data suggest a reduction in SSTs during the latest Spathian and early Anisian (Fig. 4) (Sun et al., 2012). Cooling of marine waters would have likely been associated with invigoration of ocean circulation and lessened water column stratification (Lyu et al., 2019). Under such conditions, and in broad agreement with cerium-anomaly data for the latest Spathian (Song et al., 2012), the volume of anoxic water masses would have reduced, causing a decrease in pyrite burial (Fig. 4).

Coincident with the temperature decrease is a general fall in eustatic sea level (Haq, 2018) that would have exposed either/or previously deposited (1) pyrite-rich

shales from Early Triassic continental shelves) to weathering, (2) or extensive late Permian evaporite deposits (Zechstein). The sulphate released from pyrite oxidation and/or weathering of Permian Zechstein evaporites would be isotopically depleted (in comparison to Early Triassic $\delta^{34}S$ values of +32 ‰), thus contributing to the negative $\delta^{34}S_{evap}$ excursion at the OAB. This is in line with our model outputs, which suggest a reduction in pyrite burial to ~–0.02 Tmol/yr (e.g., negative pyrite burial is equivalent to pyrite weathering because the model otherwise specifies constant pyrite weathering). Using either atmospheric oxygen and/or ferric iron as oxidants, the weathering of pyrite would yield sulphuric acid (Kölling et al., 2019), hence exacerbating weathering rates and contributing to the high $^{87}Sr/^{86}Sr$ values at the OAB (Ikeda et al., 2017).

The recovery of $\delta^{34}S_{evap}$ values to earliest Triassic levels of 29 ‰ immediately after the OAB is concomitant with an increase in the pyrite burial flux to ~1.54 Tmol/yr at ~246 Ma (Fig. 4) (assuming a $\Delta^{34}S$ value of -40 ‰). We propose this reflects a recovery from the pyrite oxidation/evaporite weathering event responsible for causing negative $\delta^{34}S_{evap}$ excursion at the OAB. In line with decreasing $^{87}Sr/^{86}Sr$ values in the early Anisian (Ikeda et al., 2017; Xie et al., 2019), a relative decline in terrestrial weathering of sedimentary sulphides and evaporites would have reduced the flux of isotopically light sulphur into the ocean reservoir. In turn, this would have ensured rates of pyrite burial outpaced those of pyrite weathering, sequestering isotopically light sulphur from the seawater sulphate reservoir, facilitating a return to previous long-term $\delta^{34}S_{evap}$ values (Fig. 4).

Although the predicted pyrite burial rates after the OAB return to positive values, they are lower than the Early Triassic peak (Fig. 4). This is to be expected, since predicted

rates of pyrite burial began to decline prior to the weathering event at the OAB. This may indicate a gradual increase in sulphate concentrations and water column ventilation, in line with uranium isotope data that suggest a return to more oxygenated conditions in the early Anisian (Lau et al., 2016). Although organic-rich claystones in the pelagic Panthalassic Ocean suggest deposition under anoxic conditions (Muto et al., 2018; Muto, 2021), considering the uranium isotope record (Lau et al., 2016), it is likely that anoxia was restricted to oxygen minimum zones and not the entire ocean as indicated for the earliest Triassic. In addition, our model outputs are based on long-term records and changes in the global $\delta^{34}S_{evap}$ curve. Although it is likely that short-term events may coincide with minor changes in $\delta^{34}S$, our long-term $\delta^{34}S_{evap}$ curve and box model outputs are insensitive to them.

Our Middle–Late Triassic $\delta^{34}S_{evap}$ record from the Staithes S-20 core shows minimal variability around a consistent value of ~15 ‰ (Fig. 2); excluding $\delta^{34}S_{evap}$ data that are grouped together from literature sources. In accordance with this, our pyrite burial model output also exhibits relative stability, with minor fluctuations around steady state (Fig. 4). The stabilisation observed in $\delta^{34}S_{evap}$, and inferred for pyrite burial, is likely related to growth in the seawater sulphate reservoir (Bernasconi et al., 2017; Stebbins et al., 2019). Hence, more significant environmental perturbations would be required to disturb the global $\delta^{34}S_{evap}$ record. The global, and long-term impact of the Siberian Traps would have ended, enabling the Earth's climate system to re-establish more equable conditions (Sun et al., 2012). Coincident with this, strontium isotope data show a general decline in the continental weathering flux (Korte et al., 2003; Xie et al., 2019), thus reducing nutrient fluxes into the ocean, and stabilising the sulphur cycle (Payne and Kump, 2007).

Global $\delta^{34}S_{evap}$ data for the Late Triassic are sparse; therefore the $\delta^{34}S_{evap}$ curve and model output rely heavily on the Staithes S-20 record. Towards the Norian/Rhaetian boundary there is a positive $\delta^{34}S_{evap}$ excursion, which indicates an increase in pyrite burial from ~0.17 Tmol/yr at ~217 Ma to ~1.2 Tmol/yr at ~213 Ma (Fig. 4) (assuming a $\Delta^{34}S$ value of -35 ‰). Again, sensitivity tests were performed with a range of $\Delta^{34}S$ values between -25 ‰ and -50 ‰, yielding estimates for pyrite burial between 1.67 and 1.15 Tmol/yr, respectively (see Supplementary). As before, shifting $\Delta^{34}S$ to more negative values reduced the magnitude of the predicted increase in pyrite burial; nonetheless, we still consider it a noteworthy PBE.

The precise mechanism behind this $\delta^{34}S_{evap}$ excursion is currently unclear. A likely candidate is the emplacement of the Angayucham complex (Alaska, USA) at 214 ± 7 Ma (Ernst and Buchan, 2001), which coincides with an oceanic warming event (Trotter et al., 2015), high CO_2 concentrations (Tanner, 2018), and increasing humidity in Eastern Europe (Haas et al., 2012)[55] and the Alps (McKie, 2014). Such environmental responses would have invigorated the hydrological cycle, thus increasing weathering and nutrient fluxes (Kump et al., 2000), driving oceanic productivity in surface waters and oxygen consumption at depth in the water column. These environmental changes would have stimulated pyrite burial, and hence a positive $\delta^{34}S_{evap}$ excursion. Tighter age constraint of the Angayucham Complex and additional $\delta^{34}S_{evap}$ records over this time interval are necessary to ascertain their linkage. Why a $\delta^{34}S_{evap}$ excursion is not present during the similar CPE is unclear and requires further investigation.

A direct comparison between LIP-induced environmental change in the geologic record and anthropogenic climate forcing is complex and ambitious. However, the fact

that modern CO_2 emissions are potentially 14 times greater than peak emission rates during the EPME (Cui and Kump, 2015; Jurikova et al., 2020) is a matter of grave concern. The environmental changes recorded in our $\delta^{34}S_{evap}$ record and the EPME lasted on the order of 10 million years before the sulphur and carbon biogeochemical cycles became stabilised. Current anthropogenic emissions have already shown a measurable impact on marine ecosystems globally (Cheung and Frölicher, 2020), a reduction in the pH of surface waters (Orr et al., 2005), a decline in oxygen concentration (Schmidtko et al., 2017), and an increase in ocean stratification (Li et al., 2020). Understanding the long-term record of global Earth system perturbations caused by an elevation in greenhouse gases will improve our understanding of marine anoxia, weathering and pyrite burial events in the geologic record.

References

Algeo, T.J., Henderson, C.M., Tong, J., Feng, Q., Yin, H., Tyson, R.V., 2013. Plankton and productivity during the Permian-Triassic boundary crisis: An analysis of organic carbon fluxes. *Glob. Planet. Change*, 105, 52-67. DOI: 10.1016/j.gloplacha.2012.02.008

Algeo, T.J., Twitchett, R.J., 2010. Anomalous Early Triassic sediment fluxes due to elevated weathering rates and their biological consequences. *Geology*, 38, 1023-1026. DOI: 10.1130/G31203.1

Alroy, J., Aberhan, M., Bottjer, D.J., Foote, M., Fürsich, F.T., Harries, P.J., Hendy, A.J.W., Holland, S.M., Ivany, L.C., Kiessling, W., Kosnick, M.A., Marshall, C.R., McGowan, A.J., Miller, A.I., Olszewski, T.D., Patzkowsky, M.E., Peters, S.E., Villier, L., Wagner, P.J., Bonuso, N., Borkow, P.S., Brenneis, B., Clapham, M.E., Fall, L.M., Ferguson, C.A., Hanson, V.L., Krug, A.Z., Layou, K.M., Leckey, E.H., Nürnberg, S., Powers, C.M., Sessa, J.A., Simpson, C.,

Tomašových, A., Visaggi, C.C., 2008. Phanerozoic trends in the global diversity of marine invertebrates. *Science*, 321, 97-100. DOI: 10.1126/science.1156963

Benton, M.J., Newell, A.J., 2014. Impacts of global warming on Permo-Triassic terrestrial ecosystems. *Gondwana Res.* 25, 1308-1337. DOI: 10.1016/j.gr.2012.12.010

Bernasconi, S.M., Meier, I., Wohlwend, S., Brack, P., Hochuli, P.A., Bläsi, H., Wortmann, U.G., Ramseyer, K., 2017. An evaporite-based high-resolution sulfur isotope record of Late Permian and Triassic seawater sulfate. *Geochim. Cosmochim. Acta*, 204, 331-349. DOI: 10.1016/j.gca.2017.01.047

Broadley, M.W., Barry, P.H., Ballentine, C.J., Taylor, L.A., Burgess, R., 2018. End-Permian extinction amplified by plume-induced release of recycled lithospheric volatiles. *Nat. Geosci.* 11, 682-687. DOI: 10.1038/s41561-018-0215-4

Bryant, R.N., Jones, C., Raven M.R., Gomes, M.L., Berelson, W.M., Bradley, A.S., Fike, D.A., 2018. Sulfur isotope analysis of microcrystalline iron sulfides using secondary ion mass spectrometry imaging: Extracting local paleo-environmental information from modern and ancient sediments. *Rapid Commun. Mass Spectrom.* 33, 491-502. DOI: 10.1002/rcm.8375

Burgess, S.D., Bowring, S.A., 2015. High-precision geochronology confirms voluminous magmatism before, during, and after Earth's most severe extinction. *Sci. Adv.* 1, 1-14. DOI: 10.1126/sciadv.1500470

Canfield, D.E., Farquhar, J., Zerkle, A.L., 2010. High isotope fractionations during sulfate reduction in a low-sulfate euxinic ocean analog. *Geology*, 38, 415-418. DOI: 10.1130/G30723.1

Chen, Z-Q, Benton, M.J., 2012. The timing and pattern of biotic recovery following the end-Permian mass extinction. *Nat. Geosci.* 5, 375-383. DOI: 10.1038/ngeo1475

Cheung, W.W.L., Frölicher, T.L., 2020. Marine heatwaves exacerbate climate change impacts for fisheries in the northeast Pacific. *Sci. Rep.* 10, 6678. DOI: 10.1038/s41598-020-63650-z

Cohen, K.M., Finney, S.C., Gibbard, P.L., Fan, J.-X., 2013. The ICS International Chronostratigraphic Chart. *Episodes*, 36, 199-204.

Cui, Y., Kump, L.R., 2015. Global warming and the end-Permian extinction event: Proxy and modeling perspectives. *Earth-Sci. Rev.* 149, 5-22. DOI: 10.1016/j.earscirev.2014.04.007

Dal Corso, J., Bernardi, M., Sun, Y., Song, H., Seyfullah, L.J., Preto, N., Gianolla, P., Ruffell, A., Kustatscher, E., Roghi, G., Merico, A., Hohn, S., Schmidt, A.R., Marzoli, A., Newton, R.J., Wignall, P.B., Benton, M.J., 2020. Extinction and dawn of the modern world in the Carnian (Late Triassic). *Sci. Adv.* 6, eaba0099. DOI: 10.1126/sciadv.aba0099

Dal Corso, J., Mills, B.J.W., Chu, D., Newton, R.J., Song, H., 2022. Background Earth system state amplified Carnian (Late Triassic) environmental changes. *Earth Planet. Sci. Lett.* 578, 117321. DOI: 10.1016/j.epsl.2021.117321

Ernst, R.E., Buchan, K.L., 2001. "Large mafic magmatic events through time and links to mantle plume heads", in *Mantle plumes: Their identification through time: Geological Society of America Special Paper 352*. Editors: Ernst, R.E., Buchan, K.L., 352, 483-575.

Grasby, S.E., Bond, D.P.D., Wignall, P.B., Yin, R., Strachan, L.J., Takahashi, S., 2021. Transient Permian-Triassic euxinia in the southern Panthalassa deep ocean. *Geology*, 49, 889-893. DOI: 10.1130/G48928.1

Haas, J., Budai, T., Raucsik, B., 2012. Climatic controls on sedimentary environments in the Triassic of the Transdanubian Range (Western Hungary). *Palaeogeogr. Palaeoclimatol. Palaeoecol.* 353-355, 31-44. DOI: 10.1016/j.palaeo.2012.06.031

Haq, B.U., 2018. Triassic eustatic variations reexamined. *GSA Today*, 28

Ikeda, M., Tada, R., Ozaki, K., 2017. Astronomical pacing of the global silica cycle recorded in Mesozoic bedded cherts. *Nat. Commun.* 8, 1-9. DOI: 10.1038/ncomms15532

Johnson, D.I., Present, T.M., Li, M., Shen, Y., Adkins, J.F., 2021. Carbonate associated sulfate (CAS) $\delta^{34}S$ heterogeneity across the End-Permian Mass Extinction in South China. *Earth Planet. Sci. Lett.* 574, 117172. DOI: 10.1016/j.epsl.2021.117172

Jurikova, H., Gutjahr, M., Wallmann, K., Flögel, S., Liebetrau, V., Posenato, R., Angiolini, R., Garbelli, C., Brand, U., Wiedenbeck, M., Eisenhauer, A., 2020. Permian-Triassic mass extinction pulses driven by major marine carbon cycle perturbations. *Nat. Geosci.* 13, 745-750. DOI: 10.1038/s41561-020-00646-4

Kaiho, K., Oba, M., Fukuda, Y., Ito, K., Ariyoshi, S., Gorjan, P., Riu, Y., Takahashi, S., Chen, Z-Q., Tong, J., Yamakita, S., 2012. Changes in depth-transect redox conditions spanning the end-Permian mass extinction and their impact on the marine extinction: Evidence from biomarkers and sulfur isotopes. *Glob. Planet. Change*, 94-95, 20-32. DOI: 10.1016/j.gloplacha.2012.05.024

Kölling, M., Bouimetarhan, I., Bowles, M.W., Felis, T., Goldhammer, T., Hinrichs, K-U., Schulz, M., Zabel, M., 2019. Consistent CO_2 release by pyrite oxidation on continental shelves prior to glacial terminations. *Nat. Geosci.* 12, 929-934. DOI: 10.1038/s41561-019-0465-9

Korte, C., Kozur, H.W., Bruckshen, P., Veizer, J., 2003. Strontium isotope evolution of Late Permian and Triassic seawater. *Geochim. Cosmochim. Acta*, 67, 47-62. DOI: 10.1016/S0016-7037(02)01035-9

Kump, L.R., Brantley, S.L., Arthur, M.A., 2000. Chemical weathering, atmospheric CO_2, and climate. *Annu. Rev. Earth Planet. Sci.* 28, 611-667. DOI: 10.1146/annurev.earth.28.1.611

Kurtz, A.C., Kump, L.R., Arthur, M.A., Zachos, J.C., Paytan, A., 2003. Early Cenozoic decoupling of the global carbon and sulfur cycles. *Paleoceanography*, 18, 1090. DOI: 10.1029/2003PA000908

Lau, K.V., Maher, K., Altiner, D., Kelley, B.M., Kump, L.R., Lehrmann, D.J., Silva-Tamayo, J.C., Weaver, K.L., Yu, M., Payne, J.L., 2016. Marine anoxia and delayed Earth system recovery after the end-Permian extinction. *Proc. Natl. Acad. Sci.* 113, 2360-2365. DOI: 10.1073/pnas.1515080113

Leavitt, W.D., Halevy, I., Bradley, A.S., Johnston, D.T., 2013. Influence of sulfate reduction rates on the Phanerozoic sulfur isotope record. *Proc. Natl. Acad. Sci.* 110, 11244-11249. DOI: 10.1073/pnas.1218874110

Li, G., Cheng, L., Zhu, J., Trenberth, K.E., Mann, M.E., Abraham, J.P., 2020. Increasing ocean stratification over the past half-century. *Nat. Clim. Change*, 10, 1116-1123. DOI: 10.1038/s41558-020-00918-2

Lyu, Z., Zhang, L., Algeo, T. J., Zhao, L., Chen, Z-Q., Li, C., Ma, B., Ye, F., 2019. Global ocean circulation changes during the Smithian-Spathian transition inferred from carbon sulfur-cycle records. *Earth Sci. Rev.* 195, 114–132. DOI: 10.1016/j.earscirev.2019.01.010

McKie, T., 2014. Climatic and tectonic controls on Triassic dryland terminal fluvial system architecture, central North Sea. *Int. Assoc. Sedimentol. Spec. Publ.* 46, 19-58. DOI: 10.1002/9781118920435.ch2

McKie, T., 2017. "Palaeogeographic evolution of latest Permian and Triassic salt basins in northwest Europe", in *Permo-Triassic salt provinces of Europe, North Africa and the Atlantic margins, tectonics and hydrocarbon potential*. Editors Soto, J.J., Flinch, J.F., Tari, G. (Amsterdam Netherlands: Elsevier), 159-173. DOI: 10.1016/B978-0-12-809417-4.00008-2

Muto, S., 2021. Recurrent deposition of organic-rich sediments in Early Triassic pelagic Panthalassa and its relationship with global oceanic anoxia: New data from Kyoto, Southwest Japan. *Glob. Planet. Change*, 197, 103402. DOI: 10.1016/j.gloplacha.2020.103402

Muto, S., Takahashi, S., Yamakita, S., Suzuki, N., Suzuki, N., Aita, Y., 2018. High sediment input and possible oceanic anoxia in the pelagic Panthalassa during the latest Olenekian and early Anisian: Insights from a new deep-sea section in Ogama, Tochigi, Japan.

Palaeogeogr. Palaeoclimatol. Palaeoecol. 490, 687-707. DOI: 10.1016/j.palaeo.2017.11.060

Newby, S.M., Owens, J.D., Schoepfer, S.D., Algeo, T.J., 2021. Transient ocean oxygenation at end-Permian mass extinction onset shown by thallium isotopes. *Nat. Geosci.* 14, 678-683. DOI: 10.1038/s41561-021-00802-4

Newton, R.J., Pevitt E.L., Wignall, P.B., Bottrell, S.H., 2004. Large shifts in the isotopic composition of seawater sulphate across the Permo-Triassic boundary in northern Italy. *Earth Planet. Sci. Lett.* 218, 331-345. DOI: 10.1016/S0012-821X(03)00676-9

Orr, J.C., et al. 2005. Anthropogenic ocean acidification over the twenty-first century and its' impacts on calcifying organisms. *Nature*, 437, 681-686. DOI: 10.1038/nature04095

Owens, J. D., Gill, B.C., Jenkyns, H.C., Bates, S.M., Severmann, S., Kuypers, M.M.M., Woodfine, R.G., Lyons, T.W., 2013. Sulfur isotopes track the global extent and dynamics of euxinia during Cretaceous Ocean Anoxic Event 2. *Proc. Natl. Acad. Sci.* 110, 18407-18412. DOI: 10.1073/pnas.1305304110

Pasqiuer, V., Sansjofre, P., Rabineau, M., Revillon, S., Houghton, J., Fike, D.A., 2017. Pyrite sulfur isotopes reveal glacial-interglacial environmental changes. *Proc. Natl. Acad. Sci.* 114, 5941-5945. DOI: 10.1073/pnas.1618245114

Payne, J.L., Clapham, M.E., 2012. End-Permian Mass Extinction in the oceans: an ancient analog for the twenty-first century. *Annu. Rev. Earth Planet. Sci.* 40, 89-111. DOI: 10.1146/annurev-earth-042711-105329

Payne, J.L., Kump, L.R., 2007. Evidence for recurrent Early Triassic massive volcanism from quantitative interpretation of carbon isotope fluctuations. *Earth Planet. Sci. Lett.* 256, 264-277. DOI: 10.1016/j.epsl.2007.01.034

Payne, J.L., Lehrmann, D.J., Wei, J., Orchard, M.J., Schrag, D.P., Knoll, A.H., 2004. Large perturbations of the carbon cycle during recovery from the End-Permian extinction. *Science*, 305, 506-509. DOI: 10.1126/science.1097023

Rennie, V.C.F., Paris, G., Sessions, A.L., Abramovich, S., Turchyn, A.V., Adkins, J.F., 2018. Cenozoic record of $\delta^{34}S$ in foraminiferal calcite implies an early Eocene shift to deep-ocean sulfide burial. *Nat. Geosci.* 11, 761-765. DOI: 10.1038/s41561-018-0200-y.

Richardson, J.A., Keating, C., Lepland, A., Hints, O., Bradley, A.S., Fike, D.A., 2019. Silurian records of carbon and sulfur cycling from Estonia: The importance of depositional environment on isotopic trends. *Earth Planet. Sci. Lett.* 512, 71-82. DOI: 10.1016/j.epsl.2019.01.055

Richardson, J.A., Lepland, A., Hints, O., Prave, A.R., Gilhooly III, W.P., Bradley, A.S., Fike, D.A., 2021. Effects of early marine diagenesis and site-specific depositional controls on carbonate-associated sulfate: Insights from paired S and O isotopic analyses. *Chem. Geol.* 584, 120525. DOI: 10.1016/j.chemgeo.2021.120525

Rothman, D.H., Fournier, G.P., French, K.L., Summons, R.E., 2014. Methanogenic burst in the end-Permian carbon cycle. *Proc. Natl. Acad. Sci.* 111, 5462-5467. DOI: 10.1073/pnas.1318106111

Saitoh, R., Kaiho, K., Oba, M., Takahashi, S., Chen, Z-Q., Tong, J., 2013. A terrestrial vegetation turnover in the middle of the Early Triassic. *Glob. Planet. Change*, 105, 152-159. DOI: 10.1016/j.gloplacha.2012.07.008

Schmidtko, S., Stramma, L., Visbeck, M., 2017. Decline in global oceanic oxygen content during the past five decades. *Nature*, 542, 335-339. DOI: 10.1038/nature21399

Shen, J., Schoepfer, S.D., Feng, Q., Zhou, L., Yu, J., Song, H., Wei, H., Algeo, T.J., 2015. Marine productivity changes during the end-Permian crisis and Early Triassic recovery. *Earth-Sci. Rev.* 149, 136-162. DOI: 10.1016/j.earscirev.2014.11.002

Song, H., Tong, J., Algeo, T.J., Song, H., Qui, H., Zhu, Y., Tian, L., Bates, S., Lyons, T.W., Luo, G., Kump, L.R., 2014. Early Triassic seawater sulfate drawdown. *Geochim. Cosmochim. Acta*, 128, 95-113. DOI: 10.1016/j.gca.2013.12.009

Song, H., Wignall, P.B., Tong, J., bond, D.P.G., Song, H., Lai, X., Zhang, K., Wang, H., Chen, Y., 2012. Geochemical evidence from bio-apatite for multiple oceanic anoxic events during Permian-Triassic transition and the link with end-Permian extinction and recovery. *Earth Planet. Sci. Lett.* 353-354, 12-21. DOI: 10.1016/j.epsl.2012.07.005

Sun, Y., Joachimski, M.M., Wignall, P.B., Yan, C., Chen, Y., Jiang, H., Wang, L., Lai, X., 2012. Lethally hot temperatures during the Early Triassic greenhouse. *Science*, 338, 366-370. DOI: 10.1126/science.1224126

Sun, H., Xiao, Y., Gao, Y., Zhang, G., Casey, J.F., Shen, Y., 2018. Rapid enhancement of chemical weathering recorded by extremely light seawater lithium isotopes at the Permian-Triassic boundary. *Proc. Natl. Acad. Sci.* 115, 3782-3787. DOI: 10.1073/pnas.1711862115

Tanner, L.H., 2018. “Climates in the Late Triassic: perspectives, proxies and problems”, in *The Late Triassic world: Earth in a time of transition*. *Topics in Geobiology*. Editor: Tanner, L.H., (Cham, Switzerland: Springer) 46, 59-90. DOI: 10.1007/978-3-319-68009-5_3

Trotter, J.A., Williams, I.S., Nicora, A., Mazza, M., Rigo, M., 2015. Long-term cycles of Triassic climate change: a new $\delta^{18}O$ record from conodont apatite. *Earth Planet. Sci. Lett.* 415, 165-174. DOI: 10.1016/j.epsl.2015.01.038

Wignall, P.B., Bond, D.P.G., Kuwahara, K., Kakuwa, Y., Newton, R.J., Poulton, S.W., 2010. An 80 million year oceanic redox history from Permian to Jurassic pelagic sediments of the Mino-Tamba terrane, SW Japan, and the origin of four mass extinctions. *Glob. Planet. Change*, 71, 109-123. DOI: 10.1016/j.gloplacha.2010.01.022

Wu, Y., Chu, D., Tong, J., Song, H., Dal Corso, J., Wignall, P.B., Song, H., Du, Y., Cui, Y., 2021. Six-fold increase of atmospheric pCO_2 during the Permian-Triassic mass extinction. *Nat. Commun.* 12, 2137. DOI: 10.1038/s41467-021-22298-7

Xie, T., Zhang, Q., Hu, S., Zhou, C., Huang, J., Wen, W., 2019. The Mesozoic maximum of $^{87}Sr/^{86}Sr$ ratio: a critical turning point after the end-Permian mass extinction. *Carbonates Evaporites*, 34, 1021-1029. DOI: 10.1007/s13146-018-0475-5

Zhang, Y., Wen, H., Zhu, C., Fan, H., Xiao, J., Wen, J., 2021. Molybdenum isotopic evidence for anoxic marine conditions during the end-Permian mass extinction. *Chem. Geol.* 575, 12059. DOI: 10.1016/j.chemgeo.2021.120259

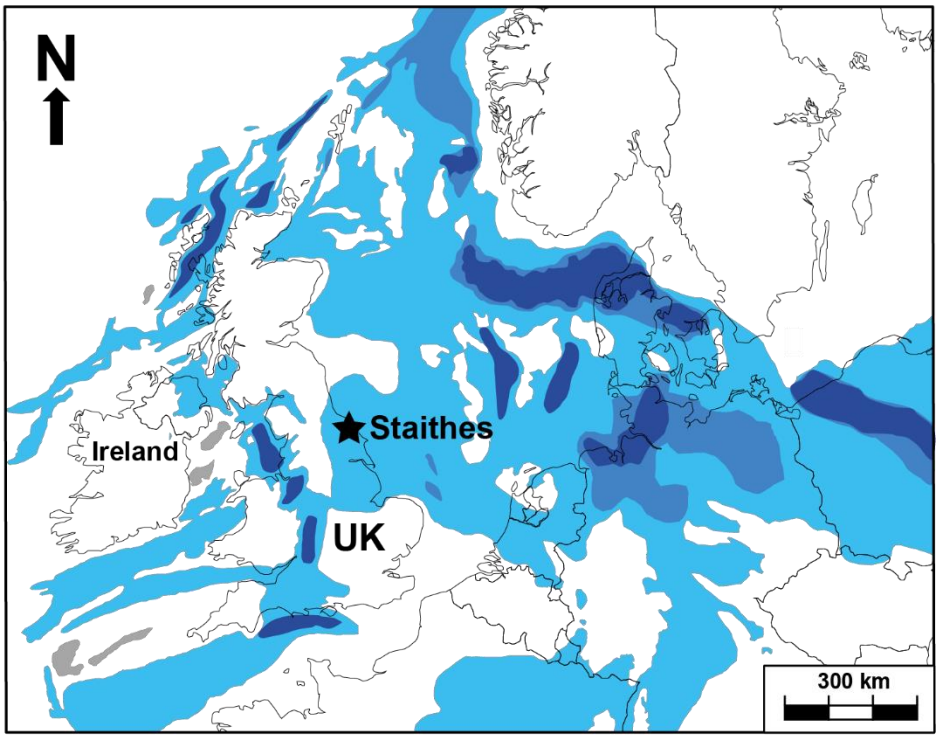

Figure 1: *The location of the Staithes S-20 borehole displayed by the black star, and the distribution of Permian-Triassic sedimentary basins of NW Europe marked by the blue tones. The darker tones represent thicker sedimentary sequences that accumulated along the main rift axes (adapted from McKie, 2017).*

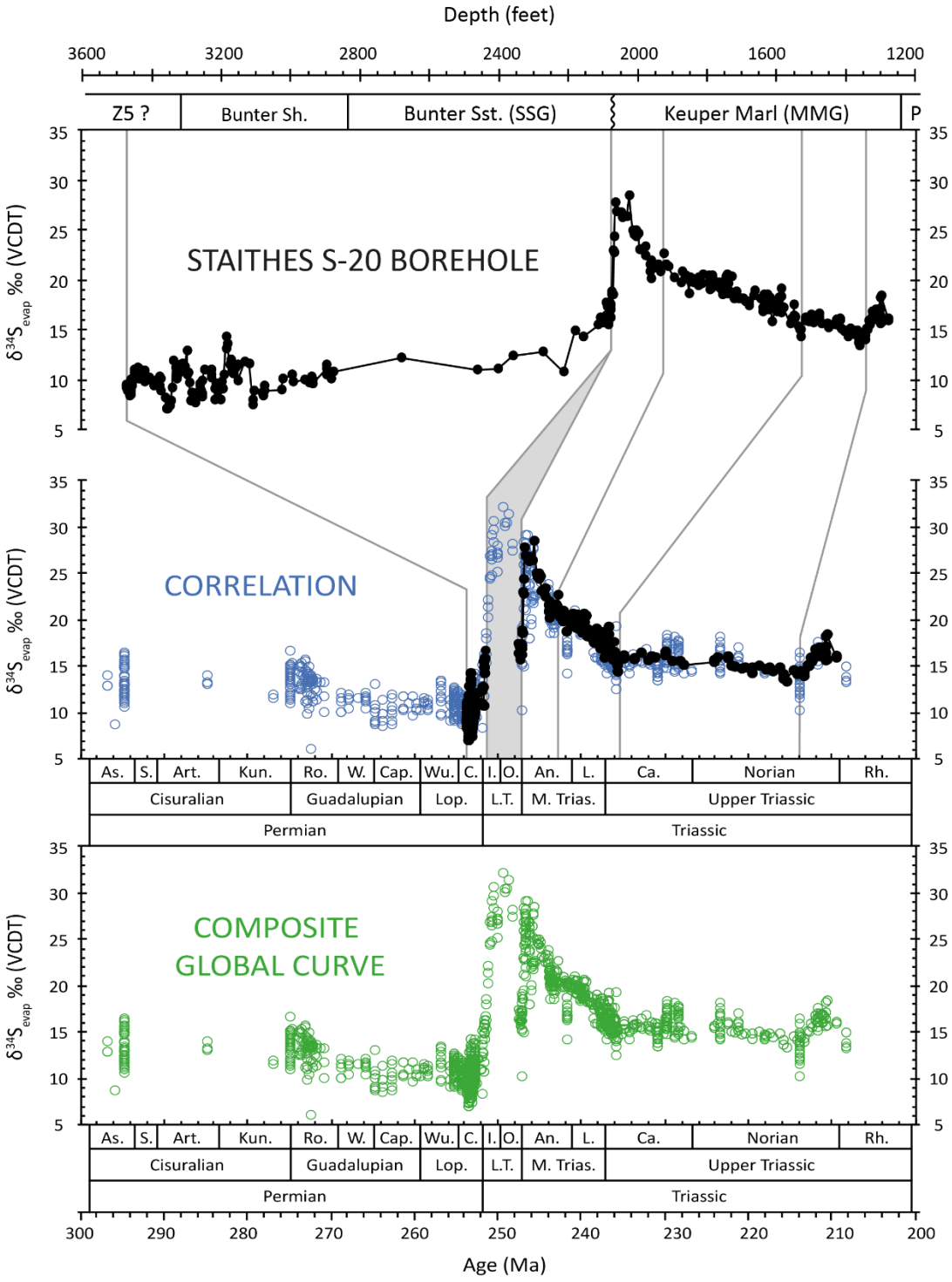

Figure 2: *Sulphur isotope records derived from sedimentary evaporites of the Staithes S-20 borehole, northeast Yorkshire (top). The lithostratigraphy of the borehole is also displayed. The correlation between the global composite curve and the Staithes record (middle) is based primarily upon trends and inflection points within the isotope records. The Staithes record was combined with the global composite to create a single composite curve (bottom; see Appendix 1).*

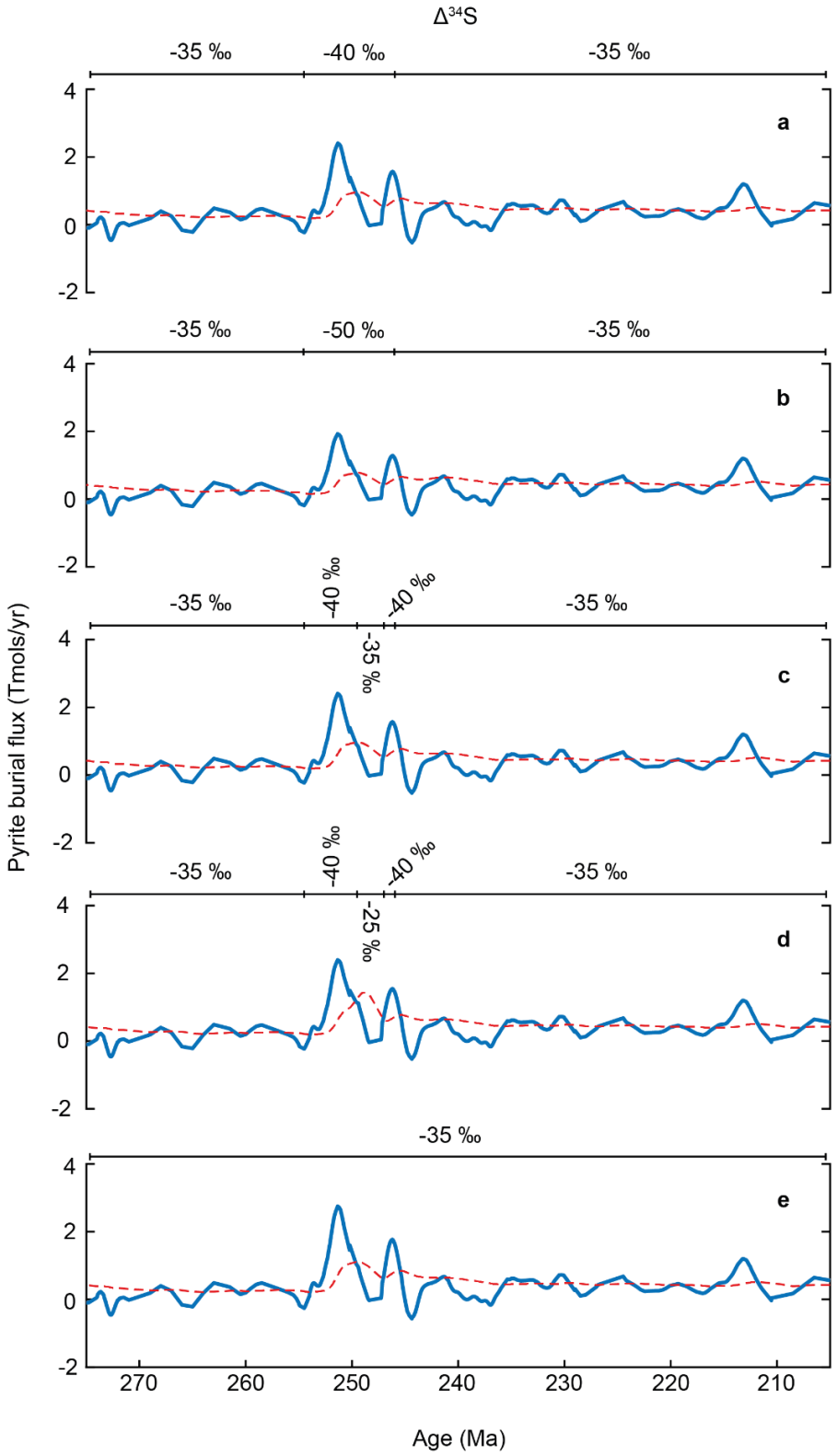

Figure 3: *Sensitivity of the modelled pyrite burial flux to changes in the fractionation factor for the chemical reduction of sulphate to sulphide ($\Delta^{34}S$), and subsequent pyrite formation. The bar above each model output displays the value set for $\Delta^{34}S$ at different intervals of time. The only parameter changed between each model run is $\Delta^{34}S$, enabling us to test the influence of this specific parameter on the inferred pyrite burial flux.*

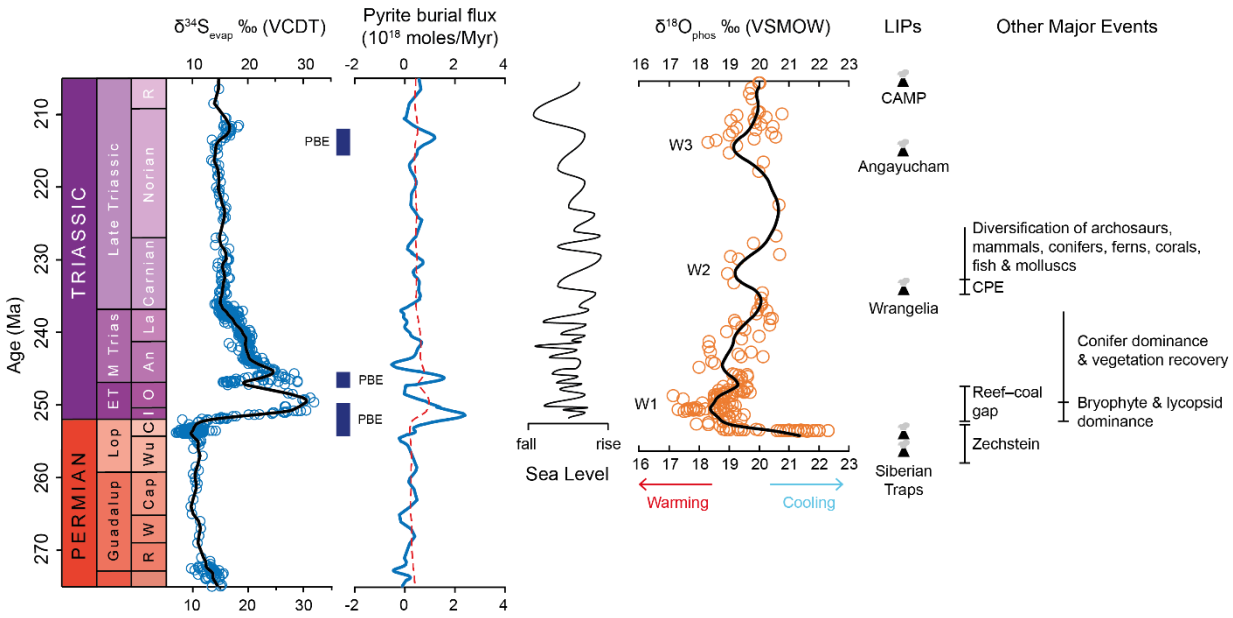

Figure 4: *Sulphur and oxygen (Sun et al., 2012; Trotter et al., 2015) isotope records, modelled pyrite burial flux (Fig. 3a) and environmental and biological changes for the Permian-Triassic. The sulphur and oxygen isotope data were fitted with a smoothing spline to produce the curves. The pyrite burial flux was calculated with the use of a stable isotope box model (Kurtz et al., 2003) (see Appendix 1). The predicted pyrite burial events are indicated with the abbreviation 'PBE'. The blue line represents the calculated values, and the red dashed line illustrates the results assuming steady state. Environmental and biological events (Chen and Benton, 2012; Saitoh et al., 2013) of significance are included to display how our isotope records and model outputs relate to the broader environmental context of the latest Permian and Triassic.*

Chapter 3

Citation: Salisbury, J., Gröcke, D.R., McKie, T., 2023. Sulphur isotope stratigraphy of drill cuttings and stratigraphic correlation of Permian-Triassic evaporites. *Front. Earth Sci.* 11, 1216365. DOI: 10.3389/feart.2023.1216365

Sulphur isotope stratigraphy of drill cuttings and stratigraphic correlation of Permian-Triassic evaporites

Jack Salisbury[1*], Darren R. Gröcke[1*], Tom McKie[2]

1. Stable Isotope Biogeochemistry Laboratory (SIBL), Department of Earth Sciences, Durham University, Durham University, South Road, Durham DH1 3LE, UK

2. Shell UK Exploration and Production, 1 Altens Farm Road, Nigg, Aberdeen AB12 3FY, UK

** = corresponding authors: jack.salisbury@durham.ac.uk, d.r.grocke@durham.ac.uk*

The stratigraphy of the European late Permian-Triassic commonly lacks chronostratigraphic constraint due to the scarcity of diagnostic fossils for biostratigraphy. This is particularly true for the UK, and as a result, stratigraphic correlation within and between sedimentary basins is primarily reliant on lithostratigraphy. Evaporitic sulphate can be used to develop time series of $\delta^{34}S_{evap}$ data that can be utilised for stratigraphic correlation. However, the availability of continuous drillcore is limited, whilst drill cuttings are commonly acquired but are widely overlooked for stable isotope stratigraphy. We derive a $\delta^{34}S_{evap}$ record from drill cuttings from the southern North Sea Basin, and successfully correlate it with an equivalent published $\delta^{34}S_{evap}$ record from a continuous drillcore in the Cleveland Basin, Yorkshire, UK. We have chosen seven points in the $\delta^{34}S_{evap}$ records for stratigraphic correlation, defining eight packages of isotopically distinct coeval strata. This is significant, as the ubiquity of drill cuttings presents the opportunity to derive $\delta^{34}S_{evap}$ curves with high geospatial resolution. Equivalent gamma ray logs were used for correlation and compared with the $\delta^{34}S_{evap}$ curves. The correlations agree relatively well, however, the $\delta^{34}S_{evap}$ correlation permits the development of more robust chronostratigraphic constraints. Specifically, the $\delta^{34}S_{evap}$ records constrain the age of the Bunter Shale and Bunter Sandstone in the western Southern North Sea to the latest Permian. This has significant implications for understanding the stratigraphy and palaeogeographic evolution of UK Permian-Triassic sedimentary basins, and may have economic implications, since the Bunter Sandstone is being considered as a potential reservoir for CO_2 storage in the UK sector.

1. Introduction

The late Permian and Triassic time intervals have received a great deal of interest over the past 50 years, due to numerous events of geological significance, most notably the End Permian Mass Extinction (EPME) and the End Triassic Extinction (ETE) — two of the 'Big Five' extinction events (Raup and Sepkoski, 1982; Sepkoski, 1996). Both the Permian–Triassic boundary (PTB) interval and the ETE are associated with major biogeochemical perturbations. In particular, the sulphur cycle exhibits significant shifts in the sulphur isotopic composition ($\delta^{34}S$) of seawater sulphate (Newton et al., 2004; Horacek et al., 2010; Bernasconi et al., 2017; He et al., 2020). Despite this knowledge, high-resolution $\delta^{34}S$ records remain sparse between these major extinction events, with many studies focusing primarily on specific, short intervals of time, such as the PTB (Newton et al., 2004; Schobben et al., 2015) and the Early Triassic (Lyu et al., 2019; Song et al., 2019). The sedimentary environment for much of the European Permo-Triassic was arid and continental (with episodic marine influence) (Kutzbach and Gallimore, 1989; Parrish, 1993), characterised by abundant evaporite-bearing sediments (McKie, 2017). Thus, these evaporitic sedimentary sequences may provide an ideal opportunity to generate marine $\delta^{34}S_{evap}$ records for correlation.

Stable isotope stratigraphy has been successful in deriving chronostratigraphic correlations at high resolution (e.g., Jenkyns et al., 2002; Korte and Kozur, 2010; Yao, et al., 2019; Paytan et al., 2020). Specifically, carbon isotope stratigraphy has been applied using marine and terrestrial organic matter and carbonate (see Gröcke, 2020). In addition, sulphur isotope stratigraphy has also proved successful for correlation using marine evaporites, barite and carbonate-associated sulphate (CAS) ($\delta^{34}S_{evap}$, $\delta^{34}S_{barite}$,

$\delta^{34}S_{CAS}$, respectively: see review by Paytan et al., 2020). Despite the high-resolution achieved with $\delta^{34}S_{barite}$ records (Markovic et al., 2015; Paytan et al., 1998, 2004, 2012; Yao et al., 2018, 2020), barite is predominantly acquired from pelagic sediments, and thus only provides insight into the previous 130 million years (Yao et al., 2019). Although $\delta^{34}S_{CAS}$ records have been widely employed to understand the ancient sulphur cycle (e.g., Newton et al., 2004; Luo et al., 2010; Song et al., 2014; Crockford et al., 2019; He et al., 2019, 2020), their suitability as a stratigraphic and palaeoenvironmental tool is under scrutiny due to issues of diagenesis (Rennie and Turchyn, 2014; Present et al., 2015, 2019; Richardson et al., 2019, 2021; Murray et al., 2021; Bryant et al., 2022). Accordingly, much of the variability in $\delta^{34}S_{CAS}$ across the PTB and Early Triassic has been attributed to post-depositional alteration (Bernasconi et al., 2017; Johnson et al., 2021). Therefore, it would conclude that evaporites are the most reliable proxy to generate pre-Cretaceous global marine $\delta^{34}S$ curves.

The $\delta^{34}S$ of marine sedimentary sulphates (e.g., evaporites) is assumed to be indicative of coeval seawater sulphate. The respective contributions and isotopic composition of sulphur fluxes entering and leaving the ocean reservoir act to control the $\delta^{34}S$ of seawater sulphate ($\delta^{34}S_{sulphate}$) over geologic time (Bernasconi et al., 2017; Crockford et al., 2019; Paytan et al., 2012, 2020). It is generally assumed that for much of the Phanerozoic, oceanic sulphate has largely remained well-mixed and isotopically homogenous (Paytan et al., 2012; Present et al., 2020). Therefore, coeval sedimentary sulphates will exhibit comparable absolute $\delta^{34}S_{sulphate}$ values, providing high-resolution stratigraphic correlation across sedimentary basins, especially over periods of significant isotopic change (Yao et al., 2019; Paytan et al., 2020): for example, over the PTB interval (e.g., Claypool et al., 1980; Bernasconi et al., 2017).

The late Permian–Early Triassic time interval is associated with a major perturbation in the sulphur cycle, that is characterised by a rapid increase in the $\delta^{34}S$ of seawater sulphate (recorded in $\delta^{34}S_{CAS}$ and $\delta^{34}S_{evap}$) from ~+12 ‰ in the late Permian to >+30 ‰ in the earliest Triassic (Newton et al., 2004; Insalaco et al., 2006; Horacek et al., 2010; Luo et al., 2010; Song et al., 2014; Schobben et al., 2015; Bernasconi et al., 2017). This major positive $\delta^{34}S$ excursion has been interpreted as a result of an enhanced pyrite burial flux, related to the expansion of ocean anoxia after the emplacement of the Siberian Traps large igneous province in the late Permian (Newton et al., 2004; Bernasconi et al., 2017; Salisbury et al., 2022). Bernasconi et al. (2017) compiled and produced a $\delta^{34}S_{evap}$ record from the latest Permian to Middle/Late Triassic from multiple sedimentary basins. The resultant $\delta^{34}S_{evap}$ curve showed that the record was not erratic in nature, but changed systematically through time, and hence could be used for stratigraphic correlation: as previously indicated for $\delta^{34}S_{barite}$ (Paytan et al., 1998, 2004, 2012, 2020). Salisbury et al. (2022) produced a high-resolution $\delta^{34}S_{evap}$ curve for the Middle and Late Triassic using evaporitic minerals (e.g., gypsum, anhydrite, halite) from a continuous drillcore, Staithes S-20 borehole, in Yorkshire, England. This updated $\delta^{34}S_{evap}$ record revealed a new, prominent negative excursion of ~10 ‰ at the Olenekian/Anisian boundary (Salisbury et al., 2022). Although the mechanism for this excursion is currently unclear, one possibility is a weathering pulse, interrupting the pyrite burial event with an influx of isotopically light sulphur (Salisbury et al., 2022). The $\delta^{34}S_{evap}$ curve quickly recovers in the earliest Anisian to pre-excursion values after which it exhibits a gradual decline for the remainder of the Triassic to the Norian/Rhaetian boundary (Salisbury et al., 2022). The global $\delta^{34}S_{evap}$ curve produced in Salisbury et al.

(2022) will provide a basis from which to correlate other sedimentary sequences and basins for the Triassic.

In the Triassic strata of the UK, laterally extensive evaporite beds are used to correlate within and between sedimentary basins based primarily upon the principles of lithostratigraphy (Warrington et al., 1980). The validity of this approach, in some cases, is questionable, especially when correlating between a chain of halite-bearing basins, as a hydrologically restricted basin cannot, by definition, export brines to an adjacent basin in the chain (Warren, 2006). This, and the diachroneity of lithostratigraphic boundaries, limits the validity of lithostratigraphic correlations in deriving a robust chronostratigraphic framework for the Permian–Triassic in the UK. Boreholes offer a continuous, unweathered stratigraphic interval and are thus preferable to outcrop (e.g., Staithes S-20). However, only partial cores are usually taken, primarily due to limited time and costs, and the perceived lack of value of information collected outside the economic target interval. In contrast, drill cuttings, depending on the drilling technique used, are commonly collected and retained. If one could analyse drill cuttings and create a similar long-term $\delta^{34}S_{evap}$ curve, then it would offer the potential to produce more stratigraphic records geo-spatially and thus, generate a more robust temporal record for stratigraphic correlation. Ultimately, this approach could be developed in conjunction with biostratigraphy, chemostratigraphy (Metzger et al., 2014; Eldrett et al., 2021) and magnetostratigraphy when possible.

Although promising, drill cuttings present other issues that require consideration, including sampling density, caving, and contamination. Cuttings are collected in batches that reflect an average depth interval, which will vary in resolution depending on drilling

and sampling rates. In addition, the integrity of samples from a specific depth may prove questionable, due to the mixing of fragments during the extraction process. Mixing can occur via caving, whereby cuttings from higher stratigraphic levels combine with those at a deeper level where the drill bit is located, or through mixing within the drilling fluid as it is returned to the surface. Drilling fluids may also contaminate samples for specific types of chemical analyses (Kubo et al., 2016). However, recent studies have demonstrated the validity of drill cuttings for carbon isotope stratigraphy, in part through comparison with $\delta^{13}C$ records from cored intervals and outcrop (Metzger et al., 2014; Eldrett et al., 2021). Sanei et al. (2020) demonstrated that with sufficient cleaning of drill cuttings, total organic carbon (TOC) values are comparable to those directly obtained from cored intervals. To our knowledge, only a single study has demonstrated the suitability of borehole cuttings for sulphur isotope stratigraphy (Cao et al., 2016), however, the authors did not demonstrate the validity of drill cuttings for evaporitic lithologies.

In this study, we targeted drill cuttings from an offshore southern North Sea Basin borehole (42/28-2) that spans the late Permian to Late Triassic time interval (Figure 1). This borehole was chosen primarily because lithostratigraphic correlation suggests it spans a stratigraphic interval equivalent to that of the Staithes S-20 borehole (Salisbury et al., 2022). The primary aim of this study was to determine if drill cuttings through an evaporite-bearing sedimentary sequence can be used for sulphur isotope stratigraphy. We successfully correlate the $\delta^{34}S_{evap}$ curve generated from drill cuttings at site 42/28-2 to the Staithes S-20 curve, demonstrating the validity of drill cuttings for correlation between sedimentary basins. Thus, although we advise that future studies should always consider the impact of drilling fluids and post-drilling washing techniques, the excellent

correlation between 42/28/-2 and Staithes S-20 suggests they had little effect on $\delta^{34}S_{evap}$ values (in this study).

2. Geological setting

During the late Permian and Triassic, Britain was located at a palaeolatitude of ~20 °N (Newell, 2018), and deposition occurred under a largely arid to semi-arid climate (McKie and Williams, 2009) conducive to evaporite deposition (Fig. 1). Late Permian rifting provided the Boreal Ocean with restricted access to the subsiding southern Permian Basin (Smith, 1989; McKie, 2017), facilitating the deposition of the Zechstein carbonate-evaporite cycles. Ongoing rifting during the Triassic subsequently opened access routes to the south, allowing ingress of Tethyan seawater into the southern Permian Basin (McKie, 2017). In this study, we focused on the time interval that spans from the uppermost Zechstein (Changhsingian – latest Permian) through to the offshore equivalent of the Keuper Marl of the Mercia Mudstone Group (MMG), the Triton and Dudgeon formations (Norian, Late Triassic) (Fig. 2).

In total, the Zechstein is composed of seven carbonate-evaporite cycles (Tucker, 1991). In this study, the uppermost Zechstein is represented in both boreholes as thick-bedded halite. Overlying the Zechstein evaporites are the terminal splay/playa deposits of the Bunter Shale, followed by the Bunter Sandstone — the offshore equivalent of the Sherwood Sandstone Group (SSG) of eastern England (Noy et al., 2012). The latter is predominantly composed of arenaceous sandstones, largely representing a fluvial-aeolian depositional regime (Ambrose et al., 2014; McKie, 2017). Monsoonal rainfall on the Variscan mountains and smaller basement massifs fed extensive braided river systems (Geluk et al., 2018) that flowed towards basin centre playa and sabkha (Fig. 1).

However, intermittent periods of aridity suppressed fluvial deposition rates and facilitated aeolian reworking (McKie, 2017). Biostratigraphic age constraints suggest a Middle Triassic (Anisian) age for the Otter Sandstone (Sherwood Sandstone Group) in Devon (Holloway et al., 1989; Spencer and Storrs, 2002) and an Early Triassic age for the Buntsandstein and its' equivalents in continental Europe (Scholze et al., 2016, 2017). However, such constraints are lacking for the Bunter Sandstone in the Cleveland and SNS basins (Warrington et al., 1980).

The SSG is overlain by the MMG (and offshore equivalents), with the boundary being marked by the transition from sandstones to mudstones (Howard et al., 2008; Newell et al., 2018). The MMG is composed of green/grey mudstones interbedded with siltstone, and bedded halite is interspersed with nodular gypsum and anhydrite throughout the succession. In the UK sector, deposition coincided with the southerly retreat of the SSG beginning in the Middle Triassic, with fluvial systems replaced by a hypersaline playa lake and coastal sabkha environment (Howard, 2008) (Fig. 1). This environmental shift facilitated the deposition of evaporites, including bedded halites (i.e., the Röt) and nodular sulphates. Episodic marine flooding during the Anisian and Ladinian is evidenced by acritarchs and lingula in various locations (Warrington, 1974; Wilson, 1993; Ambrose and Wakefield, 2015; Warrington and Pollard, 2021). Evaporite formation and deposition continued intermittently until the latest Triassic. During the latest Triassic, a major marine transgression occurred (Peacock, 2004) leading to the deposition of the Penarth Group (Lott and Warrington, 1988; Warrington and Ivimey-Cook, 1992; Gallois, 2009), that is biostratigraphically constrained to the Rhaetian (Lott and Warrington, 1988; Warrington, 1997; Hounslow and Ruffell, 2006). This interval represents the transition from marginal marine to fully marine deposition, which

became well established during the Hettangian with the deposition of the Lias Group (Wignall and Bond, 2008; Gallois, 2009).

Despite intensive study, the units of the SSG and MMG commonly lack any age-diagnostic fossils for biostratigraphic constraint and hence, dominantly rely on lithostratigraphy. Although, the marine Triassic stratigraphy of continental Europe (i.e., Muschelkalk) is aided by biostratigraphic constraints (Narkiewicz, 1999; Márquez-Aliaga et al., 2000; Bachman and Kozur, 2004; Franz et al., 2013; Chen et al., 2019), the UK sector facies are particularly impoverished in age-diagnostic fossils, in part due to the lack of marine carbonates when compared with continental Europe (e.g., Horacek et al., 2010; Boschetti et al., 2011). As a result, it is common for this region to lack sufficient chronostratigraphic calibration for the Triassic interval (McKie and Williams, 2009). Therefore, alternative techniques are required to constrain and corroborate the Triassic lithostratigraphic framework of northwest Europe (especially the UK) with continental Europe. Due to the presence of evaporite minerals throughout the MMG, sulphur isotope stratigraphic correlation is an ideal candidate to address this issue.

3. Methods

Gamma ray data were obtained for boreholes Staithes S-20 (NZ71NE/14; grid reference, NZ 476034E 518000N) and 42/28-2 (54.078556, 0.454889). The onshore Staithes S-20 borehole is located in the Cleveland Basin, England, whereas borehole 42/28-2 is located offshore in the southern North Sea (Figure 1). The sulphur isotope record of Staithes S-20 is presented in Salisbury et al. (2022). Borehole drill cuttings from 42/28-2 were sampled at the British Geological Survey, Keyworth, Nottingham. The washed drill cuttings were collected at variable depth intervals, providing a total of 50 samples for

sulphur isotope analysis. The sampling resolution varies throughout the borehole, depending on the abundance of evaporite minerals suitable for sampling. Each sample represents a depth range and is thus viewed as a lithological average over that depth interval.

Each drill cutting sample was inspected under an optical microscope and individual random chips of gypsum, anhydrite and/or halite were picked and transferred into 1.5 ml micro-centrifuge tubes. Approximately 1–3 g of evaporite samples were placed into a 15 ml centrifuge tube with 10 % NaCl solution. Blanks of NaCl produced no visible barium sulphate ($BaSO_4$). The evaporites were left to sit in the solution for between 24–48 hrs and agitated every few hours during the working day. Upon dissolution, the samples underwent centrifugation for 5 minutes at 3000 rpm, before the supernatant was poured into 50 ml centrifuge tubes for subsequent $BaSO_4$ precipitation. Between 15–20 ml of 10 % barium chloride ($BaCl_2$) was added to the evaporite-dissolved solution. This solution often turned cloudy immediately indicating that $BaSO_4$ was being precipitated, according to the following equation:

$$\mathrm{BaCl_2 + SO_4^{2-} \rightarrow BaSO_4 + 2Cl^{2-}} \quad [1]$$

The pH of the solution was reduced to ~1–2 with the addition of 3M HCl to prevent the precipitation of barium carbonate ($BaCO_3$). The samples were left for at least 24 hrs for $BaSO_4$ precipitation, after which they were centrifuged at 3000 rpm for 5 minutes. The $BaCl_2$/HCl supernatant was discarded according to safety regulations for appropriate waste disposal. The resultant pellet of $BaSO_4$ was rinsed with ~30–40 ml of deionised water to neutralise the sample. Neutrality was often achieved after three rinses. The centrifuge tube containing the $BaSO_4$ was placed in a drying oven set at 80°C

for between 24 and 48 hrs. The $BaSO_4$ was then crushed into a fine powder using an agate pestle and mortar and archived in a 1.5 ml micro-centrifuge tube.

For sulphur isotope analysis, each sample was weighed out (0.2–0.4 mg) into 6×4 tin capsules. Stable sulphur isotope analysis was performed in the Stable Isotope Biogeochemistry Laboratory (SIBL) at Durham University using a Thermo Scientific EA IsoLink™ coupled to a Thermo Scientific Delta V Plus isotope-ratio mass-spectrometer. Evaporite sulphur isotope ratios are expressed in standard delta (δ) notation in per mil (‰) relative to Vienna Canyon Diablo Triolite (VCDT) according to the following equation:

$$\delta^{34}S = \left[\frac{((^{34}S/^{32}S)_{sample} - (^{34}S/^{32}S)_{VCDT})}{(^{34}S/^{32}S)_{VCDT}}\right] * 1000 \quad [2]$$

The $\delta^{34}S$ data were normalised through calibration against four international standards (IAEA-S-1, IAEA-S-2, IAEA-S-3, NBS 127), providing a linear range in $\delta^{34}S$ between –32.5 ‰ and +22.6 ‰. An internal barium sulphate (Acros Organics silver sulphate, Catalogue number: 194070100, lot: A0384698) was analysed throughout the analytical period and produced an average $\delta^{34}S$ value of -18.1 ‰ ± 0.25 (1σ) (*n* = 14). Analytical uncertainty of $\delta^{34}S$ was ±0.15 ‰ (1 σ) for replicate analyses of the international standards during the production of this dataset. Reproducibility of sample $\delta^{34}S_{evap}$ was the same or better. Total sulphur of the sample is calculated as part of the isotopic analysis using an internal standard, sulphanilamide (S = 18.619 %).

4. Results/discussion

4.1. Gamma ray correlation

Gamma ray profiles for the Staithes S-20 and 42/28-2 boreholes are presented in Figure 3. The correlation used the diagnostic log motifs of lithological units that are known to

be persistent over greater distances than the spacing between the two study wells (Bachman et al., 2010). These log motifs are calibrated against core in other wells within the basin. In the Permian Zechstein at the base of 42/28-2, gamma ray values are generally low (~50 API), punctuated by brief peaks to ~200 API. After a final low, gamma ray values increase to ~150 API at the boundary with the Bunter Shale. Only the top of the Zechstein was cored in Staithes S-20. Gamma ray values fall to around ~0 API at ~3500 ft, corresponding to an interval of bedded halite, before increasing to ~130 API at the base of the Bunter Shale (similar to borehole 42/28-2), enabling correlation between the two boreholes.

Both the Staithes S-20 and 42/28-2 boreholes show relatively stable gamma ray profiles during the lower Bunter Shale (around ~110 API). Gamma ray profiles exhibit a more erratic response during the upper Bunter Shale, beginning at 3100 ft in Staithes S-20 and ~7700 ft in borehole 42/28-2. This marks the base of the Rogenstein Member, which includes interbedded sandstones that contribute to the erratic behaviour in gamma ray data. In both records, the boundary between the Bunter Shale and Bunter Sandstone is marked by a sharp upwards decrease in gamma. The Bunter Sandstone exhibits relatively stable but low gamma ray values, around ~60 API, and is particularly distinct in the 42/28-2 borehole record. The Bunter Sandstone terminates with a sharp increase in gamma ray, corresponding to an unconformity at ~2080 ft in Staithes S-20 and ~6200 ft in 42/28-2. Evidence for a hiatus in sedimentation is observed directly in the core of Staithes S-20 but is only inferred in borehole 42/28-2 based on gamma ray records and regional correlation (Bachman et al., 2010). Throughout the overlying MMG, the gamma ray record is slightly elevated in Staithes S-20. This offset may be a product of different tools or calibration and both records remain relatively stable. Brief lower

gamma Mercia Mudstone packages likely mark the position of greater evaporite proportion, as the low potassium content of the rock reduces the background gamma API values.

4.2. Preservation of primary $\delta^{34}S_{evap}$ signals

The precipitation of gypsum is associated with a minor fractionation factor ($\Delta^{34}S_{precipitate\text{-}brine}$), with experimental studies reporting a range between +1.59 and +2 ‰ (Thode and Monster, 1965; Holser and Kaplan, 1966; Nielsen, 1978; Raab and Spiro, 1991; Van Driessche et al., 2016). Although the $\delta^{34}S$ of both the brine and precipitate decrease progressively with continued evaporation, the results of Raab and Spiro (1991) suggest relatively similar $\Delta^{34}S_{precipitate\text{-}brine}$ values are maintained until the middle of the halite stability field. Thus, it is generally assumed that the $\delta^{34}S$ of a marine Ca-sulphate is indicative of the isotopic composition of the brine from which it precipitated (Schreiber and Tabakh, 2000). Considering that we exclusively sampled calcium-sulphates and halite, it is unlikely that changes in mineralogy and/or sulphur isotope reservoir effects associated with prolonged restriction had a major impact on the $\delta^{34}S_{evap}$ records from boreholes 42/28-2 and Staithes S-20.

The $\delta^{34}S_{evap}$ correlation presented in this study is surprising in that the 42/28-2 sediments have been exposed and saturated with drilling fluids: unfortunately, there is no record of what drilling fluids were used when coring. Samples can be fully covered in fluids during the drilling process and washing them away entirely is difficult (Kubo et al., 2016), thus potentially impacting the integrity of sample geochemistry (e.g., Stuckman et al., 2019; Sanei et al., 2020). $\delta^{34}S_{evap}$ values in drill cuttings are vulnerable to contamination by drilling fluids, which can be characterised by a range of different

chemical compositions (Ball et al., 2012). However, the similarity between both the Staithes S-20 and 42/28-2 $\delta^{34}S_{evap}$ records in this study would suggest that the drilling fluids used had little to no effect on the sedimentary sulphate. Despite this, future studies should always be aware that the type of drilling fluid used may impact the sulphur isotope record.

Evaporites form in hydrographically isolated marginal marine basins with restricted circulation (Warren, 2010). Local depositional and diagenetic (i.e., post-depositional) processes can alter a global marine $\delta^{34}S_{evap}$ signal recorded in evaporites (Lu et al., 2001; Crockford et al., 2019), potentially limiting the use of $\delta^{34}S_{evap}$ data for stratigraphic correlation. Local effects include riverine inputs of continental sulphate from weathered pyrite and/or evaporites (Lu et al., 2001; Bottrell and Newton, 2006), reservoir effects associated with evaporite precipitation during periods of prolonged restriction (Raab and Spiro, 1991), and microbial sulphur cycling (e.g., microbial sulphate reduction) and subsequent pyrite burial (Bernasconi et al., 2017). Diagenetic effects include syn-sedimentary dissolution/precipitation of halite, the replacement of halite with gypsum (and *vice versa*) soon after burial (Schreiber and Tabakh, 2000), microbial sulphate reduction below the sediment-water interface (Jorgensen et al., 2019) and a cycle of diagenesis during burial and uplift (Ortí et al., 2022). The latter involves the formation of anhydrite from the dehydration of primary gypsum at moderate to deep burial depths, followed by the rehydration of anhydrite to form secondary gypsum during uplift (Ortí et al., 2022). The sulphur isotopic effect of the dehydration/rehydration of Ca-sulphates associated with burial and uplift is not well understood. Current evidence suggests it is associated with only minor sulphur isotope

fractionation (see Ortí et al., 2022 for details), and is unlikely to have imparted any major effect on our $\delta^{34}S_{evap}$ records.

During burial to temperatures exceeding 120°C, thermochemical sulphate reduction can occur, involving the chemical reduction of sulphate to sulphide, and the sulphurisation of organic matter (see review by Cai et al., 2022). This process has been associated with significant sulphur isotope fractionations in metal sulphide deposits (Cai et al., 2022). However, only a minor degree of sulphur isotope fractionation occurs between sulphate and sulphide in most petroleum-related sour gas settings (Worden et al., 1997; Cai et al., 2022), likely due to the complete reduction of any anhydrite that dissolves, with sulphate dissolution being rate limiting (Meshoulum et al., 2016; Cai et al., 2022). It is understood that diagenetic fluids exhibit a high degree of spatial isotopic heterogeneity and will produce more scattered $\delta^{34}S$ values in rocks that have interacted with diagenetic fluids, limiting the stratigraphic reproducibility of $\delta^{34}S_{evap}$ records between different basins (Metzger et al., 2014). Thus, a high degree of stratigraphic reproducibility in $\delta^{34}S$ is generally considered to be evidence of a global isotopic signal (Metzger et al., 2014). The $\delta^{34}S_{evap}$ curve from Staithes S-20 has been shown to represent a global record of marine sulphate (Salisbury et al., 2022). The small degree of scatter and/or minor offsets between the $\delta^{34}S_{evap}$ curves of Staithes S-20 and 42/28-2 may reflect local depositional and minor diagenetic effects, but the robust correlation between them (Figure 4), as well as their agreement with the global $\delta^{34}S_{evap}$ record (Salisbury et al., 2022), suggest that the long-term trends in the $\delta^{34}S_{evap}$ data represent a global marine sulphur isotope signal.

4.3. Sulphur isotope correlation

The $\delta^{34}S_{evap}$ record from borehole 42/28-2 is presented alongside Staithes S-20 (Salisbury et al., 2022) in Figure 4. Clear stratigraphic trends are apparent in both $\delta^{34}S_{evap}$ records even at different sample resolutions. The principles of sulphur isotope stratigraphy and isotope correlation are based on; (1) the assumption that the sulphur isotope composition of the ocean is isotopically homogenous at any given time, and hence, the absolute $\delta^{34}S_{evap}$ value; (2) the trend in the $\delta^{34}S_{evap}$ is directly comparable (i.e., positive *versus* negative); and (3) inflection points in $\delta^{34}S_{evap}$ represent a shift from one slope to another. It would be appealing to correlate all the trends and inflections points in Figure 4, however, caution needs to be exercised due to the different sampling resolution between the boreholes. Thus, in Figure 4 we have only chosen to correlate seven points through the latest Permian to Late Triassic time interval. In addition, we have chosen to use one lithostratigraphic correlation which will be discussed below.

During the correlation process between borehole 42/28-2 and Staithes S-20, the stratigraphy is assumed to be proportionally equivalent and each stratigraphic element (apart from truncation by the unconformity) is assumed to expand or contract at a similar rate (see left-hand side Figure 4). If a comparable sample resolution was obtained for borehole 42/28-2, then the correlation between the boreholes (core *versus* cuttings) would have been stronger. However, this was not possible due to the stratigraphic resolution of the drill cuttings collected and the fact that many cutting samples did not contain any evaporitic minerals for isotopic analysis. Similar concerns (e.g., stratigraphic thickness and time, as well as sample resolution) were highlighted by Gröcke (2020)

when performing carbon isotope stratigraphy for correlation. The same issues apply for all types of correlation using isotope stratigraphy.

Cyclic variability in $\delta^{34}S_{evap}$ is observed through the Zechstein and lower Bunter Shale intervals in Staithes S-20 (3100 to 3500 ft: Figure 4). This apparent cyclicity is not observed in the equivalent interval of borehole 42/28-2 (7700 to 9680 ft), although this may be in part due to lower sample resolution (Figure 4a and 4b). If the cyclicity observed in Staithes S-20 reflects global changes in the sulphate isotopic reservoir, then the cycles may prove very useful in high-resolution correlation of the Zechstein throughout Europe. Future sulphur isotope studies of the Zechstein should be performed at high resolution to assess reproducibility of the apparent cyclicity observed in Staithes S-20. After this period of cyclicity, $\delta^{34}S_{evap}$ gradually increases throughout the Bunter Shale and Bunter Sandstone from approximately +8 ‰ to +15 ‰ in both boreholes. This range in $\delta^{34}S_{evap}$ constrains the age of these stratigraphic units to the latest Permian (Claypool et al., 1980; Crockford et al., 2019; Present et al., 2020; Salisbury et al., 2022), suggesting the placement of the PTB in this part of the Southern Permian Basin should be shifted from the upper boundary of the Zechstein evaporites to a point within the Bunter Sandstone (Figure 5). This is significant, due to its' apparent conflict with biostratigraphic constraints for an Early to Middle Triassic age for Bunter Sandstone equivalents in southern England and Germany (see above). Although, this part of the record is more difficult to accurately correlate based on principles (2) and (3) described above, a late Permian age for the lower Bunter in the SNS Basin suggests that towards the basin margins, the Bunter stratigraphic motif is aliased by an older continental clastic system. By extension, it is also possible that the lower parts of the onshore Sherwood Sandstone Group in northern England also extend into the late Permian.

Due to erosion associated with the Hardegsen unconformity in the Early Triassic (Bachman et al., 2010), the $\delta^{34}S_{evap}$ curves of Staithes S-20 and 42/28-2 fail to record the large positive $\delta^{34}S_{evap}$ excursion characteristic of the Early Triassic. The entire evaporite-based stratigraphic interval of the Staithes S-20 borehole hinges on the constraint of a single palynological age (earliest Anisian), which is obtained from immediately above the unconformity (see Salisbury et al., 2022). $\delta^{34}S_{evap}$ values of > +15 ‰ above the unconformity in Staithes S-20 also support an Anisian age when compared with the global composite record as discussed in Salisbury et al. (2022). Based on absolute $\delta^{34}S_{evap}$ values at this point it is evident that borehole 42/28-2 records the Anisian recovery to pre-excursion $\delta^{34}S_{evap}$ values in the Olenekian prior to the negative excursion (see Figure 4). $\delta^{34}S_{evap}$ values in borehole 42/28-2 show a declining trend, similar to that which is recorded in Staithes S-20, for the remainder of the Triassic — ending with $\delta^{34}S_{evap}$ values of ~ +12 ‰ in the Norian.

As shown in Figure 4 the correlation is somewhat more uncertain when there are larger gaps in the $\delta^{34}S_{evap}$ record (e.g., Bunter Sandstone) from borehole 42/28-2. This is to be expected, as lower resolution records will fail to capture the full extent of isotopic variability (especially short-term changes), creating the false impression of greater isotopic heterogeneity between sedimentary basins (Metzger et al., 2014). It is thus unclear whether the lack of cyclicity at the base of 42/28-2 (discussed above) reflects a difference in the evolution of the sulphur cycle between the Cleveland and southern North Sea basins during this time interval. We present two potential correlations (see Figure 4a and 4b) between Staithes S-20 and borehole 42/28-2 during the latest Permian. Figure 4a assumes that the lithostratigraphic boundary between Z5 and the Bunter Shale is age equivalent in both boreholes (dashed correlation line). In contrast,

Figure 4b displays a correlation scheme based entirely upon the $\delta^{34}S_{evap}$ data, thus suggesting a different age for the boundary between Z5 and the Bunter Shale in each borehole, taking account of the possible diachroneity of lithostratigraphic boundaries. Each of these correlations are plausible but highlight the issue when performing sulphur isotope correlation during time intervals with little isotopic variability (akin to strontium isotope stratigraphy). Additional techniques such as evaporite palynology (Gibson & Wellman, 2021) may help to constrain age and sulphur isotope correlation during the late Permian Zechstein. Despite this, the correlation between 42/28-2 and Staithes S-20 looks exceptionally good, even with different sampling resolutions.

It should be noted that data resolution is not the only factor to consider when attempting to derive robust, high-resolution isotope stratigraphic correlations. As briefly discussed above, the rate and magnitude of sulphur isotope variability are of crucial importance (see Yao et al., 2019). Between the depths of 6760 ft and 5940 ft in the borehole 42/28-2 dataset, robust correlations can be achieved with the Staithes S-20 record, despite the relatively low sample resolution of 42/28-2. This is due to the abrupt and significant shift in the $\delta^{34}S_{evap}$ record during this depth interval (see Figure 4), which is also reflected in the global $\delta^{34}S_{evap}$ curve (see Salisbury et al., 2022). Therefore, if the time-interval studied exhibits high sulphur isotopic variability, a sample resolution comparable to our Staithes S-20 record may not be essential. This study has thus demonstrated that drill cuttings can be confidently used for $\delta^{34}S_{evap}$ stratigraphic correlation of sedimentary sequences between sedimentary basins.

4.4. Wireline log-based lithostratigraphy versus $\delta^{34}S_{evap}$ correlation

To compare the gamma ray and sulphur isotope correlations, we used the gamma ray correlation lines shown in Figure 3 to correlate the $\delta^{34}S_{evap}$ curves from Staithes S-20 and borehole 42/28-2 (Figure 6). Seven confident gamma ray motifs were correlated based on their visual similarity. An additional gamma ray correlation was tentatively assigned in the middle Bunter Shale (see Figure 3, dashed line) at the shift from moderate scatter to high scatter in the record. Based on these correlation lines, the $\delta^{34}S_{evap}$ curves are also strikingly similar, however, there are some key differences. For example, based on gamma ray correlation, borehole 42/28-2 extends further back in time in Zechstein cycle Z5. Thus, using gamma ray stratigraphy only the top 4 samples in Z5 from borehole 42/48-2 correlate with the Staithes S-20 $\delta^{34}S_{evap}$ record (Figure 6).

Another key difference is in the correlation of the Röt Halite Member (Triassic). Gamma ray correlation would erroneously imply that the Röt Halite Member extends into the Ladinian, whilst the sulphur isotope correlation constrains it to the Anisian (Figures 7). It is plausible this may reflect errors in the application of lithostratigraphy during the original logging process. In the case of the Staithes S-20 borehole, the lack of clear halite intervals defining both the Röt and Muschelkalk halites, and the facies transition from the limestone-prone Muschelkalk into clastic basin margin facies, has made the log motifs ambiguous. This demonstrates how $\delta^{34}S_{evap}$ records provide a critical constraint on the validity of lithostratigraphy for stratigraphic correlation, particularly where the lithostratigraphic data exhibit greater ambiguity, such as basin margin settings.

Published data provide further contrasting age estimates. Previous lithostratigraphic correlations suggest an Olenekian age for the Röt Halite Member (Warrington et al., 1980), while more recent work suggests an early Anisian age, in broad agreement with our $\delta^{34}S_{evap}$ record (Bachmann et al., 2010). Isotopic analysis of fluid inclusions suggests a late Early Triassic age for the Röt in the Netherlands, Germany and Poland, reporting $\delta^{34}S$ values between +27.1 ‰ and +32 ‰ (Kovalevych et al., 2002). In contrast, we only record $\delta^{34}S_{evap}$ values between +18.5 ‰ and +25.4 ‰ (Figure 4). The reason for this difference is currently unclear, however, it should be noted that Kovalevych et al. (2002) used a different analytical method for sulphur isotope analysis (e.g., offline SO_2 generation *versus* online continuous flow IRMS at SIBL). Furthermore, the Röt may have formed earlier to the east of the UK and SNS. Additional sulphur isotope analyses of the Röt Halite Member are required to constrain its' age and determine if this lithostratigraphic unit is diachronous or synchronous across basins.

Correlations using gamma ray and $\delta^{34}S_{evap}$ data suggest that the successions in each well are broadly comparable across the Cleveland and SNS basins (Figure 7). This can be clearly seen in the Anisian interval (Figure 7). The position of the Hardegsen unconformity can be located using the gamma ray logs (Figure 3) and the Anisian exhibits a high rate and magnitude of sulphur isotopic variability (Figure 4), enabling a robust correlation to be made. Interestingly, the correlation schemes exhibit greatest disagreement during the Ladinian, Carnian and Norian (Figure 7). In particular, the sulphur isotope correlation suggests the top of the Mercia Mudstone in borehole 42/28-2 extends into the Carnian–Norian, while the gamma ray correlation suggests it extends until just below the Norian–Rhaetian boundary, possibly reflecting issues with depth averaging between the gamma ray and $\delta^{34}S_{evap}$ records. In this case the sulphur isotope

correlation scheme would be favoured, demonstrating the capacity for sulphur isotope stratigraphy to capture lithofacies diachroneity.

The $\delta^{34}S_{evap}$ correlation based on gamma ray is quite robust but has limitations when compared to the sulphur isotope correlation, which is independent of lithostratigraphy (Figure 7). Due to the 'layer cake' appearance of the Triassic southern North Sea, lithostratigraphy assumes that the deposition of one facies is "time-equivalent" to the same facies in another basin. When using gamma ray to correlate $\delta^{34}S_{evap}$ one is forcing it to fit in line with the principles of lithostratigraphy. The deposition of an evaporite in one basin may not be time equivalent to the deposition of an evaporite in a nearby basin, and hence, wireline log correlations of apparently similar log motifs could cross time boundaries. The stability and residence time of sulphur in the ocean precludes crossing time boundaries as at any given time the ocean will have a homogenous $\delta^{34}S_{evap}$ signature (Paytan et al., 2012). Therefore, as time changes, so will the $\delta^{34}S_{evap}$ signature of the ocean. In Figure 6 it is assumed that the gamma ray correlation is a timeline and hence, only four $\delta^{34}S_{evap}$ data from borehole 42/28-2 are correlatable to the Staithes S-20 record for the Z5 lithology (see Figure 4a). However, if we consider that the Z5 evaporite sequence in borehole 42/28-2 is "time-equivalent" to the base of the Bunter Shale in the Staithes S-20 core/basin, then this would create a very different correlation curve (see Figure 4b). Thus, a significant strength of sulphur isotope stratigraphy is that it provides independent validation on whether straight lithostratigraphic correlations are accurate, differentiating between log motifs that appear similar but represent strata of distinct ages.

The above discussion reflects the importance of sample resolution and isotopic variability in deriving robust stratigraphic correlations (see Yao et al., 2019 for further discussion). The $\delta^{34}S_{evap}$ data from the Zechstein and the base of the Bunter Shale lack the sample resolution and isotopic variability to facilitate high-resolution correlations. In contrast, although the sample resolution is comparable in the Mercia Mudstone Group, the greater isotopic variability enables high-resolution correlations to be made using $\delta^{34}S_{evap}$ alone (Figures 4 and 7). For intervals where high sampling resolution cannot be achieved, or where the $\delta^{34}S$ record exhibits relative stability through time, we suggest a multidisciplinary approach, integrated with wireline log stratigraphy, to produce a global $\delta^{34}S$ evaporite curve for correlation. With further research, it is anticipated that the $\delta^{34}S$ curve from evaporites may become comparable to how strontium isotope stratigraphy is used for global correlation of marine sediments. More importantly, placing evaporite-bearing strata into more constrained stratigraphic timelines will increase our knowledge of these extreme environments in Earth's history.

4.5. Implications for carbon capture and storage

As discussed, our $\delta^{34}S_{evap}$ records from the Staithes S-20 and 42/28-2 boreholes provide further chronostratigraphic constraint for the late Permian–Triassic strata of the Cleveland and UK SNS basins. In particular, the base of the Bunter Sandstone has been assigned to the latest Permian, suggesting the PTB may occur within the Bunter Sandstone at these locations (Fig. 5). This enables the degree of Hardegsen erosion to be better constrained stratigraphically (i.e., when it initiated and stopped in a basin). This will help to develop more accurate palaeogeographic maps for the latest Permian and Triassic of the UK. This is of particular significance due to the interest in the Bunter

Sandstone as a potential reservoir for carbon capture and storage (CCS) (Holloway et al., 2006; Newell and Shariatipour, 2016; Alshakri et al., *in press*).

The use of geological reservoirs for the storage of sequestered carbon dioxide (CO_2) as a super-critical fluid is thought to be a key technology for addressing anthropogenic climate change (Bickle, 2009). The Bunter Sandstone and other equivalents within the Sherwood Sandstone Group are considered suitable candidates for CO_2 storage (Brook et al., 2003; Holloway et al., 2006). This is due to the Bunter Sandstone's favourable reservoir properties (Chadwick et al., 2008; Dobbs et al., 2018), with fair to good porosity and permeability (Noy et al., 2012), and suitable stratigraphic position, whereby it is sealed by a durable caprock, the overlying saliferous Mercia Mudstone Group (Armitage et al., 2013). In addition, its supposed sheet-like geometry is predicted to be conducive to effective pressure dissipation and reliable injectivity.

It should be noted, however, that an accurate understanding of the regional stratigraphic framework is essential for reliably estimating the suitability of a reservoir for CO_2 storage. For example, the spatial variability in properties (Ringrose, 2020) such as sand:shale ratios, porosity, and permeability within the Bunter Sandstone can be mapped for assessing its' suitability for CO_2 storage. These assessments are likely erroneous if our revised stratigraphic framework for the western margin SNS is correct, as authors of previous research will have contoured the properties from sandstones of different ages. In addition, although drillcore can provide useful insights, it is common for analogous facies to be studied at outcrop to provide a broader view of the heterogeneities present within reservoir zones (e.g., Newell and Shariatipour, 2016). However, such studies commonly focus on the onshore Sherwood Sandstone outcrops,

which were deposited by large river systems during the Early Triassic, a time interval characterised by a warmer and wetter climate than the late Permian (Trotter et al., 2015). Thus, if the base of the Bunter Sandstone in the western margin SNS is truly latest Permian in age then the depositing rivers would have experienced lower volume discharges leading to different reservoir architectures and heterogeneities (Issautier et al., 2014). As a result, alternative analogue facies may need to be found from more ephemeral fluvial systems. These issues will impact the reliability of dynamic models used to predict the outcome of different scenarios, such as injection rates, well counts and locations (e.g., Noy et al., 2012; Williams et al., 2013; Tucker, 2018; Ringrose, 2020). This could lead to suboptimal developments, financial implications and a potential to fail contractual obligations.

5. Conclusions

Sulphur isotope stratigraphy using evaporites has the potential to enhance chronostratigraphic constraints for Permian–Triassic strata of the UK and continental Europe. Unfortunately, complete drill cores are uncommon and thus, determining whether drill cuttings are suitable for constructing $\delta^{34}S_{evap}$ records is essential. A $\delta^{34}S_{evap}$ record was produced from drill cuttings of borehole 42/28-2 in the southern North Sea basin. This $\delta^{34}S_{evap}$ record was compared to the onshore Staithes S-20 borehole. Our findings show that $\delta^{34}S_{evap}$ records derived from drill cuttings can be used for stratigraphic correlation, although we advise that during periods of relative stability in $\delta^{34}S_{evap}$ a multidisciplinary approach is adopted (i.e., coupled with gamma ray stratigraphy). Based on our $\delta^{34}S_{evap}$ records between the Cleveland Basin and southern North Sea Basin in this study, the deposition of the Bunter Shale and Bunter Sandstone

is determined to have initiated in the latest Permian, while the youngest age of the MMG is Anisian (Middle Triassic). Neither $\delta^{34}S_{evap}$ curves record the Early Triassic due to erosion associated with the Hardegsen unconformity. Our findings thus suggest that the PTB should be defined somewhere within the Bunter Sandstone, and not at the upper boundary of the Zechstein evaporites in the Cleveland and Southern North Sea basins. This implies that our current understanding of the regional lithostratigraphy is likely overly simplistic and fails to capture the full extent of facies diachroneity, particularly on the basin margins. This is especially noteworthy for the Bunter Sandstone, due to interest in its' possible suitability as a reservoir for CO_2 storage in the UK.

6. References

Alshakri, J., Hampson, G.J., Jaquemyn, C., Jackson, M., Petrovskyy, D., Geiger, S., Machado Silva, J.D., Judice, S., Rahman, F., Costa Sousa, M., 2023. "A screening assessment of the impact of sedimentological heterogeneity on CO_2 migration and stratigraphic-baffling potential: Sherwood and Bunter Sandstones, UK", in *Enabling Secure Subsurface Storage in Future Energy Systems*. Editors: Miocic, J.M., Heinemann, N., Edlmann, K., Alcade, J., Schultz, R.A., (Geological Society of London Special Publications 528). DOI: 10.1144/SP528-2022-34

Ambrose, K., Hough, E., Smith, N.J.P., Warrington, G., 2014. Lithostratigraphy of the Sherwood Sandstone Group of England, Wales and south-west Scotland. *British Geological Survey Research Report, RR/14/01*.

Ambrose, K., Wakefield, O., 2015. Permo-Triassic rocks of Nottingham. *Mercian Geologist* 18, 260–263

Armitage, P.J., Worden, R.H., Faulkner, D.R., Aplin, A.C., Butcher, A.R., Espie, A.A., 2013. Mercia Mudstone Formation caprock to carbon capture and storage sites: petrology and petrophysical characteristics. *J. Geol. Soc*. 170, 119-132. DOI: 10.1144/jgs2012-049

Bachmann, G.H., Geluk, M.C., Warrington, G., Becker-Roman, A., Beutler, G., Hagdorn, H., Hounslow, M.W., Nitsch, E., Röhling, H-G., Simon, T., Szulc, A., 2010. "Triassic", in *Petroleum geological atlas of the Southern Permian Basin area*. Editors: Doornenbal, J.C., Stevenson, A.G. EAGE Publications b.v., Houten, 149-173

Bachman, G.H., Kozur, H.W., 2004. The Germanic Triassic: correlations with the international chronostratigraphic scale, numerical ages and Milankovitch cyclicity. *Hallesches Jahrb. Geowiss.* 26, 17-62. DOI: 10.25673/91844

Ball, A.S., Stewart, R.J., Schliephake, K., 2012. A review of the current options for the treatment of and safe disposal of drill cuttings. *Waste Manag. Res.* 30, 457-473. DOI: 10.1177/0734242X11419892

Bernasconi, S.M., Meier, I., Wohlwend, S., Brack, P., Hochuli, P.A., Bläsi, H., Wortmann, U.G., Ramseyer, K., 2017. An evaporite-based high-resolution sulfur isotope record of Late Permian and Triassic seawater sulfate. *Geochim. Cosmochim. Acta*, 204, 331-349. DOI: 10.1016/j.gca.2017.01.047

Bickle, M.J., 2009. Geological carbon storage. *Nat. Geosci.* 2, 815-818. DOI: 10.1038/ngeo687

Boschetti, T., Cortecci, G., Toscani, L., Iacumin, P., 2011. Sulfur and oxygen isotopic compositions of Upper Triassic sulfates from northern Apennines (Italy): paleogeographic and hydrogeochemical implications. *Geol. Acta* 9, 129-147.

Bottrell, S.H., Newton, R.J., 2006. Reconstruction of changes in global sulfur cycling from marine sulfate isotopes. *Earth Sci. Rev.* 75, 59-83. DOI: 10.1016/j.earscirev.2005.10.004

Bryant, R.N., Present, T.M., Ahm, A-S.C., McClelland, H-L.O., Razionale, D., Blättler, C.L., 2022. Early diagenetic constraints on Permian seawater chemistry from the Capitan Reef. *Geochim. Cosmochim. Acta*, 328, 1-18. DOI: 10.1016/j.gca.2022.04.027

Brook, M., Shaw, K., Vincent, C., Holloway, S., 2003. Storage Potential of the Bunter Sandstone in the UK sector of the southern North Sea and the adjacent onshore area of Eastern England. British *Geological Survey Commissioned Report, CR/03/154*, 37

Cai, C., Li, H., Li, K., Wang, D., 2022. Thermochemical sulfate reduction in sedimentary basins and beyond: A review. *Chem. Geol.* 607, 121018. DOI: 10.1016/j.chemgeo.2022.121018

Cao, H., Kaufman, A.J., Shan, X., Cui, H., Zhang, G., 2016. Sulfur isotope constraints on marine transgression in the lacustrine Upper Cretaceous Songliao Basin, northeastern China. *Palaeogeogr. Palaeoclimatol. Palaeoecol.* 451, 152-163. DOI: 10.1016/j.palaeo.2016.02.041

Chadwick, R.A., Arts, R., Bernstone, C., May, F., Thibeau, S., Zweigel, P., 2008. Best practice for the storage of CO_2 in saline aquifers. *British Geological Society Special Publication No. 14*, 1-267

Chen, Y., Scholze, F., Richoz, S., Zhang, Z., 2017. Middle Triassic conodont assemblages from the Germanic Basin: implications for multi-element taxonomy and biogeography. *J. Syst. Palaeontol.* 17, 359-377. DOI: 10.1080/14772019.2018.1424260

Claypool, G.E., Holser, W.T., Kaplan, I.R., Sakai, H., Zak, I., 1980. The age curves of sulfur and oxygen isotopes in marine sulfate and their mutual interpretation. *Chem. Geol.* 28, 199-260. DOI: 10.1016/0009-2541(80)90047-9

Crockford, P.W., Kunzmann, M., Bekker, A., Hayles, J., Bao, H., Halverson, G.P., Peng, Y., Bui, T.H., Cox, G.M., Gibson, T.M., Wörndle, S., Rainbird, R., Lepland, A., Swanson-Hysell, N.L., Master, S., Sreenivas, B, Kuznetsov, A., Krupernik, V., Wing, B.A., 2019. Claypool continued: Extending the isotopic record of sedimentary sulfate. *Chem. Geol.* 513, 200-225. DOI: 10.1016/j.chemgeo.2019.02.030

Dobbs, M.R., Cuss, R.J., Ougier-Simonin, A., Parkes, D., Graham, C.C., 2018. Yield envelope assessment as a preliminary screening tool to determine a carbon capture and storage viability in depleted southern north-sea hydrocarbon reservoirs. *Int. J. Rock Mech. Min. Sci.* 102, 15-27. DOI: 10.1016/j.ijrmms.2017.11.018

Eldrett, J.S., Vieira, M., Gallagher, L., Hampton, M., Blaauw, M., Swart, P.K., 2021. Late Cretaceous to Palaeogene carbon isotope, calcareous nannofossil and foraminifera stratigraphy of the Chalk Group, Central North Sea. *Mar. Pet. Geol.* 124, 104789. DOI: 10.1016/j.marpetgeo.2020.104789

Franz, M., Henniger, M., Barnasch, J., 2013. The strong diachronous Muschelkalk/Keuper facies shift in the Central European Basin: implications from the type-section of the Erfurt Formation (Lower Keuper, Triassic) and basin-wide correlations. *Int. J. Earth Sci.* 102, 761-780. DOI: 10.1007/s00531-012-0823-y

Gallois, R.W., 2009. The lithostratigraphy of the Penarth Group (Late Triassic) of the Severn Estuary area. *Geoscience in South-West England*, 12, 71-84.

Geluk, M., McKie, T., Kilhams, B., 2018. “An introduction to the Triassic: current insights into the regional setting and energy resource potential of NW Europe”, in *Mesozoic Resource Potential in the Southern Permian Basin*. Editors: Kilhams, B., Kukla, P.A., Mazur, S., McKie, T., Mijnlieff, H.F., van Ojik, K., (Geological Society London, Special Publications) 469, 139-147. DOI: 10.1144/SP469.

Gibson, M.E., Wellman, C.H., 2021. The use of spore-pollen assemblages to reconstruct vegetation changes in the Permian (Lopingian) Zechstein deposits of northeast England. *Rev. Palaeobot. Palynol.* 288, 104399. DOI: 10.1016/j.revpalbo.2021.104399

Gröcke, D.R., 2020. “Carbon isotope stratigraphy: Principles and applications”, in *Stratigraphy and Timescales*. Editor: Montenari, M., (London: Elsevier Academic Press) 5, 1-40. DOI: 10.1016/bs.sats.2020.08.002

He, T., Dal Corso, J., Newton, R.J., Wignall, P.B., Mills, B.J.W., Todaro, S., Stefano, P.D., Turner, E.C., Jamieson, R.A., Randazzo, V., Rigo, M., Jones, R.E., Dunhill, A.M., 2020. An enormous sulfur isotope excursion indicates marine anoxia during the end-Triassic mass extinction. *Sci. Adv.* 6, eabb6704. DOI: 10.1126/sciadv.abb6704

He, T., Zhu, M., Mills, B.J.W., Wynn, P.M., Zhuravlev, A.Y., Tostevin, R., Pogge von Strandmann, P.A.E., Yang, A., Poulton, S.W., Shields, G.A., 2019. Possible links between extreme oxygen perturbations and the Cambrian radiation of animals. *Nat. Geosci.* 12, 468-474. DOI: 10.1038/s41561-019-0357-z

Holloway, S., Milodowski, A.E., Strong, G.E., Warrington, G., 1989. The Sherwood Sandstone Group (Triassic) of the Wessex Basin, southern England. *Proc. Geol. Assoc.* 100, 383-394. DOI: 10.1016/S0016-7878(89)80056-2

Holloway, S., Vincent, C.J., Kirk, K.L., 2006. Industrial carbon dioxide emissions and carbon dioxide storage potential in the UK. *British Geological Survey Commercial Report, CR/06/185*

Holser, W.T., Kaplan, I.R., 1966. Isotope geochemistry of sedimentary sulfates. *Chem. Geol.* 1, 93-135. DOI: 10.1016/0009-2541(66)90011-8

Horacek, M., Brandner, R., Richoz, S., Povoden-Karadeniz, E., 2010. Lower Triassic sulfur isotope curve of marine sulfates from the Dolomites, N-Italy. *Palaeogeogr. Palaeoclimatol. Palaeoecol.* 290, 65-70. DOI: 10.1016/j.palaeo.2010.02.016

Hounslow, M.W., Ruffell, A.H., 2006. "Triassic: Seasonal rivers, dusty deserts and saline lakes", in *The geology of England and Wales*. Editors Rawson, P.F., Brenchley, P., (London: Geological Society of London) 295-325. DOI: 10.1144/GOEWP.13

Howard, A.S., Warrington, G., Ambrose, K., Rees, J.G., 2008. A formational framework for the Mercia Mudstone Group (Triassic) of England and Wales. *British Geological Survey Research Report, RR/08/004*

Insalaco, E., Virgone, A., Courme, B., Gaillot, J., Kamali, M., Moallemi, A., Lotfpour, M., Monibi, S., 2006. Upper Dalan Member and Kangan Formation between the Zagros Mountains and offshore Fars, Iran: depositional system, biostratigraphy and stratigraphic architecture. *Geoarabia*, 11, 75-176. DOI: 10.2113/geoarabia110275

Issautier, B., Viseur, S., Audigane, P., le Nindre, Y-M., 2014. Impacts of fluvial reservoir heterogeneity on connectivity: Implications in estimating geological storage capacity for CO_2. *Int. J. Greenh. Gas Control* 20, 333–349. DOI: 10.1016/j.ijggc.2013.11.009

Jenkyns, H.C., Jones, C.E., Gröcke, D.R., Hesselbo, S.P., Parkinson, D.N., 2002. Chemostratigraphy of the Jurassic system: applications, limitations and implications for palaeoceanography. *J. Geol. Soc. London* 159, 351-378. DOI: 10.1144/0016-764901-130

Johnson, D.L., Present, T.M., Li, M., Shen, Y., Adkins, J.F., 2021. Carbonate associated sulfate (CAS) $\delta^{34}S$ heterogeneity across the End-Permian Mass Extinction in South China. *Earth Planet. Sci. Lett.* 574, 117172. DOI: 10.1016/j.epsl.2021.117172

Jorgensen, B.B., Findlay, A.J., Pellerin, A., 2019. The biogeochemical sulfur cycle of marine sediments. *Front. Microbiol.* 10:849. DOI: 10.3389/fmicb.2019.00849

Korte, C., Kozur, H.W., 2010. Carbon-isotope stratigraphy across the Permian – Triassic boundary: A review. *J. Asian Earth Sci.* 39, 215-235. DOI: 10.1016/j.jseaes.2010.01.005

Kovalevych, V., Peryt, T.M., Beer, W., Geluk, M., Halas, S., 2002. Geochemistry of Early Triassic seawater as indicated by the Röt Halite in the Netherlands, Germany, and Poland. *Chem. Geol.* 182, 549-563. DOI: 10.1016/S0009-2541(01)00343-6

Kubo, Y., Kido, Y., Fuwa, Y., Hoshino, H., 2016. Experiments on method for washing drill cuttings: evaluation of soaking, stirring and milling effects. *JAMSTEC Rep. Res. Dev.* 22, 39-48. DOI: 10.5918/jamstecr.22.39

Kutzbach, J.E., Gallimore, R.G., 1989. Pangaean climates: Megamonsoons of the megacontinent. *J. Geophys. Res.* 94, 3341-3357. DOI: 10.1029/JD094iD03p03341

Lott, G.K., Warrington, G., 1988. A review of the latest Triassic succession in the U.K. sector of the Southern North Sea Basin. *Proc. Yorkshire Geol. Soc.* 47, 139-147. DOI: 10.1144/pygs.47.2.13

Lu, F.H., Meyers, W.J., Schoonen, M.A., 2001. S and O (SO_4) isotopes, simultaneous modeling, and environmental significance of the Nijar messinian gypsum, Spain. *Geochim. Cosmochim. Acta*, 65, 3081-3092. DOI: 10.1016/S0016-7037(01)00553-1

Luo, G., Kump, L.R., Wang, Y., Tong, J., Arthur, M.A., Yang, H., Huang, J., Yin, H., Xia, S., 2010. Isotopic evidence for an anomalously low oceanic sulfate concentration following end-Permian mass extinction. *Earth Planet. Sci. Lett.* 300, 101-111. DOI: 10.1016/j.epsl.2010.09.041

Lyu, Z., Zhang, L., Algeo, T. J., Zhao, L., Chen, Z-Q., Li, C., Ma, B., Ye, F., 2019. Global ocean circulation changes during the Smithian-Spathian transition inferred from carbon sulfur-cycle records. *Earth Sci. Rev.* 195, 114–132. DOI: 10.1016/j.earscirev.2019.01.010

Markovic, S., Paytan, A., Wortmann, U.G., 2015. Pleistocene sediment offloading and the global sulfur cycle. *Biogeosciences*, 12, 3043-3060. DOI: 10.5194/bg-12-3043-2015

Márquez-Aliaga, A., Valenzuela-Ríos, J.I., Calvet, F., Budurov, K., 2000. Middle Triassic conodonts from northeastern Spain: biostratigraphic implications. *Terra Nova*, 12, 77-83. DOI: 10.1111/j.1365-3121.2000.00273.x

McKie, T., 2017. "Palaeogeographic evolution of latest Permian and Triassic salt basins in northwest Europe", in *Permo-Triassic salt provinces of Europe, North Africa and the Atlantic margins, tectonics and hydrocarbon potential*. Editors Soto, J.J., Flinch, J.F., Tari, G. (Amsterdam Netherlands: Elsevier), 159-173. DOI: 10.1016/B978-0-12-809417-4.00008-2

McKie, T., Williams, B., 2009. Triassic palaeogeography and fluvial dispersal across the northwest European basins. *Geol. J.* 44, 711-741. DOI: 10.1002/gj.1201

Meshoulum, A., Ellis, G.S., Ahmad, W.S., Deev, A., Sessions, A.L., Tang, Y., Adkins, J.F., Jinzhong, L., Gilhooly III, W.P., Aizenshtat, Z., Amrani, A., 2016. Study of thermochemical sulfate reduction mechanism using compound specific sulfur isotope analysis. *Geochim. Cosmochim. Acta*, 188, 73-92. DOI: 10.1016/j.gca.2016.05.026

Metzger, J.G., Fike, D.A., Smith, L.B., 2014. Applying carbon isotope stratigraphy using well cuttings for high-resolution chemostratigraphic correlation of the subsurface. *Am. Assoc. Pet. Geol. Bull.* 98, 1551-1576. DOI: 10.1306/04011412231

Murray, S.T., Higgins, J.A., Holmden, C., Lu, C., Swart, P.K., 2021. Geochemical fingerprints of dolomitization in Bahamian carbonates: Evidence from sulfur, calcium, magnesium and clumped isotopes. *Sedimentology*, 68, 1-29. DOI: 10.1111/sed.12775

Narkievicz, K., 1999. Conodont biostratigraphy of the Muschelkalk (Middle Triassic) in the central part of the Polish Lowlands. *Geol. Q.* 43, 313-328

Newell, A.J., 2018. Rifts, rivers and climate recovery: A new model for the Triassic of England. *Proc. Geol. Assoc.* 129, 352-371. DOI: 10.1016/j.pgeola.2017.04.001

Newell, A.J., Shariatipour, S.M., 2016. "Linking outcrop analogue with flow simulation to reduce uncertainty in sub-surface carbon capture and storage: an example from the Sherwood Sandstone Group of the Wessex Basin, UK", in *The value of outcrop studies in reducing subsurface uncertainty and risk in hydrocarbon exploration and production*. Editors: Bowman, M., Smyth, H.R., Good, T.R., Passey, S.R., Hirst, J.P.P., Jordan, C.J., (London: The Geological Society of London), 231-246. DOI: 10.1144/SP436.2

Newton, R.J., Pevitt, E.L., Wignall, P.B., Bottrell, S.H., 2004. Large shifts in the isotopic composition of seawater sulphate across the Permo-Triassic boundary in northern Italy. *Earth Planet. Sci. Lett.* 218, 331-345. DOI: 10.1016/S0012-821X(03)00676-9

Nielsen, H., 1978. "Sulfur isotopes in nature", in *Handbook of Geochemistry. Sect. 16-B.* Editor: Wedepohl, K.K., (Berlin: Springer)

Noy, D.J., Holloway, S., Chadwick, R.A., Williams, J.D.O., Hannis, S.A., Lahann, R.W., 2012. Modelling large-scale carbon dioxide injection into the Bunter Sandstone in the UK Southern North Sea. *Int. J. Greenh. Gas Control*, 9, 220-233. DOI: 10.1016/j.ijggc.2012.03.011

Ortí, F., Pérez-López, A., Pérez-Valera, F., Benedicto, C., 2022. Isotope composition ($\delta^{34}S$, $\delta^{18}O$) of the Middle Triassic-Early Jurassic sulfates in eastern Iberia. *Sediment. Geol.* 431, 106014. DOI: 10.1016/j.sedgeo.2022.106104

Parrish, J.T., 1993. Climate of the supercontinent Pangea. *J. Geol.* 101, 215-233. DOI: :10.1086/648217

Paytan, A., Gray, E.T., Ma, Z., Erhardt, A., Faul, K., 2012. Application of sulphur isotopes for stratigraphic correlation. *Isotopes Environ. Health Stud.* 48, 195-206. DOI: 10.1080/10256016.2011.625423

Paytan, A., Kastner, M., Campbell, D., Thiemens, M.H., 1998. Sulfur isotopic composition of Cenozoic seawater sulfate. *Science*, 282, 1459-1462. DOI: 10.1126/science.282.5393.1459

Paytan, A., Kastner, M., Campbell, D., Thiemens, M.H., 2004. Seawater sulfur isotope fluctuations in the Cretaceous. *Science*, 304, 1663-1665. DOI: 10.1126/science.1095258

Paytan, A., Yao, W., Faul, K.L., Gray, E.T., 2020. “Sulfur isotope stratigraphy”, in *Geologic time scale 2020*. Editors Gradstein F.M., Ogg, J.G., Schmitz, M.D., Ogg, G.M., (Amsterdam, Netherlands: Elsevier) 1, 259-278. DOI: 10.1016/B978-0-12-824360-2.00009-7

Peacock, D.C.P., 2004. The post-Variscan development of the British Isles within a regional transfer zone influenced by orogenesis. *J. Struct. Geol.* 26, 2225-2231. DOI: 10.1016/j.jsg.2004.05.005

Present, T.M., Adkins, J.F., Fischer, W.W., 2020. Variability in sulfur isotope records of Phanerozoic seawater sulfate. *Geophys. Res. Lett.* 47, e2020GL088766. DOI: 10.1029/2020GL088766

Present, T.M., Gutierrez, M., Paris, G., Kerans, C., Grotzinger, J.P., 2019. Diagenetic controls on the isotopic composition of carbonate-associated sulfate in the Permian Capitan Reef Complex, West Texas. *Sedimentology* 66, 2605-2626. DOI: 10.1111/sed.12615

Present, T.M., Paris, G., Burke, A., Fischer, W.W., Adkins, J.F., 2015. Large carbonate associated sulfate isotopic variability between brachiopods, micrite, and other sedimentary components in Late Ordovician strata. *Earth Planet. Sci. Lett.* 432, 187-198. DOI: 10.1016/j.epsl.2015.10.005

Raab, M., Spiro, B., 1991. Sulfur isotopic variations during seawater evaporation with fractional crystallization. *Chem. Geol.* 86, 323-333. DOI: 10.1016/0168-9622(91)90014-N

Raup, D.M., Sepkowski, J.J., 1982. Mass extinctions in the marine fossil record. *Science* 215, 1501-1503. DOI: 10.1126/science.215.4539.1501

Rennie, V.C.F., Turchyn, A.V., 2014. The preservation of $\delta^{34}S_{SO4}$ and $\delta^{18}O_{SO4}$ in carbonate-associated sulfate during marine diagenesis: A 25 Myr test case using marine sediments. *Earth Planet. Sci. Lett.* 395, 13-23. DOI: 10.1016/j.epsl.2014.03.025

Richardson, J.A., Keating, C., Lepland, A., Hints, O., Bradley, A.S., Fike, D.A., 2019. Silurian records of carbon and sulfur cycling from Estonia: The importance of depositional environments on isotopic trends. *Earth Planet. Sci. Lett.* 512, 71-82. DOI: 10.1016/j.epsl.2019.01.055

Richardson, J.A., Lepland, A., Hints, O., Prave, A.R., Gilhooly III, W.P., Bradley, A.S., Fike, D.A., 2021. Effects of early marine diagenesis and site-specific depositional controls on carbonate-associated sulfate: Insights from paired S and O isotopic analyses. *Chem. Geol.* 584, 120525. DOI: 10.1016/j.chemgeo.2021.120525

Ringrose, P., 2020. *How to store CO2 underground: insights from early-mover CCS projects*. (Switzerland: Springer Briefs in Earth Sciences, Springer Nature) 129. DOI: 10.1007/978-3-030-33113-9

Sanei, H., Ardakani, O.H., Akai, T., Akihisa, K., Jiang, C., Wood, J.M., 2020. Core vs cuttings samples for geochemical and petrophysical analysis of unconventional reservoir rocks. *Sci. Rep.* 10, 1-10. DOI: 10.1038/s41598-020-64936-y

Salisbury, J., Gröcke, D.R., Cheung, H.D.R.A., Kump, L.R., McKie, T., Ruffell, A., 2022. An 80-million-year sulphur isotope record of pyrite burial over the Permian-Triassic. *Sci. Rep.* 12, 17370. DOI: 10.1038/s41598-022-21542-4

Schobben, M., Stebbins, A., Ghaderi, A., Strauss, H., Korn, D., Korte, C., 2015. Flourishing ocean drives the end-Permian marine mass extinction. *Proc. Natl. Acad. Sci.* 112, 10298-10303. DOI: 10.1073/pnas.1503755112

Scholze, F., Schneider, J.W., Werneburg, R., 2016. Conchostracans in continental deposits of the Zechstein-Buntsandstein in central Germany: Taxonomy and biostratigraphic implications for the position of the Permian-Triassic boundary within the Zechstein Group. *Palaeogeogr. Palaeoclimatol. Palaeoecol.* 449, 174-193. DOI: 10.1016/j.palaeo.2016.02.021

Scholze, F., Wang, X., Kirscher, U., Kraft, J., Schneider, J.W., Götz, A.E., Joachimski, M.M., Bachtadse, V., 2017. A multistratigraphic approach to pinpoint the Permian-Triassic boundary in continental deposits: The Zechstein-Lower Buntsandstein transition in Germany. *Glob. Planet. Change* 152, 129-151. DOI: 10.1016/j.gloplacha.2017.03.004

Schreiber, B.C., Tabakh, M.E., 2000. Deposition and early alteration of evaporites. *Sedimentology* 47, 215-238. DOI: 10.1046/j.1365-3091.2000.00002.x

Sepkoski Jr, J.J., 1996. "Patterns of Phanerozoic extinction: a perspective from global databases", in *Global events and event stratigraphy in the Phanerozoic*. Editor: Walliser, O.H., (Berlin, Springer) 35-51. DOI: 10.1007/978-3-642-79634-0_4

Smith, D.B., 1989. The late Permian paleogeography of north-east England. *Proc. Yorkshire Geol. Soc.* 47, 285-312. DOI: 10.1144/pygs.47.4.285

Song, H., Du, Y., Algeo, T. J., Tong, J., Owens, J. D., Song, H., Tian, L., Qiu, H., Zhu, Y., Lyons, T.W., 2019. Cooling-driven oceanic anoxia across the Smithian/Spathian boundary (mid-Early Triassic). *Earth Sci. Rev.* 195, 133–146. DOI: 10.1016/j.earscirev.2019.01.009

Song, H., Tong, J., Algeo, T.J., Song, H., Qui, H., Zhu, Y., Tian, L., Bates, S., Lyons, T.W., Luo, G., Kump, L.R., 2014. Early Triassic seawater sulfate drawdown. *Geochim. Cosmochim. Acta*, 128, 95-113. DOI: 10.1016/j.gca.2013.12.009

Spencer, P.S., Storrs, G.W., 2002. A re-evaluation of small tetrapods from the Middle Triassic Otter Sandstone Formation of Devon, England. *Palaeontology* 45, 447-467

Stuckman, M.Y., Lopano, C.L., Berry, S.M., Hakala, J.L., 2019. Geochemical solid characterization of drill cuttings, core and drilling mud from Marcellus Shale Energy development. *J. Nat. Gas Sci. Eng.* 68, 102922. DOI: 10.1016/j.jngse.2019.102922

Thode, H.G., Monster, J., 1965. Sulfur isotope geochemistry of petroleum, evaporites, and ancient seas. *Am. Assoc. Pet. Geol. Mem.* 4, 367-377.

Trotter, J.A., Williams, I.S., Nicora, A., Mazza, M., Rigo, M., 2015. Long-term cycles of Triassic climate change: a new $\delta^{18}O$ record from conodont apatite. *Earth Planet. Sci. Lett.* 415, 165-174. DOI: 10.1016/j.epsl.2015.01.038

Tucker, M.E., 1991. Sequence stratigraphy of carbonate-evaporite basins: models and application to the Upper Permian Zechstein of northeast England and adjoining North Sea. *J. Geol. Soc. London* 148, 1019-1036. DOI: 10.1144/gsjgs.148.6.1019

Tucker, O., 2018. *Carbon capture and storage*. (Bristol: IOP Publishing) 46. DOI: 10.1088/978-0-7503-1581-4

Van Driessche, A.E.S., Canals, A., Ossorio, M., Reyes, R.C., García-Ruiz, J.M., 2016. Unravelling the sulfate sources of (giant) gypsum crystals using gypsum isotope fractionation factors. *J. Geol.* 124, 235-245. DOI: 10.1086/684832

Warren, J.K., 2006. *Evaporites: Sediments, Resources and Hydrocarbons*. (Berlin: Springer) 1036. DOI: 10.1007/3-540-32344-9.

Warren, J.K., 2010. Evaporites through time: Tectonic, climatic and eustatic controls in marine and nonmarine deposits. *Earth Sci. Rev.* 98, 217-268. DOI: 10.1016/j.earscirev.2009.11.004

Warrington, G., 1974. The stratigraphy and palaeontology of the 'Keuper' Series of the central Midlands of England. *Quart. J. Geol. Soc.* 126, 183-223. DOI: 10.1144/gsjgs.126.1.0183

Warrington, G., 1997. The Lyme Regis borehole, Dorset – palynology of the Mercia Mudstone, Penarth and Lias groups (Upper Triassic-Lower Jurassic). *Proc. Ussher Soc.* 9, 153-157.

Warrington, G., Audley-Charles, M.G., Elliott, R.E., Evans, W.B., Ivimey-Cook, H.C., Kent, P., Robinson, P.L., Shotton, F.W., Taylor, F.M., 1980. A correlation of Triassic rocks in the British Isles. *Geol. Soc. Lond.,* Special Report No. 13

Warrington, G., Ivimey-Cook, H.C., 1992. "Triassic", in *Atlas of palaeogeography and lithofacies: Geological Society Memoir, London*. Editors Cope, J.C.W., Ingham, J.K., Rawson, P.F., 13, 97-106. DOI: 10.1144/GSL.MEM.1992.013.01.11

Warrington, G., Pollard, J.E., 2021. On the records of the brachiopod '*Lingula*' and associated fossils in Mid-Triassic deposits in England. *Proc. Yorkshire Geol. Soc.* 63, 1-9. DOI: 10.1144/pygs2020-015

Wignall, P.B., Bond, D.P.G., 2008. The End-Triassic and Early Jurassic mass extinction records in the British Isles. *Proc. Geol. Assoc.* 119, 73-84. DOI: 10.1016/S0016-7878(08)80259-3

Wilson, A.A., 1993. The Mercia Mudstone Group (Trias) of the Cheshire Basin. *Proc. Yorkshire Geol. Soc.* 49, 171-188. DOI: 10.1144/pygs.49.3.171

Worden, R.H., Smalley, P.C., Fallick, A.E., 1997. Sulfur cycle in buried evaporites. *Geology* 25, 643-646. DOI: 10.1130/0091-7613(1997)025<0643:SCIBE>2.3.CO;2

Yao, W.Q., Paytan, A., Griffith, E.M., Martínez-Ruiz, F., Markovic, S., Wortmann, U.G., 2020. A revised seawater sulfate S-isotope curve for the Eocene. *Chem. Geol.* 532, 119382. DOI: 10.1016/j.chemgeo.2019.119382

Yao, W.Q., Paytan, A., Wortmann, U.G., 2018. Large-scale ocean deoxygenation during the Paleocene-Eocene Thermal Maximum. *Science* 361, 804-806. DOI: 10.1126/science.aar8658

Yao, W., Wortmann, U.G., Paytan, A., 2019. “Sulfur isotopes — Use for stratigraphy during times of rapid perturbations”, in *Stratigraphy and timescales*. Editor Montenari, M., (Amsterdam: Elsevier Academic Press) 4, 1-33. DOI: 10.1016/bs.sats.2019.08.004

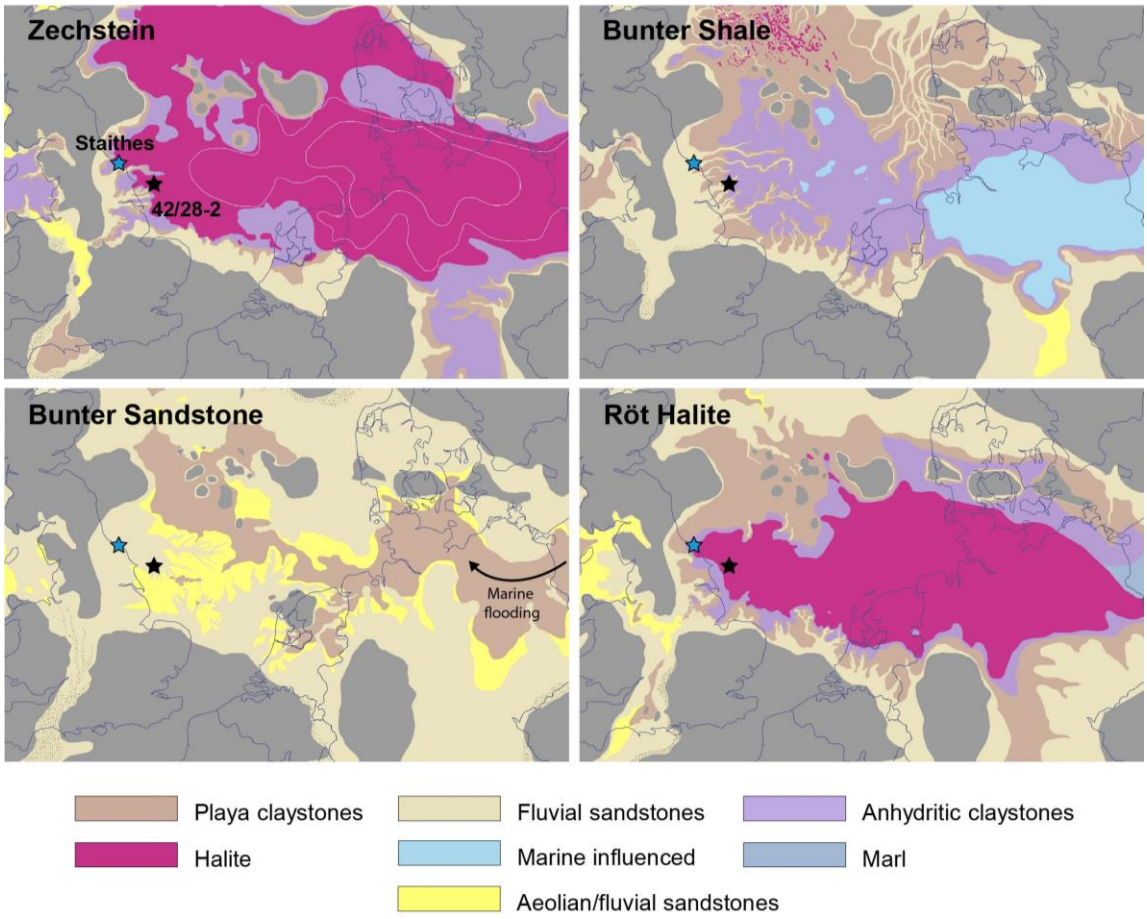

Figure 1: *Palaeogeographic context of the stratigraphic units discussed in the text. The location of each borehole is marked with a star. See top left figure for labels.*

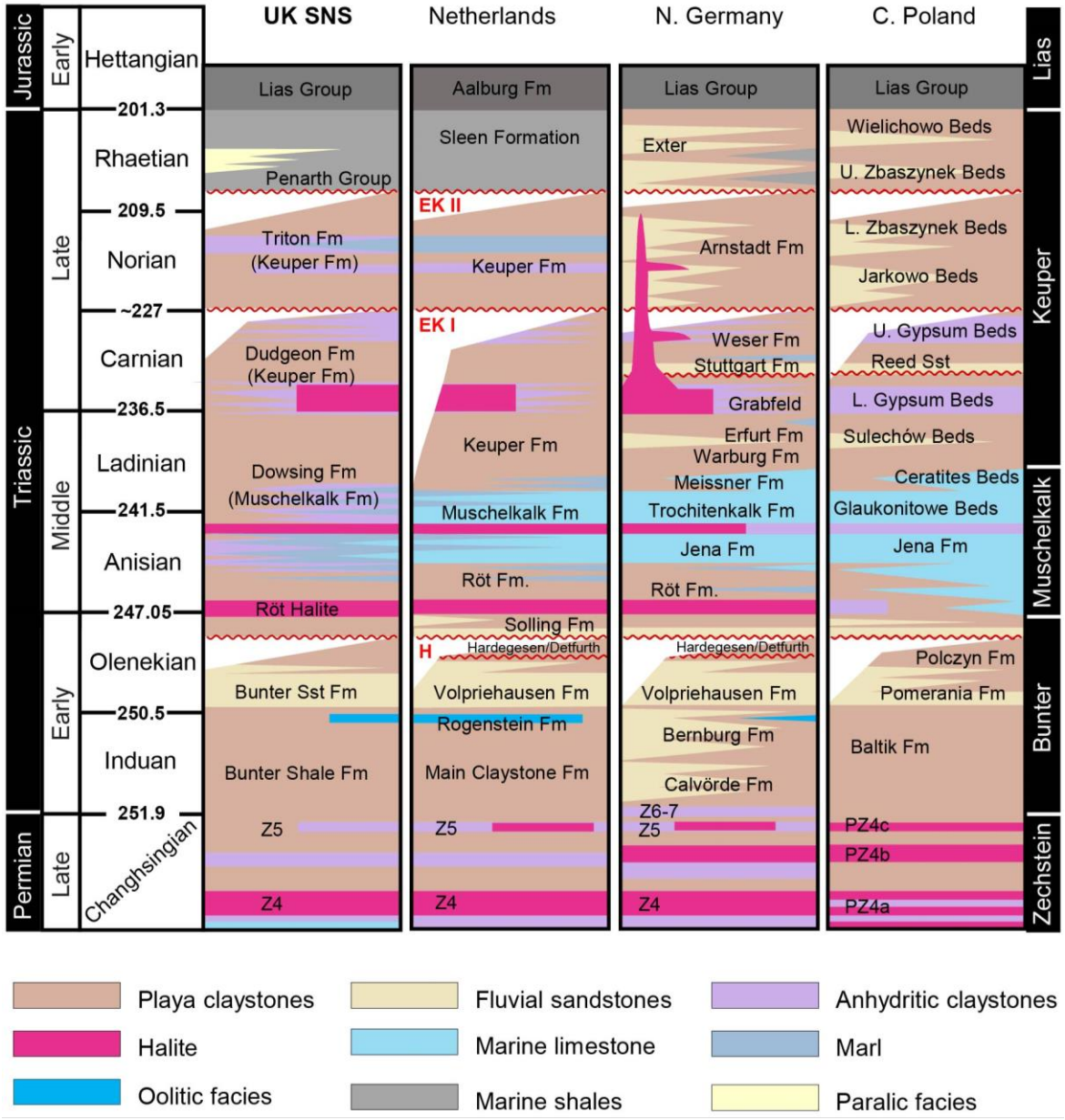

Figure 2: *The established lithostratigraphic framework for the UK Southern North Sea (SNS), and neighbouring regions with equivalent strata, including the Netherlands, northern Germany, and Poland. The major lithostratigraphic units are provided, along with the regional names and stratigraphic position of rock formations. H marks the position of the Solling (Hardegsen) Unconformity. EK I and II denote the early Kimmerian unconformities. Chronology follows Salisbury et al. (2022).*

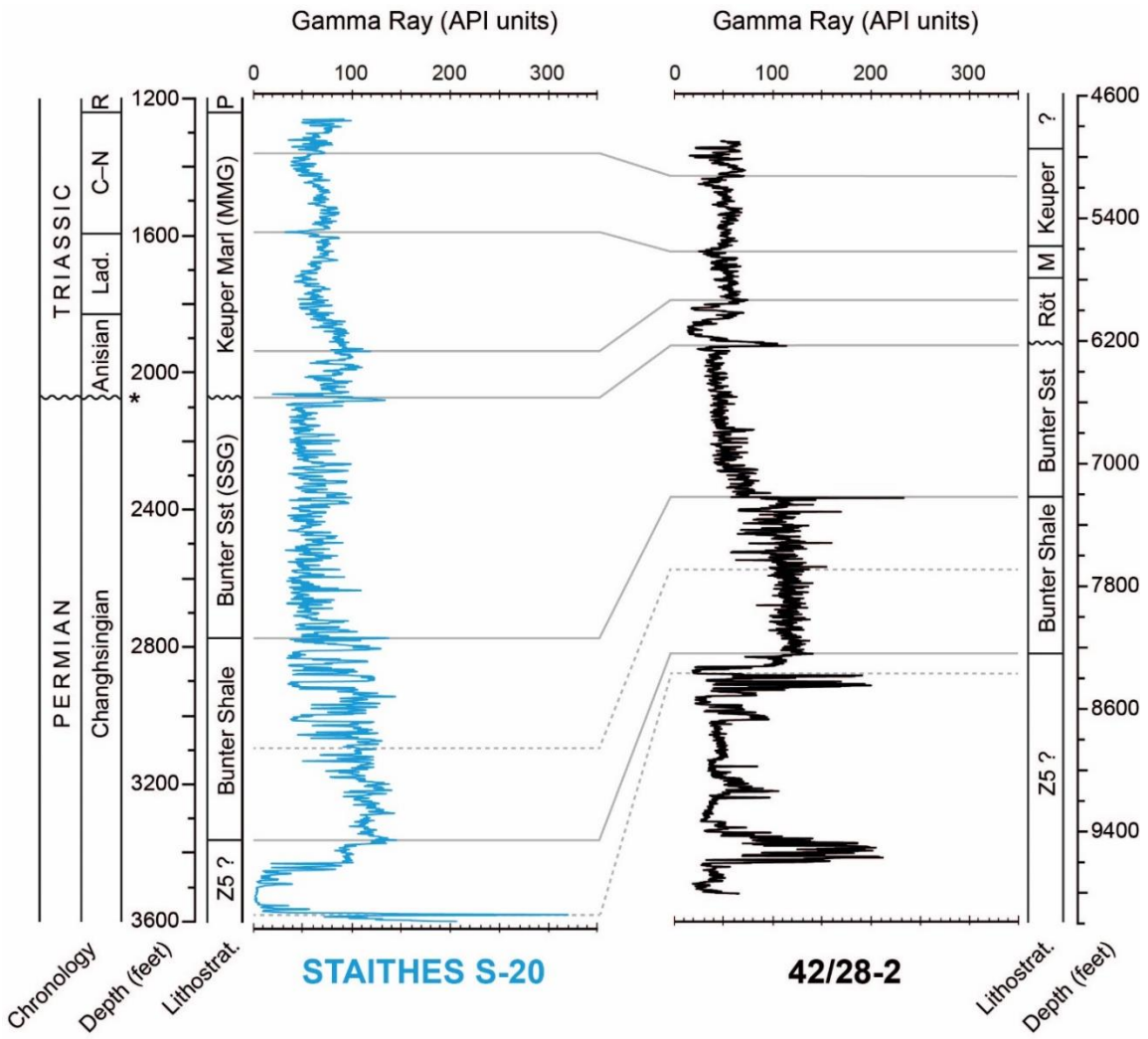

Figure 3: *Correlation of the Staithes S-20 and 42/28-2 boreholes based upon gamma ray logs. The wells are vertical, and depths are measured along hole. The Hardegsen Unconformity is marked by the irregular line. A star (*) denotes a palynological age constraint (see Salisbury et al., 2022). Lad – Ladinian, C-N – Carnian-Norian, R – Rhaetian, SSG – Sherwood Sandstone Group, MMG – Mercia Mudstone Group, M – Muschelkalk. Chronology follows Salisbury et al. (2022).*

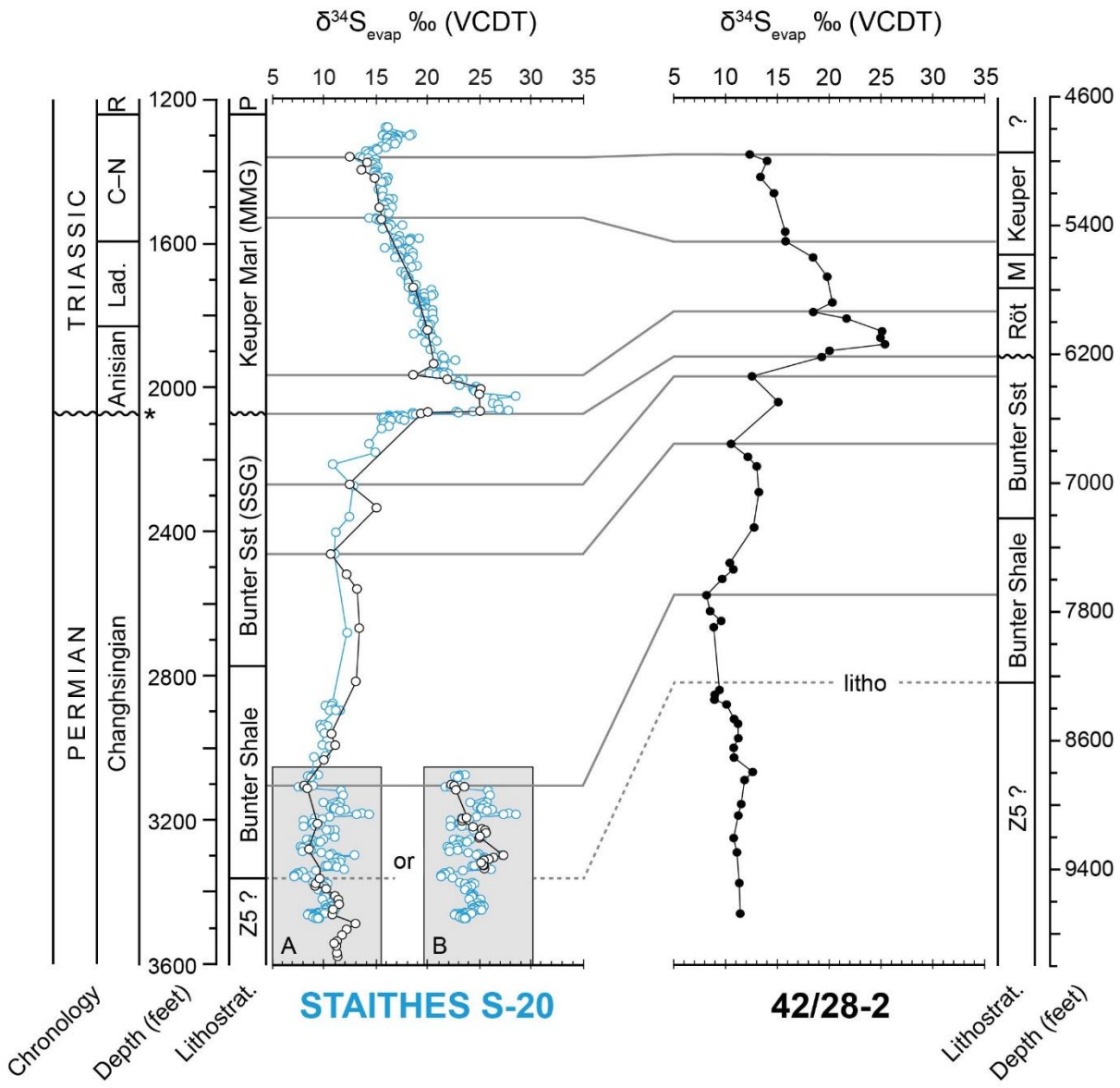

Figure 4: *Sulphur isotope stratigraphy of borehole 42/28-2 compared and correlated to Staithes S-20 (Salisbury et al., 2022). Seven correlation lines were determined based primarily upon trends and inflection points within the sulphur isotope records. One correlation based on lithostratigraphic relationships is marked by the dashed line. Two possible correlation schemes for the base of the sulphur isotope records are presented (A and B). (left) The $\delta^{34}S_{evap}$ record of 42/28-2 (black and white dots) stretched and compressed within the correlation lines and overlain onto the equivalent record of Staithes S-20 (blue and white dots). (right) The raw $\delta^{34}S_{evap}$ record of 42/28-2 (black filled dots) without being stretched and/or compressed.*

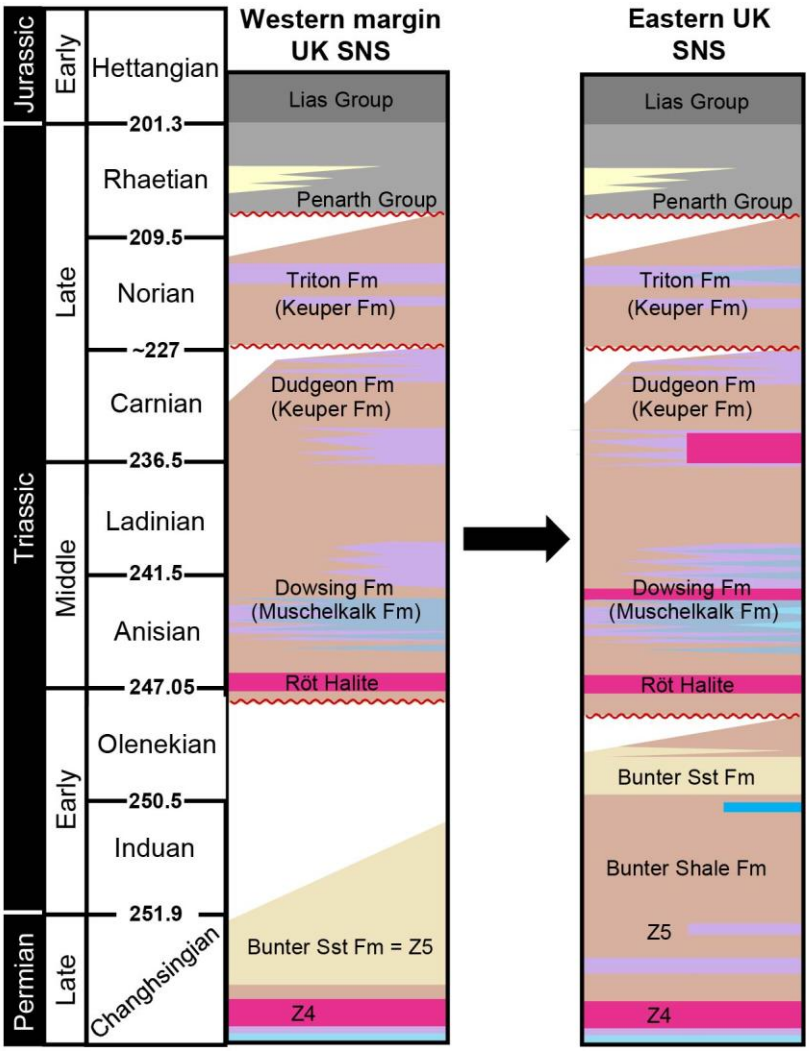

Figure 5: *Proposed revision to the lithostratigraphic framework of the western margin UK Southern North Sea (SNS) compared with the established lithostratigraphy of the eastern UK SNS. Unconformities are marked with red irregular lines.*

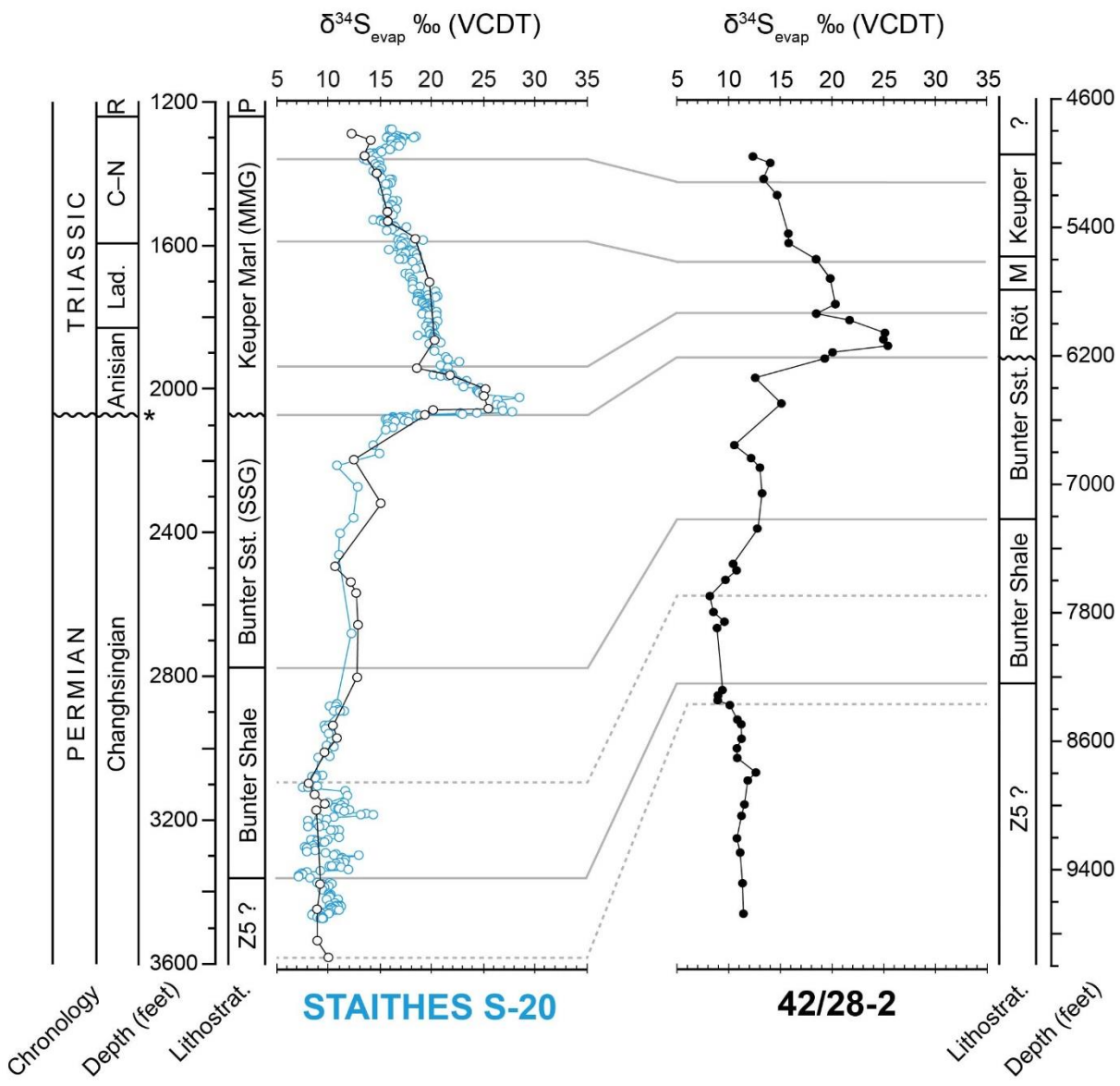

Figure 6: *Sulphur isotope stratigraphy of 42/28-2 compared and correlated with the equivalent record of Staithes S-20 (Salisbury et al., 2022). Nine correlation lines were drawn according to the correlation scheme based on gamma ray logs (see Figure 3). (left) The $\delta^{34}S_{evap}$ record of 42/28-2 (black and white dots) stretched and compressed within the correlation lines and overlain onto the equivalent record of Staithes S-20 (blue and white dots). (right) the raw $\delta^{34}S_{evap}$ record of 42/28-2 (black filled dots) without being stretched and compressed.*

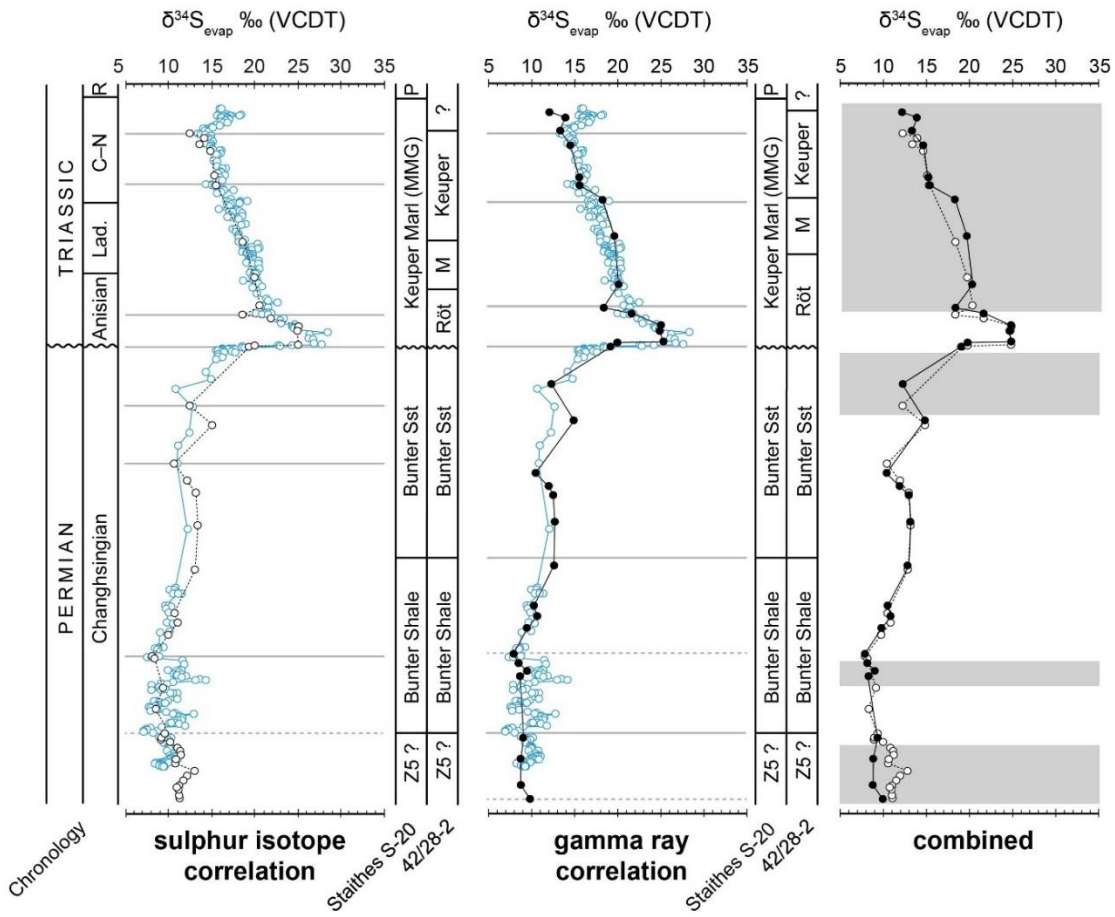

Figure 7: *Comparison between the sulphur isotope and gamma ray correlation schemes. (left) Stratigraphic correlation based upon the sulphur isotope records, as presented in Figure 4. The lithostratigraphic boundaries for Staithes S-20 are based on the original log, while those for 42/28-2 are adjusted based upon the correlation schemes with Staithes S-20. (middle) The correlation scheme based upon the gamma ray logs. (right) The $\delta^{34}S_{evap}$ record of Staithes S-20 and 42/28-2 based on the sulphur isotope and gamma ray correlation schemes. Stratigraphic intervals within which the correlation schemes are in relative agreement are marked with the white shading, while the grey shading represents stratigraphic intervals within which the correlation schemes disagree.*

Chapter 4

Sulphur isotope stratigraphy of the Triassic Sherwood Sandstone and Mercia Mudstone groups, United Kingdom

Jack Salisbury[1*], Darren R. Gröcke[1*], Tom McKie[2], H.D.R. Ashleigh Cheung[1], Robert Raine[3]

1. Department of Earth Sciences, Durham University, South Road, Durham DH1 3LE, UK

2. Shell UK Exploration and Production, 1 Altens Farm Road, Nigg, Aberdeen AB12 3FY, UK

3. Geological Survey of Northern Ireland, Dundonald House, Belfast BT4 3SB, UK

** = corresponding authors: jack.salisbury@durham.ac.uk, d.r.grocke@durham.ac.uk*

Evaporite-prone, dryland continental basin-fills, such as the UK Triassic, lack abundant fossil control on their chronostratigraphy and tend to rely on other techniques, such as heavy mineral correlation and magnetostratigraphy, for correlation and age dating. Here we report on the novel use of evaporite-based sulphur isotope ($\delta^{34}S_{evap}$) profiles for the Sherwood Sandstone and Mercia Mudstone groups, from the Larne, East Irish Sea, and Wessex basins. Through comparison with the established global composite $\delta^{34}S_{evap}$ age curve, our $\delta^{34}S_{evap}$ profiles assist in providing further localised chronostratigraphic constraint to evaporitic strata of the UK Triassic, beyond which is achievable with sparse biostratigraphy alone. We report $\delta^{34}S_{evap}$ values from the lowermost Sherwood Sandstone Group that appear to align well with those of Permian seawater, potentially in agreement with previous research that reported comparable $\delta^{34}S_{evap}$ values from the Sherwood Sandstone of the Cleveland and UK southern North Sea basins. Our $\delta^{34}S_{evap}$ data from the Larne Basin provide further chronostratigraphic calibration to the Sherwood Sandstone-Mercia Mudstone boundary, agreeing well with the age assignment of this lithostratigraphic boundary within the established stratigraphic framework for this region. In addition, we provide the first high-resolution $\delta^{34}S_{evap}$ profile from halites and evaporitic mudstones of the East Irish Sea Basin, providing additional chronostratigraphic constraint to a basin which is especially impoverished in fossil content.

Our $\delta^{34}S_{evap}$ profiles from the Mercia Mudstone Group of the Wessex Basin and the Glenstaghey and Knocksoghey formations of the Larne Basin, are largely offset from Triassic seawater $\delta^{34}S_{evap}$ age curve, which we interpret as an overwhelming terrestrial $\delta^{34}S$ sulphate signal. Thus, through comparison with the global composite $\delta^{34}S_{evap}$ curve, we apply our $\delta^{34}S_{evap}$ data to provide further insight into the degree of

marine influence during evaporite deposition, helping to reconcile the long-standing controversy over the marine vs continental origin of UK Triassic evaporites, leading the way to an enhanced understanding of the sedimentary dynamics of these basins.

1. Introduction

Sulphate (SO_4^{2-}) is the second most abundant anion in modern seawater. It's sulphur isotopic composition ($\delta^{34}S$) has fluctuated over geologic time and is primarily controlled by the isotopic composition and relative magnitude of sulphur fluxes entering and exiting the ocean reservoir (Paytan et al., 2020). Due to the relatively large residence time of seawater sulphate, it is generally assumed that for much of the Phanerozoic, seawater sulphate has maintained sulphur isotopic homogeneity at any given point in geologic time (Paytan et al., 2012). Thus, time equivalent marine sedimentary sulphates are likely to exhibit similar $\delta^{34}S$ compositions, enabling stratigraphic correlation between sedimentary basins, particularly during periods of substantial $\delta^{34}S$ variability (Yao et al., 2019), such as across the Early and Middle Triassic (Claypool et al., 1980; Bernasconi et al., 2017; Salisbury et al., 2022).

The sedimentary environment of the European Permian-Triassic was largely arid and continental (with episodic marine influence) (Parrish, 1993), facilitating widespread evaporite deposition, with evaporites providing relatively consistent spatial and temporal coverage of the Triassic (McKie, 2017). In addition, the Triassic time interval includes several major perturbations in the global sulphur cycle, recorded by variability in $\delta^{34}S_{evap}$ (Claypool et al., 1980; Bernasconi et al., 2017; Salisbury et al., 2022). Recent work compiled composite Triassic $\delta^{34}S_{evap}$ profiles from evaporites of central Europe (Bernasconi et al., 2017) and Spain (Ortí et al., 2014, 2022). Their efforts greatly

expanded the chronostratigraphic coverage of the $\delta^{34}S_{evap}$ curve across this time interval and demonstrated the suitability of $\delta^{34}S_{evap}$ records for correlation.

The abundance of evaporitic sulphate within the UK (Warrington and Ivimey-Cook, 1992; McKie, 2017) presents the opportunity to further expand the coverage of the global $\delta^{34}S_{evap}$ age curve and provide additional chronostratigraphic constraint to the UK Triassic, which is particularly impoverished in fossil content (Warrington et al., 1980; Hounslow and Ruffell, 2006; McKie and Williams, 2009). The $\delta^{34}S$ analysis of Ca-sulphates within the Mercia Mudstone Group (MMG) of the Cleveland Basin and UK southern North Sea (SNS) enabled the generation of high-resolution $\delta^{34}S_{evap}$ profiles for the UK Middle-Late Triassic (Salisbury et al., 2022, 2023). These efforts have provided better localised chronostratigraphic constraint to the Mercia Mudstone Group and have expanded the coverage of the Middle-Late Triassic $\delta^{34}S_{evap}$ age curve at a high resolution (Salisbury et al., 2022, 2023). Despite this initial success, $\delta^{34}S_{evap}$ stratigraphy has yet to be applied widely to the UK Triassic and many basins continue to lack chronostratigraphic calibration beyond lithostratigraphic correlation with sparse dated sections.

Evaporites are known to form in both continental and marine depositional settings (see Warren, 2010), with evaporites of the UK Triassic often lacking features unique to a particular marine or continental setting. Accordingly, much debate persists regarding the degree of marine influence during deposition of the MMG (e.g., Wills, 1970; Taylor, 1983; Ruffell and Shelton, 1999; Hounslow and Ruffell, 2006), with apparent conflicts between sedimentological (Andeskie et al., 2018; Milroy et al., 2019), palaeontological (Warrington, 1995; Baranyi et al., 2019) and geochemical data (Taylor,

1983; Leslie et al., 1993; Salisbury et al., 2022, 2023). This uncertainty regarding the mode of formation for the evaporites of the MMG precludes a more complete understanding of the environmental and palaeogeographic evolution of the UK Triassic, as well as the dynamics of the basin-fill.

Data presented here from multiple localities in the UK offer the potential to further expand the coverage of the Triassic $\delta^{34}S_{evap}$ record, providing much needed chronostratigraphic constraint to biostratigraphically barren evaporitic strata across distinct UK sedimentary basins. In addition, through comparison with the established Triassic $\delta^{34}S_{evap}$ age curve of Salisbury et al. (2022), our $\delta^{34}S_{evap}$ profiles provide further insight into the degree of marine influence during the deposition of the Mercia Mudstone Group, offering a solution to apparent contradictions between existing datasets.

2. Geological setting

During the Late Carboniferous Variscan Orogeny, tectonic reconfiguration resulted in the coalescence of Earth's continental landmasses, heralding the formation of the Pangaean supercontinent (Peacock, 2004; Hounslow et al., 2012). Pangaea exhibited signs of instability soon after, with the initiation of rifting along the Norwegian-Greenland Rift beginning in the Late Carboniferous (Peacock, 2004), followed by punctuated rifting through the Permian and Triassic (Coward, 1995; McKie, 2014). During the mid to late Permian, the Norwegian-Greenland Rift propagated southwards into the central North Sea and along the Atlantic seaboard of the UK and Ireland (Hounslow et al., 2012). Rifting also propagated northward from the Tethys, into the central North Sea and Southern Permian Basin (McKie, 2014). The continued breakup of

Pangaea incited further rifting episodes in the Early and Late Triassic, generating the Hardegsen and Early Cimmerian unconformities, respectively (Bachmann et al., 2010). These rifting episodes formed a series of sub-sea level fault-bound rift basins (Howard et al., 2008; McKie and Williams, 2009; Newell, 2018) that provided accommodation space for sediment, and episodic access for marine waters (McKie, 2017).

During the Triassic, Britain was located within the eastern part of the supercontinent Pangaea, occupying a palaeolatitude of ~20 °N (Newell, 2018), and deposition occurred under a warm and arid to semi-arid climate (McKie and Williams, 2009; Sun et al., 2012; Trotter et al., 2015). Precipitation patterns followed a monsoonal seasonality originating from the Panthalassa and Tethys oceans (Parrish, 1993). Aridity of the continental interior was maintained by the vast expanse of continental landscape, ensuring a high degree of continentality and scarcity of open water sources (Parrish, 1993). Saline waters accumulated within sub-sea level rift basins that propagated through the warm and arid continental interior, via direct marine flooding or groundwater seepage from adjacent marine basins (Hounslow et al., 2012; McKie, 2017). During the Middle Triassic, a local increase in humidity may have accompanied the Muschelkalk marine incursion, represented in NW Europe by the limestones of the Muschelkalk (Hounslow et al., 2012). However, this incursion did not extend west beyond the easternmost southern North Sea, UK sector (Hounslow et al., 2012). Further west, deeper within the rift system, the UK Triassic is absent of any Muschelkalk-equivalent formations, with evidence of sustained aridity and consistent evaporite deposition (McKie, 2014).

Sedimentation progressed from largely fluvial/aeolian facies of the Sherwood Sandstone Group (SSG) in the late Permian-Early Triassic (Salisbury et al., 2023), through to evaporitic playa mudstones of the Mercia Mudstone Group (MMG), of the Middle-Late Triassic (Howard et al., 2008) (Fig. 1). The boundary between the SSG and MMG is generally placed at the upward transition from sandstone to mudstone (Ambrose et al., 2014), however its precise chronostratigraphic position remains poorly constrained. Magnetostratigraphy from south Devon suggests an Anisian-Ladinian age for the SSG-MMG boundary (Hounslow and McIntosh, 2003), yet the palaeontological data are insufficient to confirm an age-assignment beyond a broader Anisian age, with the chronostratigraphic position of the boundary likely being diachronous across distinct UK sub-basins (see below). Fossil content provides evidence for intermittent marine flooding during the deposition of the SSG in the Early Triassic (Warrington and Pollard, 2021) and during the Anisian and Ladinian of the Middle Triassic MMG in various locations (Warrington, 1974, 1995; Wilson, 1993; Jackson et al., 1995; Ambrose and Wakefield, 2015; Warrington and Pollard, 2021). The evaporites in the MMG largely occur as intervals of bedded halite, interspersed with nodular gypsum and anhydrite, providing relatively consistent chronostratigraphic coverage of the Middle-Late Triassic (Warrington and Ivimey-Cook, 1992; Salisbury et al., 2023).

The precise volume and stratigraphic arrangement of the salt differs between distinct UK sub-basins. In SW England, the sandstones of the SSG likely extend into the Middle Triassic based upon biostratigraphic data (see below) and magnetostratigraphy (Hounslow and McIntosh, 2003), and are overlain by anhydritic mudstones/siltstones of the Sidmouth Mudstone Formation (Whittaker and Green, 1983; Howard et al., 2008; Ambrose et al., 2014). In the centre of regional sub-basins, mudstones are replaced by

bedded halite of the Somerset Halite Formation (Whittaker, 1972; Whittaker and Green, 1983; Howard et al., 2008) of Carnian-age (Fig. 2), which has been lithostratigraphically correlated across multiple sub-basins within the region (Gallois, 2002; 2004), extending to the south in the subsurface beneath the Channel Basin (Harvey and Stewart, 1983). Overlying the Somerset Halite, anhydritic mudstones/siltstones return with the Branscombe Mudstone and Blue Anchor formations (Fig. 1) (Whittaker and Green, 1983; Howard et al., 2008). Recent efforts in applying magnetostratigraphy have assisted in providing further age constraint to the MMG of Devon, southwest England, and have enabled broader correlation with equivalent strata internationally (see Hounslow and Gallois, 2023 for details).

To the northwest in the East Irish Sea Basin (EISB), the MMG is represented by interbedded evaporitic mudstones and laterally extensive formations of clean and argillaceous halite (Fig. 1) (Jackson and Johnson, 1996; Jackson et al., 1997). The cyclic deposition of evaporitic mudstones and halite could reflect repeated phases of basin flooding and drying (Stuart, 1993) within a depositional environment possibly comparable to the contemporary Rann of Kutch (Jackson et al., 1995). The halite members pinch-out towards the southern margin of the basin, grading into undivided mudstones (Jackson and Johnson, 1996). In both southwest England and the EISB, evaporitic mudstones are overlain by shales of the Blue Anchor Formation (Whittaker and Green, 1983; Jackson and Johnson, 1996; Howard et al., 2008).

In Northern Ireland, the MMG is divided into six formations: the Lagavarra, Craiganee, Glenstaghey, Knocksoghey, Port More, and Colin Glen formations (Fig. 1) (Mitchell, 2004). At the base of the MMG, anhydritic mudstones are interbedded with

sandstones (Wilson and Manning, 1978), with the Lagavarra Formation being the transitional unit between the SSG and MMG (Mitchell, 2004). In overlying units, the MMG is characterised by anhydritic mudstones, with intervals of bedded halite occurring within the Craiganee, Glenstaghey and Knocksoghey formations (Wilson and Manning, 1978). The overlying Port More and Collin Glen formations are represented by brown mudstones and green calcareous mudstones, respectively (Wilson and Manning, 1978). Both are devoid of evaporitic material (Wilson and Manning, 1978; Mitchell, 2004) and the Collin Glen is considered a regional equivalent of the Blue Anchor Formation (Warrington et al., 1980).

During the Rhaetian, additional rifting and the expansion of connecting seaways incited a marine incursion, precluding further widespread evaporite deposition in NW Europe (Peacock, 2004, Wignall and Bond, 2008). Mudstones of the MMG were replaced by the Penarth Group in the UK (Lott and Warrington, 1988; Warrington and Ivimey-Cook, 1992), which has been classified as 'quasi-marine', due to the absence of certain fully marine fossil groups (Wignall and Bond, 2008). It is likely that the Penarth Group was deposited within a lagoonal and/or shallow marine environment (Jackson et al., 1995). The trend to fully marine deposition continued into the Early Jurassic, with the deposition of the overlying limestones of the Hettangian Lias Group (Cope et al., 1980; Mitchell, 2004; Wignall and Bond, 2008).

2.1. Biostratigraphy

Despite extensive study, the MMG of the UK Triassic commonly lacks chronostratigraphic calibration, due to a scarcity of age-diagnostic fossils. In continental Europe, the presence of the marine Muschelkalk provides additional biostratigraphic

constraint for the Middle Triassic (Narkievicz, 1999; Márquez-Aliaga et al., 2000; Franz et al., 2013; Chen et al., 2019). However, the absence of the Muschelkalk west of the southern North Sea, and a general lack of marine carbonates when compared with continental Europe (e.g., Feist-Burkhardt et al., 2008; Ortí et al., 2022), ensures the UK is particularly deprived of age-diagnostic fossils for biostratigraphy. Thus, it is common for the UK Triassic to lack chronostratigraphic calibration (McKie and Williams, 2009). The cores sampled in this work are particularly impoverished in fossil content, with only Burton Row and Staithes S-20 having any direct biostratigraphic constraint. The biostratigraphy of the prior will be discussed below, for Staithes S-20 see Salisbury et al. (2022). Fossils appropriate for biostratigraphy are known from elsewhere in the basins studied here, and act to constrain our $\delta^{34}S_{evap}$ correlation schemes.

While biostratigraphic constraints suggest an Early Triassic age for the base of the Buntsandstein and its equivalents in continental Europe (Scholze et al., 2016; 2017), no palaeontological data exist for the position of the PTB and the base of the SSG in Britain (Warrington et al., 1980). In the Wessex basin, biostratigraphic constraints are sparse for the SSG, with the Burton Row borehole failing to provide suitable sample material from the Upper and Lower sandstones of the SSG (Warrington *in* Whittaker and Green, 1983). However, at outcrop along the Devon coast, biostratigraphic data suggest a Middle Triassic age for the Otter Sandstone (SSG) (Benton, 1997; Spencer and Storrs, 2002). The fauna includes reptiles, amphibians and fish (Benton, 1997), and enable age correlation with Anisian-age formations globally (Benton, 1997; Lucas, 1998; Spencer and Storrs, 2002). Available biostratigraphic data from various locations suggest a diachronous SSG-MMG boundary across UK sub-basins (Warrington et al., 1980; Ambrose et al., 2014). For example, the SSG in the more northerly Cheshire Basin

includes a miospore assemblage assigned to the Early Triassic, as well as reptilian remains of Anisian age (Warrington, 1970), suggesting the SSG is likely older in Cheshire than in Devon.

In the EISB, the SSG is particularly impoverished in fossil content suitable for biostratigraphy, with an almost complete absence of biostratigraphic age constraints (Meadows, 2006). Further west in Northern Ireland, the biostratigraphic constraints are also limited, however sparse miospore assemblages suggest an Olenekian (Early Triassic) age in the middle-upper SSG and an Anisian age for the upper SSG (Warrington, 1995).

Much of the biostratigraphic constraint for the MMG of the Wessex Basin is derived from palynomorph assemblages of land plant origin (Warrington, 1997). At a depth of 691.50 m in the Burton Row borehole, near the top of the Somerset halite Formation, a specimen tentatively identified as *Ovalipollis pseudoalatus* was recovered (Warrington *in* Whittaker and Green, 1983). Kürschner and Herngreen (2010) assign this an age range of Ladinian to Rhaetian, however palynomorph assemblages suggest a Carnian age for equivalent saliferous beds within the nearby Puriton borehole (Warrington, 1980). Accordingly, a Carnian age may be most appropriate for the Somerset Halite Formation in the Burton Row borehole (Warrington *in* Whittaker and Green, 1983).

Recent work on outcrops within the Wessex Basin report Carnian-age palynomorphs *(Camerosporites secatus*, *Partitisporites* and *Duplicisporites* species, *Enzonalasporites spp*., *Vallasporites ignacii* and *Patinasporites densus*.) from the top of the Sidmouth Mudstone Formation, the Dunscombe Mudstone Formation (equivalent to the Somerset Halite) and the base of the overlying Branscombe Mudstone Formation

(Baranyi et al., 2019). The presence of Julian miospores *Patinasporites densus*, *Partitisporites maljawkinae* and *Partitisporites novimundanus* and the absence of Tuvalian *Ricciisporites* or *Classopollis* spp. suggests a Julian age for the Dunscombe Mudstone Formation, with the boundary between the underlying Sidmouth Mudstone Formation placed within the early Julian (Baranyi et al., 2019). If the Dunscombe Mudstone Formation is indeed time equivalent to the Somerset Halite (Howard et al., 2008), then this would support a Carnian age for the Somerset Halite Formation. However, the only known direct biostratigraphic age constraint for this formation is the palynomorph reported by Warrington *in* Whittaker and Green (1983), which as stated, was only tentatively identified as *Ovalipollis pseudoalatus*. Thus, age constraint for the Somerset Halite Formation within the Burton Row borehole remains limited.

At ~496 m depth within the Burton Row borehole, the miospore assemblages *Classopollis torosus* and *?Ricciisporites tubercalatus* were recovered, suggesting a Rhaetian age. In addition, another Rhaetian miospore assemblage, *Rhaetipollis germanicus*, was recovered at ~474 m depth (Warrington *in* Whittaker and Green, 1983). This places the Norian-Rhaetian boundary below the base of the Blue Anchor Formation within the Burton Row borehole. For the majority of the Blue Anchor Formation in the Wessex Basin, the fossils suitable for biostratigraphy are miospores (Warrington, 1974, 1980; Warrington and Whittaker, 1984), which have a greater affinity with those of the overlying Penarth Group than the underlying MMG (Warrington *in* Whittaker and Green, 1983), and are assigned a Rhaetian age (Warrington et al., 1995; Warrington, 1997). An increase in assemblage diversity is seen through the uppermost Blue Anchor Formation, along with the occurrence of acritarchs and dinoflagellate cysts (e.g., Warrington, 1980; Warrington *in* Whittaker and Green, 1983; Warrington et al., 1995), which may suggest

an increase in the degree of marine influence as the Blue Anchor Formation transitions into the Penarth Group (Warrington and Whittaker, 1984).

Biostratigraphic constraints are particularly limited in the MMG of the EISB and consist primarily of miospore assemblages (Jackson and Johnson, 1996). The preservation potential of the miospores is generally poor, and for those that are present, the diversity and abundance is low (Jackson and Johnson, 1996). Much of the established palynology is reliant upon comparison with equivalent stratigraphy in the adjacent offshore Kish Bank Basin (Naylor et al., 1993) and onshore West Lancashire and Cheshire basins (Earp and Taylor, 1986; Warrington *in* Wilson and Evans, 1990; Jackson and Johnson, 1996).

In the Irish offshore Kish Bank Basin, the miospore assemblages *Spinotriletes echinoides*, *Striatoabietites aytugii* and *Jugasporites conmilvinus* were recovered from well 33/17-1 and suggest an Early Triassic age for the lowermost MMG, while the youngest halite beds here yielded *Alisporites grauvogeli* and *Microcachrydites sittleri*, providing an Anisian upper age limit for the halite in this basin (Naylor et al., 1993). In addition, Olenekian miospores *Densosporites nejburgii* and *Endosporites papillatus* have been recovered from the MMG in well 33/21-1 (Geochem Group, 1992, biostratigraphic report). The Olenekian miospores are intriguing and could imply the Early-Middle Triassic boundary should be placed within the lowermost MMG in the Kish Bank Basin, suggesting the SSG-MMG boundary is diachronous between the Kish Bank and onshore Lancashire, where miospores constrain the base of the MMG to the Anisian (see below).

However, the vast majority of the palynomorphs recovered from the MMG halites of 33/21-1 are of Anisian age (*Stellpollenites thiergartii*, *Minutosaccus potoniei*,

Microcachryidites sittleri, Densosporites nejburgii, *Taenisporites noviaulensis* and *Striatoabieites balmei*), with the latter three forms being reported from the base of the MMG (Geochem Group, 1992, biostratigraphic report). Naylor et al. (1993) report *Striatoabietites aytugii*, *Triadispora spp*. and *Lundbladispora spp.* from the underlying Ormskirk Sandstone in 33/17-1. While *Lundbladispora spp.* is Early Triassic (Kürschner and Herngreen, 2010), *Triadispora spp.* is now considered to be at least Anisian in age (Kürschner and Herngreen, 2010; Hochuli et al., 2020). A separate report of 33/17-1 reports Anisian *Chordosporites* and *Alisporites* at the top of the Ormskirk and Anisian *Triadaspora plicata*, *Microcachryidites spp* and *Apiculatasporites spp.* in the overlying MMG halitic interval (Geochem Group, 1992, biostratigraphic report). In the 33/17-1, the gypsiferous claystones overlying the halitic intervals yielded Anisian and Ladinian miospores; *Lueckisporites triassicus*, *Microcachrydites fastidiosus* and *Microcachrydites sittleri*, respectively (Naylor et al., 1993). Thus, the Olenekian miospore assemblages could indicate an Early Triassic age for the lowermost MMG in the Kish Bank (and possibly the EISB), however they could also be a product of contamination or the reworking of Olenekian palynomoprhs. In addition, the age ranges for miospore assemblages *Densosporites nejburgii* and *Endosporites papillatus* reported from 33/21-1 are thought to extend into the Anisian (Johnson et al., 1994), and therefore these palynomorphs may be present as their youngest expression.

Palynomorphs recovered from biostratigraphic surveys of boreholes in the onshore Lancashire region suggest an Anisian to Ladinian age for the MMG in this region (Warrington *in* Wilson and Evans, 1990). The MMG up to the base of the Preesall Halite is at least largely Anisian in age, determined by the recovery of *Stellapollenites thiergartii*, *Perotrilites minor* and *Angustisulcites spp.* from the Hambleton Mudstones,

Singleton Mudstones and Thornton Mudstones (Warrington *in* Wilson and Evans, 1990), broadly equivalent to the Leyland Formation of the EISB (Jackson and Johnson, 1996). *Stellapollenites thiergartii* has been recovered from the Coat Walls Mudstone, which is broadly correlative to the base of the Dowbridge Mudstone Formation of the EISB (Warrington *in* Wilson and Evans, 1990; Jackson and Johnson, 1996). This constrains the Preesall Halite Formation to the Anisian, with the Anisian-Ladinian boundary in the EISB being placed in the base of the overlying Dowbridge Mustone Formation (Jackson and Johnson, 1996). Miospores *Retisulcites perforates*, *O. pseudoalatus*, and *Echinitosporites iliacoides* are reported from the overlying Breckells Mudstone (Warrington *in* Wilson and Evans, 1990), which is broadly equivalent to the upper Dowbridge and lower Warton Halite formations in the EISB (Jackson and Johnson, 1996). *O. pseudoalatus* first occurs in the Ladinian, disappearing in the late Rhaetian (Kürschner and Herngreen, 2010), while *R. perforates* and *E. iliacoides* are thought to extend from the Ladinian into the Carnian (Warrington *in* Wilson and Evans, 1990; Kürschner and Herngreen, 2010).

Thus, the available biostratigraphic data provide a minimum age of Ladinian for the majority of the Dowbridge Mudstone Formation, with Jackson and Johnson (1996) assigning the overlying Warton Halite Formation to the Carnian and the Elswick Mudstone Formation to the Carnian-Norian. They report assemblages containing one or more of *Camerosporites secatus*, *Retisulcites perforatus*, *Ovalipollis pseudoalatus* and *Echinitosporites iliacoides* within the Dowbridge, Warton and Elswick formations (Jackson and Johnson, 1996), ranging from Ladiniain to Rhaetian age (Kürschner and Herngreen, 2010). However, the authors do not provide details regarding the stratigraphic and geographic position of such assemblages, and thus the palynology of

the higher formations of the MMG in the EISB is especially speculative (Jackson and Johnson, 1996).

In west Lancashire, organic-walled microplankton have been recorded throughout the MMG, while prasinophyte algae and acritarchs have been reported within specific stratigraphic intervals (Warrington, 1970b; Warrington *in* Wilson and Evans, 1990). These biostratigraphic data suggest a marine connection to west Lancashire and possibly the EISB (Wilson, 1990; Warrington *in* Wilson and Evans, 1990), supporting a possible marine origin for the brines from which the halites formed (Warrington *in* Wilson and Evans, 1990).

Miospore assemblages recovered from deep boreholes provide biostratigraphic age constraint to the MMG in the Larne Basin of Northern Ireland (Warrington, 1995; Mitchell, 2004). *Verrucosisporites thuringiacus* and *Guttulapollenites hannonicus* suggest the Lagavarra Formation and the lower Craiganee Formation are likely Anisian in age (Warrington, 1995). The miospore assemblage *Stellapollenites thiergartii* indicate an Anisian age for at least the lower parts of the Glenstaghey Formation, while *Retisulcites perforatus* and *Echinitosporite iliacoides* indicate a Ladinian age for the top of the Glenstaghey Formation. Thus, the overlying Knoscksoghey Formation is at least Ladinian, and possibly Carnian, in age (Warrington, 1995). The presence of Triassic acritarchs, *Cymatiosphaera* and *Micrhystridium*, while unable to provide age constraint, suggest marine influence during the deposition of the MMG in Northern Ireland (Warrington, 1995).

The overlying Penarth Group has yielded miospores, dinoflagellate cysts, acritarchs, foraminifera test linings, bivalves, and fish (Warrigton *in* Whittaker and

Green, 1983; Lott and Warrington, 1988; Warrington, 1997). The miospore assemblages, principally *Classopollis* spp., confidently constrain the Penarth Group to the Rhaetian in multiple locations (Lott and Warrington, 1988; Warrington, 1995; Warrington, 1997; Hounslow and Ruffell, 2006).

3. Methodology

3.1. Sampling

This study is based upon the sulphur isotope analysis of evaporitic samples acquired from well cores (drillcore and drill cuttings) in the United Kingdom. The well cores sampled include GT-01 Kilroot, Carnduff-02 and Cairncastle-2 from the Larne Basin, Northern Ireland; 110/13-8 from the East Irish Sea Basin (EISB); and Burton Row of the Wessex Basin, SW England. The methods employed in this work closely follow those of Salisbury et al. (2022, 2023) used to generate the $\delta^{34}S_{evap}$ profiles of Staithes S-20 and 42/28-2. Many of the samples were taken from calcium sulphate (gypsum/anhydrite) nodules and massive beds, while others were acquired from bedded and displacive halite. Fibrous gypsum was generally avoided, due to its' association with diagenetic secondary precipitation. However, in the case of Kilroot GT-01, most of the Ca-sulphate available for sampling was fibrous and was sampled for comparative study.

Drillcore from Burton Row and drill cuttings from 110/13-8 were sampled at the British Geological Survey, Keyworth, Nottingham, while drillcore of GT-01 Kilroot, Carnduff-02 and Cairncastle-2 were sampled at the geological Survey of Northern Ireland, Belfast. For Burton Row, GT-01 Kilroot, Carnduff-02, and Cairncastle-2, anhydrite nodules and beds were sampled at regular intervals, providing consistent stratigraphic coverage across depths where the evaporites are present. In Burton Row

and Carnduff-02, dominantly halitic intervals are present and were sampled in the same manner. A total of 42 samples were acquired from GT-01 Kilroot, 250 from Carnduff-02, 7 from Cairncastle, 157 from 110/13-8, and 214 for Burton Row.

With regards to 110/13-8, drill cuttings were sampled at variable depth intervals. The sampling resolution varies throughout the borehole, depending on the abundance of evaporite minerals suitable for sampling. Each drill cuttings sample represents a depth range and is thus viewed as a lithological average over that depth interval. Drill cuttings were viewed under an optical microscope, and chips of gypsum, anhydrite and halite were transferred into 1.5 ml micro-centrifuge tubes.

3.2. Petrography

Select samples from drillcore of Burton Row were chosen at regular stratigraphic intervals. A representative slice of 1 to 1.5 cm thickness and standard size (26 x 46 mm) was cut from each sample. Each slice was subsequently reduced to 30 microns thickness and bonded to a glass slide (26 x 76 mm). Petrographic observations included mineral composition, colour, sedimentary textures and structures, diagenetic features, fossils, and notable contacts.

3.3. Sulphur isotope analysis of sulphate

The sulphur isotope analysis of sulphate was performed on gypsum, anhydrite, and halite. Gypsum and anhydrite are composed of ~20 wt % sulphur, and thus contain a high concentration of sulphate. Accordingly, the process of sulphate extraction for the gypsum/anhydrite nodules and beds from Burton Row, GT-01 Kilroot, Carnduff-02 and Cairncastle-2, simply involved the use of a dentists' drill to produce a fine powder.

In contrast, sulphate is only a trace constituent in halite and therefore requires concentration before sulphur isotope analysis can be performed. In addition, tests suggest the need to concentrate sulphate when using drill cuttings, even when dealing with gypsum/anhydrite. Thus, halite from Burton Row and Carnduff-02, as well as drill cuttings from 110/13-8, underwent sulphate concentration via barite ($BaSO_4$) precipitation. The samples were crushed into a fine powder using an agate pestle and mortar. Approximately 1-5 g of evaporitic material were transferred into 50 ml (halite) and 15 ml (drill cuttings) centrifuge tubes and submerged in a 10 % NaCl DI H_2O solution to facilitate evaporite dissolution. Blanks of NaCl produced no visible $BaSO_4$. The samples were left to dissolve for 24-48 hours and agitated every few hours during the working day. Once the dissolution process was complete, the samples underwent centrifugation at 3500 rpm for 3 minutes, before 50 % of the supernatant was decanted into 50 ml (halite) and 15 ml (drill cuttings) centrifuge tubes. Approximately 25 ml (bedded halite) and 7.5 ml (drill cuttings) of 10 % barium chloride ($BaCl_2$) was mixed with the saline solution for each sample. A few drops of 3M HCl were added, reducing the pH to 1-2 and preventing the precipitation of barium carbonate ($BaCO_3$). It was common for the solution to turn cloudy immediately, indicating the precipitation of $BaSO_4$:

$$\mathrm{BaCl_2 + SO_4^{2-} \rightarrow BaSO_4 + 2Cl^{2-}} \qquad [1]$$

The samples were left for >24 hours to ensure the $BaSO_4$ precipitation process reached completion, after which they underwent centrifugation at 3000 rpm for 5 minutes. The acidic supernatant was discarded according to safety regulations for appropriate waste disposal. For each sample, the pellet of $BaSO_4$ was rinsed with approximately 50 ml (bedded halite) or 15 ml (drill cuttings) of DI H_2O to neutralise the

sample. A neutral pH balance was achieved upon three rinses. The $BaSO_4$ was subsequently placed in a drying oven set to ~80 °C for ~48 hours. Once dry, it was crushed into a fine powder using an agate pestle and mortar.

For each sample, 0.2-0.4 mg were weighed into 5 x 3.5 tin capsules. Sulphur isotope analysis was performed in the Stable Isotope Biogeochemistry Laboratory (SIBL), Durham University, using a Thermo Scientific EA Isolink™ coupled to a Thermo Scientific Delta V Plus isotope-ratio mass-spectrometer. Evaporite sulphur isotope ratios are expressed in standard delta (δ) notation in per mil (‰) relative to Vienna Canyon Diablo Triolite (VCDT) according to the following equation:

$$\delta^{34}S = \left[\frac{(({}^{34}S/{}^{32}S)_{sample} - ({}^{34}S/{}^{32}S)_{standard})}{({}^{34}S/{}^{32}S)_{standard}}\right] * 1000 \qquad [2]$$

The $\delta^{34}S$ data were normalised through calibration against four international standards (IAEA-S-1, IAEA-S-2, IAEA-S-3, NBS 127), providing a linear range in $\delta^{34}S$ between -32.5 ‰ and +22.6 ‰. An internal barium sulphate standard (Acros Organics silver sulphate, Catalogue number: 194070100, lot: A0384698) was analysed throughout the analytical period and produced an average $\delta^{34}S$ value of −18.1 ‰ ± 0.25 (1σ) (n = 14). Analytical uncertainty of $\delta^{34}S$ is typically ±0.2 ‰ for replicate analyses of the international standards. Reproducibility of the sample $\delta^{34}S_{evap}$ data was the same or better. Total sulphur content (wt %) of the samples is calculated as part of the isotopic analysis with the use of an internal standard, sulphanilamide (S = 18.619 %).

4. Results

4.1. Petrography

Samples from Burton Row underwent petrographic analysis and were exclusively chosen from the nodular anhydritic mudstone/siltstone facies (Fig. 3). The majority of the samples have diffuse and irregular boundaries between the anhydrite nodular masses and the surrounding matrix (Fig. 3A, 3B, 3C, 3D, 3F, 3H, 3J). This is particularly apparent in a sample at 599 m depth, where small nodular masses of anhydrite exhibiting a felted texture, surround an adjacent lithic clast (Fig. 3D). The anhydrite nodules largely exhibit felted (Fig. 3A, 3B, 3C, 3D, 3E, 3F, 3G), or felted mixed with fascicular (Fig. 3B, 3H) and granular (3I, 3J), fabrics, defined according to the classification of Maiklem et al. (1969) and Kasprzyk and Ortí (1998). While the felted texture commonly exhibits varied orientations, the elongate crystals are generally not orientated randomly (Fig. 3C, 3D, 3F, 3G, 3H). Particularly strong orientation is observed in a sample at 810 m depth (Fig. 3G). The crystals are commonly smaller and orientated sub-parallel with the nodule margins (3F, 3H). A mixed texture is particularly apparent in an anhydrite nodule at 829.5 m depth, which exhibits mosaic-shape euhedral to subhedral crystals with well-developed boundary faces, alongside lathe-shaped bladed, elongate crystals, exhibiting an aligned-feltic texture (Fig. 3I, 3J).

4.2. Sulphur isotope data

4.2.1. Larne Basin

The $\delta^{34}S_{evap}$ profile of GT-01 Kilroot spans from the lower SSG to the Craiganee Formation of the MMG (Fig. 4). We report $\delta^{34}S_{evap}$ data from Ca-sulphate nodules in the

lower SSG from between 777.6 and 795.4 m depth, that range from +8.7 to +10.5 ‰. $\delta^{34}S_{evap}$ values from veined sulphates of the upper SSG (254.4-255.8 m depth) scatter between +13.2 and +28.9 ‰. From Ca-sulphate nodules of the lowermost Lagavarra Formation, we report $\delta^{34}S_{evap}$ data between +24.8 and +28.5 ‰ within a depth range of 251.2 to 251.9 m. $\delta^{34}S_{evap}$ data from veined sulphate of the Lagavarra Formation range between +18.5 and +26.4 ‰. These data exhibit a general declining trend, from +26.4 ‰ at the base of the Lagavarra Formation at 251.7 m, to +19.3 ‰ just below the Lagavarra-Craiganee boundary at 53.2 m. We report $\delta^{34}S_{evap}$ data from sulphate veins in the overlying Craiganee Formation that exhibit relative stability within a range between +18.3 and +20.4 ‰, between the depths of 26.6 and 49.8 m.

The $\delta^{34}S_{evap}$ data from Cairncastle-2 were derived from nodular calcium sulphates that span a limited stratigraphic range across the SSG-MMG boundary, which is assigned to the early Anisian according to the established lithostratigraphic framework (Fig. 1). We report $\delta^{34}S_{evap}$ data from a depth of 627.5 to 631.2 m within the Ormskirk Sandstone Formation (uppermost SSG), that range between +22.3 and +23.8 ‰ (Fig. 4). In the overlying Lagavarra Formation, we measure $\delta^{34}S_{evap}$ data from +25.03 to +27.1 ‰ (Fig. 4), within the depth range of 622.8 to 625.9 m. We also report a single $\delta^{34}S_{evap}$ value from a gypsum vein at 624.7 m depth within the Lagavarra Formation of +27.3 ‰ (Fig. 4).

The $\delta^{34}S_{evap}$ profile of Carnduff-02 extends from the Larne Halite Member of the Glenstaghey Formation through to the uppermost Knocksoghey Formation (Fig. 4), a stratigraphic interval that likely spans from the latest Anisian through to the Carnian-Norian (Fig. 1). For the Middle Triassic Glenstaghey Formation, we report $\delta^{34}S_{evap}$ data

within a range of +10.5 to +17.6 ‰ (Fig. 4). In general, the $\delta^{34}S_{evap}$ profile for the Glenstaghey Formation is isotopically lighter than the global composite curve for the late Anisian-Ladinian. In the overlying Knocksoghey Formation, we report $\delta^{34}S_{evap}$ values between +9 to +16.4 ‰ (n = 106) (Fig. 4). In the lower Knocksoghey Formation, the $\delta^{34}S_{evap}$ profile exhibits a negative excursion from +15.5 ‰ at the boundary with the underlying Glenstaghey Formation at 536.1 m depth, to +9 ‰ at 501.5 m. Subsequently, the $\delta^{34}S_{evap}$ profile rebounds to +16.4 ‰ at 420.5 m depth (Fig. 4).

4.2.2. East Irish Sea Basin

The $\delta^{34}S_{evap}$ profile of 110/13-8 extends from the lower Leyland Formation, through to the Warton Halite Formation (Fig. 5), spanning a chronostratigraphic range from the Anisian of the Middle Triassic to the Carnian of the Late Triassic according to the established lithostratigraphic framework (Fig. 1). Overall, the $\delta^{34}S_{evap}$ profile exhibits a steady declining trend, from a maximum value of +24.1 ‰ at the base of the Leyland Formation, to a minimum of +14.2 ‰ in the Warton Halite Formation (Fig. 5). For the Leyland Formation, the $\delta^{34}S_{evap}$ data vary between +17.4 and +24.1 ‰, within a depth range of 716.2 to 1243.5 m, with the lowest $\delta^{34}S_{evap}$ value of +17.4 ‰ measured from the Blackpool Mudstone Member at 1130.8 m. According to the global $\delta^{34}S_{evap}$ curve, this is lower than expected for the Middle Anisian. For the overlying Preesall Halite Formation, the $\delta^{34}S_{evap}$ data range between +18.26 and +20.80 ‰ and exhibit a general declining trend from 688.8 to 579.1 m (Fig. 5).

In the Dowbridge Mudstone Formation, the $\delta^{34}S_{evap}$ data vary between +15.8 and +18.3 ‰ (Fig. 5), broadly in line with the global composite $\delta^{34}S_{evap}$ curve for the Ladinian time interval. The declining $\delta^{34}S_{evap}$ trend is less apparent in this formation, with values

decreasing from +18.3 ‰ at the base of the Dowbridge Mudstone at 560.8 m, to +15.8 ‰ in the middle of the formation at 487.7 m. The $\delta^{34}S_{evap}$ values then increase to +16.9 ‰ at the boundary with the overlying Warton Halite Formation at 411.5 m (Fig. 5). Despite this, the $\delta^{34}S_{evap}$ data still fit well within the long-term declining trend exhibited by the overall $\delta^{34}S_{evap}$ profile of 110/13-8. For the Warton Halite Formation, the $\delta^{34}S_{evap}$ data exhibit a declining trend from a maximum $\delta^{34}S_{evap}$ value of +16.9 ‰ at the base of the formation at 381 m, through to +14.2 ‰ at 152.4 m, close to the upper boundary with the Elswick Mudstone Formation (Fig. 5).

4.2.3. Wessex Basin

The $\delta^{34}S_{evap}$ profile reported for the Burton Row borehole provides relatively consistent stratigraphic coverage from the SSG, through to the Blue Anchor Formation of the uppermost MMG (Fig. 5), which spans a chronostratigraphic range between the early Anisian to the early Rhaetian (Fig. 1). For the SSG, we report $\delta^{34}S_{evap}$ data from Ca-sulphate nodules that range between +7.4 and +13.7 ‰, from a depth of 958.7 to 907.8 m, exhibiting a relatively high degree of variability, with no apparent stratigraphic trends (Fig. 4). In the overlying Sidmouth Mudstone Formation, we report $\delta^{34}S_{evap}$ values that range between +6.5 and +12.1 ‰ and exhibit an overall increasing trend from +6.9 ‰ at 897 m depth, near the lower boundary with the SSG, to +11.6 ‰ at 795.9 m. The $\delta^{34}S_{evap}$ data from the Somerset Halite Formation exhibits a relatively large degree of scatter, within a range of +9.8 to +17.4 ‰, between 680.1 and 751.3 m depth, with the most isotopically enriched values occurring between 698 and 712.7 m (Fig. 5). For the overlying Branscombe Mudstone Formation, the $\delta^{34}S_{evap}$ data ranges between +8.5 and +11.3 ‰, from 670 to 615.7 m depth. Between the depths of 607 and 459 m within the

Branscombe Mudstone Formation, the $\delta^{34}S_{evap}$ profile exhibits an increasing trend from +11.6 to +15.6 ‰. In the overlying Blue Anchor Formation, this increasing trend in $\delta^{34}S_{evap}$ continues, reaching a maximum value of +20.5 ‰ at 425.3 m depth (Fig. 5).

5. Discussion

5.1. Preservation of primary $\delta^{34}S_{evap}$ signals

Gypsum precipitation is associated with a minor sulphur isotope fractionation factor ($\Delta^{34}S_{precipitate\text{-}brine}$), with experimental studies reporting a range between +1.6 and +2 ‰ (Thode and Monster, 1965; Holser and Kaplan, 1966; Nielsen, 1978; Raab and Spiro, 1991; Van Driessche et al., 2016). Without further seawater replenishment, the $\delta^{34}S$ of both the brine and precipitate progressively decrease with continued precipitation, however the data available suggest that similar $\Delta^{34}S_{precipitate\text{-}brine}$ values are maintained until the end of the halite stability field (Raab and Spiro, 1991). Thus, it is commonly assumed that the $\delta^{34}S$ of marine calcium sulphates and halite is indicative of the $\delta^{34}S$ of the seawater brines from which they precipitate (Schreiber and Tabakh, 2000). Considering we exclusively sampled calcium-sulphates and halite, it is unlikely that variability exhibited by our $\delta^{34}S_{evap}$ profiles can be attributed to changes in mineralogy alone.

Calcium sulphates are known to undergo a cycle of diagenesis during burial and uplift. This cycle involves the initial precipitation of primary gypsum from concentrated evaporite brines, the subsequent formation of diagenetic anhydrite through the dehydration of primary gypsum during mid to deep burial, and the rehydration of this anhydrite to secondary gypsum during uplift (Murray, 1964; Warren, 1991). The impact of this diagenetic cycle upon the isotopic composition of evaporitic sulphate is poorly

understood (see overview by Ortí et al., 2022). Worden et al. (1997) analysed the $\delta^{34}S_{evap}$ of anhydrite from the Khuff Formation, which has undergone 5000 m of burial, and provide no evidence for any substantial alteration of $\delta^{34}S_{evap}$ due to the generation of diagenetic anhydrite, with the authors suggesting $\delta^{34}S$ of the anhydrite is representative of the primary gypsum from which the anhydrite formed. The impact of diagenetic anhydrite rehydration to secondary gypsum on $\delta^{34}S_{evap}$ has received little direct study, however Triassic secondary gypsum from the Betic Cordillera, southern Spain, display Triassic marine $\delta^{34}S_{values}$ (Ortí et al., 2014) and Eocene diagenetic anhydrite and secondary gypsum largely records seawater $\delta^{34}S$ values while also displaying little offset in $\delta^{34}S_{evap}$ between each other (Carillo et al., 2014).

As stated previously, for this study we sampled both gypsum and anhydrite. In the case of Burton Row, the nodular anhydrite shows little evidence of late-stage diagenesis (Machel and Burton, 1991), with the diffuse boundaries, sub-parallel crystal orientation near the boundaries and felted (and possibly fascicular) fabrics (Fig. 3) associated with displacive growth in the host sediment during near-surface syndepositional diagenetic precipitation (Kasprzyk and Ortí, 1998; Aleali et al., 2013). Considering the above discussion, the available data suggest it is unlikely that the formation of diagenetic anhydrite or the subsequent rehydration to secondary gypsum would have imparted a substantial offset between the $\delta^{34}S$ of sulphate within the original hypersaline brines and the $\delta^{34}S_{evap}$ of the gypsum and anhydrite analysed for this study.

Evaporites can form in terrestrial and marine environments (Warren, 2010). In the prior, the $\delta^{34}S_{evap}$ would not be expected to exhibit a marine signal (see below), with

the isotopically distinct terrestrial sulphate input flux likely imparting a dominant control on the $\delta^{34}S_{evap}$ of evaporitic precipitates (Plàya et al., 2000). While marine evaporites are likely to record a marine $\delta^{34}S_{evap}$ signal, this is not guaranteed. Marine evaporites form in marginal marine environments with potentially varying degrees of hydrologic restriction (Warren, 2010). Local depositional factors can in theory alter an otherwise marine $\delta^{34}S_{evap}$ signal. Such factors include riverine inputs of continental sulphate from weathered pyrite and/or evaporites (Bottrell and Newton, 2006), reservoir effects associated with evaporite precipitation during periods of prolonged restriction (Raab and Spiro, 1991), and microbial sulphur cycling (e.g., microbial sulphate reduction) and subsequent pyrite burial (Bernasconi et al., 2017). Although the $\delta^{34}S$ of evaporitic sulphate appears less susceptible to diagenetic alteration than the $\delta^{34}S$ of carbonate-associated sulphate (Bernasconi et al., 2017; Johnson et al., 2021), diagenetic processes after deposition can offset the $\delta^{34}S$ of sulphate within an evaporite precipitate from the sulphate within the original brine source. Diagenetic effects include the synsedimentary dissolution/precipitation of halite, the replacement of halite with gypsum (and vice versa) (Schreiber and Tabakh, 2000) and microbial sulphate reduction within pore waters below the sediment-water interface (Jorgensen et al., 2019).

Broadly speaking, the $\delta^{34}S_{evap}$ records of Staithes S-20 (Salisbury et al., 2022), 42/28-2 (Salisbury et al., 2023), 110/13-8, GT-01 Kilroot and Carincastle-2 (this study) exhibit excellent reproducibility. The upper Sherwood Sandstone of Cairncastle-2 (+22.30 to +24.94 ‰) and lower Lagavarra Formation of both Cairncastle-2 (+25.03 to +27.10 ‰) and GT-01 Kilroot (+24.84 to +28.46 ‰) (Fig. 4) exhibit $\delta^{34}S_{evap}$ values in line with the global composite $\delta^{34}S_{evap}$ curve for the Early and Middle Triassic for which the upper Sherwood and Lagavarra are assigned. It should be noted that the established

depositional model for the Sherwood Sandstone Group is a fluvial/aeolian system (Ambrose et al., 2014; McKie, 2017), and thus the degree of marine/terrestrial influence is difficult to confidently establish (see section 5.2. for details). The $\delta^{34}S_{evap}$ profile of 110/13-8 from the Leyland Formation to the Warton Halite Formation exhibits a long-term declining trend (+24.09 to +14.09 ‰) (Fig. 5), comparable to that observed in the global composite Middle to Late Triassic $\delta^{34}S_{evap}$ record (see below for details).

Diagenetic fluids are likely to exhibit a high degree of spatial isotopic heterogeneity and will produce a greater degree of $\delta^{34}S$ scatter in rocks that have interacted with diagenetic fluids, limiting the degree of stratigraphic reproducibility in isotope profiles across distinct sedimentary basins (Metzger et al., 2014). In addition, the $\delta^{34}S$ of the riverine sulphate is influenced by the $\delta^{34}S$ of the local bedrock exposed to weathering and is thus likely to vary considerably across distinct sedimentary basins. (Burke et al., 2018). Accordingly, a high degree of stratigraphic reproducibility between temporally equivalent strata across distinct sedimentary basins is generally considered evidence for a global primary seawater signal (Metzger et al., 2014). Thus, the small degree of scatter and/or minor offsets between the $\delta^{34}S_{evap}$ records of Staithes S-20, 42/28-2, 110/13-8, GT-01 Kilroot and Cairncastle-2 may be a product of local depositional and/or diagenetic effects, but the robust correlation between them and the global composite curve appear to suggest that the broad and dominant trends in the $\delta^{34}S_{evap}$ records are a primary signal, with the evaporitic sulphate being derived from a common seawater source. It should of course be noted that the lower data resolution of the $\delta^{34}S_{evap}$ records from GT-01 Kilroot and Cairncastle-2 ensures that any interpretations should be made with greater caution.

5.1.2. The $\delta^{34}S_{evap}$ of secondary fibrous gypsum

The formation of displacive and fibrous gypsum veining is known to form through sulphate remobilisation during the dehydration of gypsum or rehydration of anhydrite, or alternatively through precipitation from connate waters rich in sulphate (Holliday, 1970; Tabakh et al., 1998). Generally, such fibrous sulphate forms in extensional veins (Machel, 1985; Tabakh et al., 1998), or in association with slickensides that occur due to repeated wetting and drying of a sediment body (see Milroy et al., 2019). Fibrous sulphate is present throughout the Lagavarra and Craiganee formations within the drillcore of GT-01 Kilroot (Fig. 4). In general, we report little offset between the $\delta^{34}S_{evap}$ of nodular Ca-sulphates and fibrous gypsum veins and the $\delta^{34}S_{evap}$ of veined sulphate within the Lagavarra and Craiganee formations largely appear to compare well with the global $\delta^{34}S_{evap}$ curve for the early Middle Triassic (Fig. 4). Thus, our $\delta^{34}S_{evap}$ data suggests that in most cases, the remobilisation of sulphate during gypsum vein formation was not accompanied by a noteworthy sulphur isotopic effect. This is in line with the results of Tabakh et al. (1998), who report $\delta^{34}S_{evap}$ and $\delta^{18}O_{evap}$ values from fibrous gypsum that are entirely within the range reported for the evaporites of the Passaic Formation, from which the sulphate within the veins was likely derived.

An exception to this can be seen in gypsum veins within the upper Sherwood Sandstone Group between depths of 254.77 and 255.76 m within GT-01 Kilroot, whereby the $\delta^{34}S_{evap}$ values vary considerably between +13.19 and +28.90 ‰ (Fig. 4). This degree of variability is not a feature of the global composite $\delta^{34}S_{evap}$ curve for the early Middle Triassic (Crockford et al., 2019; Salisbury et al., 2022) and are likely to be a diagenetic $\delta^{34}S_{evap}$ signal. If the veins were formed soon after deposition as slickensides,

as has been observed in the MMG of the Wessex Basin (Milroy et al., 2019), then the enrichments observed in both $\delta^{34}S_{evap}$ may be a product of diagenetic microbial sulphate reduction, which can produce enrichments in the $\delta^{34}S$ of sulphate (Boschetti et al., 2011). However, we cannot confidently confirm whether the veining can be associated with slickensides, and thus if the veins formed long after deposition, then the enrichments could be a product of sulphate recycling during repeated remobilisation (see Moragas et al., 2013).

The sulphate veins within the upper SSG which exhibit lighter $\delta^{34}S_{evap}$ values could reflect a distinction in sulphate source, a different generation of sulphate remobilisation and veining, with lighter $\delta^{34}S_{evap}$ values possibly being closer to those of primary sulphates, or interaction with isotopically light meteoric fluids. In addition, sulphide reoxidation is associated with a relatively small degree of sulphur isotope fractionation (see Fike et al., 2015). Thus, in theory, the reoxidation of sedimentary sulphides during sulphate remobilisation could contribute to the relatively light $\delta^{34}S_{evap}$ values exhibited by some of the gypsum veins in this stratigraphic interval, providing a source of isotopically light sulphate during gypsum vein formation.

As stated, the $\delta^{34}S_{evap}$ of the veins within the overlying Lagavarra Formation appear to match the global curve for the Anisian well, enabling the establishment of a possible correlation scheme. However, while the apparent correlation between these data and the Anisian interval of the global composite is at first view intriguing, it could just be coincidental. This is of course particularly important to consider due to the diagenetic origin of veined gypsum. In addition, the fact that the sulphate has been remobilised ensures that we cannot confidently determine the original stratigraphic

position of the sulphate source, with the remobilised sulphate potentially having travelled along fractures to higher or lower positions within the stratigraphy, as is the case in Watchet, Somerset (Philipp, 2008). This, along with the potential diagenetic alteration of the $\delta^{34}S$ of veined gypsum, preclude their use for stratigraphic correlation.

5.2. $\delta^{34}S_{evap}$ profiles for stratigraphic correlation of the UK Triassic

The $\delta^{34}S_{evap}$ profiles of 110/13-8, Cairncastle-2 and GT-01 Kilroot are presented alongside equivalent $\delta^{34}S_{evap}$ records from Staithes S-20 (Salisbury et al., 2022) and 42/28-2 (Salisbury et al., 2023), as well as the global composite $\delta^{34}S_{evap}$ curve of Salisbury et al. (2022) in Fig. (6). The $\delta^{34}S_{evap}$ correlation schemes between Staithes S-20, 42/28-2, and the global composite $\delta^{34}S_{evap}$ curve were established in Salisbury et al. (2022, 2023). Clear stratigraphic trends are apparent across all the $\delta^{34}S_{evap}$ profiles presented here, even with differences in sampling resolution and stratigraphic coverage (Fig. 6). The principles of sulphur isotope stratigraphy are based upon the assumptions that; (1) the $\delta^{34}S$ of seawater sulphate is homogenous at any one point in geologic time, and (2) trends in $\delta^{34}S_{evap}$ profiles are directly comparable. During correlation, the stratigraphy of distinct sections is assumed to be proportionally equivalent, and each stratigraphic element is assumed to expand or contract at a comparable rate.

For Cairncastle-2, we sampled nodular Ca-sulphates across the boundary between the Sherwood Sandstone Group and Lagavarra Formation (basal MMG), and for GT-01 Kilroot we sampled nodular Ca-sulphates at the base of the Lagavarra Formation. Together, they provide a composite $\delta^{34}S_{evap}$ record across the SSG-MMG boundary in the Larne Basin (Fig. 4). The established position for the upper boundary of the SSG in this region is the earliest Anisian of the lower Middle Triassic (Mitchell, 2004).

Interestingly, our $\delta^{34}S_{evap}$ data from the upper SSG of Cairncastle-2 range from +22.30 to +24.94 ‰ (Fig. 4), which is in line with the $\delta^{34}S_{evap}$ of the global composite curve for the earliest Anisian, as the composite $\delta^{34}S_{evap}$ record abruptly increases, recovering from a negative excursion at the Early-Middle Triassic boundary (Bernasconi et al., 2017; Salisbury et al., 2022). Thus, this would in theory enable correlation between Caincastle-2 and the global composite age curve, placing the upper Sherwood Sandstone Group within the earliest Anisian, in agreement with the established age assignment (Mitchell, 2004).

However, recent work has suggested the presence of an unconformity between the SSG and MMG in the Larne Basin, due to the apparent absence of the Ormskirk Sandstone Formation (English et al., 2024). If correct, the local absence of the upper SSG would ensure that correlating our $\delta^{34}S_{evap}$ data from the SSG of Cairncastle-2 with the global composite $\delta^{34}S_{evap}$ curve across the earliest Anisian is inappropriate. Our $\delta^{34}S_{evap}$ data from the SSG of Cairncastle-2 could instead be correlated to the upward limb of the Early Triassic positive $\delta^{34}S_{evap}$ excursion within the global curve (Bernasconi et al., 2017; Salisbury et al., 2022). However, in doing so the uppermost SSG in the Cairncastle-2 core would then be assigned to the Induan of the earliest Triassic, which would suggest the majority of the Early Triassic is absent in Cairncastle-2, and thus the Larne Basin. This is unlikely as it conflicts with known biostratigraphic data from the region which assigns the middle to upper SSG to the Olenekian, with additional data suggesting the uppermost SSG may extend into the Anisian (Warrington, 1995). The latter would of course also disagree with the placement of an unconformity between the SSG and MMG, as suggested by English et al. (2024), who loosely assign the upper boundary of the SSG to the late Olenekian.

Considering that the suggested presence of an unconformity is based upon the apparent absence of the Ormskirk and not defined by any direct age constraint (see English et al., 2024), the absence of the Ormskirk could instead be a product of lithofacies diachroneity, rather than the presence of an unconformity. In this case, the assignment of the upper SSG as earliest Anisian would remain most reasonable based on our $\delta^{34}S_{evap}$ data, and would conveniently agree with available biostratigraphy (Warrington, 1995).

The apparent preservation of primary seawater $\delta^{34}S$ values from nodular Ca-sulphates within the SSG deserves further discussion. The established depositional model for the SSG is a terrestrial fluvial-aeolian system (Ambrose et al., 2014; McKie, 2017). Thus, the extent of marine influence during the formation of evaporitic material within the SSG is even more uncertain than for the overlying MMG. Despite this, the fact that evaporites at the top of the SSG in Cairncastle-2 exhibit $\delta^{34}S_{evap}$ values in close agreement with those of the global composite $\delta^{34}S_{evap}$ curve during the earliest Anisian, and thus the time interval to which the upper SSG is assigned in the Larne Basin (Mitchell, 2004), is noteworthy and should not be overlooked. Previous work reported $\delta^{34}S_{evap}$ values from the stratigraphically equivalent Buntsandstein of northern Switzerland between +17 and +23 ‰ (Bernasconi et al., 2017). The values at the lower end of this range, between +17 and +18 ‰ from the Kaisten drillcore, are admittedly a little depleted when compared to the global composite, however the values between +20 and +23 ‰ from the Weiach and Schafisheim localities are in line with the global composite for the earliest Anisian (Bernasconi et al., 2017). The authors did not include $\delta^{34}S_{evap}$ data from the Buntsandstein within their global compilation due to concerns regarding possible terrestrial influence.

However, palaeontological and sedimentological evidence exists for at least intermittent marine influence during the deposition of the Sherwood Sandstone and Buntsandstein (Ireland et al., 1978; Polard and Steel, 1978; Heunisch and Röhling, 2016; Szulc, 2019; Becker et al., 2020; Warrington and Pollard, 2021). Recent studies present $\delta^{34}S_{evap}$ records from the SSG from Staithes S-20 (onshore UK) and 42/28-2 (see Salisbury et al., 2022; 2023). The $\delta^{34}S_{evap}$ values fall within the range for established Permian seawater (+9 to +13 ‰; Crockford et al., 2019; Salisbury et al., 2022), with the record of Staithes S-20 rising to ~+17 ‰, seemingly recording the slight rise in $\delta^{34}S_{evap}$ recorded across the PTB (Bernasconi et al., 2017). The authors interpreted this to suggest that towards the basin margins, the base of the SSG in the Cleveland and UK SNS basins is latest Permian in age (Salisbury et al., 2023), while the established framework assigns the SSG to the Early Triassic (Warrington et al., 1980).

Considering the lack of direct biostratigraphic constraint for the position of the PTB in the UK Triassic (Warrington et al., 1980), this is certainly possible, and the excellent correlation between the $\delta^{34}S_{evap}$ records could suggest that the sulphate was derived from a common (likely seawater) source. $\delta^{34}S_{evap}$ values between +8.72 and +10.54 ‰ in a anhydritic siltstone interval of the lower SSG within GT-01 Kilroot of the Larne Basin (Fig. 4) also compare well with the $\delta^{34}S_{evap}$ data reported for the SSG by Salisbury et al. (2022; 2023) (Fig. 6). When viewing the $\delta^{34}S_{evap}$ values from the SSG of GT-01 Kilroot and Cairncastle-2 together, the lower SSG appears to exhibit Permian $\delta^{34}S_{evap}$ values, while the upper SSG appears to exhibit values in line with those for Early and Middle Triassic seawater. This could in theory agree with Salisbury et al. (2022, 2023), potentially providing evidence for a Permian age for at least the lower SSG in the Larne Basin. In addition, the relatively enriched $\delta^{34}S_{evap}$ data from the upper SSG of

Caincastle-2 appear to agree with the biostratigraphy, which suggests the SSG may extend into the Early-Middle Triassic within the Larne Basin (Warrington, 1995). This contrasts with the $\delta^{34}S_{evap}$ records of Salisbury et al. (2022, 2023), which appear to indicate an almost entirely Permian age for the SSG in the Cleveland Basin and UK, SNS. Considering the spatial $\delta^{34}S$ variability exhibited by modern riverine sulphate (Burke et al., 2018), it may be surprising to observe such comparable $\delta^{34}S_{evap}$ values between datasets from geographically distinct sedimentary basins without a common source of seawater sulphate. However, it should be noted that similarly to Salisbury et al. (2022; 2023) we do not specifically determine the extent of marine 'vs' terrestrial influence during evaporite formation, as we have used sulphur isotope data alone, and not in combination with other proxies sensitive to marine 'vs' terrestrial inputs.

Our $\delta^{34}S_{evap}$ profile from nodular Ca-sulphates of GT-01 Kilroot exhibits a declining trend at the base of the Lagavarra Formation, declining from +28.46 to +24.84 ‰ (Fig. 4). The equivalent data of Cairncastle-2 range between +25.03 and +27.10 ‰, and while they do largely exhibit a declining trend, at the top of the $\delta^{34}S_{evap}$ record, the uppermost two datapoints display an increasing trend from +25.03 to +26.01 ‰ (Fig. 4). This, however, could just be considered noise, emphasised by the relatively low data resolution. The $\delta^{34}S_{evap}$ data from the Lagavarra Formation of GT-01 Kilroot and Cairncastle-2 compare well with the global composite $\delta^{34}S_{evap}$ curve for the early Middle Triassic, correlating with the declining $\delta^{34}S_{evap}$ trend established for the Anisian (Fig. 6).

This is in broad agreement with the established stratigraphic framework for the Larne Basin, which assigns the Lagavarra Formation to the Anisian, early Middle Triassic (Mitchell, 2004). The biostratigraphic constraint for this age assignment is based upon a

single Anisian palynomorph, *Guttulapollenites hannonicus*, recovered from the lower Lagavarra Formation (Warrington, 1995). The biostratigraphy is thus of low resolution, and while the palynomorph *Cycloverrutriletes presselensis* constrains the underlying SSG to the Early Triassic (Warrington, 1995), the available biostratigraphic data is insufficient to confidently determine the chronostratigraphic position of the SSG-MMG boundary. Thus, through correlation with the global $\delta^{34}S_{evap}$ of Salisbury et al. (2022), our $\delta^{34}S_{evap}$ profiles of GT-01 Kilroot and Cairncastle-2 provide further confirmation that the lowermost MMG in the Larne Basin can be placed within the Anisian (Fig. 6). Admittedly, our $\delta^{34}S_{evap}$ records for the lower MMG provide limited stratigraphic coverage (hence the dashed correlation lines on Fig. (6), as nodular and bedded evaporites do not extend beyond the lower Lagavarra Formation in GT-01 Kilroot and Cairncastle-2. Future studies concerning the lower MMG in the Larne Basin should endeavour to generate $\delta^{34}S_{evap}$ profiles with a higher stratigraphic coverage, facilitating the establishment of more confident correlation schemes and tighter age assignment.

The $\delta^{34}S_{evap}$ profile of well 110/13-8 expands the coverage of our $\delta^{34}S_{evap}$ compilation to include the evaporites of the East Irish Sea Basin (EISB). Here we sampled drill cuttings, due to the limited number of complete drillcores available from offshore wells. Through comparison with the global composite $\delta^{34}S_{evap}$ curve, we have chosen six points in the $\delta^{34}S_{evap}$ records, defining five packages of isotopically distinct coeval strata (Fig. 6). The correlation scheme we propose is based on both the $\delta^{34}S_{evap}$ records, as well as the available biostratigraphic data.

The $\delta^{34}S_{evap}$ profile of 110/13-8 exhibits the general declining trend observed in the global composite $\delta^{34}S_{evap}$ curve for the Middle and Late Triassic (Salisbury et al.,

2022). The steep decline in the $\delta^{34}S_{evap}$ profile at the base of the Leyland Formation, enables us to assign the Ross Halite Member and the lower Blackpool Mudstone Member to the early-middle Anisian. Although it should be noted that a value of +17.40 ‰ at 1130 m is lighter than the composite curve (Fig. 5, 6), which could be a product of terrestrial influence or caving. The biostratigraphy for the base of the MMG in the EISB is controversial, with Naylor et al. (1993) reporting Early Triassic palynomorphs from the base of the MMG. This would appear to contradict with our $\delta^{34}S_{evap}$ correlation scheme and other biostratigraphy reports which cite Anisian age palynomorphs at the same stratigraphic interval in the EISB (Geochem Group, 1992, biostratigraphic report) and equivalent strata of the adjacent onshore Lancashire region (Warrington *in* Wilson and Evans, 1990). When viewing the biostratigraphy alone, this would suggest that the Early Triassic palynomorphs reported by Naylor et al. (1993) were a product of the reworking, or that an unexpected degree of lithofacies diachroneity exists for the SSG-MMG boundary within the MMG across the EISB and onshore Lancashire.

However, the $\delta^{34}S_{evap}$ profile of 110/13-8 provides further confirmation to the majority of the biostratigraphic data, which implies an Anisian age for the lowermost MMG in the EISB. Interestingly, several of the palynomorphs reported by Naylor et al. (1993) from the base of the MMG (*Densosporites nejburgii* and *Endosporites papillatus*) are thought to extend into the Anisian (Johnson et al., 1994) and may therefore be present at their youngest expression. Thus, when viewing our $\delta^{34}S_{evap}$ profile alongside the majority of the available biostratigraphic data, an Anisian age for the base of the MMG in the EISB is most reasonable. This demonstrates how $\delta^{34}S_{evap}$ profiles can enable chronostratigraphic constraint at a higher resolution than sparse fossil content,

providing further confirmation to biostratigraphic age assignments and resolve apparent conflicts between biostratigraphic datasets.

We have assigned the entirety of the Leyland Formation and the Preesall Halite Formation to the Anisian (Fig. 6), condensing ~740 m of strata into a ~3.1-million-year time interval. Based upon the $\delta^{34}S_{evap}$ records, it would be appealing to extend the Preesall Halite Formation into the Ladinian, however this would conflict with known biostratigraphic data (Jackson and Johnson, 1996) and the established stratigraphic framework, which cites a general lack of halite within northwest Europe during the Ladinian (Feist-Burkhardt et al., 2008; McKie, 2017). Although direct biostratigraphic constraint is limited in the EISB, Anisian palynomorphs have been recovered from the Coat Walls Mudstone, onshore Lancashire, which is broadly equivalent to the Dowbridge Mudstone Formation of the EISB (Jackson and Johnson, 1996). Thus, assuming this biostratigraphic framework can be applied to the adjacent EISB, the Anisian is the most appropriate upper age limit for the Preesall Halite Formation.

However, due to the paucity of direct biostratigraphic constraints within the EISB, the placement of the lithostratigraphic boundary between the Preesall Halite and Dowbridge Mudstone formations at the Anisian-Ladinian time boundary by Jackson and Johnson (1996) is likely arbitrary, as the biostratigraphy is too poorly resolved to enable tight age constraint around this lithostratigraphic boundary. Thus, in theory, the Preesall Halite could extend into the Ladinian, however our $\delta^{34}S_{evap}$ data alone is insufficient for challenging the established stratigraphic framework. In addition, while large scale marine flooding occurred across northwest Europe during the Anisian, evidence for changes in climate and a greater degree of hydrologic restriction between the EISB and

Tethyan marine waters during the Ladinian (McKie, 2017) suggests large-scale marine halite deposition within the EISB during this period is unlikely. A terrestrial halite deposit is certainly possible, however our $\delta^{34}S_{evap}$ data from the Preesall Halite fall within the range expected for Middle Triassic seawater (Fig. 6), implying a likely marine origin and thus making an Anisian age more reasonable.

Therefore, here we choose to confine the Leyland and Preesall Halite formations to the Anisian, as this enables a valid $\delta^{34}S_{evap}$ correlation between the $\delta^{34}S_{evap}$ profile of 110/13-8 and the global composite of Salisbury et al. (2022), while avoiding any disagreement with the available biostratigraphy (Jackson and Johnson, 1996) and the established stratigraphic framework and depositional history of northwest Europe (McKie, 2017). Further studies should aim to sample the MMG at high resolution from additional drillcore across the EISB, to confirm the reproducibility of our $\delta^{34}S_{evap}$ data, and potentially provide tighter age constraint for lithostratigraphic boundaries.

The $\delta^{34}S_{evap}$ data for the Dowbridge Mudstone Formation consists of only five datapoints across 150 m of strata (Fig. 5), precluding the establishment of a confident correlation scheme based upon the $\delta^{34}S_{evap}$ data alone. For the overlying Warton Halite Formation, the $\delta^{34}S_{evap}$ is better resolved (Fig. 5), likely reflecting a greater abundance of evaporitic material in a dominantly halitic interval. Biostratigraphy of the onshore Lancashire region includes palynomorphs *Retisulcites perforates*, *O. pseudoalatus*, and *Echinitosporites iliacoides*, from the Breckells Mudstone (Warrington *in* Wilson and Evans, 1990). This formation is broadly equivalent to the upper Dowbridge Mudstone and lower Warton Halite of the EISB (Jackson and Johnson, 1996). All three palynomorphs are assigned an age range beginning in the Ladinian, while *R. perforates*

and *E. iliacoides* are thought to extend from the Ladinian into the Carnian (Warrington *in* Wilson and Evans, 1990; Kürschner and Herngreen, 2010). Thus, we have assigned the Dowbridge Mudstone Formation an age range from the base of the Ladinian through to the early Carnian (Fig. 6), which is marginally distinct from that of Jackson and Johnson (1996), who assign the entirety of the Dowbridge Mudstone to the Ladinian. Our $\delta^{34}S_{evap}$ data from the Dowbridge Mudstone compare well with the global composite $\delta^{34}S_{evap}$ curve for the Ladinian-early Carnian time interval, and thus suggest the age model informed by the biostratigraphy is valid. However, the relatively low resolution of our $\delta^{34}S_{evap}$ data from the Dowbridge Mudstone ensures it is difficult to establish confidant age calibration based upon isotope data.

For the overlying Warton Halite Formation, we have assigned an age range from the early to the late Carnian (Fig. 6). The $\delta^{34}S_{evap}$ data we present for the Warton Halite ranges from +14.17 and +16.91 ‰, and although it exhibits a steeper declining trend than the global composite $\delta^{34}S_{evap}$ curve, it does fall within the $\delta^{34}S$ range established for Carnian seawater sulphate (Fig. 6). The relative stability exhibited by the composite $\delta^{34}S_{evap}$ curve for the Late Triassic limits the confidence at which correlation schemes can be established. In theory, the $\delta^{34}S_{evap}$ data for the Warton Halite in 110/13-8 could be correlated with any point in the global composite from the Carnian to the late Norian.

The available biostratigraphy is particularly sparse for the Late Triassic of the EISB but does provide additional limited age constraint. Jackson and Johnson (1996) report assemblages containing one or more of *Camerosporites secatus*, *Retisulcites perforatus*, *Ovalipollis pseudoalatus* and *Echinitosporites iliacoides* within the Dowbridge, Warton and Elswick formations, ranging from Ladiniain to Rhaetian in age (Kürschner and

Herngreen, 2010). Jackson and Johnson (1996) do not provide details regarding the location or stratigraphic position of the palynomorphs but assign the Warton Halite to the Carnian and the Elswick Formation to the Carnian-Norian. Here, we apply this age model to our dataset, as our $\delta^{34}S_{evap}$ data enable a valid correlation within the constraints of this age model and are currently insufficient to challenge the established stratigraphic framework. The correlation for the upper boundary of the Warton Halite is drawn as a dashed line in Fig. (6), as the biostratigraphic data are too poorly resolved to tightly constrain its' chronostratigraphic position, and as stated, the $\delta^{34}S_{evap}$ data from this formation could be stretched further into the Late Triassic. Thus, the placement of the boundary between the Warton Halite and Elswick formations is currently uncertain, lacking age calibration.

With regards to Carnduff-02 of the Larne Basin and Burton Row of the Wessex Basin, the $\delta^{34}S_{evap}$ profiles are offset from the global composite $\delta^{34}S_{evap}$ for the Middle-Late Triassic in terms of absolute $\delta^{34}S_{evap}$ values and stratigraphic trends (Fig. 7). These isotopic offsets may reflect a non-marine $\delta^{34}S_{evap}$ signal (see below) and preclude the application of the Carnduff-02 and Burton Row $\delta^{34}S_{evap}$ profiles for stratigraphic correlation and age calibration. Thus, the age models we apply to the sampled intervals from Carnduff-02 and Burton Row are reliant upon pre-existing stratigraphic data for age calibration. Due to the low-resolution of the available biostratigraphic data, the age calibration applied here is poorly constrained, and thus the correlation lines in Fig. (7) are dashed to emphasise the uncertainty associated with the age calibration.

For Carnduff-02, the age calibration is dependent upon available biostratigraphic data (see above for details). Miospore assemblages indicate an Anisian age for the

Lagavarra and Craiganee formations (Warrington, 1995; Mitchell, 2004). Miospore assemblages from the overlying Glenstaghey Formation sampled here for $\delta^{34}S_{evap}$ analysis suggest an Anisian to Ladinian age (Warrington, 1995; Mitchell, 2004). Thus, we stretch the $\delta^{34}S_{evap}$ record for the Glenstaghey Formation from the late Anisian through to the late Ladinian (Fig. 7). Miospores from the Knocksoghey Formation suggest a minimum age of Ladinian, with the formation possibly extending into the Carnian (Warrington, 1995). Accordingly, we have assigned the Knocksoghey Formation to the late Ladinian-early Carnian (Fig. 7). Little direct palaeontological age constraint is available for the upper Knocksoghey (Warrington, 1995), and therefore the $\delta^{34}S_{evap}$ data for this formation could, in theory, be stretched further unto the Late Triassic. However, our $\delta^{34}S_{evap}$ data does not refute or confirm this, and thus we apply a more conservative age assignment.

The age assignment we apply to Burton Row is based upon both biostratigraphy and magnetostratigraphy. Recent magnetostratigraphic data from the MMG of south Devon suggest a Ladinian age (Hounslow and Gallois, 2023), which is compatible with available biostratigraphic data which suggests the underlying SSG is Anisian-age (Benton, 1997; Spensor and Storrs, 2002), and magnetostratigraphy of the SSG which indicates an Anisian-Ladinian age for the SSG-MMG boundary within the region (Hounslow and McIntosh, 2003). Accordingly, we have assigned the base of the Sidmouth Mudstone sampled here to the latest Anisian (Fig. 7). Biostratigraphic data imply a Julian age for the upper Sidmouth Mudstone (Baranyi et al., 2019), broadly in line with magnetostratigraphy (Hounslow and Gallois, 2023). Thus, we stretch the $\delta^{34}S_{evap}$ profile for the Sidmouth Mudstone from the latest Anisian through to the earliest Carnian (Fig. 7).

We assign the overlying Somerset Halite Formation to the Carnian (Fig. 7), in line with miospore assemblages from the Somerset Halite and equivalent halitic strata within the region (Warrington, 1980; Warrington *in* Whittaker and Green, 1983). Carnian-age miospores from the Dunscombe Mudstone Formation (Warrington, 1971; Baranyi et al., 2019) and the base of the overlying Branscombe Mudstone Formation (Baranyi et al., 2019) suggest that the boundary between the Somerset Halite Formation and the overlying Sidmouth Mudstone could be placed within the Carnian. However, magnetostratigraphy from the Dunscombe Mudstone suggests it should extend to the earliest Norian, with the authors questioning the accuracy of the Carnian age assignment for the reported miospores (Hounslow and Gallois, 2023). Considering the Somerset halite is viewed as broadly equivalent to the Dunscombe Mudstone (Howard et al., 2008), we could, in theory, assign the top of the Somerset Halite to the earliest Norian based upon the magnetostratigraphy. However, magnetostratigraphy has not been applied to the Somerset Halite Formation, and no direct constraint is available for the age of the upper boundary with the Branscombe Mudstone Formation. Thus, we apply the age model suggested by the available miospore assemblages from the Somerset Halite Formation and equivalent halite units in the region, restricting the Somerset halite to the Carnian (Fig. 7).

Rhaetian-age miospores from the Burton Row borehole place the Norian-Rhaetian boundary within the lowermost Blue Anchor Formation (Warrington *in* Whittaker and Green, 1983) (see above) and the overlying Blue Anchor Formation is well constrained to the Rhaetian (Warrington et al., 1995; Warrington, 1997). Considering this, we assign the Branscombe Mudstone Formation an age range from the latest Carnian through to the earliest Rhaetian (Fig. 7). Magnetostratigraphy from Devon

suggests two possible stratigraphic positions for the placement of the Norian-Rhaetian boundary, one of which, NRB1, places the Rhaetian boundary uppermost Haven Cliff Mudstone Member (Hounslow and Gallois, 2023), a local subdivision of the uppermost Branscombe Mudstone Formation (Gallois, 2001). Thus, our placement of the Rhaetian boundary within the uppermost Branscombe Mudstone Formation is broadly in line with NRB1 proposed for Devon, SW England (see Hounslow and Gallois, 2023).

Future work should endeavour to further apply evaporite-based sulphur isotope stratigraphy to the UK Triassic, to better assess the reproducibility of our $\delta^{34}S_{evap}$ profiles and expand the geospatial coverage of the $\delta^{34}S_{evap}$ record, providing further chronostratigraphic constraint to the UK Triassic. In addition, $\delta^{34}S_{evap}$ stratigraphy could be employed in combination with other stratigraphic methods, such as organic carbon isotope stratigraphy (e.g., Hesselbo et al., 2002; Miller et al., 2017; Caruthers et al., 2018; Baranyi et al., 2019; Hounslow et al., 2022) and magnetostratigraphy (e.g., Hounslow and McIntosh, 2003; Hounslow et al., 2022; Zhang et al., 2022; Hounslow and Gallois, 2023). When applied alongside evaporite-based sulphur isotope stratigraphy, such methods could help to refine $\delta^{34}S_{evap}$-based correlations and enable tighter age constraint, while also providing a means of stratigraphic correlation under circumstances where $\delta^{34}S_{evap}$ data fail to exhibit a seawater signal, as is the case for Carnduff-02 and Burton Row (see below).

5.3. Marine influence during deposition of the Mercia Mudstone Group

The origin and depositional environment of the Mercia Mudstone Group have been widely debated, with the degree of terrestrial or marine influence being poorly constrained (Wills, 1970; Warrington et al., 1980). Some have suggested that the volume

of salt present within the Mercia Mudstone Group is indicative of marine deposition (Evans et al., 1968; Ruffell and Shelton, 1999). In line with this interpretation, Warrington (1970b) suggested deposition within an epeiric hypersaline sea, likely fed by Tethyan seawater. However, it is common for the halites to exhibit stratigraphic separation from carbonates and calcium sulphates in the MMG, distinct from the cyclic arrangement of carbonates and evaporites in the marine late Permian Zechstein (Tucker, 1991), which has led some to question an entirely marine origin (Wills, 1970). Accordingly, some posit that deposition occurred within a terrestrial playa lake system (Tucker, 1977; Andeskie et al., 2018; Milroy et al., 2019), while others propose periodic flooding of peneplains or inland lake systems by seawater (Wills, 1970; Arthurton, 1980; Jackson et al., 1995).

As previously discussed, marine fossil groups have been recovered from the MMG across multiple UK sub-basins, possibly suggesting at least intermittent marine inundation (Warrington, 1970b; 1974; 1995; 1997; Wilson, 1990; 1993; Warrington *in* Wilson and Evans, 1990; Jackson et al., 1995; Mitchell, 2004; Ambrose and Wakefield, 2015; Baranyi et al., 2019; Warrington and Pollard, 2021). However, an abundance of fossil content associated with terrestrial flora and fauna (Warrington, 1970b; 1974; 1995; 1997; Warrington *in* Whittaker and Green, 1983; Earp and Taylor, 1986; Warrington *in* Wilson and Evans, 1990; Naylor et al., 1993; Johnson et al., 1994; Jackson and Johnson, 1996; Baranyi et al., 2019; Dawson et al., 2022) appear to contradict with a marine depositional model implied by the marine fossil groups.

It can be particularly difficult to confidently distinguish marine vs terrestrial deposition for ancient evaporite deposits using sedimentological and palaeontological

observations alone (Leitner et al., 2023), with geochemical methods likely being required to definitively determine the sources of the original water feeding the evaporite brines (Playà et al., 2000; Schreiber and Tabakh, 2000). Initial stable isotope data ($\delta^{34}S_{evap}$, $\delta^{13}C_{carb}$, $\delta^{18}O_{carb}$) suggest both a marine and non-marine origin for the evaporites in Staffordshire and Nottinghamshire, depending on location and formational subdivision (Taylor, 1983). Recent studies report high-resolution $\delta^{34}S_{evap}$ profiles for the MMG from the Cleveland and UK SNS basins, and through comparison with the Triassic seawater $\delta^{34}S_{evap}$ age curve, suggest a consistent marine sulphate source throughout the deposition of the MMG in these locations (Salisbury et al., 2022; 2023). Variability in Mg^{2+} concentrations, $\delta^{18}O_{carb}$ values and illite clays in the MMG of south-west Britain have been interpreted to reflect changes in the degree of marine or terrestrial influence, with concomitant increases in Mg^{2+} and $\delta^{18}O_{carb}$ indicating marine water inputs (Leslie et al., 1993). However, others have favoured a diagenetic model for the origin of the Mg-clays involving terrestrial groundwaters (Wright and Sandler, 1994).

Interestingly, high-resolution $\delta^{34}S_{evap}$ profiles presented here from the MMG of Carnduff-02 (Larne Basin) and Burton Row (Wessex Basin) do not compare well with the global composite $\delta^{34}S_{evap}$ age curve (Fig. 7). It is possible that the lack of stratigraphic reproducibility in $\delta^{34}S$ between Carnduff-02, Burton Row and the global curve suggests the $\delta^{34}S_{evap}$ data of the cores sampled are recording a dominantly non-marine $\delta^{34}S$ signal, with the terrestrial input flux providing sulphate which is isotopically distinct (usually lighter) from the $\delta^{34}S$ of seawater sulphate (Bottrell and Newton, 2006; Burke et al., 2018).

As detailed above, biostratigraphic constraints suggest an Anisian to Ladinian-Carnian age (Warrington, 1995) for the interval of the MMG sampled from Carnduff-02. Our $\delta^{34}S_{evap}$ data, with the exception of the upper Knocksoghey Formation, exhibit a consistently lighter sulphur isotopic composition and do not record the downward $\delta^{34}S_{evap}$ trend observed in the global composite during the Anisian-Ladinian (Fig. 7). For the Glenstaghey and lower Knocksoghey formations we report a relatively stable $\delta^{34}S_{evap}$ record with values between +9.0 and +17.6 ‰, while the global composite $\delta^{34}S_{evap}$ curve exhibits a general decline from +19.8 to +12.3 ‰ (Fig. 7). It is likely that the offset between our $\delta^{34}S_{evap}$ profile of Carnduff-02 and the global composite age curve reflects the input of terrestrial sulphate derived from riverine systems and groundwater. This is in line with miospore assemblages associated with terrestrial vegetation (Warrington, 1995), and the sedimentological evidence for terrestrial deposition and subaerial exposure (Mitchell, 2004; Andeskie et al., 2018).

Previous authors have suggested that the deposition of thick halite bodies, particularly the Larne Halite Member of the Glenstaghey Formation, likely required marine water inputs (Ruffell and Shelton, 1999). The Triassic rift basins within which deposition of the MMG occurred were likely sub-sea level (McKie and Williams, 2009), which would have facilitated at least intermittent seawater inundation (McKie, 2017), potentially explaining the presence of marine fossil groups in the MMG of the Larne Basin (Warrington, 1995). However, when viewing all the available sedimentological and palaeontological data, along with our $\delta^{34}S_{evap}$ profile, a largely terrestrial depositional regime seems most reasonable. Thus, it is likely that the deposition of the evaporites in the Glenstaghey and Knocksoghey formations occurred within a dominantly terrestrial saline lake environment, as suggested by Andeskie et al., (2018). Intermittent marine

inundation is certainly possible and could account for an apparent contradiction between the sedimentological evidence for terrestrial deposition (Andeskie et al., 2018), the recovery of miospores form terrestrial flora, and the presence of marine fossils (Warrington, 1995).

However, it should be noted that marine microfossils do not necessarily confirm direct marine influence. Some authors have proposed that marine microfossils within the evaporitic MMG may be aeolian-sourced, transported within aerosols from down-wind marine evaporite systems (Hounslow and Ruffell, 2006; Baranyi et al., 2019), such as the southern North Sea where there is an abundance of marine evaporites (Hounslow and Ruffell, 2006). Considering the lack of a discernible marine signal in the $\delta^{34}S_{evap}$ profile of Carnduff-02 (Fig. 7), an aeolian source for the marine microfossils in the MMG of the Larne Basin may be most appropriate. Alternatively, it is conceivable that the frequency of marine inundation events decreased with distance inland and therefore the Larne Basin experienced very few marine inundations relative to freshwater inputs as it was at the inland limit within the rift system. In this case, the marine fossils could still represent direct marine inundations, with their scarcity reflecting the infrequency of direct marine ingress. Either way, our sulphur isotope data suggest marine influence was likely restricted and transient, ensuring that the marine sulphate input flux was sufficiently limited to prevent a marine $\delta^{34}S_{evap}$ signal from being imparted upon the stratigraphy, with the $\delta^{34}S_{evap}$ signal being overwhelmed by terrestrial sulphate inputs.

In theory, marine inundation could account for an increase in $\delta^{34}S_{evap}$ observed in the upper Knocksoghey formation, with values ranging between +13.7 and +16.4 ‰, in line with the global $\delta^{34}S_{evap}$ curve during the early Carnian (Fig. 7). However, microbial

sulphate reduction in a hydrologically restricted basin could also lead to isotopic enrichment (Hardie, 1984), ensuring that the observed increase in $\delta^{34}S_{evap}$ can only be cautiously attributed to marine inundation based upon sulphur isotope data alone.

The Mercia Mudstone Group of the Wessex Basin exhibits less palaeontological evidence for marine influence than the Larne Basin. Marine acritarchs have been recovered from the MMG in Worcestershire (Warrington, 1967) but have scarcely been recovered further south. Recent work from the Wessex Basin reports marine acritarchs (*Micrhystridium* sp.) from the Arden Sandstone Member of the MMG (Baranyi et al., 2019), which is possibly associated with the Carnian Pluvial Event (Burley et al., 2023) and may be broadly time equivalent to the Somerset Halite Formation (Howard et al., 2008). Baranyi et al. (2019) also report freshwater algae (*P. moesellanum*) from the stratigraphically equivalent Dunscombe Mudstone Formation, which would appear to conflict with the marine acritarchs. Bivalves, brachiopods and shark teeth have been reported from the Arden Sandstone further north in Worcestershire, but in many cases, it could not be definitively established as to whether they are marine or aquatic species (Old et al., 1991). Overall, most of the fossil content recovered from the region are miospore assemblages from terrestrial vegetation (Warrington *in* Whittaker and Green, 1983; Warrington, 1997).

Our $\delta^{34}S_{evap}$ profile from Burton Row fails to display any trends that are comparable with the global composite $\delta^{34}S_{evap}$ curve. In fact, whilst the global record exhibits a general decline through the Middle and much of the Late Triassic (Salisbury et al., 2022), the $\delta^{34}S_{evap}$ profile of Burton Row displays an increasing trend with stratigraphic height (Fig. 7). This of course precludes correlation with geographically

distinct and temporally equivalent evaporites, while suggesting a disconnection between the evaporites of the Wessex Basin and the seawater sulphate reservoir. This is in line with the generally established model for the origin of the MMG in south-west Britain, whereby deposition took place within a terrestrial playa lake system (Tucker, 1977; Milroy and Wright, 2000; Porter and Gallois, 2008; Milroy et al., 2019; Dawson et al., 2022). For the depth interval of 897 to 795.9 m within the Sidmouth Mudstone Formation, our $\delta^{34}S_{evap}$ data range from +6.5 to +12.1 ‰. Thus, at this depth range, evaporites exhibit $\delta^{34}S_{evap}$ values that are isotopically lighter than the global composite $\delta^{34}S_{evap}$ curve during the Middle and Late Triassic (Fig. 7), possibly reflecting the isotopic influence of isotopically light riverine and groundwater sulphate sources.

Between the depths of 751.3 and 680.1 m, the $\delta^{34}S_{evap}$ profile for the Somerset Halite Formation overlaps with the global composite during the Carnian, whilst exhibiting a greater degree of $\delta^{34}S$ variability, fluctuating between extremes of +9.8 and +17.4 ‰ that are beyond the established range for Carnian seawater (Fig. 7). It is plausible that the rise in $\delta^{34}S_{evap}$ from values lighter than the seawater curve in the underlying Sidmouth Mudstone Formation to higher $\delta^{34}S_{evap}$ values in the Somerset Halite Formation could reflect an increase in the degree of marine influence during halite deposition, with the $\delta^{34}S_{evap}$ variability possibly reflecting a mixed terrestrial-marine isotopic signal. The presence of thick bedded halite could certainly suggest a marine origin for the Somerset Halite Formation, as the hydrochemistry of marine brines would provide an abundant source of NaCl (Warren, 2010).

Previous authors have struggled to reconcile the presence of large Carnian-age halite deposits and a lack of evidence for either a marine water source in the SPB or

marine flooding through the known possible ingress routes for seawater brines (Hounslow and Ruffell, 2006). During the Carnian, the rift network underwent further expansion, which likely established additional routes for possible Tethyan seawater ingress into the continental interior (McKie, 2017). Rifting along the Atlantic and Biscay regions incited the formation of sub-sea level rift basins that extended from the Bay of Biscay through to the UK Western Approaches (McKie, 2017). Halite bodies appear to follow these rift basins, extending from northern Spain, through the Bay of Biscay into the UK Western Approaches (Chapman, 1989; McKie, 2017). It has been suggested that these halite deposits were formed from marine brines as Tethyan seawater migrated along the south through the chain of sub-sea level rift basins (McKie, 2017). In theory, marine brines may have continued migrating into the Wessex Basin, EISB and west of Ireland.

However, apart from the halite bodies themselves, little direct sedimentological evidence for marine flooding through Carnian rift basins is known (McKie, 2017). In addition, the Carnian-age halites extending from the Biscay region and into the UK Western Approaches have not been subjected to detailed geochemical study to constrain the brine source. Furthermore, although our $\delta^{34}S_{evap}$ profile of 110/13-8 suggests consistent marine sulphate inputs during deposition of the Carnian Warton Halite Formation (Fig. 6), our $\delta^{34}S_{evap}$ profile of the Somerset Halite does not exhibit a clear marine $\delta^{34}S$ signal (Fig. 6) and thus does not provide direct evidence for the northward migration of Tethyan seawater brines form the Bay of Biscay through to the Wessex Basin.

As stated, the variability exhibited by our $\delta^{34}S_{evap}$ data from the Somerset Halite Formation could reflect a mixed sulphate input flux, with different sulphate sources having distinct isotopic compositions (Bottrell and Newton, 2006), thus contributing to the scatter in $\delta^{34}S_{evap}$. The input of marine sulphate via the aeolian transport of salt aerosols from marine-fed evaporite systems in adjacent basins has been suggested previously (Hounslow and Ruffell, 2006) to reconcile the presence of large Carnian halite bodies with a lack of direct evidence for seawater ingress. This process has been observed to occur readily in modern saline lake settings, such as Lake Eyre in Australia and Bristol Dry Lake in California (Clark and Smith, 1981; Dare-Edwards, 1984; Rosen, 1991). It is likely that an aerosol source of sulphate was active during the deposition of the Somerset Halite, possibly through deflation of evaporites in seawater-fed saline lakes within the North Sea (Hounslow and Ruffell, 2006). Despite this, it should be noted that while our $\delta^{34}S_{evap}$ data allow for this input flux, they do not directly confirm it. In addition, it is not possible to confidently constrain the magnitude of the aerosol input flux with the data available, however considering the volume of salt present in Carnian halite deposits, it seems unlikely that the aerosol flux could have been the sole input of salt.

Inputs of sulphate via groundwater seepage and fluvial systems would have certainly contributed during the deposition of the Somerset Halite, just as we suggest for the anhydritic mudstones above and below the halitic interval in Burton Row, contributing isotopically light sulphate to the local sulphate pool. The bedded halite and mudstones layers would have likely required multiple flooding events (Hounslow and Ruffell, 2006), which could have been achieved through riverine flooding, similarly to contemporary saline lake systems, Bristol Dry Lake and Lake Eyre (Handford, 1982;

Magee et al., 1995). Halite-rich beds in the Wessex Basin are associated with depressions related to reactivated Variscan faults (Gallois, 2004) and could have formed as salt pans in the centre of inland playa systems, as proposed for the Permian Eden Shales (Worley, 2005). This would seemingly account for the lack of a consistent marine $\delta^{34}S_{evap}$ signal. However, the distribution of stratigraphically equivalent halite-rich beds has been confirmed within the centre of the Somerset Basin and across the Wessex Basin (Gallois, 2004) and thus, the halite in south-west Britain covers a far greater spatial extent when compared to the halite of the Eden Shales. Despite controversy regarding the specific routes for seawater ingress during the Carnian, it is conceivable that marine waters could intermittently flood a terrestrial playa lake system but be insufficient to impart a consistent marine $\delta^{34}S_{evap}$ signal (see Legler and Schneider, 2008).

In the case of the Somerset Halite Formation in Burton Row, the scatter we observe in the $\delta^{34}S_{evap}$ data may reflect a mixed isotopic signal, with contributions from aerosols, fluvial flooding, groundwater seepage, and direct marine flooding. With the data available, the relative magnitude of each flux cannot yet be confidently ascertained. However, considering the size of the seawater sulphate reservoir, the degree of scatter in $\delta^{34}S_{evap}$ profile would suggest that inputs of marine sulphate were insufficient in magnitude and/or consistency to maintain a consistent marine signal during the deposition of the Somerset Halite Formation.

Between the depths of 670 and 574.5 m within the Branscombe Mudstone Formation, the $\delta^{34}S_{evap}$ data of Burton Row range between +8.53 to +11.9 ‰ (excluding an outlier of +15.8 ‰) and are thus isotopically lighter than the global composite $\delta^{34}S_{evap}$ curve for the Late Triassic (Fig. 7). The dominant facies at this stratigraphic depth interval

are red/brown mudstones and siltstones with abundant anhydrite nodules (Fig. 4). The nodules would have likely formed displacively within the sediment body, near the top of the water table (Warren, 1991; Kasprzyk and Ortí, 1998). A comparable facies is reported from the Twyning drillcore of the Wessex Basin (Milroy et al., 2019). As stated, Milroy et al. (2019) interpret the MMG of the Wessex basin to have formed within a non-marine continental setting but did not apply any stable isotope systems. In some cases, nodular anhydrite can form within terrestrial playa settings in a manner that is indistinguishable to anhydrite which forms in marine sabkhas (Kendall, 1978), emphasising the need for geochemical investigation. The offset between our $\delta^{34}S_{evap}$ data from the Sidmouth Mudstone and Branscombe Mudstone (670 and 574.5 m) formations, and the global composite $\delta^{34}S_{evap}$ curve could be a product of hydrologic disconnection with the seawater sulphate reservoir. Thus, our $\delta^{34}S_{evap}$ data from the Sidmouth Mudstone and Branscombe Mudstone formations provide further confirmation to previous sedimentological analyses that suggested a possible terrestrial origin for the MMG in south-west Britain but lacked the geochemical data necessary for a more confidant determination (Tucker, 1977; Milroy and Wright, 2000; Porter and Gallois, 2008; Milroy et al., 2019; Dawson et al., 2022).

It should be noted that a comparable anhydritic mudstone/siltstone facies is present within the MMG of the Staithes S-20 drillcore between approximately 530 and 415 m depth (Fig. 6). Despite the lithologic similarities, the Staithes S-20 $\delta^{34}S_{evap}$ profile exhibits a consistent marine signature, confirmed through correlation with another $\delta^{34}S_{evap}$ record from equivalent strata within the region (Salisbury et al., 2023), as well as the global composite $\delta^{34}S_{evap}$ curve (Salisbury et al., 2022).

In addition, between the depths of 640 and 516 m in Staithes S-20, we observe a facies of thinly laminated silty mudstones with dolomite interbeds and occasional anhydrite nodules and gypsum veining (Fig. 6). A comparable facies has been reported from the Wessex Basin by Milroy et al. (2019). In both cases, bleached dolomitic siltstones are interbedded with dark grey silty mudstones. Ripple laminae are abundant, particularly within the silty mudstones, with occasional desiccation features and abundant tepee structures (Fig. 6). Milroy et al. (2019) suggest a terrestrial depositional origin, but as previously stated, did not employ geochemical methodologies to constrain the source of any constituent evaporites. The desiccation cracks, tepee structures and wavy bedding would imply repeated cycles of wetting and drying and would thus be commonly associated with a terrestrial depositional setting (e.g., Milroy et al., 2019).

Thus, our $\delta^{34}S_{evap}$ data from Staithes S-20 enable us to suggest a consistent marine source for the evaporites in this location, despite the sedimentological features of ambiguous origin. Likewise, we observe a comparable anhydritic mudstone facies that is common to both Burton Row and Staithes S-20, yet the $\delta^{34}S_{evap}$ record of the prior suggests terrestrial deposition, whilst the $\delta^{34}S_{evap}$ record of Staithes S-20 implies consistent marine deposition. This geochemical contrast of course persists in spite of the sedimentological similarities, potentially highlighting the difficulty emphasised by previous authors in determining the degree of marine influence involved with evaporite formation based upon sedimentology alone (see Leitner et al., 2023).

From a depth of 583 m within the Branscombe Mudstone Formation, the $\delta^{34}S_{evap}$ profile of Burton Row exhibits an increasing trend, achieving relative stability in $\delta^{34}S_{evap}$ between +11.9 and 16.8 ‰, from 576 to 459 m depth (Fig. 4). It is possible that this

enrichment in $\delta^{34}S_{evap}$ could reflect a progressive increase in the degree of marine influence through the Late Triassic. Between 576 and 459 m depth, the $\delta^{34}S_{evap}$ data do correlate relatively well with the composite $\delta^{34}S_{evap}$ curve for the Late Triassic (Fig. 7), which also maintains relative stability during the Late Triassic until the onset of a positive excursion in the Late Norian (Salisbury et al., 2022). Admittedly, we do not observe such an excursion in our $\delta^{34}S_{evap}$ profile, however this could simply be a product of insufficient data resolution and/or imprecise age determination for the global composite and does not necessarily refute a marine $\delta^{34}S$ signal.

We observe a facies shift from predominantly reddish brown anhydritic siltstones to interbedded reddish brown and greenish grey anhydritic mudstones, however this occurs at a depth of around 482 m, above the depth at which the increase in $\delta^{34}S_{evap}$ first occurs (Fig. 4). Thus, we cannot directly relate the observed $\delta^{34}S_{evap}$ enrichment with the facies shift. This, however, does not refute the possibility of an increase in marine influence, as transitions between coastal and inland playa environments are not necessarily associated with major changes in sedimentological character (see Leitner et al., 2023), with Legler and Schneider (2008) reporting $\delta^{34}S_{evap}$ evidence for marine flooding during the deposition of the Permian Rotliegend, without an associated lithological shift.

The $\delta^{34}S_{evap}$ data from the Blue Anchor Formation, between 447 and 425 m depth in Burton Row, exhibits a sharp increasing trend from +16.7 to +20.5 ‰ (Fig. 4). The recovery of the palynomorphs *Classopollis torosus* and *Rhaetipollis germanicus* from the underlying uppermost Branscombe Mudstone Formation within Burton Row (Warrington *in* Whittaker and Green, 1983), constrain the Blue Anchor to the Rhaetian,

however the composite $\delta^{34}S_{evap}$ curve for the Rhaetian does not record such an excursion, remaining stable around an average of +14.4 ‰ (Salisbury et al., 2022). It should be noted though, that the resolution of the global composite $\delta^{34}S_{evap}$ curve for the Rhaetian is particularly poor. Thus, in this case, the lack of an increasing trend in the global $\delta^{34}S_{evap}$ record during this time interval does not necessarily suggest the positive excursion in the $\delta^{34}S_{evap}$ profile is a non-marine signal.

Previous work suggests the Blue Anchor Formation in south-west Britain represents a transitional environment between the MMG and Penarth Group, with playa lake systems of the Late Triassic potentially experiencing increases in salinity during the late Norian-Rhaetian, inciting further gypsum formation (Hounslow et al., 2012). Sedimentological and palaeontological evidence suggest an increase in marine influence during the deposition of the upper Blue Anchor Formation (Mayall, 1981; Hounslow et al., 2012). However, it is within the uppermost Blue Anchor Formation where we report the most enriched $\delta^{34}S_{evap}$ value of +20.5 ‰ in Burton Row, exhibiting the greatest degree of offset from the Rhaetian $\delta^{34}S_{evap}$ average (Fig. 7).

Pre-existing stable isotope work report $\delta^{34}S_{evap}$ values of +15 and +16.6 ‰ from nodular gypsum in the Blue Anchor Formation of Somerset (Taylor, 1983), in line with the global composite. Taylor (1983) argue the lighter value of +15 ‰ likely reflects a mixed continental-marine signal, while the value of +16.6 ‰ reflects an increase in marine influence, however in the context of subsequent studies, the lighter value is still in line with the global composite for the Rhaetian (see Salisbury et al., 2022 and references therein). Thus, the lower $\delta^{34}S_{evap}$ values we report from the Blue Anchor Formation, between +14 and +17 ‰ are in line with Rhaetian seawater. However, when

viewed within the context of the pre-existing Rhaetian $\delta^{34}S_{evap}$ data (Taylor, 1983; Salisbury et al., 2022), we cannot confidently attribute the $\delta^{34}S_{evap}$ data >+17 ‰ to marine sulphate inputs. It is possible that the $\delta^{34}S_{evap}$ excursion we report is a product of microbially-mediated sulphur cycling, such as microbial sulphate reduction, sequestering isotopically light sulphate (Jorgensen et al., 2019) and enriching the local sulphate pool. This could occur under conditions of marine deposition, potentially reconciling the sedimentological evidence for marine sedimentation in the upper Blue Anchor of the Wessex Basin (Mayall, 1981; Hounslow et al., 2012) and the isotopic offset we observe between the most enriched $\delta^{34}S_{evap}$ values of Burton Row and Rhaetian seawater.

With regards to the EISB, the broad long-term stratigraphic trends in the $\delta^{34}S_{evap}$ profile of 110/13-8 appears to correlate relatively well with the global composite curve of Salisbury et al. (2022) (Fig. 6). Thus, our $\delta^{34}S_{evap}$ data imply a relatively consistent seawater $\delta^{34}S$ signal, and thus suggest persistent marine influence. Rare marine fossils and isotopic signatures from broadly equivalent playa facies within the EISB, Irish Sea and adjacent onshore UK sub-basins also suggest at least intermittent marine influence (Warrington, 1970; Warrington, 1970b; Taylor, 1983; Naylor et al., 1989; Warrington *in* Wilson and Evans, 1990; Wilson, 1990; Thompson and Meadows, 1997). However, these data are of low resolution and/or from distinct sub-basins, while our $\delta^{34}S_{evap}$ profile of 110/13-8 constitutes the highest-resolution $\delta^{34}S_{evap}$ record derived directly from the EISB.

Admittedly, while the $\delta^{34}S_{evap}$ profile of 110/13-8 broadly agrees with the composite $\delta^{34}S_{evap}$ curve for the Middle-Late Triassic, the $\delta^{34}S_{evap}$ data from the

Blackpool Mudstone Member exhibits a greater degree of variability than expected for the Anisian time interval (Fig. 6). This could reflect diagenetic effects, local depositional factors, such as a localised increase in the flux of terrestrial sulphate, or the redistribution of material via caving during the drilling process. The latter is a problem inherent to the use of drill cuttings in stable isotope stratigraphy. Metzger et al. (2014) tested for caving by selecting samples across intervals of isotopic variability (i.e., a positive or negative excursion) and analysed individual chips of material from each sample for $\delta^{13}C_{carb}$ analysis. Unfortunately, individual evaporite chips were too small for $BaSO_4$ precipitation, and thus this methodology could not be applied in this case.

Despite the $\delta^{34}S_{evap}$ variability observed within the Blackpool Mudstone Formation, as stated the broad stratigraphic trend within the $\delta^{34}S_{evap}$ profile of 110/13-8 agrees well with the global composite $\delta^{34}S_{evap}$ curve (Fig. 6). With regards to the Anisian halites of the EISB, marine influence likely originates from marine ingress via a complex post-Hardegsen pathway, facilitating marine seepage from the SPB (McKie, 2017), with thinly bedded limestones and subaqueously deposited shales providing evidence for marine influence along the possible ingress route (Arthurton, 1980; McKie, 2017). The Carnian halites of the EISB were likely separated from the SPB (Hounslow et al., 2012) and the EISB halite bodies likely were likely fed via Tethyan marine ingress routes through rift systems along the Atlantic and Biscay regions (McKie, 2017). Future studies should endeavour to sample material from additional wells in the EISB to determine the reproducibility of the trends in our $\delta^{34}S_{evap}$ profile for 110/13-8.

Overall, our $\delta^{34}S_{evap}$ data suggest a nuanced view of the degree of marine influence during the deposition of the MMG across the UK. Although the MMG in many

UK sub-basins contains palaeontological evidence for marine deposition (see above), the fossils are commonly of low resolution and do not definitively determine the dominant source of the sulphate within the evaporite brines. As discussed above, we observe an offset between our $\delta^{34}S_{evap}$ profiles for Carnduff-02 and Burton Row with each other and the global composite. This, however, contrasts with the evaporites of northeast England (Staithes S-20), the UK southern North Sea (42/28-2), and the East Irish Sea Basin (110/13-8), for which the $\delta^{34}S_{evap}$ profiles exhibit close agreement with the global composite $\delta^{34}S_{evap}$ curve (Fig. 6).

One possible interpretation for this contrast is a spatial and temporal distinction in the extent of marine influence during evaporite deposition. A hydrologic disconnection between the Larne Basin, the Wessex Basin and seawater during MMG deposition would have prevented sulphate within the local brines from recording global perturbations in the $\delta^{34}S$ of seawater sulphate. In addition, the terrestrial sulphate reservoir is smaller than the seawater sulphate reservoir and is thus more susceptible to perturbation driven by local isotopic variability, controlled primarily by the $\delta^{34}S$ of the sulphur bearing lithologies exposed to the local weathering environment (Bottrell and Newton, 2006). This could possibly explain why the $\delta^{34}S_{evap}$ profiles of Carnduff-02 and Burton Row are distinct from each other as well as the global composite age curve. In contrast, the $\delta^{34}S_{evap}$ profiles of Staithes S-20, 42/28-2 and 110/13-8 exhibit trends comparable with the global composite curve, enabling correlation (see above). This suggests the variability in their isotope profiles records global perturbations in seawater sulphate (Salisbury et al., 2022; 2023), and thus the brines and their constituent sulphate likely had a largely marine origin.

Therefore, while our $\delta^{34}S_{evap}$ data from Carnduff-02 and Burton Row broadly agree with recent work that propose a terrestrial depositional model for the evaporites of the Larne and Wessex basins (Andeskie et al., 2018; Milroy et al., 2019), the proposition by Andeskie et al. (2018) that this model can be applied to the MMG more broadly is likely overly simplistic. Instead, our $\delta^{34}S_{evap}$ data suggest a more nuanced view, in that the degree of marine influence varied across distinct UK sub-basins during the deposition of the MMG, with apparently conflicting models of deposition potentially coexisting between locations. By providing direct insight into the likely source of the sulphate (marine or terrestrial) within the evaporite brines, $\delta^{34}S_{evap}$ data can assist in addressing apparent conflicts between different datasets (i.e., sedimentological, and palaeontological), providing greater clarity to the overall depositional model for an evaporite system. For example, as discussed above, marine microfossils do not provide definitive proof of direct marine influence (Hounslow and Ruffell, 2006; Baranyi et al., 2019). However, if the $\delta^{34}S_{evap}$ data provide a dominantly non-marine signal, this would suggest a direct marine source for the microfossils is less likely, or that the marine inundations that deposited the fossils were very infrequent. In the latter case, the flooding events would likely have left very little depositional record beyond the marine fossils themselves, as opposed to relatively continuous continental conditions with higher aggradation rates. Either way, $\delta^{34}S_{evap}$ data can provide greater confidence to interpretations regarding the degree of marine influence that would otherwise remain equivocal, based upon the sedimentological and palaeontological data alone.

It should be noted however, that although our $\delta^{34}S_{evap}$ data has provided further clarity regarding the extent of marine influence during deposition of the MMG, uncertainties remain. This is largely due to the fact that while the $\delta^{34}S$ of sulphate within

an evaporite basin is strongly influenced by the relative magnitude of the terrestrial and marine sulphate input fluxes, other factors impart a control on the overall $\delta^{34}S_{evap}$ signal (Hardie, 1984). Thus, the possibility that the increase in $\delta^{34}S_{evap}$ at the top of the Knocksoghey Formation in Carnduff-02 and the progressive increase in $\delta^{34}S_{evap}$ values through the Branscombe Mudstone Formation in Burton Row are indicative of increasing marine influence cannot be definitively proven with our $\delta^{34}S_{evap}$ data alone. For example, an increase in the degree of hydrologic restriction during evaporite deposition, along with microbial sulphate reduction could incite a localised enrichment in $\delta^{34}S_{evap}$ (Hardie, 1984). Future studies could endeavour to apply additional geochemical proxies such as Cl/Br and $\delta^{18}O_{evap}$, which are also sensitive to marine/terrestrial influence during evaporite deposition (Hardie, 1984; Playà et al., 2000). In addition, organic geochemical proxies, such as MTTC and pristane/phytane ratios can be applied in combination as a proxy for palaeosalinity in deep time (Luo et al., 2019), and could thus be employed as a tool for constraining degrees of hydrologic restriction during evaporite deposition.

Strontium isotopes have been successfully applied in mapping the degree of marine influence during evaporite deposition in the Spanish Triassic (Playà et al., 2000), however their applicability to the UK Triassic remains questionable. The $^{87}Sr/^{86}Sr$ system is more sensitive to terrestrial inputs than $\delta^{34}S$, due to differences in the terrestrial and marine reservoir sizes of strontium and sulphate (Denison et al., 1998). While the Triassic evaporites of Spain were in close direct connection with the Tethys Ocean, the UK was further west within the rift system (McKie, 2017), and thus any marine Sr inputs would likely be overwhelmed by the terrestrial input flux. This can be observed in the Permian Rotliegend of Germany, where $\delta^{34}S_{evap}$ data imply intermittent seawater

ingress, while $^{87}Sr/^{86}Sr$ data suggest an apparently conflicting and consistent terrestrial model of deposition (Legler and Schneider, 2008).

6. Conclusions

Evaporite-based sulphur isotope stratigraphy has the potential to enhance the chronostratigraphic constraint of evaporite-bearing sedimentary rocks that are particularly abundant within the UK Triassic. Here, we apply this methodology to the Larne, East Irish Sea and Wessex basins, generating high-resolution $\delta^{34}S_{evap}$ records from evaporitic sulphate. Through comparison with $\delta^{34}S_{evap}$ records published previously from the Cleveland and UK, southern North Sea basins, our efforts assist in expanding the coverage of the $\delta^{34}S_{evap}$ record in the UK Triassic.

Through comparison with the established global composite $\delta^{34}S_{evap}$ age curve, and with additional constraints imposed by the available biostratigraphic data, we have derived correlation schemes between the $\delta^{34}S_{evap}$ profiles of the lowermost MMG in the Larne Basin, the MMG of the EISB and the global age curve, as well as the $\delta^{34}S_{evap}$ records of Staithes S-20 and 42/28-2. This has enabled us to derive tighter age constraint for several subdivisions of the MMG across distinct UK sedimentary basins, that generally lack robust biostratigraphic age constraint.

In addition, characterising the $\delta^{34}S$ of evaporitic sulphate, has provided further insight into the degree of marine influence during evaporite deposition in the UK Triassic. Our $\delta^{34}S_{evap}$ data from the lowermost MMG in the Larne Basin, and the MMG in the EISB, Cleveland and southern North Sea basins provide relatively consistent marine isotopic signatures, suggesting hydrologic connection between the evaporite brines and the seawater sulphate reservoir during deposition. In contrast, offsets between the

$\delta^{34}S_{evap}$ profiles of Burton Row Carnduff-02 of the Wessex and Larne basins, respectively, suggest prolonged periods of hydrologic disconnection between the evaporite brines and seawater sulphate during deposition. When viewed in the context of other palaeontological and sedimentological data, our $\delta^{34}S_{evap}$ profiles enable the mapping of marine influence during deposition of the MMG across the locations sampled as part of this study. In doing so, our results assist in reconciling apparent conflicts between biostratigraphic and sedimentological/mineralogical data and provide greater clarity for the depositional model of the sampled evaporite systems.

It should be noted, however, that the $\delta^{34}S_{evap}$ compilation of this study is not exhaustive, and sampling sites were at times irregularly distributed stratigraphically and spatially. Further sample sites should be selected for $\delta^{34}S_{evap}$ analysis within the basins sampled here, to better assess the local reproducibility of the isotopic trends we observe. In addition, evaporite-based $\delta^{34}S$ stratigraphy should be more widely applied to the UK Triassic, as many basins have yet to be targeted for $\delta^{34}S_{evap}$ analysis. Future studies should also endeavour to apply other stratigraphic techniques, such as $\delta^{13}C_{org}$ stratigraphy and magnetostratigraphy, alongside the generation of $\delta^{34}S_{evap}$ records. In doing so, this will help to enhancing the confidence of the resulting stratigraphic correlation schemes, while providing a means of establishing enhanced chronostratigraphic calibration in instances where the $\delta^{34}S_{evap}$ profiles fail to exhibit a primary seawater signal. Due to the sensitivity of sulphur cycle to various forcings, subsequent work could also focus on applying $\delta^{34}S_{evap}$ records with $\delta^{18}O_{evap}$, Cl/Br and organic geochemical data to constrain the degree of marine influence during evaporite deposition with greater confidence.

7. References

Aleali, M., Rahimpour-Bonab, H., Moussavi-Harami, R., Jahani, D., 2013. Environmental and sequence stratigraphic implications of anhydrite textures: A case from the Lower Triassic of the Central Persian Gulf. *J. Asian Earth Sci.* 75, 110-125. DOI: 10.1016/j.jseaes.2013.07.017

Ambrose, K., and Wakefield, O. (2015). Permo-Triassic rocks of Nottingham. *Mercian Geol.* 18, 260–263.

Ambrose, K., Hough, E., Smith N.J.P., Warrington, G., 2014. Lithostratigraphy of the Sherwood Sandstone Group of England, Wales and south-west Scotland. *British Geological Survey Research Report*, RR/14/01

Andeskie, A.S., Benison, K.C., Eichenlaub, L.A., Raine, R., 2018. Acid-saline-lake systems of the Triassic Mercia Mudstone Group, County Antrim, Northern Ireland. *J. Sediment. Res.* 88, 385-398. DOI: 10.2110/jsr.2018.14

Arthurton, R.S., 1980. Rhythmic sedimentary sequences in the Triassic Keuper Marl (Mercia Mudstone Group) of Cheshire, northwest England. *Geol. J.* 15, 43-58. DOI: 10.1002/gj.3350150106

Bachmann, G.H., Geluk, M.C., Warrington, G., Becker-Roman, A., Beutler, G., Hagdorn, H., Hounslow, M.W., Nitsch, E., Röhling, H-G., Simon, T., Szulc, A., 2010. “Triassic”, in *Petroleum geological atlas of the Southern Permian Basin area*. Editors: Doornenbal, J.C., Stevenson, A.G. EAGE Publications b.v., Houten, 149-173

Baranyi, V., Miller, C.S., Ruffell, A., Hounslow, M.W., Kürschner, W.M., 2019. A continental record of the Carnian Pluvial Episode (CPE) from the Mercia Mudstone

Group (UK): palynology and climatic implications. *J. Geol. Soc.* 176, 149-166. DOI: 10.1144/jgs2017-150

Becker, A., Fijałkowska-Mader, A., Jasionowski, M., 2020. Marine vs. terrestrial environments during Early Triassic deposition on the northeastern margin of the Central European Basin – a multidisciplinary study on the Middle Buntsandstein of the Bartoszyce IG 1 borehole, NE Poland. *Geol. Q.* 64, 1023-1047. DOI: 10.7306/gq.1566

Benton, M.J., 1997. The Triassic reptiles from Devon. *Proc. Ussher Soc.* 9, 141-152.

Bernasconi, S.M., Meier, I., Wohlwend, S., Brack, P., Hochuli, P.A., Bläsi, H., Wortmann, U.G., Ramseyer, K., 2017. An evaporite-based high-resolution sulfur isotope record of Late Permian and Triassic seawater sulfate. *Geochim. Cosmochim. Acta*, 204, 331-349. DOI: 10.1016/j.gca.2017.01.047

Boschetti, T., Cortecci, G., Toscani, L., Iacumin, P., 2011. Sulfur and oxygen isotope compositions of Upper Triassic sulfates from northern Apennines, Italy: paleogeographic and hydrogeochemical implications. *Geol. Acta*, 9, 129-147

Bottrell, S.H., Newton, R.J., 2006. Reconstruction of changes in global sulfur cycling from marine sulfate isotopes. *Earth Sci. Rev.* 75, 59-83. DOI: 10.1016/j.earscirev.2005.10.004

Burke, A., Present, T.M., Paris, G., Rae, E.C.M., Sandilands, B.H., Gaillardet, J., Peucker-Ehrenbrink, B., Fischer, W.W., McClelland, J.W., Spencer, R.G.M., Voss, B.M., Adkins, J.F., 2018. Sulfur isotopes in rivers: Insights into global weathering budgets, pyrite oxidation, and the modern sulfur cycle. *Earth Planet. Sci. Lett.* 496, 168-177. DOI: 10.1016/j.epsl.2018.05.022

Burley, S.D., Radley, J.D., Coram, R.A., 2023. 'A hard rain's a-gonna fall': torrential rain, flash floods and desert lakes in the Late Triassic Arden Sandstone of Central England. *Geol. Today*, 39, 90-98. DOI: 10.1111/gto.12430

Carrillo, E., Rosell, L., Ortí, F., 2014. Multiepisodic evaporite sedimentation as an indicator of palaeogeographic evolution in foreland basins (South-eastern Pyrenean basin, Early-Middle Eocene). *Sedimentology*, 61, 2086-2112. DOI: 10.1111/sed.12140

Caruthers, A.H., Gröcke, D.R., Kaczmarek, S.E., Rine, M.J., Kuglitsch, Kuglitsch, J., Harrison III, W.B., 2018. Utility of organic carbon isotope data from the Salina Group halite (Michigan Basin): A new tool for stratigraphic correlation and paleoclimate proxy source. *Geol. Soc. Am. Bull.* 130, 1782-1790. DOI: 10.1130/B31972.1

Chapman, T.J., 1989. "The Permian to Cretaceous structural evolution of Western Approaches Basin (Melville sub-basin), UK", in *Inversion tectonics*. Editors: Cooper, M.A., Williams, G.D. Geological Society of London, Special Publications, 44, 177-200. DOI: 10.1144/GSL.SP.1989.044.01.11

Chen, Y., Scholze, F., Richoz, S., Zhang, Z., 2019. Middle Triassic conodont assemblages from the Germanic Basin: Implications for multi-element taxonomy and biogeography. *J. Syst. Palaeontol.* 17, 359-377. DOI: 10.1080/14772019.2018.1424260

Clark, N.J., Smith, R.B., 1981. Observations of salt particles in the atmosphere in the vicinity of an inland salt lake: Lake Eyre, South Australia. *Atmos. Res.* 22, 91-104. DOI: 10.1016/0169-8095(88)90001-4

Claypool, G.E., Holser, W.T., Kaplan, I.R., Sakai, H., Zak, I., 1980. The age curves of sulfur and oxygen isotopes in marine sulfate and their mutual interpretation. *Chem. Geol.* 28, 199-260. DOI: 10.1016/0009-2541(80)90047-9

Cope, J.C.W., Getty, T.A., Howarth, M.K., Morton, N., Torrens, H.S., 1980. A correlation of Jurassic rocks in the British Isles Part One: Introduction and Lower Jurassic. *Geol. Soc. Lond.*, Special Report No. 14

Coward, M.P., 1995. "Structural and tectonic setting of the Permo-Triassic basins of north-west Europe", in *Permian and Triassic rifting in north-west Europe*. Editor: Boldy, S.A.R. (London: Geological Society of London, Special Publications) 91, 7-39. DOI: 10.1144/GSL.SP.1995.091.01.02

Crockford, P.W., Kunzmann, M., Bekker, A., Hayles, J., Bao, H., Halverson, G.P., Peng, Y., Bui, T.H., Cox, G.M., Gibson, T.M., Wörndle, S., Rainbird, R., Lepland, A., Swanson-Hysell, N.L., Master, S., Sreenivas, B, Kuznetsov, A., Krupernik, V., Wing, B.A., 2019. Claypool continued: Extending the isotopic record of sedimentary sulfate. *Chem. Geol.* 513, 200-225. DOI: 10.1016/j.chemgeo.2019.02.030

Dare-Edwards, A.J., 1984. Aeolian clay deposits of south-eastern Australia: Parna or loessic clay? *Trans. Inst. Br. Geogr.* 9, 337-344. DOI: 10.2307/622237

Dawson, G.J., Burley, S.D., Ruffell, A., Benton, M.J., Duffin, C.J., 2022. A new exposure of the North Curry Sandstone Member (Dunscombe Mudstone Formation, Mercia Mudstone Group: Carnian, Triassic), near Taunton, Somerset (UK): The location of Charles Moore's vertebrate specimens resolved. *Proc. Geol. Assoc.* 133, 526-537. DOI: 10.1016/j.pgeola.2022.06.009

Denison, R.E., Kirkland, D.W., Evans, R., 1998. Using strontium isotopes to determine the age and origin of gypsum and anhydrite beds. *J. Geol.* 106, 1-17. DOI: 10.1086/515996

Earp, J.R., Taylor, B.J., 1986. Geology of the country around Chester and Winsford. *Memoir British Geological Survey, Sheet 109* (England and Wales).

English, K.L., English, J.M., Moscardini, R., Haughton, P.D.W., Raine, R.J., Cooper, M., 2024. Review of Triassic Sherwood Sandstone Group reservoirs of Ireland and Great Britain and their future role in geoenergy applications. *Geoenergy*, 2, geoenergy2023-2024. DOI: 10.1144/geoenergy2023-042

Evans, W.B., Wilson, A.A., Taylor, B.J., Price, D., 1968. Geology of the country around Macclesfield, Congleton, Crewe and Middlewich. *Mem. Geol. Surv. U.K.* 328 pp.

Feist-Burkhardt, S., Götz, A.E., Szulc, J., Borkhataria, R., Geluk, M., Haas, J., Hornung, J., Jordan, P., Kempf, O., Michalík, J., Nawrocki, J., Reinhardt, L., Ricken, W., Röhling, H-G., Rüffer, T., Török, A., Zühlke, R., 2008. "Triassic", in *The geology of Central Europe Volume 2: Mesozoic and Cenozoic*. Editor McCann, T. Geological Society of London, 749-821. DOI: 10.1144/CEV2P.1

Fike, D.A., Bradley, A.S., Rose, C.V., 2015. Rethinking the ancient sulfur cycle. *Annu. Rev. Earth Planet. Sci.* 43, 593-622. DOI: 10.1146/annurev-earth-060313-054802

Franz, M., Henniger, M., Barnasch, J., 2013. The strong diachronous Muschelkalk/Keuper facies shift in the Central European basin: Implications from the type-section of the Erfurt Formation (Lower Keuper, Triassic) and basin-wide correlations. *Int. J. Earth Sci.* 102, 671-780. DOI: 10.1007/s00531-012-0823-y

Gallois, R.W., 2001. The lithostratigraphy of the Mercia Mudstone Group (mid-late Triassic) of the south Devon coast. *Proc. Ussher Soc.* 10, 195-204

Gallois, R.W., 2004. The distribution of halite (rock-salt) in the Mercia Mudstone Group (mid to late Triassic) in south-west England. *Geoscience South-West Engl.* 10, 383-389

Handford, C.R., 1982. Sedimentology and evaporite genesis in a Holocene continental-sabkha playa basin – Bristol Dry Lake, California. *Sedimentology*, 29, 239-253. DOI: 10.1111/j.1365-3091.1982.tb01721.x

Hardie, L.A., 1984. Evaporites: Marine or non-marine. *Am. J. Sci.* 284, 193-240. DOI: 10.2475/ajs.284.3.193

Harvey, M.J., Stewart, S.A., 1998. "Influence of salt on the structural evolution of the Channel Basin", in *Development, evolution and petroleum geology of the Wessex Basin*. Editor Underhill, J.R., Geological Society London, Special Publications, 133, 241-266. DOI: 10.1144/GSL.SP.1998.133.01.11

Hesselbo, S.P., Robinson, S.A., Surlyk, F., Piasecki, S., 2002. Terrestrial and marine extinction at the Triassic-Jurassic boundary synchronized with major carbon-cycle perturbation: A link to initiation of massive volcanism? *Geology*, 30, 251-254. DOI: 10.1130/00917613(2002)030<0251:TAMEAT>2.0.CO;2

Heunisch, C., Röhling, H-G., 2016. Early Triassic phytoplankton episodes in the Lower and Middle Buntsandstein of the Central European Basin. *Z. Dt. Ges. Geowiss.* 167, 227-248. DOI: 10.1127/zdgg/2016/0070

Hochuli, P.A., Schneebeli-Hermann, E., Brack, P., Ramseyer, K., Rebetez, D., 2020. Palynology and chemostratigraphy of Middle Triassic successions in northern

Switzerland (Weiach, Benken, Leuggern) and southern Germany (Weizen, Freudenstadt). *Riv. Ital. Paleontol. Stratigr.* 126, 363-394. DOI: 10.13130/2039-4942/13421

Holser, W.T., Kaplan, I.R., 1966. Isotope geochemistry of sedimentary sulfates. *Chem. Geol.* 1, 93-135. DOI: 10.1016/0009-2541(66)90011-8

Holliday, D.W., 1970. The petrology of secondary gypsum rocks. *J. Sediment. Petrol.* 40, 734-744. DOI: 10.1306/74D7202C-2B21-11D7-8648000102C1865D

Hounslow, M.W., Gallois, R., 2023. Magnetostratigraphy of the Mercia Mudstone Group (Devon, UK): implications for regional relationships and chronostratigraphy in the Middle to Late Triassic of Western Europe. *J. Geol. Soc.* 180, jgs2022-173. DOI: 10.1144/jgs2022-173

Hounslow, M.W., Harris, S.E., Karloukovski, V., Mørk, A., 2022. Geomagnetic polarity and carbon isotope stratigraphic assessment of the late Carnian-earliest Norian in Svalbard: Evidence for a major hiatus and improved Boreal to Tethyan correlation. *Nor. J. Geol.* 102, 202204. DOI: 10.17850/njg102-1-4

Hounslow, M.W., McIntosh, G., 2003. Magnetostratigraphy of the Sherwood Sandstone Group (Lower and Middle Triassic), south Devon, UK: detailed correlation of the marine and non-marine Anisian. *Palaeogeogr. Palaeoclimatol. Palaeoecol.* 193, 325-348. DOI: 10.1016/S0031-0182(03)00235-9

Hounslow, M.W., McKie, T., Ruffell, A.H., 2012. “Permian to Late Triassic post-orogenic collapse and rifting, arid deserts, evaporating seas and mass extinctions” in *The*

geological history of Britain and Ireland. Editors Woodcock, N.H., Strachan, R.A., (Wiley: Chichester) 2, 301-321.

Hounslow, M.W., Ruffell, A.H., 2006. "Triassic: Seasonal rivers, dusty deserts and saline lakes", in *The geology of England and Wales*. Editors Rawson, P.F., Brenchley, P., (London: Geological Society of London) 295-325. DOI: 10.1144/GOEWP.13

Howard, A.S., Warrington, G., Ambrose, K., Rees, J.G., 2008. A formational framework for the Mercia Mudstone Group (Triassic) of England and Wales. British Geological Survey Research Report, RR/08/004

Ireland, R.J., Pollard, J.E., Steel, R.J., Thompson, D.B., 1978. Intertidal sediments and trace fossils from the Waterstones (Scythian-Anisian?) at Daresbury, Cheshire. *Proc. Yorks. Geol. Soc.* 41, 399-436. DOI: 10.1144/pygs.41.4.399

Jackson, D.I., Jackson, A.A., Evans, D., Wingfield, R.T.R., Barnes R.P., Arthur, M.J., 1995. United Kingdom offshore regional report: the geology of the East Irish Sea (London: HMSO for the British Geological Survey)

Jackson, D.I., Johnson, H., 1996. Lithostratigraphic nomenclature of the Triassic, Permian and Carboniferous of the UK offshore East Irish Sea Basin. British Geological Survey, Nottingham

Jackson, D.I., Johnson, H., Smith, N.J.P., 1997. "Stratigraphical relationships and a revised lithostratigraphical nomenclature for the Carboniferous, Permian and Triassic rocks of the offshore East Irish Sea Basin", in *Petroleum geology of the Irish Sea and adjacent areas*. Editors Meadows, N.S., Trueblood, S.P., Hardman, M., Cowan, G.

Geological Society of London Special Publication, 124, 11-32. DOI: 10.1144/GSL.SP.1997.124.01.02

Johnson, D.I., Present, T.M., Li, M., Shen, Y., Adkins, J.F., 2021. Carbonate associated sulfate (CAS) $\delta^{34}S$ heterogeneity across the End-Permian Mass Extinction in South China. *Earth Planet. Sci. Lett.* 574, 117172. DOI: 10.1016/j.epsl.2021.117172

Johnson, H., Warrington, G., Stoker, S.J., 1994. 6. "Permian and Triassic of the Southern North Sea" in *Lithostratigraphic nomenclature of the UK North Sea*. Editors Knox, R.W.O'B., Cordey, W.G., (British Geological Survey: Nottingham)

Jorgensen, B.B., Findlay, A.J., Pellerin, A., 2019. The biogeochemical sulfur cycle of marine sediments. *Front. Microbiol.* 10, 849. DOI: 10.3389/fmicb.2019.00849

Kasprzyk, A., Ortí, F., 1998. Palaeogeographic and burial controls on anhydrite genesis: the Badenian basin in the Carpathian Foredeep (southern Poland, western Ukraine). *Sedimentology*, 45, 889-907. DOI: 10.1046/j.1365-3091.1998.00190.x

Kendall, A.C., 1978. Facies models 11. Continental and supratidal (sabkha) evaporites. *Geosci. Can.* 5, 66-78.

Kürschner, W.M., Herngreen, G.F.W., 2010. "Triassic palynology of central and northwestern Europe: a review of palynofloral diversity patterns and biostratigraphic subdivisions", in *The Triassic timescale*. Editor: Lucas, S.G., (London: Geological Society of London, Special Publications) 334, 263-283. DOI: 10.1144/SP334.11

Legler, B., Schneider, J.W., 2008. Marine ingressions into the Middle/Late Permian saline lake of the Southern Permian Basin (Rotliegend, Northern Germany) possibly linked to

sea-level highstands in the Arctic rift system. *Palaeogeogr. Palaeoclimatol. Palaeoecol.* 267, 102-114. DOI: 10.1016/j.palaeo.2008.06.009

Leitner, C., Köster, M., Finger, F., 2023. Saltern, mudflat, and dry playa: Playa basin types of a retreating epeiric sea (Keuper, Germany). *J. Sediment. Res.* 93, 840-856. DOI: 10.2110/jsr.2023.013

Leslie, A.B., Spiro, B., Tucker, M.E., 1993. Geochemical and mineralogical variations in the upper Mercia Mudstone Group (Late Triassic), southwest Britain: correlation of outcrop sequences with borehole geophysical logs. *J. Geol. Soc., London*, 150, 67-75. DOI: 10.1144/gsjgs.150.1.0067

Lott, G.K., Warrington, G., 1988. A review of the latest Triassic in the U.K. sector of the southern North Sea Basin. *Proc. Yorks. Geol. Soc.* 47, 139-147. DOI: 10.1144/pygs.47.2.139

Lucas, S.G., 1998. Global Triassic tetrapod biostratigraphy and biochronology. *Palaeogeogr. Palaeoclimatol. Palaeoecol.* 143, 347-384. DOI: 10.1016/S0031-0182(98)00117-5

Luo, G., Yang, H., Algeo, T.J., Hallmann, C., Xie, S., 2019. Lipid biomarkers for the reconstruction of deep-time environmental conditions. *Earth Sci. Rev.* 189, 99-124. DOI: 10.1016/j.earscirev.2018.03.005

Machel, H-G., 1985. Fibrous gypsum and fibrous anhydrite in veins. *Sedimentology*, 32, 443-454. DOI: 10.1111/j.1365-3091.1985.tb00523.x

Machel, H.G., Burton, E.A., 1989. Burial-diagenetic sabkha-like gypsum and anhydrite nodules. *J. Sediment. Petrol.* 61, 394-405. DOI: 10.1306/D4267721-2B26-11D7-8648000102C1865D

Magee, J.W., Bowler, J.M., Miller, G.H., Williams, D.L.G., 1995. Stratigraphy, sedimentology, chronology and palaeohydrology of Quaternary lacustrine deposits at Madigan Gulf, Lake Eyre, South Australia. *Palaeogeogr. Palaeoclimatol. Palaeoecol.* 113, 3-42. DOI: 10.1016/0031-0182(95)00060-Y

Maiklem, W.R., Bebout, D.G., Glaister, R.P., 1969. Classification of anhydrite – a practical approach. *Bull. Can. Pet. Geol.* 17, 194-233. DOI: 10.35767/gscpgbull.17.2.194

Márquez-Aliaga, A., Valenzuela-Ríos, J. I., Calvet, F., Budurov, K., 2000. Middle Triassic conodonts from northeastern Spain: Biostratigraphic implications. *Terra Nova*, 12, 77-83. DOI: 10.1111/j.1365-3121.2000.00273.x

Mayall, M.J., 1981. The Late Triassic Blue Anchor Formation and the initial Rhaetian marine transgression in south-west Britain. *Geol. Mag.* 118, 377-384. DOI: 10.1017/S0016756800032246

McKie, T., 2014. Climatic and tectonic controls on Triassic dryland terminal fluvial system architecture, central North Sea. *Int. Assoc. Sedimentol. Spec. Publ.* 46, 19-58. DOI: 10.1002/9781118920435.ch2

McKie, T., 2017. “Palaeogeographic evolution of latest Permian and Triassic salt basins in northwest Europe”, in *Permo-Triassic salt provinces of Europe, North Africa and the Atlantic margins, tectonics and hydrocarbon potential*. Editors Soto, J.J., Flinch, J.F., Tari,

G. (Amsterdam Netherlands: Elsevier), 159-173. DOI: 10.1016/B978-0-12-809417-4.00008-2

McKie, T., Williams, B., 2009. Triassic palaeogeography and fluvial dispersal across the northwest European basins. *Geol. J.* 44, 711-741. DOI: 10.1002/gj.1201

Meadows, N.S., 2006. The correlation and sequence architecture of the Ormskirk Sandstone Formation in the Triassic Sherwood Sandstone Group of the East Irish Sea Basin, NW England. *Geol. J.* 41, 93-122. DOI: 10.1002/gj.1034

Metzger, J.G., Fike, D.A., Smith, L.B., 2014. Applying carbon-isotope stratigraphy using well cuttings for high-resolution chemostratigraphic correlation of the subsurface. *Am. Assoc. Pet. Geol. Bull.* 98, 1551-1576. DOI: 10.1306/04011412231

Milroy, P., Wright, V.P., 2000. A highstand oolitic sequence and associated facies from a Late Triassic lake basin, south-west England. *Sedimentology*, 47, 187-209. DOI: 10.1046/j.1365-3091.2000.00288.x

Milroy, P., Wright, V.P., Simms, M.J., 2019. Dryland continental mudstones: Deciphering environmental changes in problematic mudstones from the Upper Triassic (Carnian to Norian) Mercia Mudstone Group, south-west Britain. *Sedimentology*, 66, 2557-2589. DOI: 10.1111/sed.12626

Miller, C.S., Peterse, F., da Silva, A-C., Baranyi, V., Reichart, G.J., Kürschner, W.M., 2017. Astronomical age constraints and extinction mechanisms of the Late Triassic Carnian crisis. *Sci. Rep.* 7, 2557. DOI: 10.1038/s41598-017-02817-7

Mitchell, W.I., 2004. “Chapter 10: Triassic”, in *The geology of Northern Ireland – our natural foundation*. Editor Mitchell, W.I., (Belfast: Geological Survey of Northern Ireland) 133-144

Murray, R.C., 1964. Origin and diagenesis of gypsum and anhydrite. *J. Sediment. Petrol.* 34, 512-523. DOI: 10.1306/74D710D2-2B21-11D7-8648000102C1865D

Moragas, M., Martínez, C., Baqués, V., Playà, E., Travé, A., Alías, G., Cantarero, I., 2013. Diagenetic evolution of a fractured evaporite deposit (Vilobí Gypsum Unit, Miocene, NE Spain). *Geofluids*, 13, 180-193. DOI: 10.1111/gfl.12017

Narkievicz, K., 1999. Conodont biostratigraphy of the Muschelkalk (Middle Triassic) in the central part of the Polish Lowlands. *Geol. Q.* 43, 313-328.

Naylor, D., Haughey, N., Clayton, G., Graham, J.R., 1993. “The Kish Bank Basin, offshore Ireland”, in *Petroleum geology of northwest Europe: Proceedings of the 4th conference*. Editor Parker, J.R., Geological Society, London, Petroleum Geology Conference Series, 4, 845-855. DOI: 10.1144/004084

Naylor, H., Turner, P., Vaughan, D.J., Boyce, A.J., Fallick, A.E., 1989. Genetic studies of red bed mineralization in the Triassic of the Cheshire Basin, northwest England. *J. Geol. Soc. London*. 146, 685-699. DOI: 10.1144/gsjgs.146.4.0685

Neilsen, H., 1978. “Sulfur isotopes in nature”, in *Handbook of geochemistry*. Editor Wedepohl, K.K., (Berlin, Springer), 16, 1-48

Newell, A., 2018. Rifts, rivers and climate recovery: A new model for the Triassic of England. *Proc. Geol. Assoc.* 129, 352-371. DOI: 10.1016/j.pgeola.2017.04.001

Old, R.A., Hamblin, R.J.O., Ambrose, K., Warrington, G., 1991. *Geology of the country around Redditch. Memoir of the British Geological Survey, sheet 183 (England and Wales)*. HMSO, London

Ortí, F., Peréz-López, A., García-Veigas, J., Rosell, L., Cendón, D.I., Pérez-Valera, F., 2014. Sulfate isotope compositions ($\delta^{34}S$, $\delta^{18}O$) and strontium isotopic ratios ($^{87}Sr/^{86}Sr$) of Triassic evaporites in the Betic Cordillera (SE Spain). *Revista de la Sociedad Geológica de España*, 27, 79–89.

Ortí, F., Peréz-López, A., Pérez-Valera, F., Benedicto, C., 2022. Isotope composition ($\delta^{34}S$, $\delta^{18}O$) of the Middle Triassic-Early Jurassic sulfates in eastern Iberia. *Sediment. Geol.* 431, 106104. DOI: 10.1016/j.sedgeo.2022.106104

Parrish, J.T., 1993. Climate of the supercontinent Pangea. *J. Geol.* 101, 215-233. DOI: 10.1086/648217

Paytan, A, Gray, E.T., Ma, Z., Erhardt, E., Faul, K., 2012. Application of sulfur isotopes for stratigraphic correlation. *Isot. Environ. Health Stud.* 48, 195-206. DOI: 10.1080/10256016.2011.625423

Paytan, A., Yao, W., Faul, K.L., Gray, E.T., 2020. "Sulfur isotope stratigraphy", in *Geologic time scale 2020*. Editors Gradstein F.M., Ogg, J.G., Schmitz, M.D., Ogg, G.M., (Amsterdam, Netherlands: Elsevier) 1, 259-278. DOI: 10.1016/B978-0-12-824360-2.00009-7

Peacock, D.C.P., 2004. The post-Variscan development of the British Isles within a regional transfer zone influenced by orogenesis. *J. Struct. Geol.* 26, 2225-2231. DOI: 10.1016/j.jsg.2004.05.005

Philipp, S.J., 2008. Geometry and formation of gypsum veins in mudstones at Watchet, Somerset, SW England. *Geol. Mag.* 145, 831-844. DOI: 10.1017/S0016756808005451

Playà, E., Ortí, F., Rosell, L., 2000. Marine to non-marine sedimentation in the upper Miocene evaporites of the Eastern Betics, SE Spain: sedimentological and geochemical evidence. *Sediment. Geol.* 133, 135-166. DOI: 10.1016/S0037-0738(00)00033-6

Pollard, J.E., Steel, R.J., 1978. Intertidal sediments in the Auchenhew Beds (Triassic) of Arran. *Scott. J. Geol.* 14, 317-328. DOI: 10.1144/sjg14040317

Porter, R.J., Gallois, R.W., 2008. Identifying fluvio-lacustrine intervals in thick playa-lake successions: An integrated sedimentology and ichnology of arenaceous members in the mid-late Triassic Mercia Mudstone Group of south-west England, UK. *Palaeogeogr. Palaeoclimatol. Palaeoecol.* 270, 381-398. DOI: 10.1016/j.palaeo.2008.07.020

Raab, M., Spiro, B., 1991. Sulfur isotopic variations during seawater evaporation with fractional crystallization. *Chem. Geol.* 86, 323-333. DOI: 10.1016/0168-9622(91)90014-N

Rosen, M.R., 1991. Sedimentologic and geochemical constraints on the evolution of Bristol Dry Lake Basin, California, U.S.A. *Palaeogeogr. Palaeoclimatol. Palaeoecol.* 84, 229-257. DOI: 10.1016/0031-0182(91)90046-T

Ruffell, A., Shelton, R., 1999. The control of sedimentary facies by climate during phases of crustal extension: examples from the Triassic of onshore and offshore England and Northern Ireland. *J. Geol. Soc. London*, 156, 779-789. DOI: 10.1144/gsjgs.156.4.0779

Salisbury, J., Gröcke, D.R., Cheung, H.D.R.A., Kump, L.R., McKie, T., Ruffell, A., 2022. An 80-million-year sulphur isotope record of pyrite burial over the Permian-Triassic. *Sci. Rep.* 12, 17370. DOI: 10.1038/s41598-022-21542-4

Salisbury, J., Gröcke, D.R., McKie, T., 2023. Sulphur isotope stratigraphy of drill cuttings and stratigraphic correlation of Permian-Triassic evaporites. *Front. Earth Sci.* 11, 1216365. DOI: 10.3389/feart.2023.1216365

Scholze, F., Schneider, J.W., Werneburg, R., 2016. Conchostracans in continental deposits of the Zechstein-Buntsandstein transition in central Germany: Taxonomy and biostratigraphic implications for the position of the Permian-Triassic boundary within the Zechstein Group. *Palaeogeogr. Palaeoclimatol. Palaeoecol.* 449, 174-193. DOI: 10.1016/j.palaeo.2016.02.021

Scholze, F., Wang, X., Kirscher, U., Kaft, J., Schneider, J.W., Götz, A.E., Joachimski, M.M., Bachtadse, V., 2017. A multistratigraphic approach to pinpoint the Permian-Triassic boundary in continental deposits: The Zechstein-Lower Buntsandstein transition in Germany. *Glob. Planet. Change*, 152, 129-151. DOI: 10.1016/j.gloplacha.2017.03.004

Schreiber, B.C., Tabakh, M.E., 2000. Deposition and early alteration of evaporites. *Sedimentology*, 47, 215-238. DOI: 10.1046/j.1365-3091.2000.00002.x

Spencer, P.S., Storrs, G.W., 2002. A re-evaluation of the small tetrapods from the Middle Triassic Otter Sandstone Formation of Devon, England. *Palaeontology*, 45, 447-467. DOI: 10.1111/1475-4983.00245

Stuart, I.A., 1993. “The geology of the North Morecombe Gas Field, East Irish Sea Basin” in *Petroleum geology of the northwest Europe: Proceedings of the 4th conference*. Editor Parker J.R., (London: The Geological Society) 4, 883-895. DOI: 10.1144/0040883

Sun, Y., Joachimski, M.M., Wignall, P.B., Yan, C., Chen, Y., Jiang, H., Wang, L., Lai, X., 2012. Lethally hot temperatures during the Early Triassic greenhouse. *Science*, 338, 366-370. DOI: 10.1126/science.1224126

Szulc, J., 2019. Lower Triassic marine Buntsandstein deposits in the Central European Basin. *Z. Dt. Ges. Geowiss.* 170, 311-320. DOI: 10.1127/zdgg/2019/0190

Tabakh, M.E., Schreiber, B.C., Warren, J.K., 1998. Origin of fibrous gypsum in the Newark Rift Basin, eastern North America. *J. Sediment. Res.* 68, 88-99.

Taylor, S.R., 1983. A stable isotope study of the Mercia Mudstone Group (Keuper Marl) and associated sulphate horizons in the English Midlands. *Sedimentology*, 30, 11-31. DOI: 10.1111/j.1365-3091.1983.tb00647.x

Thode, H.G., Monster, J., 1965. Sulfur isotope geochemistry of petroleum, evaporites, and ancient seas. *Am. Assoc. Pet. Geol. Mem.* 4, 367-377.

Thompson, J., Meadows, N.S., 1997. “Clastic sabkhas and diachroneity at the top of the Sherwood Sandstone Group: East Irish Sea Basin”, in *Petroleum geology of the Irish Sea and adjacent areas*. Editors: Meadows, N.S., Trueblood, S.P., Hardman, M., Cowan, G., (London: Geological Society of London [Special Publications]) 124, 237-251. DOI: 10.1144/GSL.SP.1997.124.01.15

Trotter, J.A., Williams, I.S., Nicora, A., Mazza, M., Rigo, M., 2015. Long-term cycles of Triassic climate change: A new $\delta^{18}O$ record from conodont apatite. *Earth Planet. Sci. Lett.* 415, 165-174. DOI: 10.1016/j.epsl.2015.01.038

Tucker, M.E., 1977. The marginal Triassic deposits of South Wales: continental facies and palaeogeography. *Geol. J.* 12, 169-188. DOI: 10.1002/gj.3350120205

Tucker, M.E., 1991. Sequence stratigraphy of carbonate-evaporite basins: Models and applications to the Upper Permian Zechstein of northeast England and adjoining North Sea. *J. Geol. Soc. Lond.* 148, 1019-1036. DOI: 10.1144/gsjgs.148.6.1019

Van Driessche, A.E.S., Canals, A., Ossorio, M., Reyes, R.C., García-Ruiz, J.M., 2016. Unravelling the sulfate sources of (giant) gypsum crystals using gypsum isotope fractionation factors. *J. Geol.* 124, 235-245. DOI: 10.1086/684832

Warren, J.K., 1991. "Sulfate dominated sea-marginal and platform evaporative settings: Sabkhas and salinas, mudflats and salterns", in *Evaporites, petroleum and mineral resources*. Editor: Melvin, J.L., (Amsterdam: Elsevier) 69-

Warren, J.K., 2010. Evaporites through time: Tectonic, climatic and eustatic controls in marine and nonmarine deposits. *Earth Sci. Rev.* 98, 217-268. DOI: 10.1016/j.earscirev.2009.11.004

Warrington, G., 1967. Correlation of the Keuper series of the Triassic by miospores. *Nature*, 214, 1323-1324. DOI: 10.1038/2141323a0

Warrington, G., 1970. The "Keuper" series of the British Trias in the Northern Irish Sea and neighbouring areas. *Nature*, 226, 254-256. DOI: 10.1038/226254a0

Warrington, G., 1970b. The stratigraphy and palaeontology of the 'Keuper' Series of the central Midlands of England. *Quart. J. Geol. Soc.* 126, 183–223. DOI: 10.1144/gsjgs.126.1.0183

Warrington, G., 1971. Palynoogy of the New Red Sandstone of the South devon coast. *Proc. Ussher Soc.* 2, 307-314

Warrington, G., 1974. Studies in the palynological biostratigraphy of the British Trias. 1. Reference sections in west Lancashire and north Somerset. *Rev. Palaeobot. Palynol.* 17, 133-147. DOI: 10.1016/0034-6667(74)90095-5

Warrington, G., 1980. Palynological studies of Triassic rocks in central Somerset (Abstract). *Proc. Ussher Soc.* 5, 90

Warrington, G., 1983. "Appendix 4: Mesozoic micropalaeontological studies", in *Geology of the country around Weston-super-Mare*. Editors Whittaker, A., Green, G.W., (London: HMSO) 131-132

Warrington, G., 1995. The Permian, Triassic and Jurassic in Northern Ireland: A palynological study with special reference to the hydrocarbon prospectivity of the Larne – Lough Neagh Basin. Geological Survey of Northern Ireland. Technical Report GSNI/95/7

Warrington, G., 1997. The Lyme Regis Borehole, Dorset – Palynology of the Mercia Mudstone, Penarth and Lias Groups (Upper Triassic-Lower Jurassic). *Proc. Ussher Soc.* 9, 153-157

Warrington, G., Ivimey-Cook, H.C., 1992. "Triassic", in *Atlas of palaeogeography and lithofacies: Geological Society Memoir, London*. Editors Cope, J.C.W., Ingham, J.K., Rawson, P.F., 13, 97-106. DOI: 10.1144/GSL.MEM.1992.013.01.11

Warrington, G., Ivimey-Cook, H.C., Edwards, R.A., Whittaker, A., 1995. The Late Triassic-Early Jurassic succession at Selworthy, west Somerset, England. *Proc. Ussher Soc.* 8, 426-432

Warrington, G., Pollard, J.E., 2021. On the records of the brachiopod 'Lingula' and associated fossils in Mid-Triassic deposits in England. *Proc. Yorks. Geol. Soc.* 63, 1–9. DOI: 10.1144/pygs2020-015

Warrington, G., Whittaker, A., 1984. The Blue Anchor Formation (Late Triassic) in Somerset. *Proc. Ussher Soc.* 6, 100-107

Warrington, G., Audley-Charles, M.G., Elliott, R.E., Evans, W.B., Ivimey-Cook, H.C., Kent, P., Robinson, P.L., Shotton, F.W., Taylor, F.M., 1980. A correlation of Triassic rocks in the British Isles. *Geol. Soc. Lond.,* Special Report No. 13

Whittaker, A., 1972. The Somerset Saltfield. *Nature*, 238, 265-266. DOI: 10.1038/238265a0

Whittaker, A., 1983. "Appendix 1: Burton Row Borehole, Brent Knoll", in *Geology of the country around Weston-super-Mare*. Editors Whittaker, A., Green, G.W., (London: HMSO) 121-123

Whittaker, A., Green, G.W., 1983. Geology of the county around Weston-Super-Mare. *Mem. Geol. Surv. G.B.,* Sheet 279 with parts of 263 and 295. (London: HMSO) 147 pp.

Wignall, P.B., Bond, D.P.G., 2008. The end-Triassic and Early Jurassic mass extinction records in the British Isles. *Proc. Geol. Assoc.* 119, 73-84. DOI: 10.1016/S0016-7878(08)80259-3

Wills, L.J., 1970. The Triassic succession in the central Midlands in its regional setting. *Quart. J. Geol. Soc.* 126, 225-283. DOI: 10.1144/gsjgs.126.1.0225

Wilson, A.A., 1990. The Mercia Mudstone Group (Trias) of the East Irish Sea Basin. *Proc. Yorks. Geol. Soc.* 48, 1-22. DOI: 10.1144/pygs.48.1.1

Wilson, A. A., 1993. The Mercia Mudstone Group (Trias) of the Cheshire Basin. *Proc. Yorks. Geol. Soc.* 49, 171–188. DOI: 10.1144/pygs.49.3.171

Wilson, A.A., Evans, W.B., 1990. Geology of the country around Blackpool. *Memoir of the British Geological Survey*, Sheet 66 (England and Wales)

Wilson, H.E., Manning, P.I., 1978. Geology of the Causeway Coast. *Mem. Geol. Surv. North. Irel.* 2, Sheet 7

Woods, P.J.E., 1973. Potash exploration in Yorkshire: Boulby Mine pilot borehole. *Tans. Inst. Miner. Metall. Trans.* 82B, 99-106

Worden, R.H., Smalley, P.C., Fallick, A.E., 1997. Sulfur cycle in buried evaporites. *Geology*, 25, 643-646. DOI: 10.1130/0091-7613(1997)025<0643:SCIBE>2.3.CO;2

Worley, N.E., 2005. The occurrence of halite in the Permian A Bed Evaporite, Kirkby Thore, Cumbria. *Proc. Yorks. Geol. Soc.* 55, 199-203. DOI: 10.1144/pygs.55.3.199

Wright, V.P., Sandler, A., 1994. A hydrogeological model for the early diagenesis of Late Triassic alluvial sediments. *J. Geol. Soc., London*, 151, 897-900. DOI: 10.1144/gsjgs.151.6.0897

Yao, W., Wortmann, U.G., Paytan, A., 2019. “Sulfur isotopes — Use for stratigraphy during times of rapid perturbations”, in *Stratigraphy and timescales*. Editor Montenari, M., (Amsterdam: Elsevier Academic Press) 4, 1-33. DOI: 10.1016/bs.sats.2019.08.004

Zhang, Y., Ogg, J.G., Franz, M., Bachmann, G.H., Szurlies, M., Röhling, H-G., Li, M., Rolf, C., Obst, K., 2020. Carnian (Late Triassic) magnetostratigraphy from the Germanic Basin allowing global correlation of the Mid-Carnian Episode. *Earth Planet. Sci. Lett.* 541, 116275. DOI: 10.1016/j.epsl.2020.116275

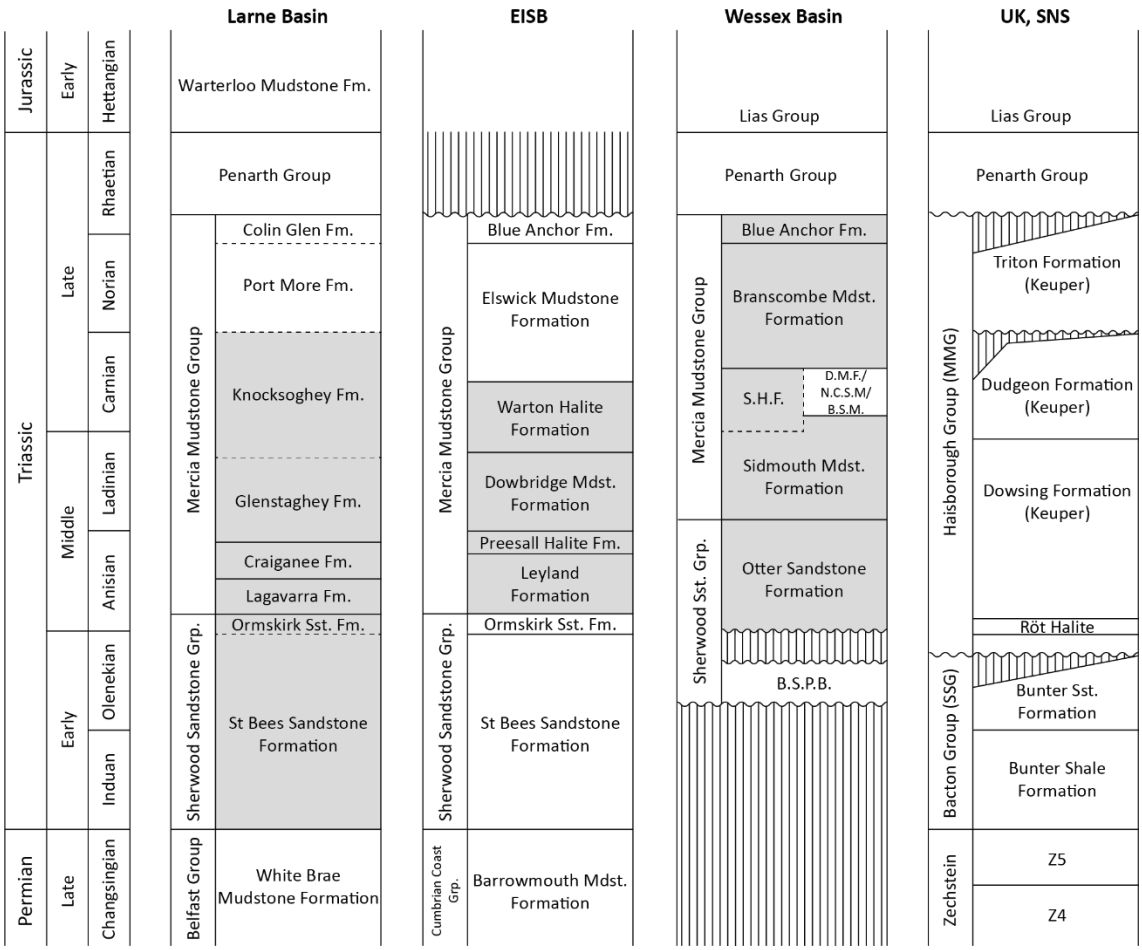

Figure 1: *The established lithostratigraphic framework for the UK Triassic in the regions considered as part of this study. The major lithostratigraphic units are provided, along with the regional names and stratigraphic position of rock formations. The grey shaded intervals are those from which samples were analysed for this study. Abbreviations: Sst. = sandstone; Mdst. = mudstone; Fm. = formation; Grp. = group; S.H.F. = Somerset Halite Formation; D.M.F. = Duncombe Mudstone Formation; N.C.S.M. = North Curry Sandstone Member; B.S.M. = Butcombe Sandstone Member. The lithostratigraphy of the Larne Basin, East Irish Sea Basin (EISB), Wessex Basin, and UK Southern North Sea (SNS) are based upon Mitchell (2004), Jackson and Johnson (1996), Howard et al. (2008) and Salisbury et al. (2023), respectively.*

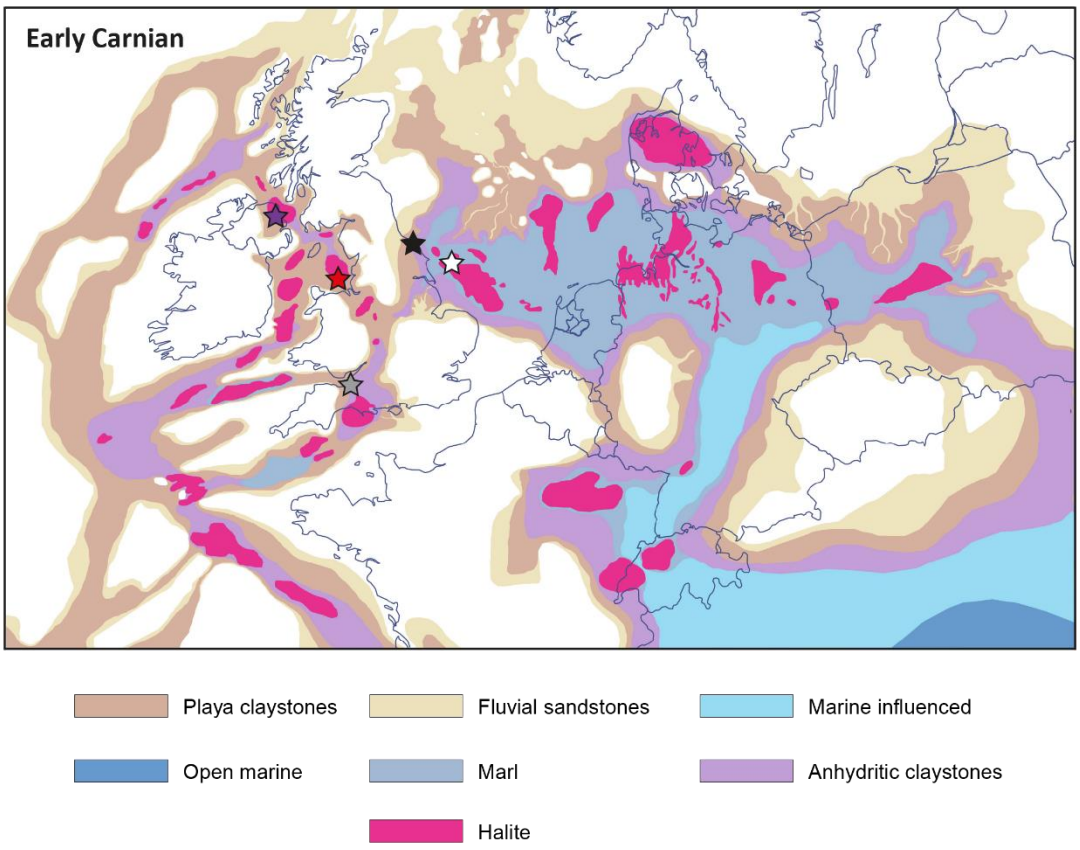

Figure 2: *Palaeogeography of northwest Europe during the early Carnian (Late Triassic). Sample site locations: Purple star represents the locations of GT-01 Kilroot, Cairncastle-2 and Carnduff-02, due to the close geographic proximity of these sample sites. The red star represents 110/13-8 of the East Irish Sea Basin (EISB), the grey star Burton Row of the Wessex Basin, the black star Staithes S-20 of the Cleveland Basin and the white star 42/28-2 of the UK Southern North Sea (SNS).*

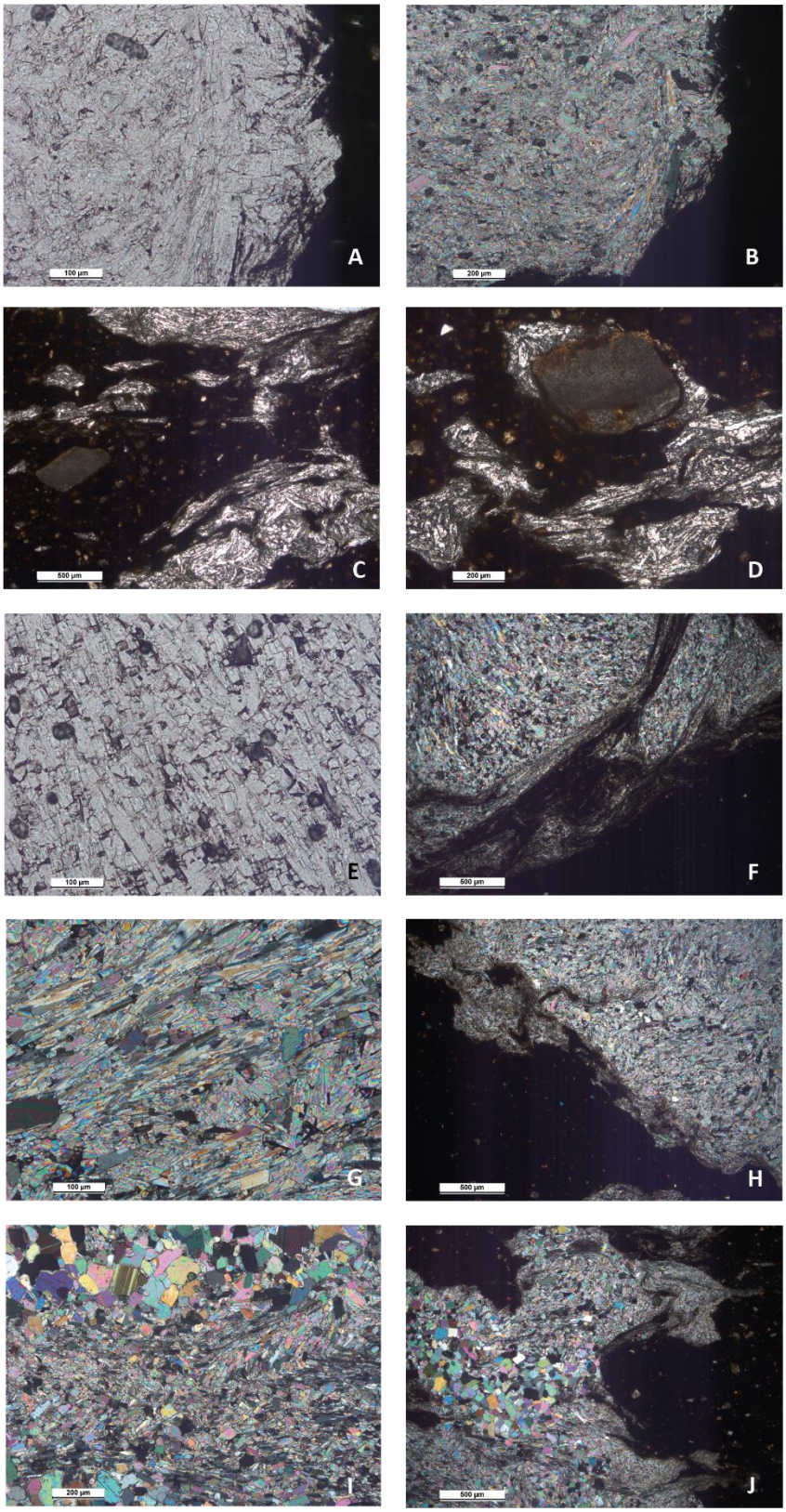

Figure 3: *Thin section views of the nodular anhyritic siltstone/mudstone facies of the Mercia Mudstone Group, Burton Row borehole. (A) An anhydrite nodule and contact with matrix (10 x magnification) at 429.5 m depth in transmitted light; (B) An anhydrite nodule and contact with matrix (5 x magnification) at 429.5 m depth in cross-polarised*

light; (C) Small anhydritie nodules (2.5 x magnification) at 599 m depth in transmitted light; (D) Small anhydrite nodules (5 x magnification) at 599 m depth in transmitted light; (E) A large anhydrite nodule (10 x magnification) at 622 m depth in transmitted light; (F) anhydrite nodule and contact with matrix (2.5 x magnification) at 622 m depth in cross-polarised light; (G) Anhydrite nodule (10 x magnification) at 810 m depth in cross-polarised light; (H) Anhydrite nodule and contact with matrix (2.5 x magnification) at 810 m depth in cross-polarised light; (I) Anhydrite nodule (5 x magnification) at 829.5 m depth in cross-polarised light; (J) Anhydrite nodule and contact with matrix (2.5 x magnification) at 829.5 m depth in cross-polarised light.

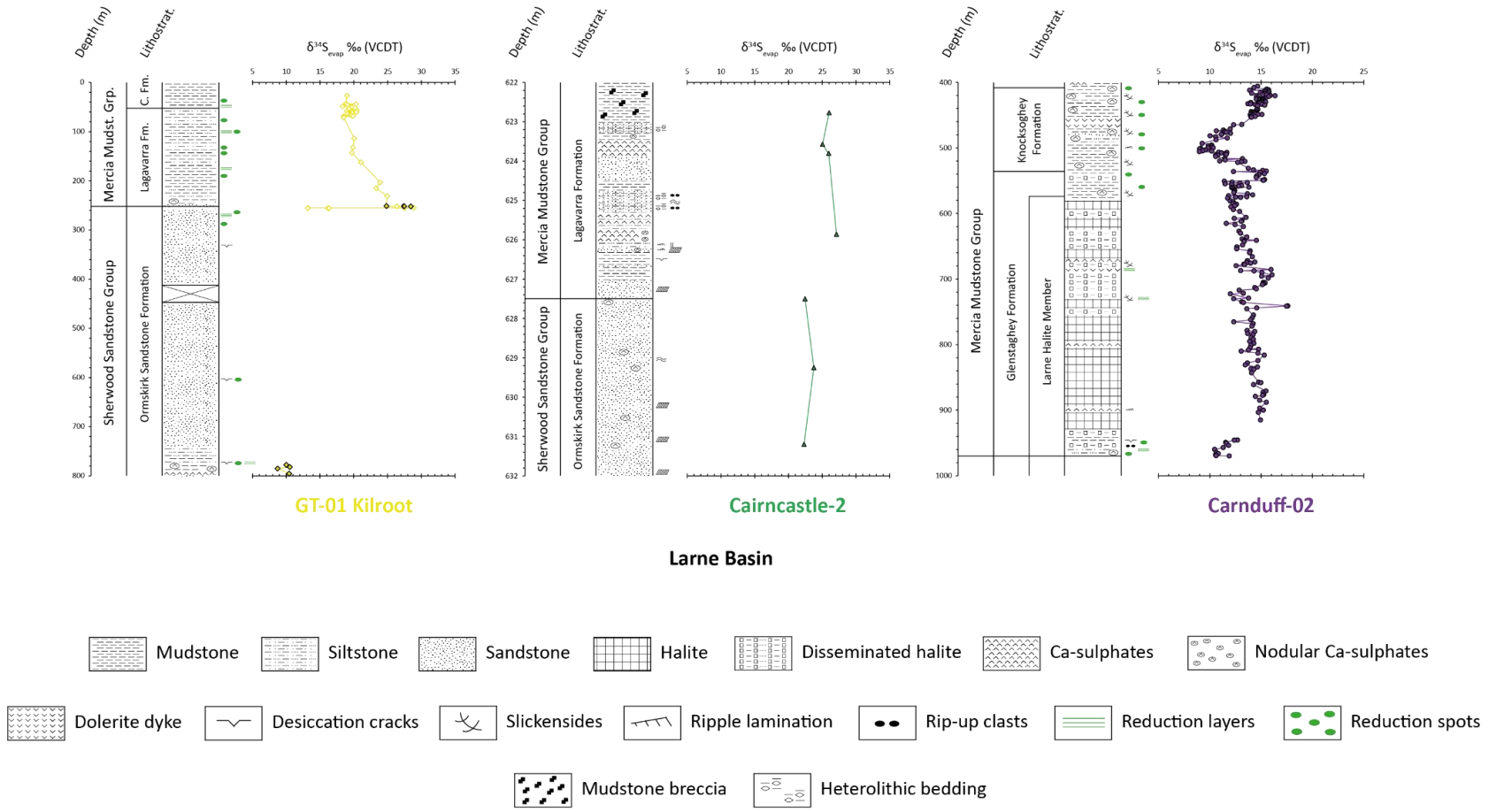

Figure 4: *The $\delta^{34}S_{evap}$ profiles of GT-01 Kilroot (left), Cairncastle-2 (middle) and Carnduff-02 (right). For GT-01 Kilroot, the $\delta^{34}S_{evap}$ values from nodular Ca-sulphates are represented by the filled symbols, while $\delta^{34}S_{evap}$ values from veined Ca-sulphate are represented by empty symbols. The stratigraphic log for GT-01 Kilroot is based upon the original drillers report, the log for Cairncastle-2 is based upon our own observations and the log for Carnduff-02 is based upon the original drillers report and the log of Andeskie et al. (2018).*

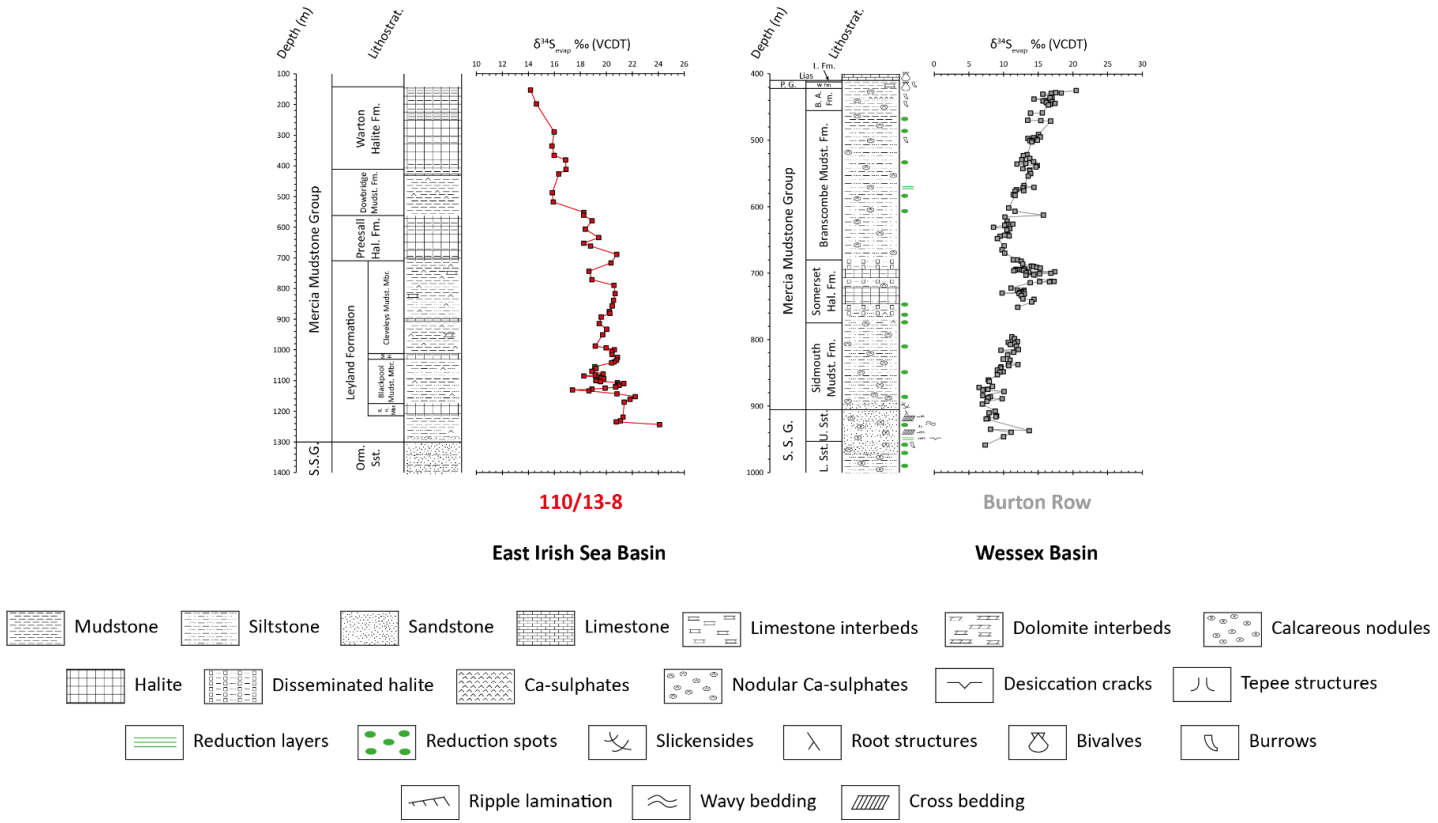

Figure 5: *The $\delta^{34}S_{evap}$ profiles for 110/13-8 of the East Irish Sea Basin (EISB) (left) and Burton Row of the Wessex Basin (right). The stratigraphic log for 110/13-8 is based upon the original drilling report and the stratigraphic log for Burton Row is based upon a combination of our own observations and Whittaker in Whittaker and Green (1983). Abbreviations: Sst. = sandstone; Mudst. = mudstone; Hal. = halite; Fm. = formation; S.S.G. = Sherwood Sandstone Group; Orm. Sst. = Ormskirk Sandstone; R. H. Mbr. = Rossall Halite Member; M. H. = Mythop Halite; L. Sst. = Lower Sandstone; U. Sst. = Upper Sandstone; B. A. Fm. = Blue Anchor Formation; P. G. = Penarth Group; W. Fm. = Westbury Formation; L. Fm. = Lilstock Formation.*

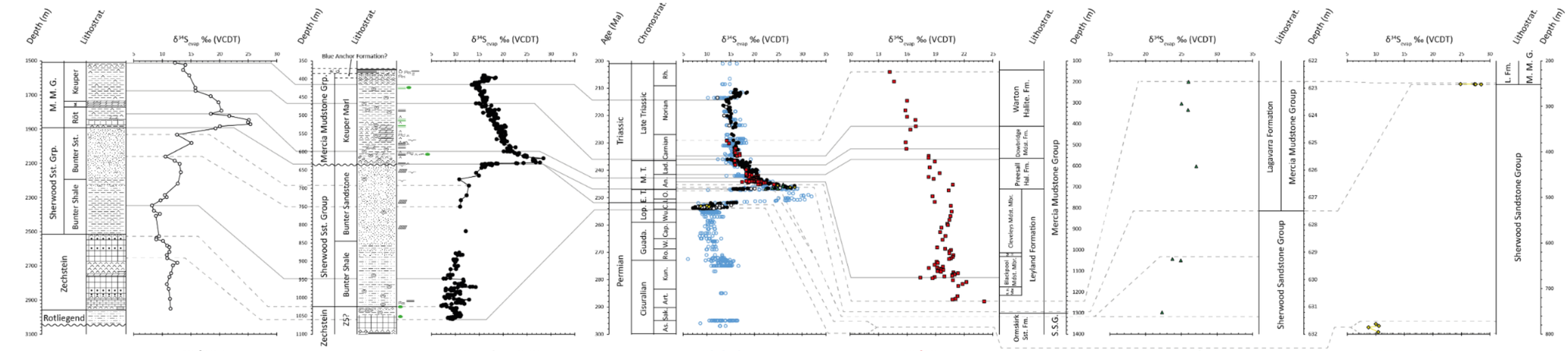

Figure 6: *Correlation scheme between the global composite $\delta^{34}S_{evap}$ curve of Salisbury et al. (2022) and the $\delta^{34}S_{evap}$ profiles of 42/28-2 (Salisbury et al., 2023), Staithes S-20 (Salisbury et al., 2022), 110/13-8, Cairncastle-2 and GT-01 Kilroot (this study). The log of Staithes S-20 is based upon Woods (1973) and our own direct observations, while the log of 42/28-2 is based upon the drilling report. The correlation schemes for 42/28-2 and Staithes S-20 were established in Salisbury et al. (2022, 2023). The correlation lines are based primarily upon trends and inflection points within the $\delta^{34}S_{evap}$ profiles, with biostratigraphic data providing further constraint (see main text). Solid grey correlation lines represent correlations made with relative confidence, while the dashed grey lines represent correlations associated with a greater degree of uncertainty. The $\delta^{34}S_{evap}$ profiles are stretched and compressed within the correlation lines and overlain onto the global composite $\delta^{34}S_{evap}$ curve. Abbreviations: S.S.G. = Sherwood Sandstone Group; M.M.G. = Mercia Mudstone Group; P.G. = Penarth Group; R. H. Mbr. = Rossall Halite Member; M.H. = Mythop Halite; L.F. = Lagavarra Formation; M. = Muschelkalk; E.T. = Early Triassic; M.T. = Middle Triassic; As. = Asselian; Sak = Sakmarian; Art. = Artinskian; Kun. = Kungurian; Ro. = Roadian; W. = Wordian; Cap. = Capitanian; Wu. = Wuchiapingian; C. = Changhsingian; I. = Induan; O. = Olenekian; An. = Anisian; Lad. = Ladinian; Rh. = Rhaetian.*

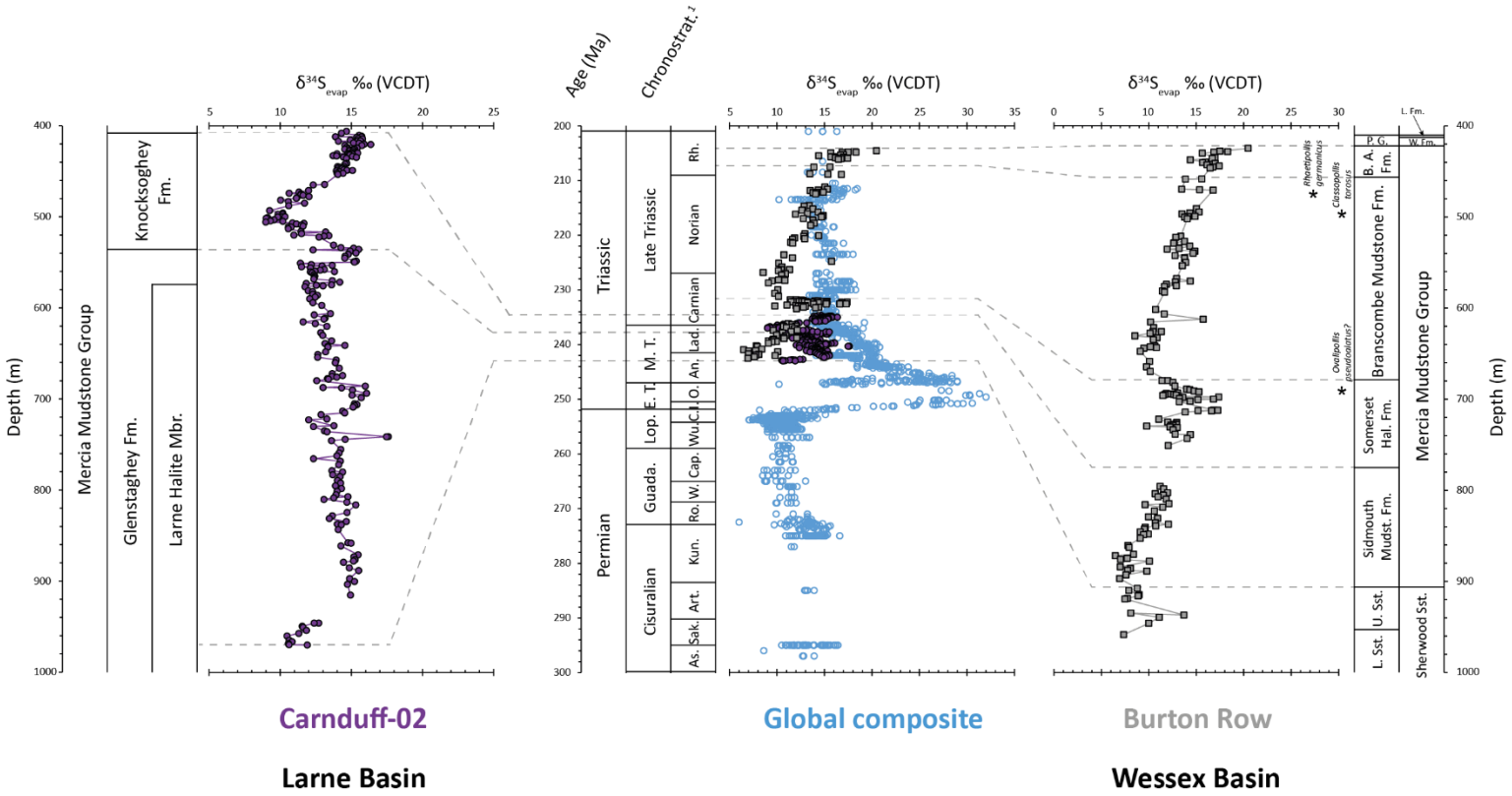

Figure 7: *The $\delta^{34}S_{evap}$ profiles of Carnduff-02 (Larne Basin) and Burton Row (Wessex Basin) compared with the global composite curve. The age models for Carnduff-02 and Burton Row are based upon published biostratigraphy and magnetostratigraphy, and not upon the sulphur isotope records. Accordingly, the correlation lines are drawn as dashed grey lines, to relfect the uncertainty associated with their placement. The $\delta^{34}S_{evap}$ profiles are stretched and compressed within the correlation lines and overlain onto the global composite $\delta^{34}S_{evap}$ curve. The global composite curve includes data from the literature (Salisbury et al., 2022), data from 42/28-2 (Salisbury et al., 2023) and data from GT-01 Kilroot and Cairncastle-2 (this study). For the abbreviations, see Fig. 6*

Chapter 5

Biogeochemical changes in a hypersaline sabkha of the late Permian Eden Shales, UK: Stable isotopes and organic geochemistry

Jack Salisbury[1*], Vincent Grossi[2], Eva E. Stüeken[3], Balkis Eddhif[4], Arnauld Vinçon-Laugier[4], Ross Collin[5], Tom McKie[6], Darren R. Gröcke[1]

1. Stable Isotope Biogeochemistry Laboratory (SIBL), Department of Earth Sciences, Durham University, South Road, Durham DH1 3LE, UK

2. Aix Marseille Univ, Université de Toulon, CNRS, IRD, Mediterranean Institute of Oceanography (MIO), Marseille, France

3. School of Earth and Environmental Sciences, University of St Andrews, St Andrews KY16 9TS, UK

4. Univ Lyon, UCBL, ENS Lyon, CNRS, Laboratoire de Géologie de Lyon (LGL-TPE), Villeurbanne, France

5. Saint-Gobain Interior Solutions, Geological and Mining Services, East Leake, Loughborough LE12 6HX, UK

6. Shell UK Exploration and Production, 1 Altens Farm Road, Nigg, Aberdeen AB12 3FY, UK

** = corresponding author: jack.salisbury@durham.ac.uk*

The Eden Shales are largely composed of evaporitic mudstones and siltstones, deposited during the late Permian, a time interval associated with major biological and climatic perturbations. The evaporitic lithology of the Eden Shales is characteristic of the warm and arid palaeoenvironment of the late Permian and has been inferred to represent deposition within a playa lake system. However, it can be difficult to confidently distinguish between evaporites of marine and nonmarine origin, with the model of deposition for the Eden Shales remaining a subject of debate. Here, we present a suite of stable isotopic and molecular geochemical data to refine our understanding of the biogeochemical conditions of the palaeoenvironment during deposition. While our interpretations remain speculative, we define two intervals characterised by distinct biogeochemistry, Stage 1 spanning the A Bed evaporite, and Stage 2, including evaporite beds B and C. We suggest that Stage 1 may represent deposition within a playa lake system, in line with the established depositional framework. This, however, remains somewhat speculative, in part due to possible diagenetic overprinting of $\delta^{34}S_{evap}$. In Stage 2, we suggest a possible increase in the degree of marine influence, with $\delta^{34}S_{evap}$ data in close comparison with values established for late Permian seawater. In addition, we report extreme enrichment in $\delta^{13}C_{org}$ (>0 ‰), broadly concomitant with a decline in $\delta^{15}N_{tot}$, highly variable $\delta^{34}S_{CRS}$ values, a low Pr/Ph ratio (0.48) and the detection of saturate and aromatic carotenoids associated with cyanobacteria and phototrophic sulphur bacteria, respectively. We suggest the $\delta^{13}C_{org}$ enrichments, declining $\delta^{15}N_{tot}$ and presence of a saturate carotenoid, β-carotane, reflect phototrophic productivity under conditions of hypersalinity, while variable $\delta^{34}S_{CRS}$ and the presence of aromatic carotenoids indicate

sulphate limitation and the expansion of photic zone euxinia, possibly within microbial mat communities.

1. Introduction

The Late Permian and Triassic have received much attention over the previous 50 years due to numerous events of geological significance, including the End Permian Mass Extinction (EPME), one of the 'Big Five' extinction events (Sepkoski, 1996). The depositional environment of the UK Late Permian and Triassic was largely arid and continental (Parrish, 1993), with frequent and repeated marine influence, facilitating widespread evaporite deposition (McKie, 2017). Recent advances in the application of evaporite-based sulphur isotope ($\delta^{34}S_{evap}$) records for stratigraphy have seen success in establishing further age calibration for evaporites of the UK Triassic (Salisbury et al., 2022; Salisbury et al., *in prep.*), while also assisting in further constraining the degree of marine influence during evaporite deposition across distinct UK sub-basins (Salisbury et al., *in prep.*).

The late Permian evaporitic stratigraphy of the Vale of Eden, northwest England, presents the opportunity to generate additional $\delta^{34}S_{evap}$ records to establish further chronostratigraphic constraint to late Permian UK evaporites. In addition, much controversy persists regarding the specific environmental and biogeochemical conditions that characterised the deposition of the Eden Shales, with the degree of marine influence continuing to lack constraint (Holliday et al., 1993; Hughes, 2003; Worley, 2005). The currently established model involves initial evaporite deposition within terrestrial saline lakes (Worley, 2005), followed by an expansion in the spatial coverage of the evaporitic facies and a possible increase in marine influence (Burgess

and Holliday, 1974; Hughes, 2003); This, however, lacks any robust geochemical constraint. It can be particularly difficult to distinguish between marine and nonmarine evaporites based upon sedimentology alone (e.g., Leitner et al., 2023), and thus, there is a need to better establish the nature of the palaeoenvironment during deposition of the Eden Shales via geochemical methodologies.

Evaporites form under extreme conditions, often being deposited in arid and warm climates. They exhibit high degrees of salinity and can be characterised by extremes in acidity or alkalinity (Warren, 2010; 2021). As a result, they have been associated with unique isotope systematics, often mediated by communities of halotolerant organisms adapted to the inhospitable evaporitic environment, with extreme enrichments in carbon (e.g., Schidlowski et al., 1984; Stiller et al., 1984; Birgel et al., 2015; Dorador et al., 2018) and nitrogen isotopes (e.g., Isaji et al., 2019). The evaporitic depositional environment of the Eden Shales, and the presence of structures tentatively identified as microbial mats throughout the stratigraphy (Arthurton, 1971; Burgess and Holliday, 1974; Hughes, 2003), present the opportunity to study the biogeochemistry and geobiology of hypersaline environments in deep time. Here, we apply a range of geochemical tools, including stable isotope systems and lipid biomarker analysis, to provide further constraint to the biogeochemical evolution of the Eden Shales.

2. Geological setting

The Vale of Eden is a small N–S-trending fault-bounded basin (Ruffell et al., 2006) that likely formed in an intermontane setting during early Permian extension along the Pennine and Dent fault systems (Underhill et al., 1988; Hughes, 2003). Permian strata

rest unconformably upon the Carboniferous, with the unconformity a product of erosion that was initiated during the late carboniferous Variscan Orogeny and continued into the early Permian (Ruffell et al., 2006). In most parts of NW England, including the Vale of Eden, the Permian stratigraphy is divided into the Appleby and Cumbrian Coast groups (Hughes, 2003; Ruffell et al., 2006) (Fig. 1). They are overlain by the Early Triassic St Bees Sandstone of the Sherwood Sandstone Group (SSG); however, the precise stratigraphic position of the Permian-Triassic boundary is unclear (Arthurton, 1971) (see below). The gradual northward movement of the Gondwanan-Laurasian landmass (Ruffell et al., 2006) and, in the late Permian, a general warming trend in Earth's climate (Chumakov and Zharkov, 2003), contributed to warm and arid to semi-arid conditions (Macchi, 1981), facilitating widespread evaporite deposition (Fig. 2).

The boundary between the Penrith Sandstone Formation and the late Permian Eden Shales in the Vale of Eden shows evidence of diachroneity, with a sharp contact in the north and centre of the basin, and a gradational boundary in the south (Arthurton and Wadge, 1981; Ruffell et al., 2006). The Eden Shales exhibit substantial spatial lithologic variability, including mudstones, siltstones, fine- to coarse-grained sandstones and conglomerates, along with dolomite and an abundance of evaporites, including gypsum/anhydrite nodules, beds and late diagenetic displacive gypsum veins, as well as localised volumes of halite (Burgess and Holliday, 1979; Hughes, 2003; Worley, 2005). In addition, stromatolitic layers and *Esteria* have also been reported from particular stratigraphic intervals (Arthurton, 1971; Ruffell et al., 2006). Units of abundant evaporitic material have been designated as evaporite beds A through to D, with a dolomitic interval known as the Belah Dolomite occurring beneath D Bed (see Burgess and Holliday, 1979; Arthurton and wadge, 1981; Hughes; 2003 for details).

A Bed has a restricted spatial extent of approximately 20 km^2 (Hughes, 2003; Worley, 2005), and grades laterally to the south into the Hilton Plant Beds, an interval of laminated sandstones, with calcareous/dolomitic mudstones and siltstones, scattered Ca-sulphate nodules, stromatolitic layers and transported plant material (Burgess and Holliday, 1979; Hughes, 2003; Ruffell et al., 2006). The overlying evaporite beds, along with the Belah Dolomite, are sufficient in thickness and distribution to act as stratigraphic markers for lithostratigraphic correlation beyond the Vale of Eden (Holliday, 1993; Holliday et al., 2001; Hughes, 2003). Overlying the D Bed evaporites, the Eden Shales transition into sandstones of likely aeolian origin (Burgess and Holliday, 1979), before gradually grading vertically into fluvial sandstones of the St Bees Sandstone (Sherwood Sandstone Group) (Hughes, 2003; Ruffell et al., 2006).

The environment of deposition for the Eden Shales is generally viewed as a continental playa lake system, with Burgess and Holliday (1979) reporting a variety of sedimentary structures throughout the Eden Shales of the Hilton Beck borehole, including fluvial cross-lamination, mud flake conglomerates, soft-sediment deformation, desiccation cracks and adhesion ripples. Along with the evaporites, these features have been viewed as representative of a terrestrial depositional regime, in which evaporites were deposited within continental playa lakes, with fluvial influence and intermittent aeolian reworking (Burgess and Holliday, 1979; Hughes, 2003; Worley, 2005; Ruffell et al., 2006). Possible marine influence, and its' extent if present, remains speculative. The small spatial extent of A Bed has reinforced the view that it should be defined as an evaporite-bearing facies of continental origin (Arthurton et al., 1978), infilling a depression within the pre-existing strata directly underlying the Cumbrian Coast Group (Worley, 2005; Hughes, 2003; Ruffell et al., 2006). In addition, there is no evidence for

direct flooding from the Brakavellia Sea of the East Irish Sea Basin (EISB) at this time, nor does it seem likely that a cross-Pennine connection had yet been established with the Southern North Sea (Ruffell et al., 2006). Thus, it has been suggested that the playa lake was fed by a fluvial system (Hughes, 2003; Worley, 2005), and that the Ca-sulphates and halite formed in a terrestrial setting. Accordingly, the laterally equivalent Hilton Plant Beds likely represent a sheet flood deposit, formed at the periphery of the A Bed saline lake system, and deposited from the fluvial system feeding the lake (Burgess and Holliday, 1979; Hughes, 2003; Ruffell et al., 2006).

In contrast, some have suggested the overlying evaporites formed through the ingress of marine groundwaters (Burgess and Holliday, 1979; Hughes, 2003). Lithostratigraphic correlation between the Vale of Eden, EISB, west Cumbria, the Carlisle Basin, and the southern North Sea (Holliday, 1993; Holliday et al., 2001), has been interpreted to suggest a cross-Pennine connection with the marine evaporites of the SNS since the deposition of beds B and C, relating the evaporites of the Eden Shales within the Vale of Eden to sea level high stands in the SNS (Holliday, 1993). In addition, sparse marine microfossils have also been recovered from the EZ1 in the Annan sub-basin north of the Vale of Eden (Holliday et al., 2001). However, subsequent findings reveal another possible seawater ingress route along the west of the UK, generated during Late Permian extension along the Norwegian-Greenland Rift, which propagated south along the Atlantic Margin and into the Irish Sea (Coward, 1995; McKie, 2017). Zechstein-equivalent evaporitic sabkha and halite are present in West Orkney (Hitchen et al., 1995) and continue south to the west of Ireland (McKie, 2017). In addition, there exists a well-developed clastic fringe along the basin margin of the UK SNS, including sandy fluvial fans, marking the westerly edge of marine deposition within the basin (Moscariello,

2005; McKie, 2017). Thus, assuming marine influence was active during deposition of the Eden Shales, it seems the most likely route for seawater ingress would have been along the west of the UK, with a cross-Pennine connection, if present, accounting for a relatively minor contribution.

It should be stressed that lithostratigraphic correlation and marine microfossils do not directly confirm marine inundation and there have currently been no attempts to directly constrain the source of the evaporite brines with geochemical methods. Thus, other than the Belah Dolomite, there exists no direct confirmation of marine inundation during the deposition of the Eden Shales.

2.1. Biostratigraphy and age assignment

Due to the hypersaline and arid nature of the depositional environment, the Permian stratigraphy of the UK is impoverished in fossil content suitable for biostratigraphy (Smith et al., 1972). The Permian stratigraphy of the Vale of Eden is no exception to this, and with a particular scarcity of age-diagnostic fossils, a lack of precise age-calibration persists (Hughes, 2003). The age assignment for the Appleby Group is based primarily upon sporadic vertebrate tracks and miospores (Ruffell et al., 2006). Vertebrate tracks in the Penrith Sandstone identified as *Chelichnus* have been recorded from Penrith and suggest a Late Permian age for much of the Appleby Group (see Holliday et al., 2004 for details). Miospores recovered from the Penrith Sandstone where it interfingers with the base of the overlying Eden Shales are comparable to those found in the Eden Shales, and thus further constrain the uppermost Penrith Sandstone to the Late Permian (Holliday et al., 2004; Warrington, 2008).

For the Eden Shales of the Cumbrian Coast Group, miospore assemblages of Late Permian (Wuchiapingian or Changhsingian) age for the strata below and including the Belah Dolomite (Holliday et al., 2004; Warrington, 2008). The overlying uppermost Cumbrian Coast Group have failed to yield fossil material from which an age assignment can be established (Ruffell et al., 2006). However, lithostratigraphic correlation based upon geophysical log signatures suggests that strata ~35m above the Belah Dolomite can be recognised as correlatives of the Bröckelscheifer Member (Holliday et al., 1993). Thus, the uppermost Cumbrian Coast Group could be assigned to the Early Triassic (Ruffell et al., 2006) (Fig. 1), although it should be emphasised that there are no biostratigraphic data to confirm this.

3. Methodology

3.1. Sampling

Samples were acquired from the latest Permian Eden Shales of drillcore KT1153, drilled near Kirkby Thore, Cumbria, NW England. 1 m intervals of core were powdered and homogenised by British Gypsum, and thus each sample represents a lithological average over a 1 m stratigraphic interval.

3.2. Sulphur isotope analysis of sulphate and sulphide

The samples underwent sulphate concentration via barium sulphate ($BaSO_4$) precipitation. Approximately 3-5 g of powdered sample were submerged in ~50 ml of a 10 % NaCl deionised water solution to facilitate the dissolution of evaporitic material. Blanks of NaCl produced no visible $BaSO_4$. The material was left to sit in solution for 24-48 hours and agitated every few hours during the working day. Upon dissolution, the

samples underwent centrifugation at 3,500 rpm for 5 minutes. Approximately 50 % of the saline solution for each sample was transferred into a 50 ml centrifuge tube. 20-25 ml of 10 % barium chloride ($BaCl_2$) was added, with the solution often turning cloudy immediately, indicating $BaSO_4$ precipitation. The pH of the solution was reduced to ~1-2 with the addition of 3M HCl to prevent the precipitation of barium carbonate ($BaCO_3$). The samples were left for ~24 hours to ensure the $BaSO_4$ precipitation process reached completion. The $BaSO_4$ underwent centrifugation at 3,500 rpm for 3 minutes, after which the $BaCl_2$/HCl supernatant was discarded according to safety regulations for appropriate waste disposal. The resultant pellet of $BaSO_4$ was rinsed with ~30–40 mL of deionised water to neutralise the sample. Neutrality was often achieved after three rinses. The $BaSO_4$ was placed in a drying oven set at 80°C for between 24 and 48 hours. Once dry, it was then crushed into a fine powder using an agate pestle and mortar and archived in a 1.5 ml centrifuge tube.

Sulphide was extracted from 1-1.5 g of untreated powdered sample following a sequential chromium reduction method modified from Canfield et al. (1986). Sulphur is first liberated as hydrogen sulphide (H_2S) from acid-volatile sulphides (AVS), such as greigite, mackinawite, troilite, pyrrhotite, marcasite, sphalerite, via reaction with HCl. Subsequently, pyrite sulphur is released using a chromium(II) chloride solution. Over a hot plate and under a distillation line in a nitrogen atmosphere, we reacted our samples with ~20 ml of 6M HCl to release sulphur from AVS components and left the sample to react for ~1-1.5 hours. The resultant H_2S was trapped using a silver nitrate solution, converting the sulphur into silver sulphide ($NH_4(OH)$). Subsequently, ~20 ml of the 1M chromous chloride solution was added to the sample and HCl and was left to react over the hot plate for ~3 hours. Again, the resultant H_2S was trapped using a $AgNO_3$.The Ag_2S

precipitate was cleaned using 1M ammonium hydroxide ($NH_4(OH)$) and subsequently rinsed with ultra-pure (18 MΩ·cm) water. The Ag_2S was then separated from the supernatant via filtration through a vacuum filter system using cellulose nitrate membrane filters. The samples were subsequently dried in a drying oven and crushed into a fine powder using an agate pestle and mortar.

For sulphur isotope analysis, each sample was weighed into 5 x 3.5 mm tin capsules, with a desired weight range of 0.2-0.4 mg for $BaSO_4$ and 0.1-0.15 mg for CRS and AVS. In some cases, the AVS yield was too small to separate the precipitate from the filter paper and as a result, it was common for AVS to be combusted along with the filter paper during isotopic analysis. This prevents an accurate calculation of sulphur content (wt %) but has no impact on the sulphur isotope data. Stable sulphur isotope analysis was performed in the Stable Isotope Biogeochemistry Laboratory (SIBL) at Durham University using a Thermo Scientific EA IsoLink™ coupled to a Thermo Scientific Delta V Plus isotope-ratio mass-spectrometer. Sulphur isotope ratios are expressed in standard delta (δ) notation in per mil (‰) relative to Vienna Canyon Diablo Triolite (VCDT). The $\delta^{34}S$ data were normalised through calibration against four international standards (IAEA-S-1, IAEA-S-2, IAEA-S-3, NBS 127), providing a linear range in $\delta^{34}S$ between -32.5 ‰ and +22.6 ‰. An internal barium sulphate (Acros Organics silver sulphate, catalogue number: 194070100, lot: A0384698) was analysed throughout the analytical period and produced an average $\delta^{34}S$ value of -18.1 ‰ ± 0.25 (1 σ) (n = 14). Analytical uncertainty of $\delta^{34}S$ is typically ±0.2 ‰ (2 σ) for replicate analyses of the international standards. Reproducibility of the sample $\delta^{34}S_{evap}$ data was the same or better. Total sulphur content (wt %) of the samples was calculated as part of the isotopic analysis with the use of an internal standard, sulphanilamide (S = 18.619 wt %).

3.3. Carbon isotope analysis of bulk organic matter

Powdered samples underwent acidification to remove carbonate phases and isolate the organic matter for subsequent carbon isotope analysis. Approximately 5 g of powdered sample were acidified with ~50 ml of 3M HCl at room temperature. The samples were left to acidify for ~24 hours, after which they underwent centrifugation at 3,500 rpm for 3 minutes. In an effort to assess potential biases in the measured $^{13}C_{org}$ values due to the presence of dolomite in the samples, aliquots of a sample at 40.58 m depth were also acidified either with phosphoric acid at room temperature or with 6M HCl heated to ~60 °C. The acidic solution was discarded, and the samples were neutralised with ~50 ml of DI-water, with neutralisation being achieved after 5 rinses. The samples were subsequently placed in a drying oven set to ~55 °C and left for ~48 hours. Once dry, the decalcified residues were homogenised using an agate pestle and mortar and transferred into 1.5 ml centrifuge tubes for storage.

For carbon isotope analysis, the samples were weighed into tin capsules, with a desired weight range between 1 and 70 mg depending on TOC (wt %) content. Isotope analysis was performed in SIBL at Durham University using a Costech Elemental Analyser (ECS 4010) coupled to a Thermo Finnigan Delta V Advantage isotope-ratio mass-spectrometer. Carbon isotope ratios were corrected for ^{17}O contribution and reported in standard delta (δ) notation in per mil (‰) relative to Vienna Pee Dee Belemnite (VPDB). The $\delta^{13}C_{org}$ data were normalised through calibration against four international standards (USGS 40, USGS 24, IAEA 600, IAEA CH6), providing a linear range in $\delta^{13}C$ between +2 and -47 ‰. Analytical uncertainty for $\delta^{13}C_{org}$ was typically ±0.1 ‰ (2 σ) for replicate analyses of the international standards and typically <0.2 ‰ for replicate

sample analyses. The elemental analyser was set to “no dilution mode” and all analyses produced a CO_2 signal > 800 mV, providing maximum confidence in the $\delta^{13}C$ values. Total organic carbon content (wt %) was calculated as part of the isotopic analysis using an internal standard, glutamic acid (C = 40.82 wt %).

3.4. Nitrogen isotope analysis

Untreated (raw) powdered sediment samples were weighed into tin capsules, with a desired weight range of 20-70 mg. Isotope analysis was performed in SIBL at Durham University using a Costech Elemental Analyser (ECS 4010) coupled to a Thermo Finnigan Delta V Advantage isotope-ratio mass-spectrometer. The Costech Elemental Analyser was fitted with a carbosorb trap to prevent acidic gases, such as CO_2, from entering the mass spectrometer. In addition, the elemental analyser was set to macro-oxygen to ensure complete combustion of the sample, liberating all available nitrogen. Total nitrogen content (wt %) was calculated as part of the isotopic analysis. Nitrogen isotope ratios were reported in standard delta (δ) notation in per mil (‰) relative to air. The $\delta^{15}N$ data were normalised against four international standards (IAEA-600, IAEA-N1, IAEA-N2, USGS 40). Isotopic analyses were performed in “no dilution mode”, with all analyses producing an N_2 signal >800 mV, providing maximum confidence in $\delta^{15}N$. Analytical accuracy in $\delta^{15}N$ was better than 0.3 ‰ (2σ) based on standards and replicate sample analyses.

3.5. Lipid biomarker analysis

Ten untreated (raw) powdered samples were selected for lipid biomarker analysis at regular intervals, to ensure representative stratigraphic coverage. For each sample, approximately 15 g of rock powder were extracted using a sonicator with a solvent

mixture of dichloromethane (DCM): methanol (MeOH) (4:1 v/v). The sample subsequently underwent centrifugation at 4000 rpm for 3 minutes. The solvent extract was pipetted out, and the sonication process was repeated three times for a total of four extractions. The total lipid extract (TLE) was reduced to a few mL under a stream of nitrogen and filtered into 15 ml vials. To remove the asphaltenes, the remaining solvent was evaporated to dryness under nitrogen before the addition of 250 µl of DCM, followed by the gradual addition of 10 ml of heptane under magnetic stirring. The mixture was stirred for 30 minutes and left overnight at room temperature to ensure complete precipitation of the asphaltenes. The asphaltene precipitate was then removed via filtration and the asphaltene-free TLE was separated into three distinct fractions by column chromatography over 4g of silica gel (Kieselgel 60). An aliphatic fraction was eluted with 40 ml of hexane, followed by an aromatic fraction with 40 ml of hexane: DCM (1:1, v/v), and a polar fraction with 40 ml of DCM: MeOH (3:1, v/v). Elemental sulphur was removed from each fraction using copper curls activated with 2M HCl.

Aliphatic and aromatic lipid fractions were analysed by gas chromatography equipped with a flame ionisation detector (GC-FID; Agilent 6890N) or coupled to mass spectrometry (GC-MS; Agilent 7890B GC coupled to a 5977B MSD) for the semi-quantification and identification of the different compounds, respectively. The GC were equipped with an on-column injector and compound separation was achieved with a HP5 MS UI capillary column (30 m x 0.25 mm, film thickness 0.25 µm). The helium carrier gas was set to a constant flow of 1 mL/min. The GC oven was programmed at 60 °C (0.5 min hold), heated to 130 °C at 20 °C/min, then 320 °C at 4 °C/min, with the final temperature being held for 20 minutes. The MS was used at 70 eV with an m/z range

from 50 to 700. Compounds were identified on the basis of their mass spectral characteristics and retention times using synthetic standards.

4. Results

4.1. Chemostratigraphy

The $\delta^{34}S_{evap}$ (i.e., the $\delta^{34}S$ of sulphate) data for A Bed range between -3.61 ‰ and +10.57 ‰ (Fig. 3). Between the depths of 98.35 m and 86.69 m, the $\delta^{34}S_{evap}$ values scatter between +1.06 ‰ and +8.35 ‰, before showing a negative excursion to a minimum of -3.61 ‰ at 84.36 m depth. The data abruptly increase from -2.43 ‰ at 80.20 m, to +7.34 ‰ at 79.60 m depth, and subsequently oscillate between +6.27 ‰ and +10.57 ‰ to a depth of 68.57 m (Fig. 3). As is the case for all data in this study, we do not report $\delta^{34}S_{evap}$ data between beds A and B, as the drillcore within this depth interval was disposed of prior to sampling. From a depth of 48.82 m at the base of B Bed, through to 35.38 m, the $\delta^{34}S_{evap}$ data range between +8.15 ‰ and +12.12 ‰ (Fig. 3).

For sedimentary sulphides, we report $\delta^{34}S$ data for chromium-reduced sulphide ($\delta^{34}S_{CRS}$) and acid-volatile sulphides ($\delta^{34}S_{AVS}$) (Fig. 3). At the base of A Bed, $\delta^{34}S_{CRS}$ values exhibit a declining trend from -4.72 ‰ at 98.35 m, to -39.31 ‰ 87.69 m. The $\delta^{34}S_{CRS}$ data subsequently oscillate between -37.87 ‰ and -28.62 ‰ between 86.69 m and 69.17 m depth. Within A Bed, $\delta^{34}S_{AVS}$ data range between -22.6 ‰ and +6.5 ‰, generally maintaining a state of isotopic enrichment when compared with $\delta^{34}S_{CRS}$. An exception to this occurs at a depth of 89.93 m, where we observe a $\delta^{34}S_{CRS}$ value of -19.85 ‰ and a $\delta^{34}S_{AVS}$ of -20.52 ‰. Between 48.82 m and 35.38 m, including both B bed and C bed, the $\delta^{34}S_{CRS}$ data exhibit large variations, between -37.49 ‰ and -0.30 ‰. On the other hand,

the $\delta^{34}S_{AVS}$ do not show as much variation, oscillating between -11.03 ‰ and +4.72 ‰ and maintaining a state of isotopic enrichment compared to $\delta^{34}S_{CRS}$ (Fig. 3).

The $\delta^{15}N_{tot}$ data for A Bed range from +4.98 ‰ to +10.86 ‰, exhibiting a positive excursion from +7.14 ‰ at 98.35 m depth to a maximum value of +10.86 ‰ at 86.50 m, subsequently decreasing to +5.31 ‰ at 68.57 m. Across beds B and C, within a depth range of 48.82 m and 35.38 m, the $\delta^{15}N_{tot}$ data are more poorly resolved but exhibit a declining trend from +8.07 ‰ to +4.01 ‰ (Fig. 3). The C/N and $\delta^{15}N_{tot}$ data exhibit comparable stratigraphic trends. The C/N data for A Bed exhibit a sharp increasing trend from 7.71 at 98.35 m through to 31.34 at 86.69 m and is thus broadly coincident with the increase in $\delta^{15}N_{tot}$. In addition, the negative excursion in $\delta^{15}N_{tot}$ across evaporite beds B and C is concomitant with a decline in C/N values from 19.5 to 6.1 (Fig. 3).

The $\delta^{13}C_{org}$ data exhibit relative stability around -24 ‰ within A bed, except for a minor positive excursion to -20.42 ‰ around 90 m (Fig. 3). Between 48.82 m and 35.38 m which includes B and C beds, the $\delta^{13}C_{org}$ profile exhibits more variability but shows two positive shifts within B and C beds, reaching maximum values of around -5 ‰ and +1.64 ‰, respectively (Fig. 3).

4.2. Molecular analyses

Preliminary GC-MS analysis of the aliphatic and aromatic hydrocarbon fractions of selected samples showed a varying content and degree of preservation of the soluble organic matter, which depends on the OM content of the samples. Figure 4 illustrates an example of a GC-MS chromatogram of an aliphatic fraction of the sample at 40.58 m containing >3% TOC within the massive anhydrite C-bed. Linear hydrocarbons ranging from C_{16} to C_{37} and with a dominant distribution of the C_{25}-C_{33} are observed in addition

to the acyclic isoprenoids pristane (Pr) and Phytane (Ph) and a series of bacterial hopanes. This sample also shows the significant presence of the saturated carotenoid β-carotane and of the weak but unambiguous presence of three aromatic carotenoids isorenieratane, β-isorenieratane and okenane, the presence of which was confirmed by the co-injection of standards (Fig. 4). These aromatic carotenoids, specific of anoxygenic phototrophic bacteria, were not detected in samples from other Beds, but β-carotane, characteristic of oxygenic phototrophs, was also present just below, within a mass of bedded anhydrite within A Bed (Figs. 3, 5).

The pristane/phytane (Pr/Ph) ratio, potentially indicative of variable redox and/or salinity conditions, could be calculated in 4 of the ca. 10 samples investigated for their lipid biomarker composition. In spite of the low stratigraphic resolution, values of this ratio range from 0.68 to 0.99 between 84.36 m and 79 m depth in A bed, and from 0.88 to 0.48 between 45.02 m and 40.58 m depth in beds B and C, the lowest Pr/Ph value being observed within evaporite bed C (Fig. 3).

5. Discussion

5.1. Biogeochemical evolution during deposition of the Eden Shales

On the basis of our high-resolution isotope records from KT1153, we present a detailed view of the biogeochemical evolution of a saline lake/sabkha environment during deposition of the Eden Shales. Two clearly distinct stages (stage 1 and stage 2) can be defined, with stage 1 persisting throughout the deposition of A Bed and stage 2 during the deposition of beds B and C (Fig. 3).

5.1.1. Biogeochemical conditions during deposition of A Bed

Sulphur isotopes can provide insight into the biogeochemical evolution of the Eden Shales evaporite system and are most likely controlled by microbial sulphate reduction (MSR), whereby sulphate is chemically reduced to sulphide via several intermediate species (Fike et al., 2015). MSR strongly discriminates against ^{34}S, with a maximum isotopic depletion of 66 ‰ reported in pure cultures (Sim et al., 2011) and 70 ‰ in natural cultures (Canfield et al., 2010). The degree of fractionation is controlled by physiological and environmental/depositional factors, including redox and sulphate availability (e.g., Canfield et al., 2010; Gomes and Hurtgen, 2015; Pasquier et al., 2017; Bryant et al., 2018; Rennie et al., 2018; Jovovic et al., 2020). It is expressed exactly as ε_{MSR}, the in-situ fractionation during MSR, or as $\Delta^{34}S$, the degree of isotopic offset between initial sulphate and sulphide (Canfield, 2001), with the difference between ε_{MSR} and $\Delta^{34}S$ controlled largely by sulphate availability (see Gomes and Hurtgen, 2015 for details).

Our $\delta^{34}S_{CRS}$ data exhibits a consistent ^{34}S-depletion relative to $\delta^{34}S_{AVS}$ (Fig. 3), as has been reported previously (e.g., Zaback and Pratt, 1992; Weber et al., 2016), suggesting the constituent sulphide within the AVS was characterised by a smaller $\Delta^{34}S$ (between initial sulphate and AVS) during formation. In sediments, AVS is commonly associated with iron sulphide minerals such as greigite and mackinawite (Rickard and Morse, 2004), although the specific source of the AVS in our samples cannot be precisely confirmed. However, assuming that much of the AVS is sourced from minerals such as greigite and mackinawite, then the relative ^{34}S-enrichment of AVS in KT1153 could suggest that such mineral species formed under more reducing and sulphate-limited

conditions than pyrite (the dominant source of CRS), such as at greater sediment depths or within isolated micro-environments, likely after pyrite formation during early diagenesis. Such conditions would have reduced the net $\Delta^{34}S$ between initial sulphate and AVS. While ε_{MSR} likely remained constant, a Rayleigh distillation effect would have generated a ^{34}S-enrichment of pore-water sulphate, facilitating the progressive ^{34}S-enrichment of pore-water sulphide with continued MSR (Fike et al., 2015) (Fig. 6).

The $\delta^{34}S_{CRS}$ data exhibit rather depleted values (< -30 ‰) for much of A Bed (Fig. 3), suggesting strong MSR and sufficient sulphate availability. This is intriguing considering the established depositional model for A Bed, which assigns the depositional environment to that of a saline lake, likely isolated from the seawater reservoir (Hoilliday et al., 1993; Worley et al., 2005). It is of course possible that the established depositional model for A Bed is incorrect, as it is based primarily based upon the relatively small spatial coverage of A Bed when compared to beds B and C (Hughes et al., 2003). If this is the case, then the light $\delta^{34}S_{CRS}$ data could be facilitated through conditions of abundant sulphate provided by a direct connection to the seawater reservoir. However, currently our geochemical data are insufficient to confirm either way and we will thus maintain the established depositional model.

In theory, one may expect hydrologic isolation of a saline lake system to be associated with closed-system sulphur isotope systematics, whereby Rayleigh distillation effects generate ^{34}S-enrichments of sedimentary sulphides, as has been reported for Jurassic saline lakes (Stüeken et al. 2019). In modern environments, enriched sedimentary sulphides have been reported from sediments below sulphidic and sulphate-poor waters, whereby the release of ^{34}S-enriched sulphate from anoxic

porewaters is a primary sulphate source, generating an enrichment in the $\delta^{34}S$ of sedimentary sulphides forming from the reduction of porewater-derived sulphate (Jørgensen et al., 2004; Canfield et al., 2010). However, MSR can still be associated with large ε_{MSR} values even under relatively low sulphate concentrations (see Canfield et al., 2010), with depleted $\delta^{34}S_{CRS}$ values being reported from low-sulphate environments (e.g., Habicht et al., 2002; Canfield et al., 2010; Weber et al., 2016).

Even if the system was hydrologically restricted and possibly characterised by suboxic redox conditions, it is conceivable that a sufficient abundance of sulphate was available for microbial sulphate reducers at the sediment/water depths at which MSR was active. Indeed, the abundance of bedded anhydrite within A Bed, which would have likely formed as primary gypsum, suggests a consistent supply of sulphate for the deposition of bedded calcium sulphates.

A possible sulphate source could be weathering-derived sulphate, which would likely be the primary sulphate source for a terrestrial saline lake system isolated from seawater. In theory, this sulphate could be transported via groundwater seepage and/or direct fluvial discharge (Fig. 7), as occurs in modern continental evaporite systems (e.g., Magee et al., 1995). Terrestrial inputs could also contribute to the elevation in C/N values concomitant with the light $\delta^{34}S_{CRS}$ values and enrichment in $\delta^{15}N_{tot}$ (Fig. 3) (see below), providing not only a source of terrestrial sulphate, but also terrestrial biomass.

It is worth noting that $\delta^{34}S_{evap}$ values down to ~-3 ‰ are extremely depleted, even if the dominant sulphate source is derived from the terrestrial weathering environment. By comparison, the global average $\delta^{34}S$ value for sulphate in modern fluvial systems is +4.8 ‰ (±4.9 ‰) (Burke et al., 2018) while seawater at that time had a

composition between approximately +10 and +14 ‰ (Claypool et al., 1980; Salisbury et al., 2022). While we do not measure any biomarkers indicative of sulphide oxidising bacteria, sulphide oxidation could have occurred elsewhere in the basin, generating a source of isotopically light sulphate which was subsequently transported to the evaporitic lake via a fluvial system. Much of the known major sources of sulphide within the region were likely buried during deposition of the Eden Shales (Stone et al., 2010), it is of course very difficult to constrain the material exposed to the weathering environment at the time of deposition.

Another source of $\delta^{34}S_{evap}$ depletion could be late-stage diagenetic sulphate remobilisation. The Eden Shales of KT1153 do include abundant fibrous gypsum veins, which form during the dehydration of gypsum, usually as extensional veins (El Tabakh et al., 1998) or in association with slickensides (e.g., Milroy et al., 2019). It is common for the constituent sulphate of gypsum veins to exhibit a $\delta^{34}S_{SO4}$ comparable to that of the evaporite from which the remobilised sulphate was sourced (Moragas et al., 2013; Salisbury et al., *in prep*.). When fractionation does occur, it usually takes the form of a $\delta^{34}S_{SO4}$ enrichment in response to a Rayleigh distillation effect associated with repeated cycles of remobilisation under closed system conditions with respect to the supply of sulphate (Moragas et al., 2013). However, it is conceivable that considering the relatively high concentration of sedimentary sulphides within A Bed (see Appendix 2), during the late-stage diagenetic remobilisation of sulphate, sulphides could have undergone abiotic oxidation during interaction with diagenetic fluids. This would have generated a flux of isotopically light sulphate, mixing with sulphate remobilised from pre-existing evaporites and drawing down the $\delta^{34}S_{SO4}$ of gypsum veins which subsequently precipitated.

Concomitant with the negative $\delta^{34}S_{evap}$ excursion, $\delta^{15}N_{tot}$ values exhibit a positive excursion, increasing from ~+7 ‰ at the base of A Bed, to a maximum of +10.86 ‰ at a depth of 86.5 m. Several mechanisms for $\delta^{15}N_{tot}$ enrichment are known (Fig. 7) and will be discussed individually.

One possible mechanism for $\delta^{15}N_{tot}$ enrichment occurs under conditions of alkalinity, whereby ammonia can exhibit volatility (Bastos et al., 2022). Ammonia is sourced from the partitioning of diagenetically-derived ammonium, a process that heavily discriminates against ^{15}N (Stüeken et al., 2019). The ^{14}N-enriched ammonia subsequently escapes to the atmosphere, generating an isotopic enrichment in the residual ammonium pool (Stüeken et al., 2019; Bastos et al., 2022). This mechanism could also explain the high C/N values (>30) we report concomitant with the observed increase in $\delta^{15}N_{tot}$ (Fig. 3). Ammonia is less readily incorporated into clay minerals, and thus the diagenetic transformation of ammonia from ammonium would likely generate a preferential loss of N (relative to carbon) from the sediments, inciting an increase in C/N ratios (Stüeken et al., 2019).

However, while this mechanism appears to fit the geochemical data ($\delta^{15}N_{tot}$ and C/N), there are several issues which we argue ensure it is an unlikely mechanism in this instance. Firstly, while the $\delta^{15}N_{tot}$ values are enriched, reaching a maximum of +10.86 ‰, high pH conditions have been associated with even more extreme enrichments >+15 ‰ (Stüeken et al., 2019) with enriched $\delta^{15}N_{tot}$ values >+15 ‰ (up to +28 ‰) reported from modern alkaline lakes (Lent et al., 1995; Menzel et al., 2013) and $\delta^{15}N_{tot}$ values of ~+30 ‰ reported from Archean alkaline lakes (Stüeken et al., 2015). Furthermore, the lithology of the section cored in KT1153 also suggests a high pH may in fact be unlikely

in this instance, as the Ca-sulphates (nodular and bedded) present would be unlikely to form in such abundance from alkaline brines (Warren, 2010, 2021).

An alternative possible mechanism for generating the observed $\delta^{15}N_{tot}$ enrichment relates to high salinity levels, with ammonium experiencing ^{15}N-enrichment in response to hypersalinity (Isaji et al., 2019; Bastos et al., 2021). Under conditions of hypersalinity, nitrification is inhibited, causing an associated suppression in rates of denitrification and anammox. As a result, efficient recycling of ammonium occurs amongst purple sulphur bacteria and cyanobacteria, stimulating high rates of primary productivity and generating ^{15}N-enriched ammonium (Isaji et al., 2019). In addition, under hypersalinity, gaseous ammonia can escape to the due to a decrease in gas solubility with increasing salinity. During this process, ^{14}N-rich ammonia preferentially escapes, causing a ^{15}N-enrichment of ammonium within the saline brines (interpretation A in Fig. 7) (see Isaji et al., 2019 for details).

It is plausible that this mechanism was active during deposition of A Bed, generating our observed increase in $\delta^{15}N_{tot}$, and has been invoked to explain $\delta^{15}N$ enrichments reported from the Permian Irati and Whitehill formations (Bastos et al., 2021). The ammonium recycling processes that occur in the absence of nitrification and suppression of denitrification and anammox were reported from modern microbial mat structures (Isaji et al., 2019). Although no such structures have been reported from KT1153, possible mat structures have been found elsewhere within A Bed (Worley, 2024, *pers. comm.*), and thus an additional source of ^{15}N-enriched ammonium could be derived from such mat structures. In addition, the escape of volatile ammonia could also

contribute to the observed increase in C/N ratios concomitant with the positive $\delta^{15}N_{tot}$ excursion (Fig. 3).

The Pr/Ph ratios for A Bed range between 0.68 and 1, with 0.68 being reported during the peak of the $\delta^{15}N_{tot}$ increase (Fig. 3). While the presence of β-carotane could indicate high salinity, as it is produced by many halotolerant organisms (Fazeli et al., 2006), the Pr/Ph values most indicative of high salinity occur above in C Bed (Fig. 3). In addition, under high salinity, it would be expected for intense evaporation to incite concomitant enrichments in $\delta^{13}C_{carb}$ and $\delta^{18}O_{carb}$ (Stiller et al., 1984; Stüeken et al., 2019), as the evaporation of water favours ^{16}O (Stüeken et al., 2019) and CO_2 solubility and escape under hypersalinity incites a loss of ^{12}C (Stiller et al., 1984). In contrast to this, our $\delta^{13}C_{carb}$ and $\delta^{18}O_{carb}$ data within A Bed exhibit relatively depleted values, and gentle declining trends concomitant with the $\delta^{15}N_{tot}$ excursion, falling to a minimum of -8.11 ‰ for $\delta^{13}C_{carb}$ and -6.01 ‰ for $\delta^{18}O_{carb}$ (see supplementary). Furthermore, enrichments in $\delta^{13}C_{org}$ have been reported under evaporative conditions (e.g., Schidlowski et al., 1984; Birgel et al., 2015; Dorador et al., 2018) (see below), while our $\delta^{13}C_{org}$ data for A Bed remain relatively stable between -25 ‰ and -20 ‰ (Fig. 3).

It is of course worth noting that the volume of gypsum present in A Bed, and the halite reported from elsewhere within the basin (Worley, 2005), would suggest consistent salinity and evaporative conditions. Although our $\delta^{13}C_{carb}$ and $\delta^{18}O_{carb}$ data do not exhibit signals associated with hypersalinity, it should be noted that all samples analysed for $\delta^{13}C_{carb}$ were bulk powders, and we thus did not analyse pristine carbonate beds. As a result, the origin of the carbonate subjected to isotopic analysis cannot be confirmed. Thus, although we do not observe a strong correlation between $\delta^{13}C_{carb}$ and

$\delta^{18}O_{carb}$ or carbonate content (wt. %) (see Appendix 2), we cannot confidently overlook the possible diagenetic origin of the carbonate material, and thus any interpretation of the carbonate data must be made with caution. Also, while $\delta^{13}C_{org}$ enrichments have been linked to hypersalinity (Schidlowski et al., 1984), other factors such as microbial productivity are thought to play a major role in generating $\delta^{13}C_{org}$ enrichments (see below and Schidlowski et al., 1994; Birgel et al., 2015), and thus, a lack of ^{13}C-enriched bulk organic carbon in A Bed does not necessarily confirm a lack of hypersalinity. However, the absence of additional independent geochemical data beyond the $\delta^{15}N_{tot}$ and C/N records to confirm hypersalinity, ensures that it is difficult to invoke this mechanism for generating the observed increase in $\delta^{15}N_{tot}$.

A final possible mechanism for this ^{15}N-enrichment is partial denitrification, whereby dissolved ^{14}N-rich nitrate is utilised instead of oxygen as an electron acceptor during organic matter oxidation, and commonly occurs under suboxic conditions where O_2 availability is limited (Jenkyns et al., 2001; Mettam and Zerkle, 2021). During this process, nitrate undergoes chemical reduction, yielding an isotopically light gaseous N_2 product (Bastos et al., 2021). Quantitative denitrification would yield no net isotopic effect, as little nitrate would remain to yield a relative ^{15}N-enrichment within the system (Jenkyns et al., 2001; Mettam and Zerkle, 2021). However, under suboxic conditions, a ^{15}N-enriched residual nitrate pool remains as ^{14}N-rich gaseous N_2 escapes to the atmosphere (Jenkyns et al., 2001). The residual nitrate is subsequently assimilated by organisms, generating ^{15}N-enriched biomass (see interpretation B in Fig. 7) (Bastos et al., 2021).

Concomitant with the positive $\delta^{15}N_{tot}$ excursion, we report Pr/Ph values between 0.68 and 1, with the prior being reported at 84.36 m depth, within the depth interval with the highest $\delta^{15}N_{tot}$ values (Fig. 3). In addition, we report the occurrence of β-carotane, and although they are in lower abundance than above in Stage 2 (Fig. 5), their preservation within the geologic record would require reducing conditions, due to the susceptibility of their precursor molecules to oxidation (Hebting et al., 2006). Thus, when viewed together, the available geochemical data suggest the $\delta^{15}N_{tot}$ enrichment could have been generated via partial denitrification under suboxic conditions.

In addition, if A Bed is indeed a terrestrial saline lake, then it may have been susceptible to abundant terrestrial biomass inputs. In fact, an abundance of carbonaceous plant debris reported from clastic facies associated with evaporite beds A, B and C are indicative of a rich community of flora around the flanks of the evaporite basin (Arthurton, 1971). The A Bed evaporite grades laterally into the Hilton Plant Beds, a likely source of terrestrial plant material, which could have been weathered and transported by fluvial systems feeding the playa lake system (Burgess and Holliday, 1979; Hughes, 2003; Ruffell et al., 2006;) Thus, plant material could have contributed to the increase in C/N ratios, as terrestrial biomass generally has a higher C/N ratio than marine organic matter due to a relative abundance of N-poor compounds associated with structural tissues (Lent et al., 1995). Our $\delta^{13}C_{org}$ data from A Bed range between -20 ‰ and -25 ‰ (Fig. 3), in line with $\delta^{13}C_{org}$ values reported from Late Permian vegetation (Mishra et al., 2019; Aggarwal, et al., 2019). We do observe a relatively minor increase in $\delta^{13}C_{org}$ to -20.42 ‰ at 89.93 m within A Bed, however this is accompanied by stability in C/N at low values around 7 (mol/mol), with the heightened C/N ratios occurring above, where $\delta^{13}C_{org}$ values exhibit stability at ~-23 ‰ (Fig. 3). Thus, it seems that if the

observed increase in C/N ratios is a product of increased inputs of terrestrial biomass, this had little impact on the $\delta^{13}C$ of bulk organic carbon.

Thus, we suggest the observed increase in $\delta^{15}N_{tot}$ was most likely generated through partial denitrification under suboxic conditions, with the increase in C/N values reflecting a high relative abundance of terrestrial biomass. Future work should endeavour to generate further organic geochemical data to better constrain parameters such as redox, the relative contributions from marine 'vs' terrestrial biomass, and salinity during deposition of the Eden Shales.

5.1.2. Biogeochemical conditions during deposition of beds B and C

The stratigraphy of KT1153 transitions upwards into evaporite beds B and C, where we report geochemical evidence for distinct biogeochemical conditions, defined here as Stage 2. The $\delta^{15}N_{tot}$ data, although of a lower resolution than the nitrogen isotope record for the underlying A Bed, exhibits a declining trend from +8.07 ‰ to +4.01 ‰ (Fig. 3). This decline suggests an enhancement of nitrogen fixation, whereby diazotrophs utilise a nitrogenase enzyme to assimilate atmospheric or dissolved di-nitrogen, chemically reducing it to the more bioavailable form, ammonium (Fig. 7) (Stüeken et al., 2016; Mettam and Zerkle, 2021). The ammonium can be subsequently utilised by non-diazotrophs, with nitrogen fixation and ammonium recycling only being associated with a small degree of isotopic fractionation (Mettam and Zerkle, 2021). The most common nitrogenase enzyme (Mo-based) is associated with an average fractionation of -1 ‰ (Stüeken et al., 2016), and thus under conditions in which the dominant N sources are nitrogen fixation and ammonium recycling, organic matter will exhibit a nitrogen isotopic

composition close to that of atmospheric nitrogen ($\delta^{15}N$ = 0 ‰ ± 2 ‰) (Mettam and Zerkle, 2021).

Therefore, an increase in nitrogen fixation rate during Stage 2 would act to draw down the $\delta^{15}N$ of sedimentary biomass, in line with the declining trend in $\delta^{15}N_{tot}$ across beds B and C (Fig. 3). Certain nitrogenase enzymes (Fe- and V-nitrogenase) are less efficient and are associated with larger fractionations between -8 ‰ and -6 ‰ (Zhang et al., 2014). However, these nitrogenase enzymes are less common (Stüeken et al., 2016), and even if they were active in this case, they would have only contributed to further reducing the $\delta^{15}N$ of biomass in evaporite beds B and C. The activity of nitrogen fixation in contributing to the declining $\delta^{15}N_{tot}$ trend is further supported by the detection of a high concentration of β-carotane (Fig. 4, 5), a saturated carotenoid derived from the diagenetic degradation of β-carotene and commonly associated with cyanobacteria (Ma and Cui, 2021). Many cyanobacteria are diazotrophs, capable of directly assimilating atmospheric nitrogen, and while we do measure β-carotane below in A Bed, the concentrations are far lower (Fig. 5). Thus, the presence of β-carotane, but lack of negative $\delta^{15}N_{tot}$ signal in A Bed, is not in this case contradictory.

The Pr/Ph ratio of 0.48 that we report from a depth of 40.58 m (Fig. 3), is indicative of deposition under conditions of anoxia and hypersalinity (ten Haven et al., 1987). This is also broadly coincident with a progressive increase in $\delta^{18}O_{carb}$ between 47.89 and 35.38 m depth (see Appendix 2), which may indicate severe evaporation (Stüeken et al., 2019). An increase in the degree of anoxia concomitant with increasing salinity is conceivable, considering the lower solubility of dissolved oxygen at high salinity (Stüeken et al., 2019). This aligns well with our interpretation for the $\delta^{15}N_{tot}$ trend

during Stage 2, with increases in nitrogen fixation rates commonly associated with anoxic nitrate-deficient waters (Bastos et al., 2021). Furthermore, spikes in the TOC (wt %) content of insoluble residues are observed in Stage 2 (see Appendix 2), potentially providing further evidence of at least localised anoxia, which would have increased the preservation potential of organic matter. The potential increase in salinity, along with heightened rates of primary productivity as evidenced by the high concentration of β-carotane, could have potentially generated extreme ^{13}C-enrichments of bulk organic matter, expressed as $\delta^{13}C_{org}$ values up to a maximum of +1.64 ‰ (Fig. 3). The heightened volatility of CO_2 under conditions of hypersalinity, in combination with high rates of productivity among photoautotrophs (Fig. 7), suppressed the degree of isotopic discrimination against ^{13}C during photosynthesis (Schidlowski et al., 1994), causing extreme $\delta^{13}C_{org}$ enrichments (see below for details).

In addition to the low Pr/Ph ratio, we also report the presence of aromatic carotenoids at 40.58 m depth, including isorenieratane, β-isorenieratane and okenane (Fig. 5). These carotenoids are associated with brown green sulphur bacteria and purple sulphur bacteria, respectively (Ma and Cui, 2021). Both undertake anoxygenic photosynthesis, oxidising sulphide for its' use as an electron donor during the fixation of carbon dioxide (Frigaard and Dahl, 2008). Thus, their detection in the sedimentary record is considered evidence for photic zone euxinia (PZE).

Throughout Stage 2, we also report highly variable $\delta^{34}S_{CRS}$ data, ranging between -37.49 ‰ and -0.3 ‰ (Fig. 3). Such an extreme degree of variability in the $\delta^{34}S$ of sedimentary sulphides would indicate repeated changes in the degree of sulphate availability during MSR, with the light values of $\delta^{34}S_{CRS}$ (< -30 ‰) representing intervals

of greater sulphate availability. In contrast, the heavy $\delta^{34}S_{CRS}$ values likely represent instances where the microbial sulphate reducers had access to a more restricted pool of sulphate, likely resulting from closed system conditions and limited supply of sulphate, causing a Rayleigh distillation effect during MSR (e.g., Jovovic et al., 2020). It is plausible that the extreme scatter in $\delta^{34}S_{CRS}$ values relates to changes in the abundance of hydrogen sulphide (Fig. 7). However, the biomarker data are of low stratigraphic resolution, with the aromatic carotenoids only being measured at a depth of 40.58 m, and thus we cannot definitively link every fluctuation in $\delta^{34}S_{CRS}$ to an expansion or retraction in euxinia. What can be said, is that biomarkers indicative of PZE are broadly concomitant with extreme variability in $\delta^{34}S_{CRS}$.

Interestingly, $\delta^{34}S_{evap}$ values for evaporite beds B and C exhibit relative stability between +8.15 ‰ and +12.12 ‰ (Fig. 3), which are within the range established for late Permian seawater (Claypool et al., 1980; Bernasconi et al., 2017; Crockford et al., 2019; Salisbury et al., 2022). This would suggest that the basin was connected, at least to a certain extent, to the seawater sulphate reservoir and/or that sulphate concentrations were sufficiently high to buffer the local sulphate reservoir from isotopic perturbation. Accordingly, isorenieratane is commonly recorded from sediments associated with open water depositional settings and restricted basins, whilst okenane rarely occurs in open marine settings, being limited largely to euxinic lakes and lagoonal settings (Ma and Cui, 2021). Thus, their co-occurrence within Stage 2, could be viewed as evidence for deposition within a restricted marine environment. Previous work suggested evaporite beds B and C are more likely to be marine in origin than the underlying A Bed, but this inference was based mainly upon lithostratigraphic correlation, without additional geochemical constraint (Burgess and Holliday, 1974; Holliday et al., 1993; Hughes, 2003).

Our $\delta^{34}S_{evap}$ data, along with the detection of the aromatic carotenoids isorenieratane and okenane, thus provide the first direct geochemical evidence of a likely marine origin for the evaporites of B and C bed within the Eden Shales.

The stability in $\delta^{34}S_{evap}$ would seemingly contradict with the variability exhibited by the $\delta^{34}S_{CRS}$ record, as the microbial sulphate reducers would have been sequestering sulphate from a sulphate pool which appears to have maintained isotopic stability. One possible explanation for this would involve the MSR largely taking place within sediments or microbial mat structures below the evaporite brines. In addition, the PZE may also be largely restricted to the sediment/microbial mat structures. Anoxygenic phototrophs are commonly found within microbial mats in surface sediments and stromatolites (e.g., Arp et al., 2012). Under a shallow water column, sunlight contacting the sediment can penetrate and facilitate the development of chemical gradients, within which different microbial communities can establish niches (Ma and Cui, 2021). For example, it is common for anoxygenic phototrophs to inhabit layers of microbial mats where sunlight can still penetrate, underlying the initial oxic zone within which cyanobacteria are active, oxidising sulphide which diffuses upwards after being generated by microbial sulphate reducers occupying layers below (Birgel et al., 2015).

Thus, it is conceivable that the apparent contradiction between $\delta^{34}S_{evap}$ stability and the instability in $\delta^{34}S_{CRS}$ and biomarker evidence for PZE can be reconciled by microbial sulphur cycling taking place largely within the sediment or microbial mats underlying the saline brines. Even though sulphate reducers will still be sourcing sulphate from the overlying brines, if the concentration of sulphate within the brines was high, as the abundance of bedded Ca-sulphates suggest it would have been, then

the sulphate reservoir could have maintained resistance to perturbations in $\delta^{34}S$. In fact, hypersalinity as suggested by the low Pr/Ph ratio of 0.48, would imply high rates of evaporation, further concentrating the sulphate within the overlying brines, enhancing its' resistance to isotopic perturbation. Thus, while the scatter in the $\delta^{34}S_{CRS}$ is possibly recording the response of microbial sulphate reducers to fluctuations in sulphate availability within microbial mats or within the upper layers of sediment, the $\delta^{34}S_{evap}$ stability reflects the maintenance of a large and highly concentrated sulphate reservoir, sustained by seawater sulphate inputs.

The main issue with this hypothesis, is the lack of confirmation regarding the presence of microbial mat structures in evaporites beds B and C. While structures clearly associated with microbial mats have been reported from A Bed, the presence of mat structures within the overlying B and C beds is more controversial (Worley, 2024; *pers. comm.*). Arthurton (1974) reported features possibly associated with microbial mat structures within A Bed and at the base of B Bed, comparing them to features found in the intertidal zones of contemporary sabkhas. In addition, layered structures which may have microbial affinity are present also within C Bed (Worley, 2024; *pers. comm.*). However, no such features have been identified from the drillcore of KT1153, and those that have been reported elsewhere have not been subjected to detailed geochemical analysis. Thus, we must admit that the presence of microbial mat structures within the Eden Shales is still debated, however there are features which could be tentatively associated with a microbial origin throughout the stratigraphy. Thus, it is possible that we present geochemical data indicative of elemental cycling within microbial mat communities, without reporting direct sedimentological evidence. Future studies should endeavour to sample the layered structures tentatively assigned a microbial affinity and

subject them to petrographic and geochemical study to see whether comparable geochemical signals can be observed directly from structures of possible microbial origin.

5.2. Pathways of ^{13}C-enrichment in bulk organic matter

Isotopic compositions of bulk organic carbon (> -10 ‰ and up to +1.64 ‰), reported here within evaporite beds B and C (Fig. 3), are extremely enriched for the organic carbon pool, which is generally ^{13}C-depleted when compared with the inorganic carbon pool, due to kinetic isotope effects associated with the biological assimilation of inorganic carbon (Des Marais, 1995; Schidlowski, 2001). Extreme ^{13}C-enrichments have been reported from organic carbon phases within modern microbial mat structures under evaporative conditions. Canfield and Des Marais (1994) observe a substantial reduction in the degree of isotopic distinction between the $\delta^{13}C$ of microbial mat structures and dissolved inorganic carbon (DIC) in tidal flats and seawater evaporation ponds. Small ^{13}C-enrichments (> -15 ‰) have been observed in blue green algal mats of Baffin Bay, Texas (Behrens and Frishman, 1971) and $\delta^{13}C_{org}$ values between -8.4 ‰ and -4.4 ‰, and -16.8 ‰ and -6.1 ‰ were reported from microbial mats in Solar Lake and Gavish Sabkha, respectively (Schidlowski et al., 1984). Subsequent work reported $\delta^{13}C_{org}$ values from -20 ‰ to -5 ‰ within microbial mats of Lagoa Salgada, Brazil (Birgel et al., 2015) and recent work presents $\delta^{13}C_{org}$ data with enrichments > -10 ‰ from microbial mat structures in Laguna Puilar, Salar de Atacama, Chile (Dorador et al., 2018). In addition, ^{13}C-enrichments in inorganic carbon phases have also been reported (Stiller and Magaritz, 1974; Stiller et al, 1984; Gu et al., 2004; Lacelle et al., 2009; Planavsky et al.,

2009; Birgel et al., 2015) and are in some instances observed in direct association with $\delta^{13}C_{org}$ enrichments (Birgel et al., 2015).

It has been common for $\delta^{13}C_{carb}$ enrichments to be explained by the activity of methanogens and/or photoautotrophs (Stiller and Magaritz, 1974; Gu et al., 2004; Lacelle et al., 2009; Planavsky et al., 2009; Birgel et al., 2015). Birgel et al. (2015) report ^{13}C-enrichments in both organic carbon and carbonate from Holocene microbial mat structures, arguing these isotopic signatures cannot be attributed to photosynthetic carbon fixation alone, invoking a mechanism dependent upon the activity of methanogens. Methanogenesis, a process by which methanogenic archaea, in the absence of oxygen, convert carbon dioxide or organic matter to biomass, energy and methane (Thauer, 1998; Ferry, 2010). Although there exist three biochemical pathways by which methane is produced biotically (Ferry, 2010), they are all thought to yield a methane product depleted in ^{13}C relative to the inorganic carbon pool (Londry et al., 2008).

In the model proposed by Birgel et al. (2015), sulphate replete conditions and suppressed microbial sulphate reduction rates increase the flux of organic carbon to methanogens, which produce isotopically light methane that escapes to the atmosphere under evaporative conditions. Methanogenesis and subsequent methane escape generate a ^{13}C-enriched residual inorganic carbon pool (also see Gu et al., 2004), which is then fixed by photoautotrophs, yielding a flux of isotopically enriched biomass (Birgel et al., 2015). In support of this model, Birgel et al. (2015) report high methane concentrations, associated with archaeal membrane lipid biomarkers, which are characteristic of the activity of methanogens (Kates, 1993). While it is of course plausible

that methanogenesis, along with methane escape and photoautotrophic fixation, could have been responsible for the $\delta^{13}C_{org}$ enrichments observed in the Eden Shales, we still have no direct evidence to support this.

The samples analysed in our study are too old for membrane lipids of methanogenic archeae to have been preserved through geological time. However, the strong presence of phytane, a possible lipid biomarker of methanogens, in the C bed, may still indicate the presence of methanogenic archaea. The compound-specific carbon isotope data of this compound is currently being investigated to better constrain the biological origin of phytane. In addition, we also do observe a concomitant increase in $\delta^{13}C_{carb}$ within C Bed (see Appendix 2), but as stated, the primary origin of the carbonate phases analysed for this study cannot be confirmed. While Birgel et al. (2015) were able to confirm low sulphate concentrations in Lagoa Salgada, our $\delta^{34}S_{evap}$ data from beds B and C suggest that sulphate concentrations remained relatively constant during Stage 2 (see above). In general, high sulphate concentrations are thought to limit rates of methanogenesis in marine sediments, with much of the organic matter flux being consumed through MSR (Jørgensen et al., 2019). However, in saline lakes, MSR and methanogenesis have been observed to overlap, with methanogens utilising uncompetitive substrates under conditions of hypersalinity (Giani et al., 1984; Oren, 1999).

In addition, under high sulphate conditions, it is possible that methane produced within the sediment or microbial mat structures (if present) would be subsequently consumed through the anaerobic oxidation of methane (AOM). Anaerobic methanotrophic archaea (ANME), in consortium with microbial sulphate reducers,

oxidise methane for energy generation, utilising sulphate as the final electron acceptor (Nieman and Elvert, 2008; Knittel and Boetius, 2009). Microbial communities associated with AOM appear ubiquitous in anoxic marine sediments with sufficient concentrations of both methane and sulphate (Niemann and Elvert, 2008), including saline lake environments (Joye et al., 1999). It could therefore be argued that any methane produced via the activity of methanotrophs, would likely be consumed via AOM before release to the atmosphere, thus limiting extreme enrichments in $\delta^{13}C_{org}$. However, evidence does exist to suggest that rates of AOM can be suppressed under conditions of hypersalinity (Joye et al., 2009). In addition, at a depth of 40.58 m, the absence of lipid biomarkers specific of anaerobic methanotrophs (ANME) such a pentamethylicosane (PMI) does not argue for the occurrence of AOM during deposition of C Bed.

The presence of isorenieratane, β-isorenieratane and okenane could reflect a localised and temporary expansion in the concentration of hydrogen sulphide and anoxia, with an associated reduction in sulphate concentrations. As discussed above, these aromatic carotenoids are broadly concomitant with extreme variability in $\delta^{34}S_{CRS}$, which indicates fluctuations in sulphate availability during MSR, and may exhibit a direct association with expansions in PZE. Under such conditions, rates of AOM would be suppressed, potentially facilitating a greater methane flux, as has been suggested for periods of low seawater sulphate concentrations at various points throughout Earth history (e.g., Hall et al., 2018; He et al., 2020). This could potentially explain the detection of aromatic carotenoids at the same stratigraphic depth as the most enriched $\delta^{13}C_{org}$ value of +1.64 ‰ (Fig. 3, 4).

While we do not report direct geochemical evidence for methanogenic activity, we do detect β-carotane, a saturate carotenoid associated with the activity of photoautotrophs, such as cyanobacteria (Ma and Cui, 2022). The highest concentration of this biomarker was found at 40.58 m depth, along with isorenieratane, β-isorenieratane, okenane and the highest reported $\delta^{13}C_{org}$ value (Fig. 5). Cyanobacteria fix carbon via the C3 photosynthetic pathway, with naturally occurring communities within microbial mat structures producing an average $\delta^{13}C_{org}$ value of -16 ‰ (Schidlowski, 2000). Of course, cyanobacteria, along with brown coloured green sulphur bacteria and purple sulphur bacteria could, as suggested by Birgel et al. (2015), have fixed CO_2 from a ^{13}C-enriched DIC pool, producing a relatively ^{13}C-enriched organic carbon flux. Measurement of the ^{13}C composition of β-carotane is currently underway and will help us to confirm or refute the proposed model for the enriched $\delta^{13}C_{org}$ values observed in beds B and C.

Another possibility involves CO_2 volatility during evaporation, which has been invoked to explain enrichments in $\delta^{13}C_{carb}$ and $\delta^{13}C_{org}$ (Schidlowski et al., 1984; Stiller et al., 1984; Horton et al., 2016). Under conditions of hypersalinity and high temperatures, often associated with saline lake/sabkha environments, CO_2 can exhibit greater volatility due to a reduction in its' solubility, inciting CO_2-limited conditions (Schidlowski et al., 1985). During CO_2-limitation, the step of CO_2 diffusion into the cell of a photosynthesising microbe becomes rate-limiting (Schidlowski et al., 1985; Des Marais, 1995). CO_2 fixation via the C3 photosynthetic pathway is generally associated with a large degree of isotopic fractionation (-20 ‰ to -40 ‰), with the RuBP carboxylase reaction strongly favouring discrimination against ^{13}C (Schidlowski et al., 1984). In contrast, the diffusive step is only associated with a maximum fractionation of approximately -4 ‰

(Schidlowski et al., 1984), and thus, a shift towards the latter becoming rate limiting will ensure a suppression of CO_2 fixation as the primary source of isotopic discrimination, reducing fractionation (Schidlowski, 2000). Indeed, at 40.53 m depth, a $\delta^{13}C_{org}$ value of +1.64 ‰ and a $\delta^{13}C_{carb}$ value of +2.02 ‰ (Fig. 3 and see supplementary) would suggest a very minor degree of isotopic discrimination during the biological assimilation of inorganic carbon. However, the possible diagenetic origin of carbonate phases ensures interpretation of the carbonate data must be made cautiously.

This C Bed depth interval is also associated with a low Pr/Ph ratio of 0.48 (Fig. 3), which could reflect heightened levels of salinity, and thus potentially CO_2 volatility. In addition, the high abundance of β-carotane could itself indicate salinity, with previous work providing evidence that with increasing salinity, an increase in the relative production of β-carotene (the precursor to β-carotane) is seen from halotolerant organisms (Ben-Amotz and Avron, 1983; Gomes et al., 2003; Fazeli et al., 2006).

It should also be noted that several studies have provided evidence to suggest that salinity may not be the primary constraint in generating ^{13}C-enrichments in biomass (Des Marais et al., 1989; Schidlowski et al., 1994). In addition to salinity, primary productivity appears to impart a control over ^{13}C-enrichment, with higher rates further depleting the local DIC pool and generating conditions of CO_2-limitation (Schidlowski et al., 1994; Schidlowski, 2000). In turn, this would ensure that the isotopically indiscriminate diffusion step becomes rate limiting during CO_2 assimilation (Schidlowski et al., 1994). Accordingly, the most enriched $\delta^{13}C_{org}$ value is reported at the same depth interval as the highest concentrations of saturate and aromatic carotenoids, potentially suggesting that the ^{13}C-enricnment of biomass was concomitant with high levels of

productivity amongst photoautotrophs. However, beyond these lipid biomarkers, we have no independent means for assessing rates of productivity, and no method for confidently estimating concentrations of dissolved CO_2.

Efforts should be made to generate additional organic geochemical data from the Eden Shales, with a particular focus towards the detection of lipid biomarkers, particularly those associated with methanogenic, methanotrophic and photoautotrophic activity. The detection of biomarkers associated with methanogenic (archaea) and methanotrophic (bacteria) activity would provide direct evidence for the local production and consumption of methane, respectively. Biomarkers associated with photoautotrophs will allow a better assessment of the rates of primary productivity during deposition. In addition, attempts to generate MTTC ratios will enable their utilisation alongside the Pr/Ph ratio as a more robust palaeosalinity proxy for assessing degrees of salinity and CO_2 limitation.

6. Conclusions

Here, we report a high-resolution geochemical dataset, including a range of stable isotopic records ($\delta^{34}S_{evap}$, $\delta^{34}S_{CRS}$, $\delta^{15}N_{tot}$, $\delta^{13}C_{org}$), accompanied by preliminary organic geochemical data. These data have enabled us to define two phases of distinct biogeochemical character, Stage 1 during the deposition of A Bed, and Stage 2 during the deposition of beds B and C (Fig. 3). Stage 1 is currently the most poorly understood, however we suggest deposition occurred within a hydrologically isolated saline lake system, with sulphate and biomass inputs largely being sourced from the terrestrial weathering environment, with much of the terrestrial biomass possibly being sourced from a rich community of flora surrounding the flanks of the evaporite basin. While the

$\delta^{34}S_{CRS}$ data suggest sulphate was present in sufficient abundances to enable large net $\Delta^{34}S$ during MSR, the $\delta^{34}S_{evap}$ record appears to be overprinted by a diagenetic signal, possibly related to the late-stage diagenetic remobilisation of sulphate. An increasing trend in $\delta^{15}N_{tot}$ could be related to either partial denitrification under suboxia, or the loss of ^{14}N-rich ammonia under evaporative conditions.

In contrast, Stage 2 is characterised by evidence for greater expansions in anoxia, PZE and heightened salinity levels. Declining trends in $\delta^{15}N_{tot}$ concomitant with the maximum concentration of β-carotane reported within KT1153, indicate increases in nitrogen fixation, associated with an enhancement of cyanobacterial productivity. In addition, highly enriched $\delta^{13}C_{org}$ values (up to +1.64 ‰) are likely a response to increased salinity levels in combination with heightened productivity amongst phototrophs, suppressing the degree of ^{13}C-discrimination during photosynthetic carbon fixation. We also suggest that methanogenic activity could have contributed to the observed $\delta^{13}C_{org}$ enrichments, but the lack of sufficient lipid biomarker data prevents us from confirming the involvement of such a mechanism at this stage. Highly variable $\delta^{34}S_{CRS}$ values (between -37.49 ‰ and -0.3 ‰) suggest fluctuations in the degree of sulphate availability during MSR, and possibly relate to the presence of PZE, for which we report evidence from the presence of aromatic carotenoids charatecteristics of phototrophic sulphur bacteria (isorenieratane, β-isorenieratane and okenane).

The extreme variability in $\delta^{34}S_{CRS}$ appears to directly contradict the $\delta^{34}S_{evap}$ record, which maintains relative stability between +8.15 ‰ and +12.12 ‰, in line with values for late Permian seawater (e.g., Salisbury et al., 2022). Thus, while the $\delta^{34}S_{CRS}$ data suggest marked variability in sulphate limitation, the $\delta^{34}S_{evap}$ record indicates a relatively

constant sulphate reservoir, potentially sourced primarily from seawater ingress. We suggest this apparent contradiction reflects a stratified system, in which microbial sulphate reducers are reducing sulphate in restricted environments within mat structures or the underlying sediment, within which PZE would expand and contract, while the sulphate maintained isotopic stability within the overlying saline brines, fed by the vast seawater sulphate reservoir. The close comparison between the $\delta^{34}S_{evap}$ data we report and the established range for Permian seawater is significant, providing the first direct geochemical evidence for a hydrologic connection to seawater during deposition of evaporites beds B and C, which until now had only been inferred based upon the results of lithostratigraphic analysis (Burgess and Holliday, 1974; Holliday et al., 1993; Hughes, 2003).

Additional organic geochemical data should be gathered to better constrain environmental parameters, such as salinity, redox and the relative contributions from terrestrial and marine (phytoplanktonic, archaeal and bacterial) biomass sources. In doing so, it may be possible to better constrain the degree of hydrologic restriction during A Bed deposition, which currently remains unclear, while also providing insight into the most likely mechanism for generating the observed $\delta^{15}N_{tot}$ enrichment during Stage 1. Furthermore, compound-specific carbon and nitrogen isotope analyses could prove very informative, assisting in further constraining the nature of carbon and nitrogen cycling during deposition of the Eden Shales. Efforts should also be made in the detection of biomarkers indicative of methanogenic and/or methanotrophic activity, which in combination with more robust palaeosalinity proxies, may facilitate a better understanding of the microbially-mediated carbon cycle dynamics responsible for generating the extreme $\delta^{13}C_{org}$ enrichments during Stage 2.

7. References

Aggarwal, N., Agrawal, S., Thakur, B., 2019. Palynofloral, palynofacies and carbon isotopes of Permian coal deposits from the Godavari Valley Coalfield, South India: Insights into the age, palaeovegetation and palaeoclimate. *Int. J. Coal Geol.* 214, 103285. DOI: 10.1016/j.coal.2019.103285

Arp, G., Helms, G., Karlinska, K., Schumann, G., Reimer, A., Reitner, J., Trichet, J., 2012. Photosynthesis versus exopolymer degradation in the formation of microbialites on the Atoll of Kiritimati, Republic of Kiritimati, Central Pacific. *Geomicrobiol. J.* 29, 29-65. DOI: 10.1080/01490451.2010.521436

Arthurton, R.S., 1971. The Permian evaporites of the Langwathby Borehole, Cumberland. *Inst. Geol. Sci.* Rep. No. 71/7, 18 pp.

Arthurton, R.S., Burgess, I.C., Holliday, D.W., 1978. "Permian and Triassic", in *The geology of the Lake District*. Editor Moseley, F., (Yorkshire Geological Society Occasional Publication) No. 3, 189-206

Arthurton, R.S., Wadge, A.J., 1981. Geology of the country around Penrith. *Mem. Geol. Surv. G.B.* Sheet 24 (England and Wales). 177 pp.

Bastos, L.P.H., Rodrigues, R., Pereira, E., Bergamaschi, S., Alferes, C.L.F., Augland, L.E., Domeier, M., Planke, S., Svensen, H.H., 2021. The birth and demise of the vast epicontinental Permian Irati-Whitehill sea: Evidence from organic geochemistry, geochronology, and paleogeography. *Palaeogeogr. Palaeoclimatol. Palaeoecol.* 562, 110103. DOI: 10.1016/j.palaeo.2020.110103

Bastos, L.P.H., Jagniecki, E.A., dos Santos, W.H., da Costa Cavalcante, D., de Menezes, C.J., Alferes, C.L.F., da Silva, D.B.N., Bergamaschi, S., Rodrigues, R., Pereira, E., 2022. Organic geochemical evidence for the transition of Aptian-Albian hypersaline environments into marine restricted seas: The South Atlantic oceanic northern gateway and its implications for the pre-salt deposits. *Mar. Pet. Geol.* 140, 105632. DOI: 10.1016/j.marpetgeo.2022.105632

Behrens, E.W., Frishman, S.A., 1971. Stable carbon isotopes in blue-green algal mats. *J. Geol.* 79, 94-101. DOI: 10.1086/627590

Ben-Amotz, A., Avron, M., 1983. On the factors which determine massive β-carotene accumulation in the halotolerant alga *Dunaliella bardawil*. *Plant Physiol.* 72, 593-597. DOI: 10.1104/pp.72.3.593

Bernasconi, S.M., Meier, I., Wohlwend, S., Brack, P., Hochuli, P.A., Bläsi, H., Wortmann, U.G., Ramseyer, K., 2017. An evaporite-based high-resolution sulfur isotope record of Late Permian and Triassic seawater sulfate. *Geochim. Cosmochim. Acta*, 204, 331-349. DOI: 10.1016/j.gca.2017.01.047

Birgel, D., Meister, P., Lundberg, R., Horath, T.D., Bontognali, T.R.R., Bahniuk, A.M., De Rezende, C.E., Vasconcelos, C., McKenzie, J.A., 2015. Methanogenesis produces strong ^{13}C enrichment in stromatolites of Lagoa Salgada, Brazil: a modern analogue for Palaeo-/Neoproterozoic stromatolites? *Geobiology*, 13, 245-266. DOI: 10.1111/gbi.12130

Bottrell, S.H., Newton, R.J., 2006. Reconstruction of changes in global sulfur cycling from marine sulfate isotopes. *Earth Sci. Rev.* 75, 59-83. DOI: 10.1016/j.earscirev.2005.10.004

Bryant, R.N., Jones, C., Raven, M.R., Gomes, M.L., Berelson, W.M., Bradley, A.S., Fike, D.A., 2018. Sulfur isotope analysis of microcrystalline iron sulfides using secondary ion mass spectrometry imaging: Extracting local paleo-environmental information from modern and ancient sediments. *Rapid Commun. Mass Spectrom.* 33, 491-502. DOI: 10.1002/rcm.8375

Burgess, I.C., Holliday, D.W., 1979. Geology of the country around Brough-under-Stainmore. *Mem. Geol. Surv. G.B.* Sheet 31, including parts of sheets 25 and 30 (England and Wales). 131 pp.

Burke, A., Present, T.M., Paris, G., Rae, E.C.M., Sandilands, B.H., Gaillardet, J., Peucker-Ehrenbrink, B., Fischer, W.W., McClelland, J.W., Spencer, R.G.M., Voss, B.M., Adkins, J.F., 2018. Sulfur isotopes in rivers: Insights into global weathering budgets, pyrite oxidation, and the modern sulfur cycle. *Earth Planet. Sci. Lett.* 496, 168-177. DOI: 10.1016/j.epsl.2018.05.022

Canfield, D.E., 2001. Biogeochemistry of sulfur isotopes. *Rev. Mineral. Geochem.* 43, 607-636. DOI: 10.2138/gsrmg.43.1.607

Canfield, D.E., Des Marais, D.J., 1994. “The carbon isotope biogeochemistry of microbial mats”, in *Microbial mats: Structure, development and environmental significance*, NATO ASI Series G. Editors: Stal, L.J., Caumette, P., (Heidelberg: Springer-Verlag) 35, 255-263. DOI: 10.1007/978-3-642-78991-5_30

Canfield, D.E., Farquhar, J., Zerkle, A.L., 2010. High isotope fractionations during sulfate reduction in a low-sulfate euxinic ocean analogue. *Geology*, 38, 415-418. DOI: 10.1130/G30723.1

Canfield, D.E., Raiswell, R., Westrich, J.T., Reaves, C.M., Berner, R.A., 1986. The use of chromium reduction in the analysis of reduced inorganic sulfur in sediments and shales. *Chem. Geol.* 54, 149-155. DOI: 10.1016/0009-2541(86)90078-1

Chumakov, N.M., Zharkov, M.A., 2003. Climate during the Permian-Triassic biosphere reorganizations. Article 2. Climate of the Late Permian and Early Triassic: General inferences. *Stratigr. Geol. Correl.* 11, 361-375.

Claypool, G.E., Holser, W.T., Kaplan, I.R., Sakai, H., Zak, I., 1980. The age curves of sulfur and oxygen isotopes in marine sulfate and their mutual interpretation. *Chem. Geol.* 28, 199-260. DOI: 10.1016/0009-2541(80)90047-9

Coward, M.P., 1995. "Structural and tectonic setting of the Permo-Triassic basins of north-west Europe", in *Permian and Triassic rifting in north-west Europe*. Editor: Boldy, S.A.R., (Geological Society of London, Special Publications) 91, 7-39. DOI: 10.1144/GSL.SP.1995.091.01.02

Crockford, P.W., Kunzmann, M., Bekker, A., Hayles, J., Bao, H., Halverson, G.P., Peng, Y., Bui, T.H., Cox, G.M., Gibson, T.M., Wörndle, S., Rainbird, R., Lepland, A., Swanson-Hysell, N.L., Master, S., Sreenivas, B., Kuznetsov, A., Krupenik, V., Wing, B.A., 2019. Claypool continued: Extending the isotopic record of sedimentary sulfate. *Chem. Geol.* 513, 200-225. DOI: 10.1016/j.chemgeo.2019.02.030

Des Marais, D.J., 1995. "The biogeochemistry of hypersaline microbial mats", in *Advances in microbial ecology*. Editor Jones, J.G., (Boston, Ma: Springer) 14, 251-274. DOI: 10.1007/978-1-4684-7724-5_6

Des Marias, D.J., Nguyen, H., Cheatham, M., Cheatham, T., Munoz, E., 1989. “Carbon isotopic trends in the hypersaline ponds and microbial mats at Guerrero Negro, Baja California Sur, Mexico”, in *Microbial mats: Physiological ecology of benthic microbial communities*. Editors: Cohen, Y., Rosenberg, E., (Washington: American Society for Microbiology) 191-203

Dorador, C., Fink, P., Hengst, M., Icaza, G., Villalobos, A.S., Vejar, D., Meneses, D., Zadjelovic, V., Burmann, L., Moelzner, J., Harrod, C., 2018. Microbial community composition and trophic role along a marked salinity gradient in Laguna Puilar, Sala de Atacama, Chile. *Anton. Van Leeuw.* 111, 1361-1374. DOI: 10.1007/s10482-018-1091-z

El Tabakh, M., Schreiber, B.C., Warren, J.K., 1998. Origin of fibrous gypsum in the Newark Rift Basin, eastern North America. *J. Sediment. Res.* 68, 88-99. DOI: 10.2110/jsr.68.88

Fazeli, M.R., Tofighi, H., Samadi, N., Jamalifar, H., 2006. Effects on salinity on β-carotene production by *Dunaliella tertiolecta* DCCBC26 isolated from the Urmia salt lake, north of Iran. *Bioresour. Technol.* 97, 2453-2456. DOI: 10.1016/j.biortech.2005.10.037

Ferry, J.G., 2010. The chemical biology of methanogenesis. *Planet. Space Sci.* 58, 1775-1783. DOI: 10.1016/j.pss.2010.08.014

Fike, D.A., Bradley, A.S., Rose, C.V., 2015. Rethinking the ancient sulfur cycle. *Annu. Rev. Earth Planet. Sci.* 43, 593-622. DOI: 10.1146/annurev-earth-060313-054802

Frigaard, N-U., Dahl, C., 2008. Sulfur metabolism in phototropic sulfur bacteria. *Adv. Microb. Physiol.* 54, 103-200. DOI: 10.1016/S0065-2911(08)00002-7

Giani, D., Giani, L., Cohen, Y., Krumbein, W.E., 1984. Methanogenesis in the hypersaline Solar Lake (Sinai). *FEMS Microbiol. Lett.* 25, 219-224. DOI: 10.1111/j.1574-6968.1984.tb01460.x

Gómes, P.I., Barriga, A., Cifuentes, A.S., González, M.A., 2003. Effect of salinity on the quantity and quality of carotenoids accumulated by *Dunaliella salina* (strain CONC-007) and *Dunaliella bardawil* (strain ATCC 30861) Chlorophyta. *Biol. Res.* 36, 185-192.

Gomes, M.L., Hurtgen, M.T., 2015. Sulfur isotope fractionation in modern euxinic systems: Implications for paleoenvironmental reconstructions of paired sulfate-sulfide isotope records. *Geochim. Cosmochim. Acta*, 157, 39-55. DOI: 10.1016/j.gca.2015.02.031

Gu, B., Schelske, C.L., Hodell, D.A., 2004. Extreme ^{13}C enrichments in a shallow hypereutrophic lake: Implications for carbon cycling. *Limnol. Oceanogr.* 49, 1152-1159. DOI: 10.4319/lo.2004.49.4.1152

Habicht, K.S., Gade, M., Thamdrup, B., Berg, P., Canfield, D.E., 2002. Calibration of sulfate levels in the Archean ocean. *Science*, 298, 2372-2374. DOI: 10.1126/science.1078265

Hall, J.L.O., Newton, R.J., Witts, J.D., Francis, J.E., Hunter, S.J., Jamieson, R.J., Harper, E.M., Crame, J.A., Haywood, A.M., 2018. High benthic methane flux in low sulfate oceans: Evidence from carbon isotopes in Late Cretaceous Antarctic bivalves. *Earth Planet. Sci. Lett.* 497, 113-122. DOI: 10.1016/j.epsl.2018.06.014

He, T., Dal Corso, J., Newton, R.J., Wignall, P.B., Mills, B.J.W., Todaro, S., Di Stefano, P., Turner, E.C., Jamieson, R.A., Randazzo, V., Rigo, M., Jones, R.E., Dunhill, A.M., 2020. An

enormous sulfur isotope excursion indicates marine anoxia during the end-Triassic mass extinction. *Sci. Adv.* 6, eabb6704. DOI: 10.1126/sciadv.abb6704

Hebting, Y., Schaeffer, P., Behrens, A., Adam, P., Schmitt, G., Schneckenburger, P., Bernasconi, S.M., Albrecht, P., 2006. Biomarker evidence for major preservation pathway of sedimentary organic carbon. *Science*, 312, 1627-1631. DOI: 10.1126/science.1126372

Hitchen, K., Stoker, M.S., Evans, D., Beddoe-Stephens, B., 1995. "Permo-Triassic sedimentary and volcanic rocks in basins to the north and west of Scotland", in *Permian and Triassic rifting in northwest Europe*. Editor: Boldy, S.A.R., (Geological Society of London, Special Publications) 91, 87-102. DOI: 10.1144/GSL.SP.1995.091.01.05

Holliday, D.W., 1993. Geophysical log signatures in the Eden Shales (Permo-Triassic) of Cumbria and their regional significance. *Proc. Yorks. Geol. Soc.* 49, 345-354. DOI: 10.1144/pygs.49.4.345

Holliday, D.W., Holloway, S., McMillan, A.A., Jones, N.S., Warrington, G., Akhurst, M.C., 2004. The evolution of the Carlisle Basin, NW England and SW Scotland. *Proc. Yorks. Geol. Soc.* 55, 1-19. DOI: 10.1144/pygs.55.1.1

Holliday, D.W., Warrington, G., Brookfield, M.E., McMillan, A.A., Holloway, S., 2001. Permo-Triassic rocks in boreholes in the Annan-Canonbie area, Dumfries and Galloway, southern Scotland. *Scott. J. Geol.* 37, 97-113. DOI: 10.1144/sjg37020097

Horton, T.W., Defliese, W.F., Tripati, A.K., Oze, C., 2016. Evaporation induced ^{18}O and ^{13}C enrichment in lake systems: A global perspective on hydrologic balance effects. *Quat. Sci. Rev.* 131, 365-379. DOI: 10.1016/j.quascirev.2015.06.030

Hughes, R.A., 2003. Permian and Triassic rocks of the Appleby district (part of Sheet 30, England and Wales). British Geological Survey Research Report, RR/02/01. 21 pp.

Isaji, Y., Kawahata, H., Ogawa, N.O., Kuroda, J., Yoshimura, T., Jiménez-Espejo, F.J., Makabe, A., Shibuya, T., Lugli, S., Santulli, A., Manzi, V., Roveri, M., Ohkouchi, N., 2019. Efficient recycling of nutrients in modern and past hypersaline environments. *Sci. Rep.* 9, 3718. DOI: 10.1038/s41598-019-40174-9

Jackson, D.I., Jackson, A.A., Evans, D., Wingfield, R.T.R., Barnes R.P., Arthur, M.J., 1995. United Kingdom offshore regional report: the geology of the East Irish Sea (London: HMSO for the British Geological Survey)

Jenkyns, H.C., Gröcke, D.R., Hesselbo, S.P., 2001. Nitrogen isotope evidence for water mass denitrification during the early Toarcian (Jurassic) oceanic anoxic event. *Paleoceanography*, 16, 593-603. DOI: 10.1029/2000PA000558

Jørgensen, B.B., Böttcher, M.E., Lüschen, H., Neretin, L.N., Volkov, I.I., 2004. Anaerobic methane oxidation and a deep H_2S sink generate isotopically heavy sulfides in Black Sea sediments. *Geochim. Cosmochim. Acta*, 68, 2095-2118. DOI: 10.1016/j.gca.2003.07.017

Jørgensen, B.B., Findlay, A.J., Pellerin, A., 2019. The biogeochemical sulfur cycle of marine sediments. *Front. Microbiol.* 10, 849. DOI: 10.3389/fmicb.2019.00849

Joye, S.B., Connell, T.L., Miller, L.G., Oremland, R.S., Jellison, R.S., 1999. Oxidation of ammonia and methane in an alkaline, saline lake. *Limnol. Oceanogr.* 44, 178-188. DOI: 10.4319/lo.1999.44.1.0178

Joye, S.B., Samarkin, V.A., Orcutt, B.N., MacDonald, I.R., Hinrichs, K-U., Elvert, M., Teske, A.P., Lloyd, K.G., Lever, M.A., Montoya, J.P., Meile, C.D., 2009. Metabolic variability in

seafloor brines revealed by carbon and sulphur dynamics. *Nat. Geosci.* 2, 349-354. DOI: 10.1038/NGEO475

Jovovic, I., Grossi, V., Adam, P., Simon, L., Antheaume, I., Gelin, F., Ader, M., Cartigny, P., 2020. Quantitative and specific recovery of natural organic and mineral sulfur for (multi-)isotope analysis. *Org. Geochem.* 146, 104055. DOI: 10.1016/j.orggeochem.2020.104055

Kates, M., 1993. "Chapter 9 Membrane lipids of archaea", in *The biochemistry of archaea (archaebacteria)*. Editors: Kates, M., Kushner, D.J., Matheson, A.T., (Amsterdam: Elsevier) 26, 261-295. DOI: 10.1016/S0167-7306(08)60258-6

Knittel, K., Boetius, A., 2009. Anaerobic oxidation of methane: Progress with an unknown process. *Annu. Rev. Microbiol.* 63, 311-334. DOI: 10.1146/annurev.micro.61.080706.093130

Lacelle, D., Pellerin, A., Clark, I.D., Lauriol, B., Fortin, D., 2009. (Micro)morphological, inorganic-organic isotope geochemistry and microbial populations in endostromatolites (cf. fissure calcretes), Haughton impact structure, Devon Island, Canada: The influence of geochemical pathways on the preservation of isotope biomarkers. *Earth Planet. Sci. Lett.* 281, 202-214. DOI: 10.1016/j.epsl.2009.02.022

Leitner, C., Köster, M., Finger, F., 2023. Saltern, mudflat, and dry playa: Playa basin types of a retreating epeiric sea (Keuper, Germany). *J. Sediment. Res.* 93, 840-856. DOI: 10.2110/jsr.2023.013

Lent, R.M., Lyons, W.B., Showers, W.J., Johannesson, K.H., 1995. Late Holocene paleoclimate and paleobiologic records from sediments of Devils Lake, North Dakota. *J. Paleolimnol.* 13, 193-207. DOI: 10.1007/BF00682764

Londry, K.L., Dawson, K.G., Grover, H.D., Summons, R.E., Bradley, A.S., 2008. Stable carbon isotope fractionation between substrates and products of *Methanosarcina barkeri*. *Org. Geochem.* 39, 608-621. DOI: 10.1016/j.orggeochem.2008.03.002

Luo, G., Yang, H., Algeo, T.J., Hallmann, C., Xie, S., 2019. Lipid biomarkers for the reconstruction of deep-time environmental conditions. *Earth-Sci. Rev.* 189, 99-124. DOI: 10.1016/j.earscirev.2018.03.005

Ma, J., Cui, X., 2022. Aromatic carotenoids: Biological sources and geological implications. *Geosyst. Geoenviron.* 1, 100045. DOI: 10.1016/j.geogeo.2022.100045

Macchi, L.C., 1981. Sedimentology of the Penrith sandstone and brockrams (Permo-Triassic) of Cumbria, north-west England. (Unpublished PhD Thesis). University of Hull.

Magee, J.W., Bowler, J.M., Miller, G.H., Williams, D.L.G., 1995. Stratigraphy, sedimentology, chronology and palaeohydrology of Quaternary lacustrine deposits at Madigan Gulf, Lake Eyre, South Australia. *Palaeogeogr. Palaeoclimatol. Palaeoecol.* 113, 3-42. DOI: 10.1016/0031-0182(95)00060-Y

McKie, T., 2017. "Palaeogeographic evolution of latest Permian and Triassic salt basins in northwest Europe", in *Permo-Triassic salt provinces of Europe, North Africa and the Atlantic margins, tectonics and hydrocarbon potential*. Editors Soto, J.J., Flinch, J.F., Tari, G. (Amsterdam Netherlands: Elsevier), 159-173. DOI: 10.1016/B978-0-12-809417-4.00008-2

Menzel, P., Gaye B., Wiesner, M.G., Prasad, S., Stebich, M., Das, B.K., Anoop, A., Riedel, N., Basavaiah, N., 2013. Influence of bottom-water anoxia on nitrogen isotopic ratios and amino acid contributions of recent sediments from small eutrophic Lonar Lake, central India. *Limnol. Oceanogr.* 58, 1061-1074. DOI: 10.4319/lo.2013.58.3.10611061

Mettam, C., Zerkle, A.L., 2021. *Nitrogen isotopes in deep time* (Cambridge: Cambridge University Press). DOI: 10.1017/9781108847186

Milroy, P., Wright, V.P., Simms, M.J., 2019. Dryland continental mudstones: Deciphering environmental changes in problematic mudstones from the Upper Triassic (Carnian to Norian) Mercia Mudstone Group, south-west Britain. *Sedimentology*, 66, 2557-2589. DOI: 10.1111/sed.12626

Mishra, S., Jha, N., Stebbins, A., Brookfield, M., Hannigan, R., 2019. Palaeoenvironments, flora and organic carbon and nitrogen isotope changes across the non-marine Permian-Triassic boundary at Wybung Head, Australia. *Palaeogeogr. Palaeoclimatol. Palaeoecol.* 534, 109292. DOI: 10.1016/j.palaeo.2019.109292

Moragas, M., Martínez, C., Baqués, V., Playà, E., Travé, A., Alías, G., Cantarero, I., 2013. Diagenetic evolution of a fractured evaporite deposit (Vilobí Gypsum Unit, Miocene, NE Spain). *Geofluids*, 13, 180-193. DOI: 10.1111/gfl.12017

Morse, J.W., Rickard, D., 2004. Chemical dynamics of acid volatile sulfide. *Environ. Sci. Tech.* 38, 131-136

Moscariello, A., 2005. "Exploration potential of the mature Southern North Sea basin margins: some unconventional plays based on alluvial and fluvial fan sedimentation", in *Petroleum geology: North-West Europe and global perspectives – Proceedings of the 6th*

Petroleum Geology Conference. Editors: Dore, A.G., Vining, B.A., (London: Geological Society, London) 6, 595-605. DOI: 10.1144/0060595

Niemann, H., Elvert, M., 2008. Diagnostic lipid biomarkers and stable carbon isotope signatures of microbial communities mediating the anaerobic oxidation of methane with sulphate. *Org. Geochem.* 39, 1668-1677. DOI: 10.1016/j.orggeochem.2007.11.003

Oren, A., 1999. Bioenergetic aspects of halophilism. *Microbiol. Molec. Biol. Rev.* 63, 334-348. DOI: 10.1128/mmbr.63.2.334-348.1999

Parrish, J.T., 1993. Climate of the supercontinent Pangea. *J. Geol.* 101, 215-233. DOI: 10.1086/648217

Pasquier, V., Sansjofre, P., Rabineau, M., Revillon, S., Houghton, J., Fike, D.A., 2017. Pyrite sulfur isotopes reveal glacial-interglacial environmental changes. *Proc. Natl. Acad. Sci.* 114, 5941-5945. DOI: 10.1073/pnas.1618245114

Planavsky, N., Reid, R.P., Lyons, T.W., Myshrall, K.L., Visscher, P.T., 2009. Formation and diagenesis of modern marine calcified cyanobacteria. *Geobiology*, 7, 566-576. DOI: 10.1111/j.1472-4669.2009.00216.x

Rennie, V.C.F., Paris, G., Sessions, A.L., Abramovich, S., Turchyn, A.V., Adkins, J.F., 2018. Cenozoic record of $\delta^{34}S$ in foraminiferal calcite implies an early Eocene shift to deep-ocean sulfide burial. *Nat. Geosci.* 11, 761-765. DOI: 10.1038/s41561-018-0200-y

Ruffell, A.H., Holliday, D.W., Smith, D.B., 2006. “Permian: arid basins and hypersaline seas”, in *The geology of England and Wales*. Editors Rawson, P.F., Brenchley, P., (London: Geological Society of London) 295-325. DOI: 10.1144/GOEWP.12

Salisbury, J., Gröcke, D., Cheung, H.D.R.A., Kump, L.R., McKie, T., Ruffell, A., 2022. An 80-million-year sulphur isotope record of pyrite burial over the Permian-Triassic. *Sci. Rep.* 12, 17370. DOI: 10.1038/s41598-022-21542-4

Salisbury, J., Gröcke, D.R., McKie, T., 2023. Sulphur isotope stratigraphy of drill cuttings and stratigraphic correlation of Permian-Triassic evaporites. *Front. Earth Sci.* 11, 1216365. DOI: 10.3389/feart.2023.1216365

Salisbury, J., Gröcke, D.R., McKie, T., Cheung, H.D.R.A., Raine, R. Sulphur isotope stratigraphy of the Triassic Sherwood Sandstone and Mercia Mudstone groups, United Kingdom (*in prep.*)

Schidlowski, M., 2000. "Carbon isotopes and microbial sediments", in *Microbial sediments*. Editors: Riding, R.E., Awramik, S.M., (Berlin, Heidelberg: Springer) 84-95. DOI: 10.1007/978-3-662-04036-2_11

Schidlowski, M., 2001. Carbon isotopes as biogeochemical recorders of life over 3.8 Ga of Earth history: evolution of a concept. *Precambrian Res.* 106, 117-134. DOI: 10.1016/S0301-9268(00)00128-5

Schidlowski, M., Gorzawski, H., Dor, I.A., 1994. Carbon isotope variations in a solar pond microbial mat: Role of environmental gradients as steering variables. *Geochim. Cosmochim. Acta*, 58, 2289-2298. DOI: 10.1016/0016-7037(94)90011-6

Schidlowski, M., Matzigkeit, U., Krumbein, W.E., 1984. Superheavy organic carbon from hypersaline microbial mats. *Naturwissenschaften*, 71, 303-308. DOI: 10.1007/BF00396613

Schidlowski, M., Matzigkeit, U., Mook, W.G., Krumbein, W.E., 1985. “Carbon isotope geochemistry and ^{14}C ages of microbial mats from the Gavish Sabkha and the Solar Lake”, in *Hypersaline environments the Gavish Sabkha*. Editors: Friedman, G.M., Krumbein, W.E., (Berlin, Heidelberg: Springer) 53, 381-401. DOI: 10.1007/978-3-642-70290-7_22

Sepkoski, J.J., 1996. “Patterns of Phanerozoic extinction: A perspective from global databases”, in *Global events and event stratigraphy in the Phanerozoic*. Editor: Walliser, O.H., (Berlin: Springer) 35-51. DOI: 10.1007/978-3-642-79634-0_4

Sim, M.S., Bosak, T., Ono, S., 2011. Large sulfur isotope fractionation does not require disproportionation. *Science*, 333, 74-77. DOI: 10.1126/science.1205103

Smith, D.S., Brunstrom, R.G.W., Manning, P.I., Simpson, S., Shotton, F.W., 1972. A correlation of Permian rocks in the British Isles. Special Report No. 5. *Geol. Soc. Lond.* 130, 1-45. Stiller, M., Magaritz, M., 1974. Carbon-13 enriched carbonate in interstitial waters of Lake Kinneret sediments. *Limnol. Oceanogr.* 19, 849-853. DOI: 10.4319/lo.1974.19.5.0849

Stiller, M., Rounick, J.S., Shasha, S., 1984. Extreme carbon-isotope enrichments in evaporating brines. *Nature*, 316, 434-435. DOI: 10.1038/316434a0

Stone, P., Millward, D., Young, B., Merritt, J.W., Clarke, S.M., McCormac, M., Lawrence, D.J.D., 2010. *Northern England British regional geology*. 5th Ed. Keyworth, Nottingham: British Geological Survey

Stüeken, E.E., Buick, R., Schauer, A.J., 2015. Nitrogen isotope evidence for alkaline lakes on late Archean continents. *Earth Planet. Sci. Lett.* 411, 1-10. DOI: 10.1016/j.epsl.2014.11.037

Stüeken, E.E., Kipp, M.A., Koehler, M.C., Buick, R., 2016. The evolution of Earth's biogeochemical nitrogen cycle. *Earth Sci. Rev.* 160, 220-239. DOI: 10.1016/j.earscirev.2016.07.007

Stüeken, E.E., Martinez, A., Love, G., Olsen. P.E., Bates, S., Lyons, T.W., 2019. Effects of pH on redox proxies in a Jurassic rift lake: Implications for interpreting environmental records in deep time. *Geochim. Cosmochim. Acta*, 252, 240-267. DOI: 10.1016/j.gca.2019.03.014

ten Haven, H.L., de Leeuw, J.W., Rullkötter, J., Sinninghe Damsté, J.S., 1987. Restricted utility of the pristane/phytane ratio as a palaeoenvironmental indicator. *Nature*, 330, 641-643. DOI: 10.1038/330641a0

Thauer, R.K., 1998. Biochemistry of methanogenesis: a tribute to Marjory Stephenson. *Microbiology*, 144, 2377-2406. DOI: 10.1099/00221287-144-9-2377

Underhill, J.R., Gayer, R.A., Woodcock, N.H., Donnelly, R., Jolley, E.J., Stimpson, I.G., 1988. The Dent Fault System, northern England – reinterpreted as a major oblique-slip fault zone. *J. Geol. Soc. Lond.* 145, 303-316. DOI: 10.1144/gsjgs.145.2.030

Warren, J.K., 2010. Evaporites through time: Tectonic, climatic and eustatic controls in marine and nonmarine deposits. *Earth-Sci. Rev.* 98, 217-268. DOI: 10.1016/j.earscirev.2009.11.004

Warren, J.K., 2021. "Evaporite deposits", in *Encyclopaedia of geology (second edition)*. Editors: Alderton, D., Elias, S.A., (Oxford: Academic Press) 945-977. DOI: 10.1016/B978-0-08-102908-4.00165-X

Warrington, G., 2008. Palynology of the Permian succession in the Hilton Borehole, Vale of Eden, Cumbria, UK. *Proc. Yorks. Geol. Soc.* 57, 123-130. DOI: 10.1144/pygs.57.2.123

Weber, H.S., Thamdrup, B., Habicht, S., 2016. High sulfur isotope fractionation associated with anaerobic oxidation of methane in a low-sulfate, iron-rich environment. *Front. Earth Sci.* 4, 61. DOI: 10.3389/feart.2016.00061

Worley, N.E., 2005. The occurrence of halite in the Permian A Bed Evaporite, Kirkby Thore, Cumbria. *Proc. Yorks. Geol. Soc.* 55, 199-203. DOI: 10.1144/pygs.55.3.199

Zaback, D.A., Pratt, L.M., 1992. Isotopic composition ad speciation of sulfur in the Miocene Monterey Formation: Reevaluation of sulfur reactions during early diagenesis in marine environments. *Geochim. Cosmochim. Acta*, 56, 763-774. DOI: 10.1016/0016-7037(92)90096-2

Zhang, X., Sigman, D.M., Morel, F.M.M., Kraepiel, A.M.L., 2014. Nitrogen isotope fractionation by alternative nitrogenases and past ocean anoxia. *Proc. Natl. Acad. Sci.* 111, 4782-4787. DOI: 10.1073/pnas.1402976111

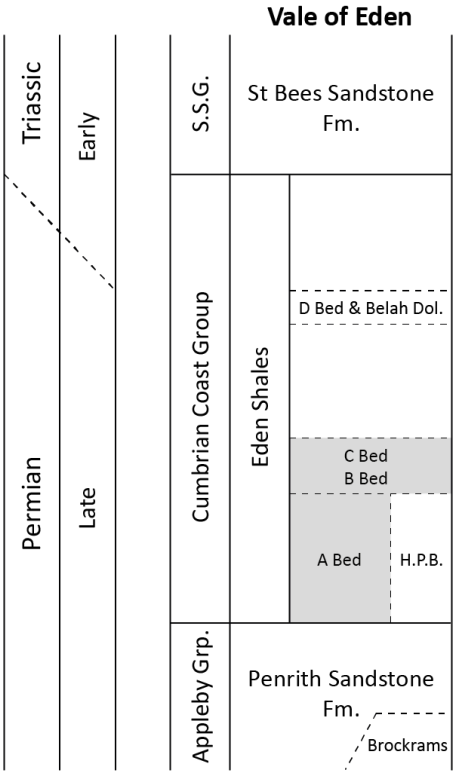

Figure 1: *The established lithostratigraphic framework for the late Permian and earliest Triassic of the Vale of Eden, Cumbria. The major lithostratigraphic units are provided, along with subdivisions of the Eden Shales Formation. The dashed line for the position of the Permian-Triassic chronostratigraphic boundary reflects the uncertainty regarding its' precise placement above the D Bed evaporite. The grey shaded intervals are those from which samples were analysed for this study. Abbreviations: Grp. = group; Fm. = formation; S.S.G. = Sherwood Sandstone Group; H.P.B. = Hilton Plant Beds; Dol. = dolomite. The lithostratigraphy is based upon Hughes (2003) and Ruffell et al. (2006).*

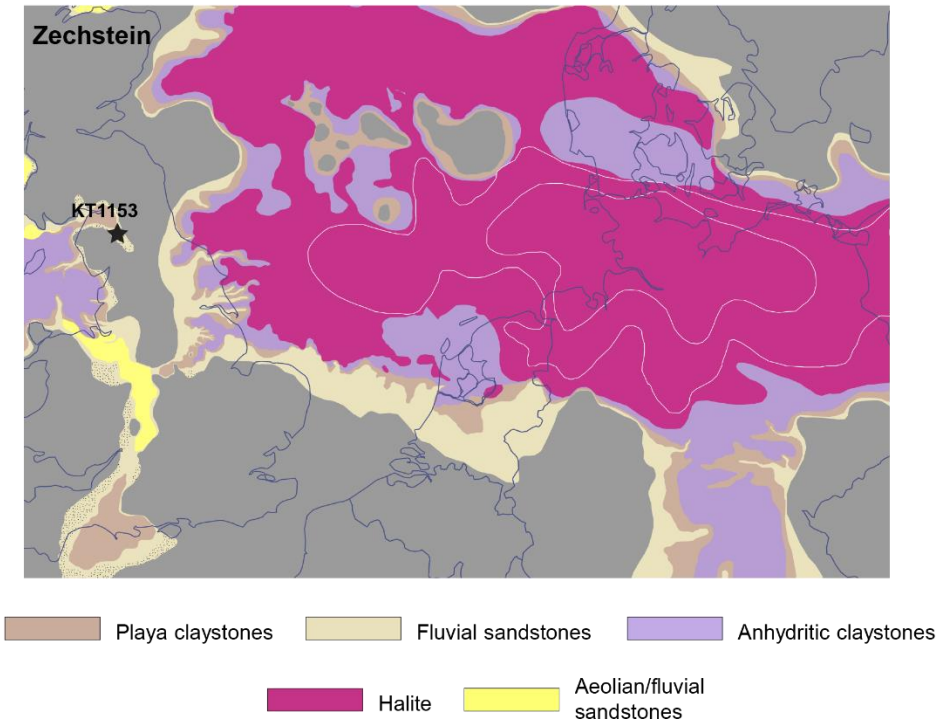

Figure 2: *Palaeogeographic context of the latest Permian. The location of drillcore KT1153 sampled for this study is marked with a black star. Adapted from Salisbury et al. (2023).*

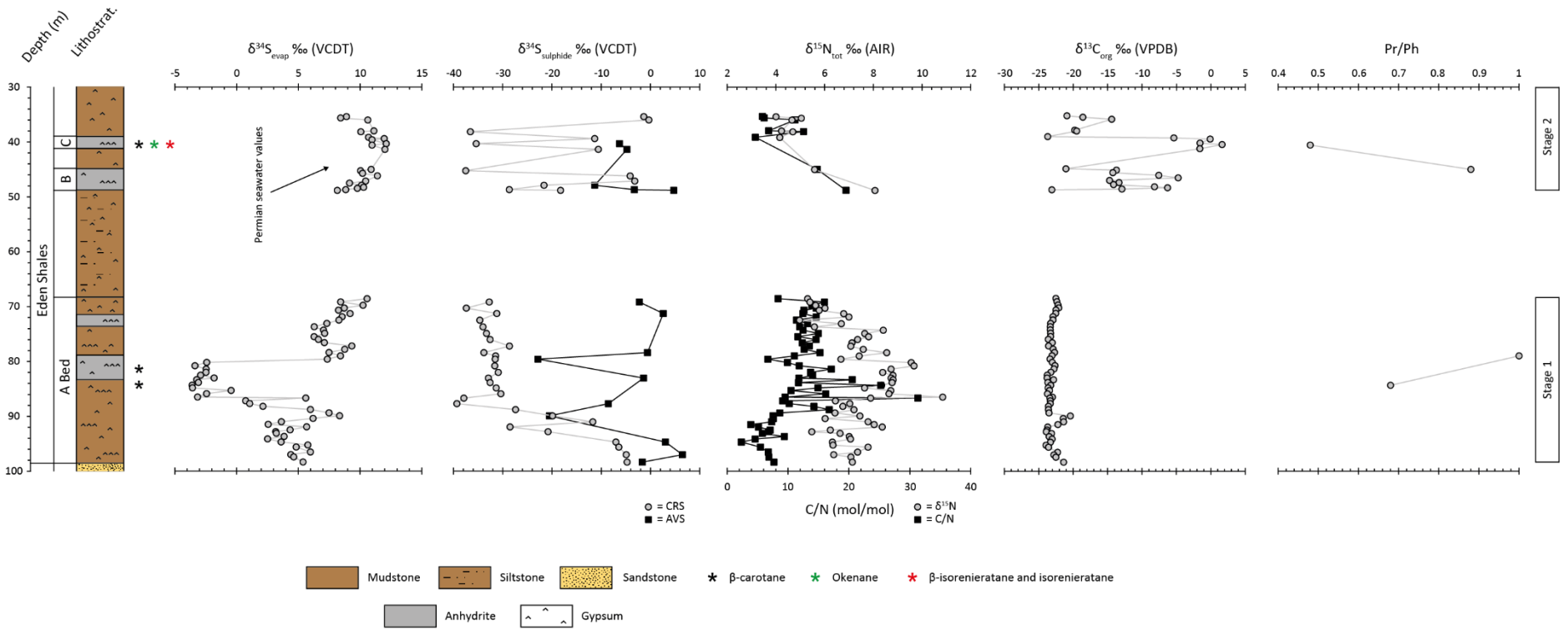

Figure 3: *Geochemical data presented against a simplified lithological log. The two biogeochemically distinct stages (Stage 1 and Stage 2) established and discussed in the text are marked on the right. The lithostratigraphy is based on the original drilling log, provided courtesy of British Gypsum.*

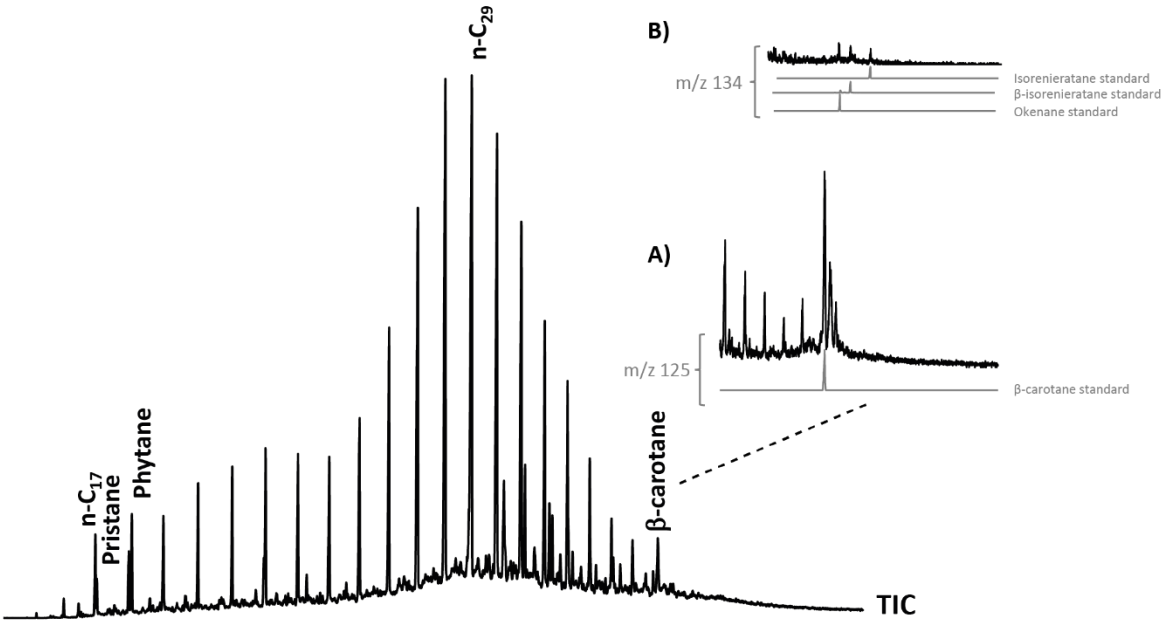

Figure 4: *(A) Total Ion Chromatogram (TIC) and partial m/z 125 fragmentogram of the saturated hydrocarbon fraction from a sample within C Bed evaporite at a stratigraphic depth of 40.58 m showing the strong presence of β-carotane. (B) The identification of isorenieratane, β-isorenieratane and okenane in the aromatic fraction of this sample is also presented.*

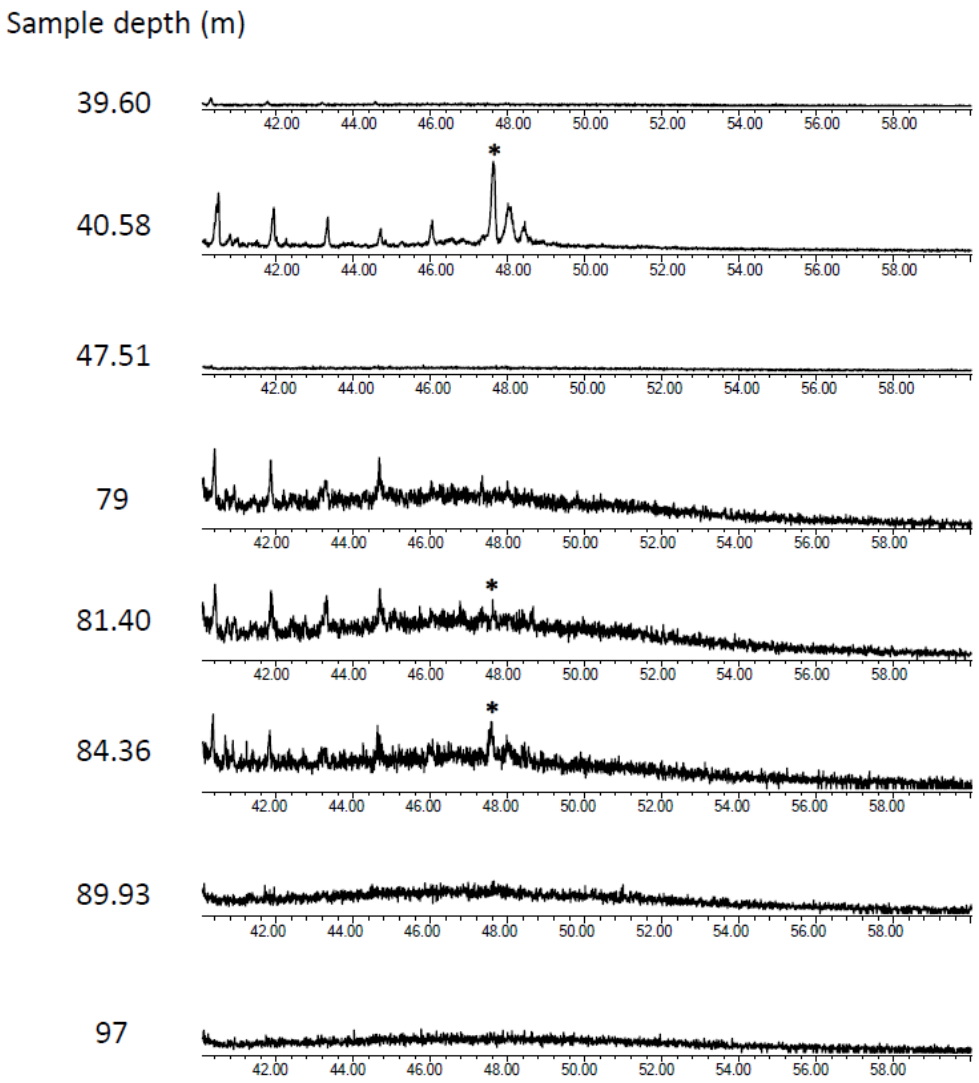

Figure 5: *Partial mass fragmentograms (m/z 125) of 8 samples across the sampled interval of drillcore KT1153. The GC-MS traces are displayed stratigraphically, with the stratigraphic depth of each sample provided. β-carotane is marked with a star (*) above the traces for the samples within which it was detected.*

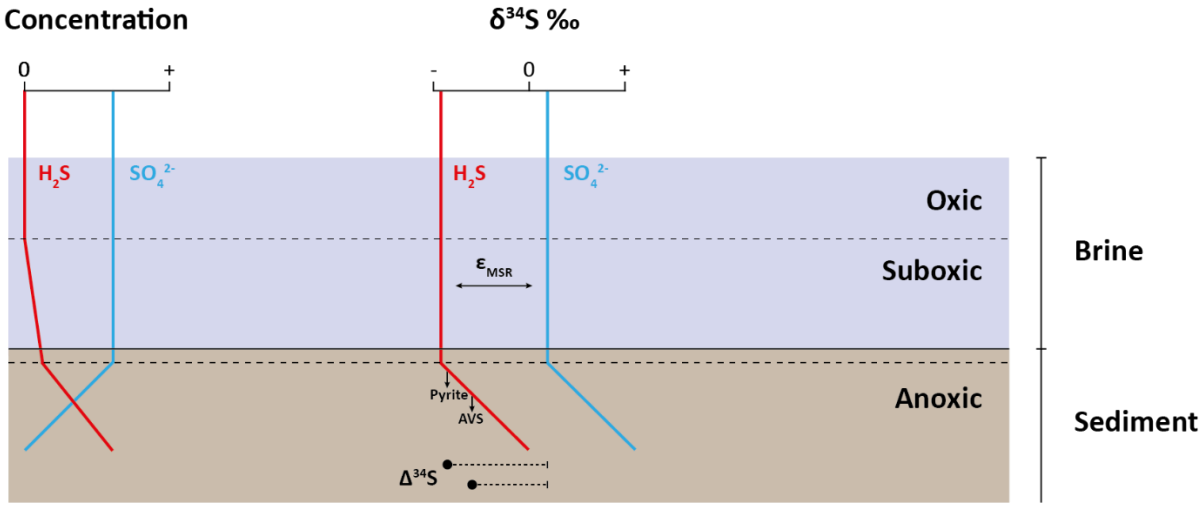

Figure 6: *Schematic diagram of the reservoir effect on the $\Delta^{34}S$ associated with sulphide formation. The concentration (left) and $\delta^{34}S$ (right) of the sulphide (H_2S, red) and sulphate (SO_4^{2-}, blue) are plotted with depth in the water column and underlying sediment. The model presented assumes sulphide formation is occurring diagenetically within the sediment body. A sharp reduction in the concentration of sulphate below the suboxic-anoxic boundary within the sediment, causes a Rayleigh distillation effect and the ^{34}S-enrichment of both sulphide and sulphate. Approximate $\delta^{34}S$ for pyrite and acid-volatile sulphide (AVS) are marked with black arrows. The magnitude of the $\Delta^{34}S$ between initial sulphate and sulphide is represented by black-filled circles and dashed lines. AVS is associated with a smaller net $\Delta^{34}S$, as its formation occurs deeper within the sediment where sulphate concentrations are lower. For further details, see Gomes and Hurtgen (2015).*

Stage 2

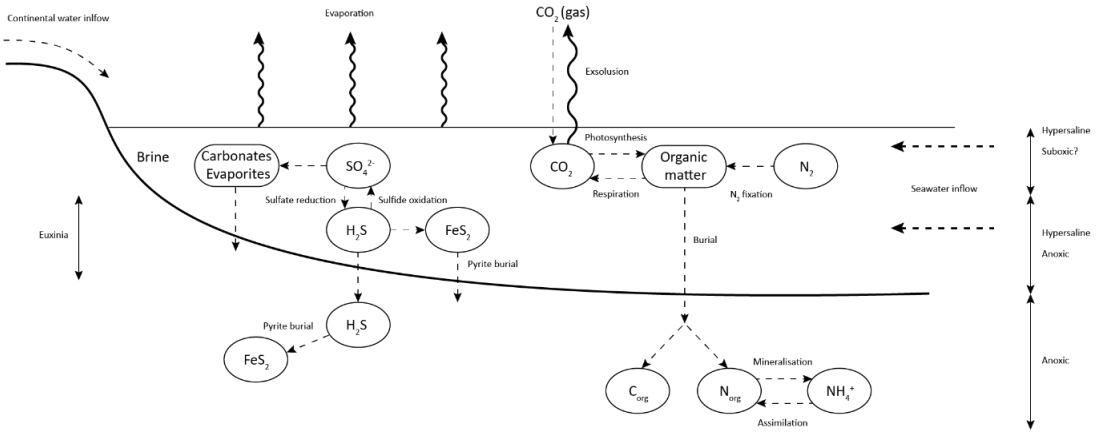

Stage 1

Interpretation A

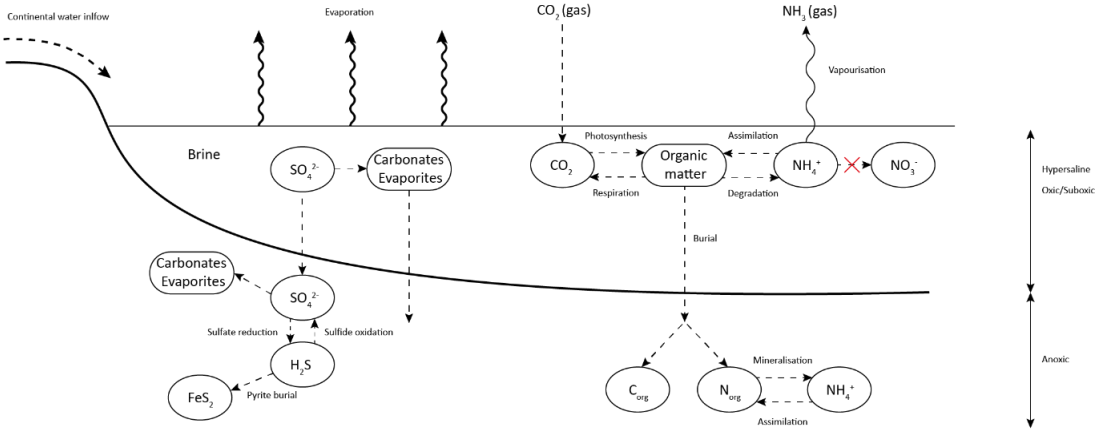

Interpretation B

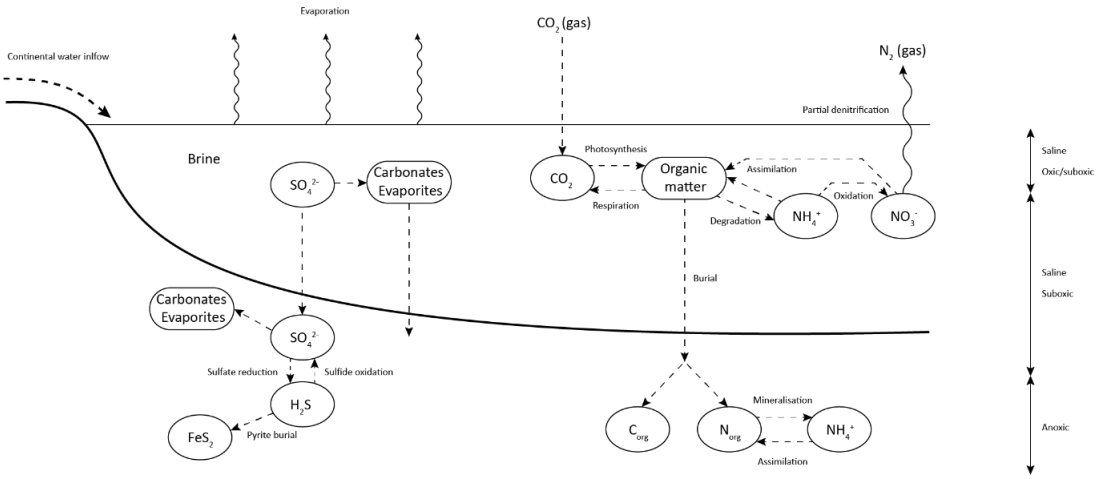

Figure 7: *Schematic diagram of the biogeochemistry during deposition of late Permian Eden Shales. Two distinct biogeochemical stages are presented, Stage 1 (A bed) and Stage 2 (beds B and C). For Stage 1, two potential interpretations for the observed increase in $\delta^{15}N_{tot}$ are presented. Interpretation A involves partial denitrification and the loss of ^{14}N-rich gaseous N_2 (see Jenkyns et al., 2001; Mettam and Zerkle 2021). Interpretation B involves the ^{15}N-enrichment of ammonium conditions of hypersalinity. In this case, the inhibition of nitrification suppresses rates of denitrification and annamox, facilitating efficient microbial recycling of ammonium. In addition, under hypersalinity, ammonia experiences volatility, with ^{14}N-rich ammonia escaping to the atmosphere. Together, ammonium recycling and ammonia volatility, generate a ^{15}N-enriched ammonium pool (see Isaji et al., 2019). During Stage 2, seawater inflow provides a source of marine sulphate. Expansion in the extent of photic zone euxinia (PZE), possibly within the uppermost sediment, microbial mat structures, or at particular depths within the brine system, led to localised sulphate limitation and the ^{34}S-enrichment of sulphides via a Rayleigh distillation effect. Efficient N_2 fixation amongst cyanobacteria generates a reduction in the $\delta^{15}N$ of total nitrogen. Furthermore, CO_2 volatility under conditions of hypersalinity, in combination with hypersalinity, generate an extreme ^{13}C-enrichment of organic matter (see Schidlowski et al., 1994).*

Chapter 6: Conclusions

The late Permian-Triassic has seen extensive study, with particular focus applied to understanding the End Permian Mass Extinction Event (EPME) and the End Triassic Extinction (ETE). These extinction events represent major shifts in the Earth's biosphere (Sepkoski, 1996) and are associated with perturbations in the isotopic composition of seawater sulphate (Claypool et al., 1980; Bernasconi et al., 2017; He et al., 2020; Salisbury et al., 2022). The success of isotope stratigraphy in developing robust correlations at a high resolution is, in part, dependent upon isotopic variability (see Yao et al., 2019). The perturbations recorded in the $\delta^{34}S$ of seawater sulphate across the late Permian-Triassic are ideal for the establishment of sulphur isotope correlation schemes. Recent studies have successfully applied evaporite-based sulphur isotope ($\delta^{34}S_{evap}$) stratigraphy to the Triassic of central Europe (Bernasconi et al., 2017) and eastern Spain (Ortí et al., 2022). However, until the work presented here, $\delta^{34}S_{evap}$-based stratigraphy has seen little application to the UK Triassic, despite the abundance of evaporitic material.

This thesis presents $\delta^{34}S_{evap}$ records from five distinct Permian-Triassic UK sedimentary basins, in order to establish further chronostratigraphic constraint to biostratigraphically barren evaporites (chapters 2, 3 and 4); provide additional insight into the degree of marine influence during the UK Triassic evaporite deposition (chapter 4); and to further elucidate the biogeochemical evolution of the Permian-Triassic, either on a long-term global scale (chapter 2) or on the scale of a single evaporite system (chapter 5).

The thesis is presented as a series of manuscripts for publication, two of which have already been published (Salisbury et al., 2022, 2023), while two are included in currently unpublished forms and are being finalised for publication (chapters 4 and 5). Accordingly, a detailed conclusion is included at the end of each chapter. Here, I consolidate and summarise the conclusions of each, while finally suggesting potential avenues for future research.

1. Establishing a UK Triassic $\delta^{34}S_{evap}$ record and modelling of the sulphur cycle

The sulphur isotope analysis of evaporitic material (ca-sulphates and halite) from the Staithes S-20 borehole, Yorkshire, England, enabled the generation of a $\delta^{34}S_{evap}$ record extending from the uppermost Zechstein, through the Bunter Shale and Bunter Sandstone (Sherwood Sandstone Group – SSG), to the upper Mercia Mudstone Group (MMG) (Fig. 2.2). At the time of publication, the Staithes S-20 $\delta^{34}S_{evap}$ represents the most high-resolution sulphur isotope record for the UK Triassic, with previously published data lacking temporal and spatial resolution (e.g., Taylor, 1983).

The compilation of various $\delta^{34}S_{evap}$ datasets from evaporites globally enabled the generation of a global composite $\delta^{34}S_{evap}$ record, assumed to represent the temporal evolution in the $\delta^{34}S$ of seawater sulphate. The close comparison between the Staithes S-20 $\delta^{34}S_{evap}$ record and the global composite age curve enabled correlation, establishing the highest resolution $\delta^{34}S_{evap}$ correlation scheme between evaporites of the UK late-Permian-Triassic, and temporally equivalent evaporites in continental Europe and further afield. At the base of the sampled interval in Staithes S-20, the $\delta^{34}S_{evap}$ data appear to exhibit cyclicity through the uppermost Zechstein and through to the lower Bunter Shale, which could in theory be employed for the purposes of stratigraphy,

assuming it is a signal of global significance. For the remainder of the Bunter Shale and overlying Bunter Sandstone, the $\delta^{34}S_{evap}$ data exhibit values (~+10-12 ‰) comparable to those of Permian seawater sulphate (Claypool et al., 1980; Crockford et al., 2019).

In the earliest Anisian, the Staithe S-20 $\delta^{34}S_{evap}$ record exhibits an abrupt decline to ~+15 ‰. This compares to the $\delta^{34}S_{evap}$ values (~+17 ‰) reported from the earliest Anisian in the southern Alps (Cortecci et al., 1981; Bernasconi et al., 2017). Due to low data resolution, and the fact that both studies report this isotopic depletion from the same formation, Bernasconi et al. (2017) were unable to confidently determine whether this represents a global seawater signal or local depositional processes. However, the fact that we report a comparable negative $\delta^{34}S_{evap}$ excursion in the earliest Anisian would suggest this may indeed be a primary seawater signal and may thus prove useful for the correlation of sections across the Early-Middle Triassic boundary globally.

The Staithes S-20 $\delta^{34}S_{evap}$ record and the global composite exhibit relative stability around +15 ‰ beginning in the Carnian. This stability is maintained until the uppermost Mercia Mudstone Group (latest Norian) within Staithes S-20, where we measure a relatively minor positive $\delta^{34}S_{evap}$ excursion to ~+19 ‰, which can be correlated to an excursion of comparable magnitude exhibited by the global composite during the latest Norian.

The establishment of a correlation scheme between Staithes S-20 and the global composite sulphur isotope age curve enabled the generation of a composite $\delta^{34}S_{evap}$, incorporating the global data and that of Staithes S-20. This composite record was assimilated into the sulphur biogeochemical box model of Kurtz et al. (2003), generating the most complete record of pyrite burial for the Triassic. For much of the record, the

model outputs agree well with previous publications, suggesting a substantial increase in the pyrite burial flux during the Early Triassic (see Newton et al., 2004; Bernasconi et al., 2017), and a possible weathering event as a driver of the Early-Middle Triassic negative $\delta^{34}S_{evap}$ excursion (see Bernasconi et al., 2017).

However, a possible positive excursion in $\delta^{34}S_{evap}$ in the latest Norian has not been widely reported before. Our model outputs suggest an increase in the pyrite burial flux would have been capable of inciting an $\delta^{34}S$ enrichment of this magnitude in the seawater sulphate reservoir. In addition, the emplacement of the Angayucham large igneous province (LIP), located today in northwestern Alaska, likely occurred within the late Norian (Ernst and Buchan, 2001), coinciding with an oceanic warming event inferred by oxygen isotope records (Trotter et al., 2015). However, it must be emphasised that the positive excursion in the late Norian of the global composite is derived from data with poor age constraint (Cortecci et al., 1981; Utrilla et al., 1992). In addition, no independent biostratigraphic age constraints exist for this depth interval within the Staithes S-20 drillcore. Thus, the signal in Staithes S-20 could be a product of local depositional factors and the excursion in the late Norian of the global composite could be a product of imprecise dating. As a result, we cannot confirm a late Norian positive $\delta^{34}S_{evap}$ excursion with the data currently available.

2. Expanding the UK $\delta^{34}S_{evap}$ curve

Building upon the success of the Staithes S-20 $\delta^{34}S_{evap}$ record, sulphur isotope stratigraphy was applied across additional UK Triassic sedimentary basins. The trends in both exhibited by the Staithes S-20 and global composite records were replicated from 42/28-2 in the Southern North Sea, UK sector (see Chapter 3), enabling stratigraphic

correlation. This is particularly significant, as the sampled interval in 42/28-2 is composed entirely of drill cuttings. In addition, $\delta^{34}S_{evap}$ data from 110/13-8 of the EISB (see Chapter 4), while exhibiting a greater degree of scatter, still exhibits the gradual declining trend characteristic of the Middle-Late Triassic, facilitating stratigraphic correlation. The scatter exhibited by the $\delta^{34}S_{evap}$ record of 110/13-8 could be a product of caving, although this is currently unclear. Despite this, the correlation schemes established with the $\delta^{34}S_{evap}$ records of 42/28-2 and 110/13-8 demonstrate the potential suitability of drill cuttings for the sulphur isotope stratigraphy of evaporites. This is noteworthy, as the ubiquity of drill cuttings greatly increases the number of sites available for sampling, providing the potential to expand the geospatial coverage of the composite Triassic $\delta^{34}S_{evap}$ record.

Similarly to the $\delta^{34}S_{evap}$ data of Staithes S-20, the $\delta^{34}S_{evap}$ record of 42/28-2 exhibits values in line with those of later Permian seawater within the Bunter Shale and Bunter Sandstone formations (see Salisbury et al., 2023 and Chapter 4). This is significant, as it could suggest that the lower Bunter Sandstone is of Permian age along the western margins of the Southern Permian Basin, and thus the Permian-Triassic boundary in the locations sampled here should be shifted to a currently undefined position within the SSG.

Interestingly, $\delta^{34}S_{evap}$ data from the SSG and the lowermost MMG (Lagavarra Formation) in the Larne Basin appear to provide a comparable signal (see Chapter 4). Data from the lower SSG in drillcore of GT-01 Kilroot range between +8 ‰ and +11 ‰ and are thus comparable to late Permian seawater. In addition, $\delta^{34}S_{evap}$ data from the lowermost Lagavarra Formation compare well with the global composite curve in the

early Anisian. $\delta^{34}S_{evap}$ data of Cairncastle-2 (also the Larne Basin) from the uppermost SSG range between +22 ‰ and +24 ‰ and are thus consistent with $\delta^{34}S_{evap}$ values established for seawater sulphate during the latest Early Triassic. When viewed together, these data suggest the lowermost SSG should also be assigned a late Permian age in the Larne Basin, and that the PTB could be placed at a position within the SSG. It should be stressed though, that these data from the Larne Basin are of low resolution due to the low abundance of evaporitic material in the SSG, preventing a precise placement of the PTB and limiting the confidence of any interpretations.

The $\delta^{34}S_{evap}$-based correlation scheme established for 110/13-8 is broadly in line with the established biostratigraphy and lithostratigraphic framework (see Chapter 4). The $\delta^{34}S_{evap}$ data suggest the upper boundary of the Preesall Halite could be shifted into the Ladinian. While it is of course true that the biostratigraphy is of low resolution and does not provide precise constraint to the chronostratigraphic position of this lithostratigraphic boundary, our $\delta^{34}S_{evap}$ data from a single core in the EISB is likely insufficient to challenge the established framework, which assigns the uppermost Preesall Halite to the Anisian. Thus, the $\delta^{34}S_{evap}$-based correlation assigns the stratigraphy from the lower boundary of the MMG to the upper boundary of the Preesall Halite to the Anisian. The Warton Halite is assigned to the Carnian, and although the $\delta^{34}S_{evap}$ data would allow for this formation to be stretched into the Norian, the available biostratigraphy suggests this is unlikely (see Jackson and Johnson, 1996). Thus, considering that an entirely Carnian age for the Warton Halite also facilitates reasonable $\delta^{34}S_{evap}$ correlation with the global composite, the Warton Halite is assigned to the Carnian in the $\delta^{34}S_{evap}$ correlation scheme presented here.

The $\delta^{34}S_{evap}$ data for Carnduff-02 (Larne Basin) and Burton Row (Wessex Basin) are offset from the global composite, attributed to a possible overwhelming terrestrial sulphate flux, and thus a terrestrial depositional model (see below). The age models for these cores are thus based upon available biostratigraphy (e.g., Warrington, 1995; Baranyi et al., 2019) and, in the case of Burton Row, magnetostratigraphy (e.g., Hounslow and Gallois, 2023). Despite the difficulties in establishing $\delta^{34}S_{evap}$-based correlations for Carnduff-02 and Burton Row, broader application of evaporite-based sulphur isotope stratigraphy to UK Triassic has been successful in the EISB and southern North Sea, as well as in the Larne Basin for the SSG and lowermost MMG. Accordingly, the results of $\delta^{34}S_{evap}$-based stratigraphy presented in this thesis justify the further application of this methodology throughout the UK Permian-Triassic and further afield.

3. Marine influence during deposition of Mercia Mudstone evaporites

The difficulty in confidently distinguishing between marine and nonmarine evaporites in the geologic record has long been recognised and results from possible ambiguities in the sedimentology and mineralogy of marine and nonmarine evaporite deposits (e.g., Hardie et al., 1984; Lowenstein et al., 1989; Warren, 2010; Leitner et al., 2023). Accordingly, much debate persists regarding the degree of marine influence during deposition of evaporites within the UK Triassic Mercia Mudstone, with apparent contradictions in sedimentological (Andeskie et al., 2018; Milroy et al., 2019), palaeontological (Warrington, 1995; Baranyi et al., 2019) and geochemical data (Taylor, 1983; Salisbury et al., 2022; 2023). Recent studies interpret mineralogical and sedimentological data from the MMG as evidence for deposition within terrestrial playa lake systems (Andeskie et al., 2018; Milroy et al., 2019). However, Andeskie et al. (2018)

and Milroy et al. (2019) did not employ geochemical methods, relying solely on petrographic and sedimentological observations.

$\delta^{34}S_{evap}$ data are sensitive to the relative magnitudes of marine 'vs' terrestrial inputs during deposition (e.g., Playà et al., 2000; Legler and Schneider, 2008). Interestingly, $\delta^{34}S_{evap}$ records for the MMG of 110/13-8 (East Irish Sea Basin - EISB), Staithes S-20 (Cleveland Basin) and 42/28-2 (southern North Sea, UK) compare well with the global composite $\delta^{34}S_{evap}$ age curve for the Triassic (see Chapter 4). This likely suggests that during evaporite deposition, sulphate was received from a common seawater source, which would maintain spatial isotopic homogeneity, thus explaining the correlation between these sample sites and the global composite Triassic $\delta^{34}S_{evap}$ curve.

In contrast, the $\delta^{34}S_{evap}$ records for Carnduff-02 (Larne Basin) and Burton Row (Wessex Basin) exhibit an apparent offset between each other and the global composite, precluding the establishment of $\delta^{34}S_{evap}$-based correlations (see Chapter 4). The most likely explanation for this isotopic offset, is an overwhelming influx of isotopically distinct terrestrial sulphate during evaporite deposition. Considering the large size of the seawater sulphate reservoir (Fike et al., 2015), the observed isotopic offset would suggest a high degree of hydrologic isolation from seawater. In addition, the $\delta^{34}S_{evap}$ data for Carnduff-02 and Burton Row are generally depleted relative to the global composite, which is what would be expected if the $\delta^{34}S_{evap}$ data were recording a dominantly terrestrial signal, as the $\delta^{34}S$ of terrestrial sulphate is often depleted relative to seawater (e.g., Burke et al., 2018).

Thus, the $\delta^{34}S_{evap}$ records presented here suggest a spatial (and possibly temporal) variability in the degree of marine influence during evaporite deposition within the UK Triassic. The particularly close comparison between the records of Staithes S-20 and 42/28-2 and the global composite may reflect the palaeogeographic position of these sample sites, maintaining closer proximity to the Southern Permian Basin, which experienced direct marine inundations (McKie, 2017). During the Anisian and the deposition of the Preesall Halite, the most likely source of marine waters for the EISB was via the Southern Permian Basin, which was itself experiencing inundation by Tethyan seawater (McKie, 2017). In the Carnian, rifting opened ingress routes through the Bay of Biscay (Chapman, 1989), potentially providing a source of seawater sulphate during the deposition of the Carnian Warton Halite Formation.

While the $\delta^{34}S_{evap}$ data from Carnduff-02 and Burton Row appear to agree with the terrestrial depositional model suggested by Andeskie et al. (2018) and Milroy et al. (2019), it should be noted that many of the sedimentological features reported in the MMG of the Larne and Wessex basins, were also reported in Staithes S-20 (see Chapter 4). Thus, the $\delta^{34}S_{evap}$ data presented in this thesis appear to provide a means to determine the degree of marine influence during evaporite deposition more confidently, despite ambiguities in the sedimentology, reconciling apparent contradictions between sedimentological, palaeontological, and geochemical datasets.

4. Biogeochemistry of the Eden Shales, Vale of Eden

In Chapter 5, a suite of stable isotopic and organic geochemical data is presented from drillcore KT1153 for the late Permian Eden Shales Formation, Vale of Eden, Cumbria. While these data remain incomplete, and the interpretations speculative, we establish

two stages defined by distinct biogeochemistry. Stage 1 spans the stratigraphic range of A Bed and Stage 2 spans evaporite beds B and C.

Previous lithostratigraphic analyses have suggested that A Bed represents deposition within a terrestrial playa lake system (Holliday, 1993; Hughes, 2003; Worley, 2005). The $\delta^{34}S_{evap}$ data exhibit a negative excursion to values < 0 ‰, which possibly reflect sulphide oxidation during sulphate remobilisation, with secondary sulphates incorporating a source of isotopically light sulphur. Interestingly, $\delta^{34}S_{CRS}$ data exhibit a depletion to values < -30 ‰, suggesting abundant sulphate availability during microbial sulphate reduction. An increase in $\delta^{15}N_{tot}$ to ~+10 ‰ is considered a response to partial denitrification and an increase in C/N ratios to values > 30 may reflect the input of terrestrial plant matter into the local evaporite system. This would fit well within the model of a terrestrial playa lake environment, with fluvial systems potentially transporting terrestrial plant biomass from the stratigraphically equivalent Hilton Plant Beds, providing an input flux of organic matter with high C/N ratios. Despite this, it should be emphasised that these data are insufficient to confirm terrestrial deposition and the biogeochemical model for Stage 1 remains speculative.

In Stage 2 (evaporite beds B and C), the $\delta^{34}S_{evap}$ data compare well with the range established for late Permian seawater, and thus potentially suggest marine influence during deposition. This is in line with previous work that suggest while A Bed may represent a terrestrial playa, beds B and C may in fact be marine in origin (Burgess and Holliday, 1979; Holliday, 1993; Hughes, 2003). It should be noted that until now, this interpretation was based primarily on lithostratigraphic analysis, and thus the data presented here constitutes the first geochemical evidence for a possible marine origin

of beds B and C. Although the data resolution in $\delta^{15}N_{tot}$ is lower than for the underlying A Bed, during Stage 2, we report a declining trend to ~+4 ‰. This is interpreted to represent an increase in nitrogen fixation rates, possibly driven by cyanobacteria. Broadly concomitant with the $\delta^{15}N_{tot}$ decrease is a detection of the saturate carotenoid β-carotane, a lipid biomarker associated with cyanobacterial productivity, and thus its presence provides further evidence that the $\delta^{15}N_{tot}$ signal is related to nitrification by cyanobacteria.

During Stage 2, the $\delta^{13}C_{org}$ data exhibit substantial variability, reaching a maximum value of +1.64 ‰, coincident with the lowest Pr/Ph value of 0.48. While extreme ^{13}C-enrichments in bulk organic matter have been reported from modern evaporative settings (e.g., Schidlowski et al., 1984; Birgel et al., 2015; Dorador et al., 2018), comparable $\delta^{13}C_{org}$ signals have scarcely been reported from ancient evaporites. Birgel et al. (2015) suggest ^{13}C-enrichments in Holocene stromatolites were generated through methanogenesis, subsequent methane escape and the assimilation of ^{13}C-enriched CO_2 by phototrophs. While this is considered as a possible pathway of ^{13}C-enrichment, in this case, direct evidence for methanogenic activity and high methane concentrations within the evaporite brine is currently lacking. Thus, here it is suggested that a combination of hypersalinity, as possibly indicated by the low Pr/Ph ratio, and high rates of productivity amongst phototrophs, as indicated by the abundance of β-carotane, together incited a ^{13}C-enrichment in bulk organic matter, as has been suggested by previous work in modern evaporative settings (Schidlowski, et al., 1994).

Concomitant with the variability in $\delta^{13}C_{org}$ values, the $\delta^{34}S_{CRS}$ data exhibit extreme variability, between extremes of -40 ‰ and 0 ‰. Within Stage 2, the aromatic

carotenoids isorenieratane, β-isorenieratane and okenane are detected, and are lipid biomarkers associated with brown-green sulphur bacteria and purple sulphur bacteria, respectively. Such bacteria oxidise sulphide during anoxygenic photosynthesis, and thus the detection of these aromatic carotenoids indicates the presence of photic zone euxinia (PZE). Thus, although the biomarker data is currently of low stratigraphic resolution, the variability in $\delta^{34}S_{CRS}$ may be related to expansions and contractions in PZE.

The stability in $\delta^{34}S_{evap}$ and variability in $\delta^{34}S_{CRS}$ may initially appear contradictory. To reconcile this, it is suggested here that the stability in $\delta^{34}S_{evap}$ is related to a locally abundant sulphate pool, maintained by seawater inputs, and enhanced through evaporative concentration. If the brown and purple sulphur bacteria occupied microbial mat structures, or the upper layers of sediment, then their presence may reflect the expansion of PZE within the mat structures, not the overlying brines. Thus, the fluctuations observed in $\delta^{34}S_{CRS}$ may reflect variability in the availability of sulphate during microbial sulphate reduction within mat structures, while the sulphate in the overlying brine maintained $\delta^{34}S$ stability. In addition, it should be noted that all the ^{13}C-enrichments in bulk organic matter have also been reported from modern microbial mat structures. That being said, the main issue for this hypothesis is the lack of direct evidence for microbial mats within KT1153. However, microbial mat structures have been reported within the Eden Shales (Arthurton, 1971; Hughes, 2003; Worley, 2024; *pers. comm.*), and thus the data presented here may be indicative of microbial-mediated sulphur and carbon cycling within mat structures, in the absence of direct sedimentological evidence.

5. Future research

The results of the work presented here present many avenues for future research. Firstly, the box modelling employed in Chapter 1 is relatively simple and could be expanded upon to provide further insight into the dynamics of sulphur cycling across the Permian-Triassic. For example, it is suggested that changes in the pyrite burial flux as predicted by the model outputs is primarily related to fluctuations in ocean redox with time. This is a reasonable assumption, particularly considering the established model the ^{34}S-enrichment of seawater sulphate across the PTB and Early Triassic (see Newton et al., 2004; Bernasconi et al., 2017). While the current modelling approach allowed for testing the role of changes in $\Delta^{34}S$ during microbial sulphate reduction and pyrite formation in possibly generating the observed variability in $\delta^{34}S_{evap}$, the simplicity of the model limited the range of sensitivity tests that could be completed. A major limitation of the model is the fact that it does not directly consider the availability of reactive iron when calculating the pyrite burial flux. While ocean redox is a constraint on pyrite formation, so is the availability of reactive iron (Canfield and Farquhar, 2009). This is particularly significant here, as previous work suggests a possible reduction in the influx of reactive iron to the ocean reservoir across the PTB, related to an increase in continental weathering rates (see Schobben et al., 2015). Thus, future work could endeavour to expand the modelling approach employed here, by incorporating the cycling of iron into the model framework. Of course, this would be best accompanied with iron isotope data from Staithes S-20 and further afield, to help further constrain the modelling approach with geochemical data.

The apparent cyclicity exhibited by $\delta^{34}S_{evap}$ through the uppermost Zechstein and lower Bunter Shale in Staithes S-20 deserves further investigation. It is currently unclear whether this cyclicity represents a global seawater signal or isotope effect associated with local depositional factors. In particular, future studies should generate $\delta^{34}S_{evap}$ records across the late Permian Zechstein and Zechstein-equivalent sequences to test the reproducibility of this $\delta^{34}S_{evap}$ signal. If the cyclicity can be reproduced from distinct sedimentary basins, then this would suggest it likely represents a primary seawater signal and could thus be utilised for high-resolution correlation of Zechstein and Zechstein-equivalent sequences, particularly if used in combination with biostratigraphy (see Gibson and Wellman, 2021).

The potential that nodular evaporites within the SSG are recording a seawater signal is of course intriguing. However, considering the terrestrial depositional model of the SSG, concerns remain regarding the precise contribution of marine and terrestrial sulphate sources during evaporite formation and the possibility of producing a mixed isotopic signal. Future studies should attempt to generate additional $\delta^{34}S_{evap}$ data from the SSG and equivalent strata in continental Europe, to test the reproducibility of the apparent marine signals observed in this work. If they can be widely reproduced across distinct basins, then this would provide further evidence that the sulphate within the evaporites was derived from a common seawater source, as terrestrial sulphate commonly exhibits a high degree of spatial $\delta^{34}S$ variability (see Burke et al., 2018). In addition, future work should endeavour to generate $\delta^{18}O_{evap}$ data, from the nodular evaporites of the SSG. Oxygen isotopes of evaporitic sulphate are also sensitive to marine 'vs' terrestrial influx (e.g., Playá et al., 2000) and thus could help to further constrain the degree of marine influence.

The $\delta^{34}S_{evap}$ record from 110/13-8 of the EISB is successful in establishing a correlation scheme between the Triassic stratigraphy of the EISB and the global composite $\delta^{34}S_{evap}$ curve. However, the record exhibits a degree of scatter which limits the confidence of any correlations established here. In fact, the $\delta^{34}S_{evap}$ record of 110/13-8 exhibits far more scatter than the record of 42/28-2 from equivalent strata in the UK southern North Sea. Of course this may simply be a product of distinct sampling resolutions, with the lower resolution of 42/28-2 potentially smoothing the $\delta^{34}S_{evap}$ curve. However, the effects of caving during the drilling process, the diagenetic alteration of $\delta^{34}S_{evap}$ signals and terrestrial sulphate inputs cannot be conclusively discounted in this case. Future work should endeavour to generate $\delta^{18}O_{evap}$ data to better constrain the extent of possible diagenetic alteration (see Boschetti et al., 2011) and marine/terrestrial influence. Furthermore, $\delta^{34}S_{evap}$ records should be generated from additional cores within the EISB. In doing so, this will help to determine the reproducibility of the trends observed in the $\delta^{34}S_{evap}$ record of 110/13-8, while potentially providing a means of mapping the spatial variability of marine influence across the EISB. If a consistent marine $\delta^{34}S$ signal can be reported form cores across the basin, then if more widely applied, $\delta^{34}S_{evap}$ stratigraphy has the potential to provide better age-calibration of the Triassic stratigraphy of the EISB, which is particularly impoverished in biostratigraphic constraint.

The possible routes of marine ingress during Carnian evaporite deposition remain poorly constrained and have led some to suggest a terrestrial depositional model of formation (e.g., Hounslow et al., 2012). Rifting is thought to have generated a possible ingress route for Tethyan seawater from the Bay of Biscay, through the Western Approaches and into the EISB (McKie, 2017). Future studies should sample the

evaporites of the Bay of Biscay and Western Approaches for $\delta^{34}S_{evap}$ stratigraphy. If evaporites in these locations preserve a marine $\delta^{34}S$ signal, this would imply that the sulphate within these evaporite systems was derived from seawater, thus providing direct geochemical evidence that the rift system through the Bay of Biscay was in fact an ingress route for seawater into the UK Triassic.

The $\delta^{34}S_{evap}$ records of Carnduff-02 and Burton Row have been interpreted to reflect nonmarine evaporite deposition within basins hydrographically isolated from the seawater reservoir. Future work should endeavour to generate complementary $\delta^{18}O_{evap}$ data, to better constrain the potential role of diagenetic overprinting. In addition, while the halites of Carnduff-02 have been subjected to detailed petrographic study (Andeskie et al., 2018), the halites of Burton Row have yet to receive comparable attention. Thus, the scatter observed in the $\delta^{34}S_{evap}$ could, in theory, represent contributions from sulphate sourced from secondary fluid inclusions, rather than a possible mixed terrestrial-marine signal as suggested in Chapter 4. Thus, future efforts should involve a more detailed petrographic analysis of the halites in Burton Row, to better characterise the constituent fluid inclusions.

With regards to the application of $\delta^{34}S_{evap}$ records to evaporite stratigraphy, one further suggestion is that this methodology be more widely applied to Triassic basins, not just in the UK, but further afield. There is an abundance of evaporitic material of Permian-Triassic age in continental Europe (Feist-Burkhardt, et al., 2008), which has not yet been subjected to sulphur isotope analysis. Preliminary data suggests a possible correlation scheme could be established between the Carnian Grabfeld Formation of Germany and the global composite curve, and thus by extension, the UK Triassic (see

Appendix 3). This is extremely promising and suggests $\delta^{34}S_{evap}$ stratigraphy should be applied more widely to the German Triassic.

In addition, Ortí et al. (2022) derived a $\delta^{34}S_{evap}$-based correlation scheme between evaporites of eastern Iberia and the composite record of Bernasconi et al. (2017). Although promising, the $\delta^{34}S_{evap}$ record from Triassic evaporites of Spain is currently of relatively low resolution and deserved further attention. In theory, $\delta^{34}S_{evap}$ stratigraphy could enable the establishment of correlation schemes between the Triassic basins of the UK, and continental Europe, at a higher resolution than has been achieved previously. In addition, effort should be made to combine this approach with independent means of correlation, such as $\delta^{13}C_{org}$ stratigraphy (e.g., Hesselbo et al., 2002; Caruthers et al., 2018; Baranyi et al., 2019), biostratigraphy (e.g., Baranyi et al., 2019) and magnetostratigraphy (e.g., Zhang et al., 2022; Hounslow and Gallois, 2023). This will enable the establishment of correlations with greater confidence, while also providing a means of stratigraphic correlation under circumstances where $\delta^{34}S_{evap}$ data fail to exhibit a seawater signal, as is the case for Carnduff-02 and Burton Row.

It would also be beneficial to target evaporite-bearing strata that span the Triassic-Jurassic boundary for sulphur isotope stratigraphy. Abundant evidence exists for biogeochemical perturbations across this major time boundary (e.g., Ruhl et al., 2011; Larina et al., 2013; Bond et al., 2023), including variability in $\delta^{34}S_{pyrite}$ (e.g., Williford et al., 2009; Luo et al., 2018). Despite this, the $\delta^{34}S$ of seawater sulphate across this time interval remains poorly constrained. Currently, the available $\delta^{34}S_{SO4}$ records are limited to low resolution $\delta^{34}S_{evap}$ records (e.g., Strauss, 1997; Crockford et al., 2019; Ortí et al., 2022) and a small number of $\delta^{34}S$ profiles from carbonate-associated sulphate ($\delta^{34}S_{CAS}$)

(He et al., 2020; Tang et al., 2023). Both the $\delta^{34}S_{CAS}$ records exhibit major positive excursions, however, the magnitude of the isotopic shifts and the broader stratigraphic trends in the $\delta^{34}S_{CAS}$ data are distinct (He et al., 2020; Tang et al., 2023), potentially reflecting the susceptibility of $\delta^{34}S_{CAS}$ data to local diagenetic and depositional factors (e.g., Rennie and Turchyn, 2014; Present et al., 2019; Rose et al., 2019).

While evaporite deposition in the UK and northwester Europe largely ceased by the Rhaetian of the Late Triassic (Warrington and Ivimey-Cook, 1992; Wignall and Bond, 2008; McKie, 2017), it continued in Spain, North Africa and the Atlantic Margin, with evaporites spanning the TJB in these locations (e.g., Holser et al., 1988; Afenzar and Essamoud, 2020; Orti et al., 2022). Preliminary $\delta^{34}S_{evap}$ data from the Lecera Formation of Spain (see Appendix 4) show relative stability and do not exhibit the variability reported for $\delta^{34}S_{CAS}$. The cause of this distinction is currently unclear and warrants further investigation. Thus, there exists an opportunity to sample evaporites of the TJB to generate further $\delta^{34}S_{evap}$ records at a higher resolution than previously achieved. In addition to sulphur isotope stratigraphy, organic carbon isotope stratigraphy should be applied as well, in case the stability of the $\delta^{34}S_{evap}$ record from the Lecera Formation is characteristic of the TJB evaporite record broadly, thus enabling the establishment of the stratigraphic position of the TJB via means independent of the sulphur isotope data. In doing so, this will facilitate comparative study between the $\delta^{34}S_{evap}$ and $\delta^{34}S_{CAS}$ records, enabling further refinement of the sulphur cycle across the TJB.

At the time of writing, the suite of geochemical data discussed in Chapter 5 presents the most detailed geochemical analysis of the late Permian Eden Shales. Despite this, the dataset remains insufficient and as a result, many of our interpretations

remain speculative, particularly regarding the biogeochemical model suggested for A Bed. A negative $\delta^{34}S_{evap}$ excursion has been interpreted here to reflect sulphide oxidation during late-stage diagenetic sulphate remobilisation, however this cannot be confirmed with the data currently available. Future work should endeavour to generate $\delta^{18}O_{evap}$ data to better constrain the source of sulphate. The $\delta^{15}N_{tot}$ increase in A Bed is viewed here as a product of partial denitrification. However, another mechanism of ^{15}N-enrichment involving ammonia volatility under conditions of hypersalinity is also considered. While this work favours the prior mechanism, the current suite of data does not provide a means of confidently determining salinity levels. Pr/Ph ratios should be plotted against MTTC ratios, which together will provide a more robust means of estimating paleosalinity (see Luo et al., 2019). Furthermore, compound-specific nitrogen isotope analysis could also be employed to better assess the source of the observed $\delta^{15}N_{tot}$ enrichment (see Isaji et al., 2019).

Future efforts could also test for the presence of biomarkers indicative of terrestrial biomass. If lipid biomarker data were to show an increase in relative abundance of terrigenous biomass during the increased C/N values observed, then this would lend further credence to the hypothesis that the increase in C/N values was a response to an increase in organic matter of land plant origin.

While the biogeochemical model proposed for Stage 2 (beds B and C) is less speculative than Stage 1, additional geochemical data is required to constrain interpretations presented in this work. It is suggested that the variability in $\delta^{34}S_{CRS}$ is a product of changes in the degree of sulphate availability during microbial sulphate reduction, related to expansions and retractions in photic zone euxinia. The presence of

the aromatic carotenoids isorenieratane, β-isorenieratane and okenane, further suggest the presence of photic zone euxinia, broadly concomitant with the variability in $\delta^{34}S_{CRS}$. However, the lipid biomarker data is currently of low resolution and thus we cannot definitively link every fluctuation in $\delta^{34}S_{CRS}$ to an expansion or retraction in euxinia. The low stratigraphic resolution of these data could be overcome through the application of iron isotopes, which are also sensitive to euxinia (see Lyons et al., 2009). It would likely be possible to generate iron isotope data at a much higher stratigraphic resolution when compared to the lipid biomarker data and would thus provide better constraint on the variability in photic zone euxinia during Stage 2.

The extreme ^{13}C-enrichments in bulk organic matter reported in this work have been tentatively attributed to CO_2 volatility under conditions of hypersalinity and enhanced primary productivity, as has been suggested by previous studies (e.g., Schidlowski et al., 1994). However, this remains somewhat speculative. The possibility of hypersalinity is based primarily on a low Pr/Ph ratio of 0.48, which of course is not a particularly robust proxy for palaeosalinity. Thus, as suggested for Stage 1, the application of MTTC ratios could provide a more robust measure of salinity levels during evaporite deposition. In addition, the model of ^{13}C-enrichment proposed by Birgel et al. (2015) could be investigated further in this case, through attempts to detect lipid biomarkers indicative of methanogenic and/or methanotrophic activity within the depth interval of $\delta^{13}C_{org}$ enrichments. Furthermore, it would be worthwhile attempting compound-specific carbon isotope analysis, to better understand the dynamics of local microbially-mediated carbon cycling (see Birgel et al., 2015). If implemented, these suggestions for future work would enable additional refinement of the proposed model for extreme enrichments in $\delta^{13}C_{org}$.

6. References

Afenzar, A., Essamoud, R., 2020. Sedimentological and sequence stratigraphy analyses of the syn-rift Triassic series of the Mohammedia-Benslimane-ElGara-Berrechid basin (Moroccan Meseta). *C. R. Géoscience*, 352, 417-441. DOI: 10.5802/crgeos.36

Andeskie, A.S., Benison, K.C., Eichenlaub, L.A., Raine, R., 2018. Acid-saline-lake systems of the Triassic Mercia Mudstone Group, County Antrim, Northern Ireland. *J. Sediment. Res.* 88, 385-398. DOI: 10.2110/jsr.2018.14

Arthurton, R.S., 1971. The Permian evaporites of the Langwathby Borehole, Cumberland. *Inst. Geol. Sci.* Rep. No. 71/7, 18 pp.

Baranyi, V., Miller, C.S., Ruffell, A., Hounslow, M.W., Kürschner, W.M., 2019. A continental record of the Carnian Pluvial Episode (CPE) from the Mercia Mudstone Group (UK): palynology and climatic implications. *J. Geol. Soc.* 176, 149-166. DOI: 10.1144/jgs2017-150

Bernasconi, S.M., Meier, I., Wohlwend, S., Brack, P., Hochuli, P.A., Bläsi, H., Wortmann, U.G., Ramseyer, K., 2017. An evaporite-based high-resolution sulfur isotope record of Late Permian and Triassic seawater sulfate. *Geochim. Cosmochim. Acta*, 204, 331-349. DOI: 10.1016/j.gca.2017.01.047

Birgel, D., Meister, P., Lundberg, R., Horath, T.D., Bontognali, T.R.R., Bahniuk, A.M., De Rezende, C.E., Vasconcelos, C., McKenzie, J.A., 2015. Methanogenesis produces strong ^{13}C enrichment in stromatolites of Lagoa Salgada, Brazil: a modern analogue for Palaeo-/Neoproterozoic stromatolites? *Geobiology*, 13, 245-266. DOI: 10.1111/gbi.12130

Bond, A.D., Dickson, A.J., Ruhl, M., Bos, R., van de Schootbrugge, B., 2023. Globally limited but severe shallow-shelf euxinia during the end-Triassic extinction. *Nat. Geosci.* 16, 1181-1187. DOI: 10.1038/s41561-023-01303-2

Boschetti, T., Cortecci, G., Toscani, L., Iacumin, P., 2011. Sulfur and oxygen isotope compositions of Upper Triassic sulfates from northern Apennines, Italy: paleogeographic and hydrogeochemical implications. *Geol. Acta*, 9, 129-147

Burgess, I.C., Holliday, D.W., 1979. Geology of the country around Brough-under-Stainmore. *Mem. Geol. Surv. G.B.* Sheet 31, including parts of sheets 25 and 30 (England and Wales). 131 pp.

Burke, A., Present, T.M., Paris, G., Rae, E.C.M., Sandilands, B.H., Gaillardet, J., Peucker-Ehrenbrink, B., Fischer, W.W., McClelland, J.W., Spencer, R.G.M., Voss, B.M., Adkins, J.F., 2018. Sulfur isotopes in rivers: Insights into global weathering budgets, pyrite oxidation, and the modern sulfur cycle. *Earth Planet. Sci. Lett.* 496, 168-177. DOI: 10.1016/j.epsl.2018.05.022

Canfield, D.E., Farquhar, J., 2009. Animal evolution, bioturbation, and the sulfate concentration of the oceans. *Proc. Natl. Acad. Sci.* 106, 8123-8127. DOI: 10.1073/pnas.0902037106

Caruthers, A.H., Gröcke, D.R., Kaczmarek, S.E., Rine, M.J., Kuglitsch, Kuglitsch, J., Harrison III, W.B., 2018. Utility of organic carbon isotope data from the Salina Group halite (Michigan Basin): A new tool for stratigraphic correlation and paleoclimate proxy source. *Geol. Soc. Am. Bull.* 130, 1782-1790. DOI: 10.1130/B31972.1

Chapman, T.J., 1989. “The Permian to Cretaceous structural evolution of Western Approaches Basin (Melville sub-basin), UK”, in *Inversion tectonics*. Editors: Cooper, M.A., Williams, G.D. Geological Society of London, Special Publications, 44, 177-200. DOI: 10.1144/GSL.SP.1989.044.01.11

Claypool, G.E., Holser, W.T., Kaplan, I.R., Sakai, H., Zak, I., 1980. The age curves of sulfur and oxygen isotopes in marine sulfate and their mutual interpretation. *Chem. Geol.* 28, 199-260. DOI: 10.1016/0009-2541(80)90047-9

Cortecci, G., Reyes, E., Berti, G., Casati, P., 1981. Sulfur and oxygen isotopes in Italian marine sulfates of Permian and Triassic ages. *Chem. Geol.* 34, 65–79. DOI: 10.1016/0009-2541(81)90072-3

Crockford, P.W., Kunzmann, M., Bekker, A., Hayles, J., Bao, H., Halverson, G.P., Peng, Y., Bui, T.H., Cox, G.M., Gibson, T.M., Wörndle, S., Rainbird, R., Lepland, A., Swanson-Hysell, N.L., Master, S., Sreenivas, B, Kuznetsov, A., Krupernik, V., Wing, B.A., 2019. Claypool continued: Extending the isotopic record of sedimentary sulfate. *Chem. Geol.* 513, 200-225. DOI: 10.1016/j.chemgeo.2019.02.030

Dorador, C., Fink, P., Hengst, M., Icaza, G., Villalobos, A.S., Vejar, D., Meneses, D., Zadjelovic, V., Burmann, L., Moelzner, J., Harrod, C., 2018. Microbial community composition and trophic role along a marked salinity gradient in Laguna Puilar, Sala de Atacama, Chile. *Anton. Van Leeuw.* 111, 1361-1374. DOI: 10.1007/s10482-018-1091-z

Ernst, R.E., Buchan, K.L., 2001. “Large mafic magmatic events through time and links to mantle plume heads”, in *Mantle plumes: Their identification through time: Geological Society of America Special Paper 352*. Editors: Ernst, R.E., Buchan, K.L., 352, 483-575.

Feist-Burkhardt, S., Götz, A.E., Szulc, J., Borkhataria, R., Geluk, M., Haas, J., Hornung, J., Jordan, P., Kempf, O., Michalík, J., Nawrocki, J., Reinhardt, L., Ricken, W., Röhling, H-G., Rüffer, T., Török, A., Zühlke, R., 2008. "Triassic", in *The geology of Central Europe Volume 2: Mesozoic and Cenozoic*. Editor McCann, T. Geological Society of London, 749-821. DOI: 10.1144/CEV2P.1

Fike, D.A., Bradley, A.S., Rose, C.V., 2015. Rethinking the ancient sulfur cycle. *Annu. Rev. Earth Planet. Sci.* 43, 593-622. DOI: 10.1146/annurev-earth-060313-054802

Gibson, M.E., Wellman, C.H., 2021. The use of spore-pollen assemblages to reconstruct vegetation changes in the Permian (Lopingian) Zechstein deposits of northeast England. *Rev. Palaeobot. Palynol.* 288, 104399. DOI: 10.1016/j.revpalbo.2021.104399

Hardie, L.A., 1984. Evaporites: Marine or non-marine? *Am. J. Sci.* 284, 193-240. DOI: 10.2475/ajs.284.3.193

He, T., Dal Corso, J., Newton, R.J., Wignall, P.B., Mills, B.J.W., Todaro, S., Stefano, P.D., Turner, E.C., Jamieson, R.A., Randazzo, V., Rigo, M., Jones, R.E., Dunhill, A.M., 2020. An enormous sulfur isotope excursion indicates marine anoxia during the end-Triassic mass extinction. *Sci. Adv.* 6, eabb6704. DOI: 10.1126/sciadv.abb6704

Hesselbo, S.P., Robinson, S.A., Surlyk, F., Piasecki, S., 2002. Terrestrial and marine extinction at the Triassic-Jurassic boundary synchronized with major carbon-cycle perturbation: A link to initiation of massive volcanism? *Geology*, 30, 251-254. DOI: 10.1130/00917613(2002)030<0251:TAMEAT>2.0.CO;2

Holliday, D.W., 1993. Geophysical log signatures in the Eden Shales (Permo-Triassic) of Cumbria and their regional significance. *Proc. Yorks. Geol. Soc.* 49, 345-354. DOI: 10.1144/pygs.49.4.345

Holser, W.T., Clement, G.P., Jansa, L.F., Wade, J.A., 1988. "Chapter 22 - Evaporite deposits of the North Atlantic Rift", in *Triassic-Jurassic rifting and opening of the Atlantic: Continental breakup and the origin of the Atlantic Ocean and passive margin, Part A*. Editor: Manspeizer, W., (Elsevier: Amsterdam) 525-557. DOI: 10.1016/B978-0-444-42903-2.50027-0

Hounslow, M.W., Gallois, R., 2023. Magnetostratigraphy of the Mercia Mudstone Group (Devon, UK): implications for regional relationships and chronostratigraphy in the Middle to Late Triassic of Western Europe. *J. Geol. Soc.* 180, jgs2022-173. DOI: 10.1144/jgs2022-173

Hounslow, M.W., McKie, T., Ruffell, A.H., 2012. "Permian to Late Triassic post-orogenic collapse and rifting, arid deserts, evaporating seas and mass extinctions" in *The geological history of Britain and Ireland*. Editors Woodcock, N.H., Strachan, R.A., (Chichester: Wiley) 2, 301-321.

Hughes, R.A., 2003. Permian and Triassic rocks of the Appleby district (part of Sheet 30, England and Wales). British Geological Survey Research Report, RR/02/01. 21 pp.

Isaji, Y., Kawahata, H., Ogawa, N.O., Kuroda, J., Yoshimura, T., Jiménez-Espejo, F.J., Makabe, A., Shibuya, T., Lugli, S., Santulli, A., Manzi, V., Roveri, M., Ohkouchi, N., 2019. Efficient recycling of nutrients in modern and past hypersaline environments. *Sci. Rep.* 9, 3718. DOI: 10.1038/s41598-019-40174-9

Jackson, D.I., Johnson, H., 1996. Lithostratigraphic nomenclature of the Triassic, Permian and Carboniferous of the UK offshore East Irish Sea Basin. British Geological Survey, Nottingham

Kurtz, A.C., Kump, L.R., Arthur, M.A., Zachos, J.C., Paytan, A., 2003. Early Cenozoic decoupling of the global carbon and sulfur cycles. *Paleoceanography*, 18, 1090. DOI: 10.1029/2003PA000908

Larina, E., Bottjer, D.J., Corsetti, F.A., Thibodeau, A.M., Berelson, W.M., West, A.J., yager, J.A., 2021. Ecosystem change and carbon cycle perturbation preceded the end-Triassic mass extinction. *Earth Planet. Sci. Lett.* 576, 117180. DOI: 10.1016/j.epsl.2021.117180

Legler, B., Schneider, J.W., 2008. Marine ingressions into the Middle/Late Permian saline lake of the Southern Permian Basin (Rotliegend, Northern Germany) possibly linked to sea-level highstands in the Arctic rift system. *Palaeogeogr. Palaeoclimatol. Palaeoecol.* 267, 102-114. DOI: 10.1016/j.palaeo.2008.06.009

Leitner, C., Köster, M., Finger, F., 2023. Saltern, mudflat, and dry playa: Playa basin types of a retreating epeiric sea (Keuper, Germany). *J. Sediment. Res.* 93, 840-856. DOI: 10.2110/jsr.2023.013

Lowenstein, T.K., Spencer, R.J., Pengxi, Z., 1989. Origin of ancient potash evaporites: Clues from the modern nonmarine Qiadam Basin of western China. *Science*, 245, 1090-1092. DOI: 10.1126/science.245.4922.1090

Luo, G., Richoz, S., van de Schootbrugge, B., Algeo, T.J., Xie, S., Ono, S., Summons, R.E., 2018. Multiple sulfur-isotopic evidence for a shallowly stratified ocean following the

Triassic-Jurassic boundary mass extinction. *Geochim. Cosmochim. Acta*, 231, 73-87. DOI: 10.1016/j.gca.2018.04.015

Luo, G., Yang, H., Algeo, T.J., Hallmann, C., Xie, S., 2019. Lipid biomarkers for the reconstruction of deep-time environmental conditions. *Earth Sci. Rev.* 189, 99-124. DOI: 10.1016/j.earscirev.2018.03.005

Lyons, T.M., Anbar, A.D., Severmann, S., Scott, C., Gill, B.C., 2009. Tracking euxinia in the ancient ocean: A multiproxy perspective and Proterozoic case study. *Annu. Rev. Earth Planet. Sci.* 37, 507-534. DOI: 10.1146/annurev.earth.36.031207.124233

McKie, T., 2017. "Palaeogeographic evolution of latest Permian and Triassic salt basins in northwest Europe", in *Permo-Triassic salt provinces of Europe, North Africa and the Atlantic margins, tectonics and hydrocarbon potential*. Editors Soto, J.J., Flinch, J.F., Tari, G. (Amsterdam Netherlands: Elsevier), 159-173. DOI: 10.1016/B978-0-12-809417-4.00008-2

Milroy, P., Wright, V.P., Simms, M.J., 2019. Dryland continental mudstones: Deciphering environmental changes in problematic mudstones from the Upper Triassic (Carnian to Norian) Mercia Mudstone Group, south-west Britain. *Sedimentology*, 66, 2557-2589. DOI: 10.1111/sed.12626

Newton, R.J., Pevitt E.L., Wignall, P.B., Bottrell, S.H., 2004. Large shifts in the isotopic composition of seawater sulphate across the Permo-Triassic boundary in northern Italy. *Earth Planet. Sci. Lett.* 218, 331-345. DOI: 10.1016/S0012-821X(03)00676-9

Ortí, F., Peréz-López, A., Pérez-Valera, F., Benedicto, C., 2022. Isotope composition ($\delta^{34}S$, $\delta^{18}O$) of the Middle Triassic-Early Jurassic sulfates in eastern Iberia. *Sediment. Geol.* 431, 106104. DOI: 10.1016/j.sedgeo.2022.106104

Playà, E., Ortí, F., Rosell, L., 2000. Marine to non-marine sedimentation in the upper Miocene evaporites of the Eastern Betics, SE Spain: sedimentological and geochemical evidence. *Sediment. Geol.* 133, 135-166. DOI: 10.1016/S0037-0738(00)00033-6

Present, T.M., Gutierrez, M., Paris, G., Kerans, C., Grotzinger, J.P., Adkins, J.F., 2019. Diagenetic controls on the isotopic composition of carbonate-associated sulphate in the Permian Capitan Reef Complex, West Texas. *Sedimentology*, 66, 2605–2626. DOI: 10.1111/sed.12615

Rennie, V.C.F., Turchyn, A.V., 2014. The preservation of $\delta^{34}S_{SO4}$ and $\delta^{18}O_{SO4}$ in carbonate-associated sulfate during marine diagenesis: A 25 Myr test case using marine sediments. *Earth Planet. Sci. Lett.* 395, 13-23. DOI: 10.1016/j.epsl.2014.03.025

Rose, C.V., Fischer, W.W., Finnegan, S., Fike, D.A., 2019. Records of carbon and sulfur cycling during the Silurian Irevikan Event in Gotland, Sweden. *Geochim. Cosmochim. Acta*, 246, 299-316. DOI: 10.1016/j.gca.2018.11.030

Ruhl, M., Bonis, N.R., Reichart, G-J., Sinninghe Damsté, J.S., Kürschner, W.M., 2011. Atmospheric carbon injection linked to End-Triassic Mass Extinction. *Science*, 333, 430-434. DOI: 10.1126/science.1204255

Salisbury, J., Gröcke, D.R., Cheung, H.D.R.A., Kump, L.R., McKie, T., Ruffell, A., 2022. An 80-million-year sulphur isotope record of pyrite burial over the Permian-Triassic. *Sci. Rep.* 12, 17370. DOI: 10.1038/s41598-022-21542-4

Salisbury, J., Gröcke, D.R., McKie, T., 2023. Sulphur isotope stratigraphy of drill cuttings and stratigraphic correlation of Permian-Triassic evaporites. *Front. Earth Sci.* 11, 1216365. DOI: 10.3389/feart.2023.1216365

Schidlowski, M., Gorzawski, H., Dor, I.A., 1994. Carbon isotope variations in a solar pond microbial mat: Role of environmental gradients as steering variables. *Geochim. Cosmochim. Acta*, 58, 2289-2298. DOI: 10.1016/0016-7037(94)90011-6

Schidlowski, M., Matzigkeit, U., Krumbein, W.E., 1984. Superheavy organic carbon from hypersaline microbial mats. *Naturwissenschaften*, 71, 303-308. DOI: 10.1007/BF00396613

Schobben, M., Stebbins, A., Ghaderi, A., Strauss, H., Korn, D., Korte, C., 2015. Flourishing ocean drives the end-Permian marine mass extinction. *Proc. Natl. Acad. Sci.* 112, 10298-10303. DOI: 10.1073/pnas.1503755112

Sepkoski, J.J., 1996. "Patterns of Phanerozoic extinction: A perspective from global databases", in *Global events and event stratigraphy in the Phanerozoic*. Editor: Walliser, O.H., (Berlin: Springer) 35-51. DOI: 10.1007/978-3-642-79634-0_4

Strauss, H., 1997. The isotopic composition of sedimentary sulfur through time. *Palaeogeogr. Palaeoclimatol. Palaeoecol.* 132, 97-118. DOI: 10.1016/S0031-0182(97)00067-9

Tang, W., Wang, J., Wei, H., Fu, X., Ke, P., 2023. Sulfur isotopic evidence for global marine anoxia and low seawater sulfate concentration during the Late Triassic. *J. Asian Earth Sci.* 251, 105659. DOI: 10.1016/j.jseaes.2023.105659

Taylor, S.R., 1983. A stable isotope study of the Mercia Mudstone Group (Keuper Marl) and associated sulphate horizons in the English Midlands. *Sedimentology*, 30, 11-31. DOI: 10.1111/j.1365-3091.1983.tb00647.x

Trotter, J.A., Williams, I.S., Nicora, A., Mazza, M., Rigo, M., 2015. Long-term cycles of Triassic climate change: A new $\delta^{18}O$ record from conodont apatite. *Earth Planet. Sci. Lett.* 415, 165-174. DOI: 10.1016/j.epsl.2015.01.038

Utrilla, R., Pierre, C., Ortí, F., Pueyo, J.J., 1992. Oxygen and sulfur isotope compositions as indicators of the origin of Mesozoic and Cenozoic evaporites from Spain. *Chem. Geol.* 102, 229-244. DOI: 10.1016/0009-2541(92)90158-2

Warren, J.K., 2010. Evaporites through time: Tectonic, climatic and eustatic controls in marine and nonmarine deposits. *Earth-Sci. Rev.* 98, 217-268. DOI: 10.1016/j.earscirev.2009.11.004

Warrington, G., 1995. The Permian, Triassic and Jurassic in Northern Ireland: A palynological study with special reference to the hydrocarbon prospectivity of the Larne – Lough Neagh Basin. Geological Survey of Northern Ireland. Technical Report GSNI/95/7

Warrington, G., Ivimey-Cook, H.C., Edwards, R.A., Whittaker, A., 1995. The Late Triassic-Early Jurassic succession at Selworthy, west Somerset, England. *Proc. Ussher Soc.* 8, 426-432

Wignall, P.B., Bond, D.P.G., 2008. The end-Triassic and Early Jurassic mass extinction records in the British Isles. Proc. Geol. Assoc. 119, 73-84. DOI: 10.1016/S0016-7878(08)80259-3

Williford, K.H., Foriel, J., Ward, P.D., Steig, E.J., 2009. Major perturbation in sulfur cycling at the Triassic-Jurassic boundary. *Geology*, 37, 835-838. DOI: 10.1130/G30054A.1

Worley, N.E., 2005. The occurrence of halite in the Permian A Bed Evaporite, Kirkby Thore, Cumbria. *Proc. Yorks. Geol. Soc.* 55, 199-203. DOI: 10.1144/pygs.55.3.199

Yao, W., Wortmann, U.G., Paytan, A., 2019. "Sulfur isotopes — Use for stratigraphy during times of rapid perturbations", in *Stratigraphy and timescales*. Editor Montenari, M., (Amsterdam: Elsevier Academic Press) 4, 1-33. DOI: 10.1016/bs.sats.2019.08.004

Zhang, Y., Ogg, J.G., Franz, M., Bachmann, G.H., Szurlies, M., Röhling, H-G., Li, M., Rolf, C., Obst, K., 2020. Carnian (Late Triassic) magnetostratigraphy from the Germanic Basin allowing global correlation of the Mid-Carnian Episode. *Earth Planet. Sci. Lett.* 541, 116275. DOI: 10.1016/j.epsl.2020.116275

Appendix 1

Supplementary information for:

An 80-million-year sulphur isotope record of pyrite burial over the Permian–Triassic

Jack Salisbury, Darren R. Gröcke*, H.D.R. Ashleigh Cheung, Lee R. Kump, Tom McKie, Alastair Ruffell*

** = corresponding authors: jack.salisbury@durham.ac.uk, d.r.grocke@durham.ac.uk*

Regional geologic setting

Tectonic reconfiguration during the Palaeozoic and Mesozoic heralded the formation of the Pangaean supercontinent during the Variscan orogeny in the Late Carboniferous (Peacock, 2004; Hounslow et al., 2012). Rifting episodes began soon after in the Late Carboniferous with the propagation of the Norwegian-Greenland rift (Peacock, 2004), and continued during the Permian and Triassic, facilitating the development of linked fault-bound rift basins (Howard et al., 2008; McKie and Williams, 2009; Newell, 2018). These basins were separated by intrabasinal highs and massifs, and further subdivided by basement highs into an arrangement of sub-basins distributed throughout NW Europe (McKie and Williams, 2009; McKie, 2017). The formation of rift basins provided accommodation space for sediment, and seasonal monsoons sourced sediment for basin infills (McKie, 2017). Further rift propagation enhanced fault connectivity, providing marine waters episodic access to the intracratonic basins, facilitating evaporite deposition (McKie, 2017).

During the Late Permian and Triassic, Britain was located at a palaeolatitiude of ~20°N in eastern Pangaea (Newell, 2018). Deposition occurred under a dominantly arid climate regime throughout the Late Permian (McKie and Williams, 2009) due to the extent of continental aggregation and lack of open water bodies (Parrish, 1993; McKie, 2017). Prior to the Zechstein transgression, the Permian strata of Britain are characteristic of a desert depositional environment (Smith, 1989). In the Late Permian, tectonic adjustments in West Orkney and the Viking Graben opened a pathway between two rift structures through which the Boreal Ocean gained periodic access to the subsiding Southern Permian Basin (SPB) (Smith, 1989; McKie, 2017). The Zechstein

deposits that formed as a result are characterised by seven carbonate-evaporite sequences (Z1 through to Z7) (Tucker, 1991). The Early to Middle Triassic Sherwood Sandstone Group (SSG) is largely representative of a fluvial depositional regime, predominantly composed of brown, red, green/grey, and yellow arenaceous sandstones (Ambrose et al., 2014). It can be subdivided into different lithofacies, including fluvial channel facies, dryland terminal splay complexes, and mixed fluvial-aeolian facies (McKie and Williams, 2009; McKie, 2017). Braided river systems were fed by monsoonal rainfall on the Variscan mountains (Brookfield, 2008; Ambrose et al., 2014; Geluk et al., 2018), and were interrupted by periods of relative aridity that suppressed rates of fluvial sediment supply and facilitated aeolian reworking (McKie, 2017).

There is a cluster of late Early Triassic unconformities and disconformities identified across NW Europe that have been traced from Poland to Ireland and from onshore Germany/Netherlands into the southern and central North Sea (Bachmann et al., 2010, Bourquin et al., 2011). The largest of these occurs at the base of the Solling Formation in Germany and is variously described as the Base Solling or Hardegsen unconformity. The erosional truncation of stratigraphy (and merging of unconformities) is most pronounced on basin margins, such as the location of the Staithes S-20 well where a single truncation surface is preserved. In this onshore UK region Medici et al. (2019) estimate removal of at least 150 m of Early Triassic stratigraphy. The truncation appears to be gentle and can be traced from several hundred kilometres offshore to the east via the progressive removal of the Hardegsen and Detfurth formations in offshore regions and downcutting into the Early Triassic when approaching the onshore UK region (McKie, 2017).

Through the Early and Middle Triassic, the southern Permian basin was a uniformly and gently subsiding thermal sag basin with persistent stratigraphic motifs expressed on seismic by parallel reflectivity and persistent well log motifs that preserve their character over distances of hundreds of kilometres. Although individual wells tend to have sporadic biostratigraphic recovery the persistence of the stratigraphic units mean they can be traced between calibration points with high confidence. Tracing well logs from east to west the progressive truncation of the Bunter stratigraphy below the unconformity, and onlap of the Rot above allows the position of the unconformity in the Staithes S-20 well to be identified.

The SSG is overlain by the Middle–Late Triassic Mercia Mudstone Group (MMG), with the boundary being placed at the transition from sandstones to mudstones (Howard et al., 2008; Newell et al., 2018). The MMG is composed of green/grey mudstone interbedded with siltstone, with thick halite deposits and nodular calcium-sulphates — gypsum/anhydrite (Howard et al., 2008). Deposition and preservation of organic material is minimal in the strata of the UK Permian and Early Triassic. Accordingly, the evaporite samples from the Staithes S-20 borehole contain very little organic matter, and thus have no impact on the generation of the sulphur isotope data in this study (see below). Deposition coincided with the southerly retreat of the SSG beginning in the Middle Triassic, as fluvial systems were replaced by a hypersaline playa lake and mudflat environment (Howard et al., 2008). A greater marine influence during the deposition of Middle to Late Triassic deposits in NW Europe is likely (Newell et al., 2018). Evaporite deposition ceased during the Rhaetian coinciding with a marine transgression (Peacock, 2004) and the deposition of the Penarth Group (Warrington and Ivimey-Cook, 1992; Gallois, 2009). Biostratigraphic age constraints enable the Penarth

Group to be confidently assigned to the Rhaetian (Lott and Warrington, 1988; Hounslow and Ruffell, 2006), marking the transition to marine deposition that becomes well-developed in the Hettangian (Wignall and Bond, 2008; Gallois, 2009).

Methods

Sampling

364 evaporite samples were collected at regular intervals from the Boulby Mine, Staithes S-20 borehole (Grid Ref: 476024, 517997, Yorkshire, England. This borehole was chosen due to its stratigraphic coverage (~668 meters) of evaporite-bearing strata that is lithostratigraphically constrained from the late Permian to Late Triassic.

Sulphur isotope analysis of sulphate

Sulphur isotope analysis of evaporitic sulphate was performed on gypsum, anhydrite, and halite. Due to the high concentration of sulphate in gypsum and anhydrite (20 wt % sulphur), the process for sulphate extraction simply involves the use of a dentist's drill to produce a fine powder. In contrast, sulphate is only a trace constituent in halite and must be concentrated. For each sample, ~1–5 g of crushed halite was submerged in 30 ml of a 10 % solution of sodium chloride – blanks of NaCl produced no visible $BaSO_4$. The halite was left to sit in the solution for 24–48 hours, and agitated every few hours during the working day. Upon the dissolution of halite, the solution underwent centrifugation for 5 minutes at 3000 rpm, before the supernatant was decanted into a 50 ml centrifuge tube for subsequent barium sulphate ($BaSO_4$) precipitation. Approximately ~20 ml of barium chloride ($BaCl_2$) was mixed with 30 ml of the saline solution to extract the

sulphate through the precipitation of barium sulphate, according to the following equation:

$$BaCl_2 + SO_4^{2-} \rightarrow BaSO_4 + 2Cl^{2-} \quad [S1]$$

The pH of the solution was reduced to ~1–2 with the addition of 3M HCl to prevent any carbonate precipitation. The solution was left for >24 hrs to precipitate $BaSO_4$, after which it was centrifuged at 3000 rpm for 5 minutes. The supernatant was subsequently discarded for waste disposal and the $BaSO_4$ was rinsed with ~50 ml of deionised water to neutralise the acidity. After three rinses, the $BaSO_4$ was dried in an oven at 80℃ for at least 24–48 hrs, and subsequently ground into a fine powder using an agate mortar and pestle.

For each sample, 0.3–0.5 mg was placed into tin capsules, with tungstic oxide (WO_3) added as a combustion-agent. Stable sulphur isotope analysis was performed in the Stable Isotope Biogeochemistry Laboratory (SIBL) at Durham University using a Costech Elemental Analyser (ECS 4010) coupled to a Thermo Scientific Delta V Plus isotope-ratio mass-spectrometer. Evaporite sulphur isotope ratios are expressed as standard delta (δ) notation in per mil (‰) relative to the Vienna Canyon Diablo Triolite (VCDT) according to the following equation:

$$\delta^{34}S_{evap} = \left[\frac{(({}^{34}S/{}^{32}S)_{sample} - ({}^{34}S/{}^{32}S)_{standard})}{({}^{34}S/{}^{32}S)_{standard}}\right] * 1000 \quad [S2]$$

The $\delta^{34}S$ data were normalised through calibration against four international standards (IAEA-S-1, IAEA-S-2, IAEA-S-3, NBS 127), providing a linear range in $\delta^{34}S$ between -32.49 ‰ and +22.62 ‰. Analytical uncertainty of $\delta^{34}S$ is typically ±0.2 ‰ for

replicate analyses of the international standards. Total sulphur is calculated as part of the isotopic analysis using an internal standard, sulphanilamide (S = 18.619 wt %).

Age assignment and data compilation

The $\delta^{34}S_{evap}$ data of sulphate from Late Permian and Triassic marine evaporites include 1001 measurements from 54 references. Three published data compilations (Bernasconi et al., 2017; Crockford et al., 2019; Present et al., 2020) were used, and the age model of Bernasconi et al. (2017) was employed for the latest Permian and Triassic. Absolute age estimates from radiometric dating were maintained by the original source. However, absolute age estimates were sparse for Permian and Triassic data sets, with many studies relying upon lithostratigraphic and/or biostratigraphic age assignments. With this in mind, the age estimates were either maintained from the above compilations and/or adjusted based upon the most up-to-date available stratigraphic information. When adjustments to age were necessary, the International Commission on Stratigraphy 2020/03 (Cohen et al., 2013; updated) was used. However, if the sequence in question had biostratigraphic age constraints, the stratigraphic timescale of Ogg et al. (2016) was used instead.

Some studies included in their compilations, sulphur isotope values from aqueous brines that had acquired sulphate through the dissolution of local evaporite-bearing strata; we avoided such data, as it was difficult to confidently assign accurate age estimates for when that occurred. We have also excluded data from non-marine evaporites. However, if the sulphur isotope ratios (and the coupled oxygen isotope data when available) correlated well with coeval seawater $\delta^{34}S$ from other sources, the data was included even if the sedimentological and petrographic evidence suggested a non-

marine and/or mixed marine/terrestrial origin. It should be stressed that despite this, a cautious approach was taken when including published data, so if there was any uncertainty as to the source of the sulphate, the sulphur isotope data was not included.

When compiling our dataset, we tried to include sulphur isotope data that capture as broad a geographic coverage as possible. This was of course limited by the published data available but was necessary to minimise the influence of local depositional and geochemical factors that may offset $\delta^{34}S$ from the global seawater $\delta^{34}S$ composition. Our compilation includes data from basins in northwest, central, southern, and eastern Europe, as well as Turkey, the Middle East, and North America. Admittedly, this presents a slight bias towards European basins.

The sulphur isotope analysis of 364 evaporite samples from the Staithes S-20 borehole, Yorkshire, England, provides one of the most high-resolution sulphur isotope curves for the latest Permian and Triassic. A sharp unconformity marking the boundary between the SSG and the MMG (Fig. S1) ensures that our record fails to capture much of the Early Triassic. Despite this unconformity, our $\delta^{34}S_{evap}$ record provides excellent stratigraphic coverage of the latest Permian and Triassic; sufficient for stratigraphic correlation. Biostratigraphic data are almost entirely absent, with the exception of one palynological age constraint just above the unconformity, dated to be earliest Anisian (Warrington, 2019, *pers. comm.*) (Fig. S2). Thus, correlation between the Staithes S-20 borehole and evaporite-bearing sequences globally is largely based upon the sulphur isotope data. Based upon general trends and inflection points in our record, we were able to correlate our $\delta^{34}S_{evap}$ curve from Staithes with our global composite record. Using this successful correlation, we divided the Staithes $\delta^{34}S_{evap}$ record according to the

subdivisions of the Triassic. Thus, for the data within each subdivision, we derived lower and upper age estimates based upon the ages given to the subdivision boundaries. For each $\delta^{34}S_{evap}$ value, a numerical age estimate was then estimated based upon the depth of the associated sample relative to the thickness of strata within the relevant Triassic subdivision and the duration of time represented by such strata.

The palynology only provides an age estimate for strata above the unconformity, not below it. Thus, a biostratigraphic age constraint for the length of time represented by the unconformity is absent. This provides us with two options; the unconformity represents either a major time gap, or a relatively minor time gap (Fig. S3). We therefore determined two age models for the Staithes S-20 $\delta^{34}S_{evap}$ curve accordingly. One significant difference between the two age models is the absence of an Early Triassic negative excursion if it is assumed the unconformity represents a minor time gap (Fig. S3B). If applied, this would have a major impact on our understanding of the response of the sulphur cycle to the End Permian Mass Extinction, and the results of the geochemical modelling. It is clear when viewing Figure S3A that a better correlation is attainable with the age model that assumes the unconformity represents a major time gap. According to Figure S3B, there is a large offset between the Staithes S-20 curve and the global composite for in the Early Triassic, in terms of both the timing and magnitude of the positive $\delta^{34}S_{evap}$ excursion.

It is also important to consider the sedimentology of the unconformity when assessing the suitability of either age model. The unconformity marks the boundary between the SSG and the MMG. It forms an abrupt transition from the arenaceous sandstone of the SSG and the Esk Evaporite Formation of the MMG (Fig. S1). We

consider this change in lithology sufficient to support the assessment that the unconformity represents a major time gap (see discussion above). Thus, the sedimentological data, in conjunction with the correlation of the Staithes S-20 $\delta^{34}S_{evap}$ curve, suggests the age model including a major time gap in the Early Triassic is most appropriate.

Preservation of geochemical signals

The precipitation of gypsum and halite is associated with a fractionation factor that ensures a slight enrichment in the precipitate relative to the residual brine, between the range of 1.6 ‰ and 2.0 ‰ according to experimental studies (Thode and Monster, 1965; Holser and Kaplan, 1966; Nielsen, 1978; Raab and Spiro, 1991; Van Driessche et al., 2016). Beyond the halite stability field, an apparent change in the fractionation factor ensures a depletion of up to 4 ‰ in the precipitate relative to the residual brine (Raab and Spiro, 1991). Despite this, we are confident that the fractionation associated with mineral precipitation (below the halite stability field) has not obscured the primary seawater signal of our sulphur isotope record, as the isotopic enrichment of gypsum/anhydrite and halite is sufficiently small to be considered negligible in evaporite basins. In addition, we avoided sampling potash deposits, and focused entirely on calcium-sulphates and halite. Considering this, it is highly unlikely that the fractionation driven by evaporite mineral precipitation can explain the variability exhibited by our $\delta^{34}S_{evap}$ curve.

The sulphur isotope geochemistry of evaporites is considered less susceptible to diagenetic alteration than the carbonate equivalent, carbonate associated sulphate (CAS) (Johnson et al., 2021; Bernasconi et al., 2017). Despite this, evaporites are not

entirely immune to diagenesis (Schreiber and Tabakh, 2000), with microbes being capable of inducing changes in the geochemistry and mineralogy of evaporite deposits (Davis and Kirkland, 1979). For example, biologically-driven conversion of primary marine gypsum to elemental sulphur (Feely and Kulp, 1957) and the subsequent precipitation of secondary gypsum can be associated with the fractionation of sulphur isotopes (Feely and Kulp, 1957; Schreiber and Tabakh, 2000).

Calcium sulphates in evaporite deposits undergo a cycle of diagenesis during burial and uplift. Initially, primary gypsum precipitates from a saturated salt-water brine undergoing evaporation. Upon moderate to deep burial, gypsum dehydrates to replacement or pore-filling anhydrite. Subsequent uplift to near-surface depths can facilitate the rehydration of anhydrite to form secondary gypsum (Murray, 1964; Hardie, 1967; Ortí et al., 2022). In environments conducive to the precipitation of primary of very early diagenetic anhydrite, the cycle is limited to the rehydration of anhydrite to secondary gypsum (Ortí et al., 2022). As discussed previously, the initial formation of primary gypsum is accompanied by a negligible degree of sulphur isotope fractionation (Raab and Spiro, 1991). Unfortunately, due to the difficulties involved with precipitating primary anhydrite under experimental conditions, the associated fractionation remains poorly understood (Hardie, 1967; Ortí et al., 2022). Interestingly, data from the Khuff Formation, Abu Dhabi, suggests the dehydration of primary gypsum to anhydrite and thermochemical sulphate reduction at depth is associated with negligible sulphur isotope fractionation (Worden et al., 1997). The impact of the dehydration of diagenetic anhydrite on the sulphur isotopic composition of secondary gypsum has received little attention, and thus the fractionation factor is not well established (Ortí et al., 2022). However, studies analysing gypsum and anhydrite of equivalent age suggest no

apparent offset in the isotopic composition between either mineral phase (Utrilla et al., 1992; Carrillo et al., 2014). Thus, we consider it unlikely that the Calcium sulphate diagenetic cycle obscured the primary seawater signal of the Ca-sulphates sampled as part of this study.

It should also be noted that evaporite deposition occurs in isolated basins with restricted access to the open ocean (Warren, 2010). Due to this, it is possible that the geochemistry of highly saline brines in evaporite basins does not reflect the geochemistry of seawater in the open ocean (Bernasconi et al., 2017), especially during periods of low seawater sulphate concentrations, which could ensure greater isotopic heterogeneity. Local sedimentary and geochemical processes, including riverine inputs, Rayleigh fractionation in a closed basin (Raab and Spiro, 1991), and the aforementioned microbial sulphur isotope fractionation, could theoretically yield an isotopic offset between sulphate in an evaporite basin and the sulphate reservoir of the global ocean. Despite this, we consider it unlikely that local depositional and diagenetic effects had a significant impact on the trends exhibited by our global composite curve, or our $\delta^{34}S_{evap}$ record from the Staithes S-20 borehole. The data presented in our global curve exhibit a relatively small degree of scatter, and thus, we are confident that the consistent pattern of the $\delta^{34}S_{evap}$ measurements suggests that our global curve provides a global record for the latest Permian–Triassic seawater sulphate. The small degree of scatter may reflect minor influences from local effects, or possible difficulties with age constraint/correlation, but the average trend presents a robust primary signal. The record from the Staithes S-20 borehole exhibits no major, sudden shifts in $\delta^{34}S$, which suggests: (1) no significant unconformities (i.e., time gaps) except for that discussed above and in the main paper; (2) no diagenetic alteration of the sulphur isotope

signature of these evaporites; (3) evaporite mineralogy had no effect on the $\delta^{34}S_{evap}$ curve; and (4) the evaporative basin in Yorkshire was still connected to the marine sulphate reservoir during the latest Permian and Triassic.

Model of the sulphur cycle

To explore the mechanisms responsible for the observed variability in the Triassic $\delta^{34}S$ curve, we employed the box model of Kurtz et al. (2003). This is a reverse-driven model and is controlled by our composite $\delta^{34}S_{evap}$ record. We establish boundary conditions (see Table S1), and the model yields an estimate for the pyrite burial flux with time (10^{18} moles S/m.y.).

The mass of sulphur in the ocean reservoir is controlled by the balance between the sulphur input fluxes and output burial fluxes (Gill et al., 2011). Biogeochemical perturbations that yield imbalances between the flux rates of sulphur can induce changes in the mass of marine sulphate over time. In the model, this relationship is represented by the following equation:

$$\frac{dM_0^S}{dt} = F_W^S - \left(F_{gyp} + F_{py}\right) \quad [S3]$$

The mass of marine sulphur is represented by $\mathrm{M}_0^{\mathrm{S}}$. The input fluxes of sulphur into the ocean reservoir via continental weathering and volcanic degassing are represented by a single variable, $\mathrm{F}_{\mathrm{W}}^{\mathrm{S}}$, and set to a constant value (see Table S1). Output fluxes include the burial of gypsum (F_{gyp}) and pyrite (F_{py}).

Similarly, the isotopic composition of oceanic/atmospheric sulphate is primarily controlled by the respective contributions and isotopic composition of the sulphur fluxes entering and exiting the ocean reservoir (Paytan et al., 2011; Bernasconi et al., 2017).

Therefore, variation in the stable sulphur isotopic composition of rocks and sediments is generally considered to be a product of perturbations in the biogeochemical cycling of sulphur (Richardson et al., 2019), such as changes in the rates of weathering and pyrite burial (Gill et al., 2007). This relationship is expressed in our model through the following equation, derived from multiplying the terms for the reservoir (i.e., its mass) and sulphur fluxes in Equation S3 by their isotopic compositions:

$$\frac{d}{dt}(M_0^S \delta_0^S) = F_W^S \delta_W^S - F_{gyp}\delta_0^S - F_{py}(\delta_0^S + \Delta_S) \quad [S4]$$

The sulphur isotopic composition of the marine reservoir is represented by δ_0^S. It should be noted that the minor fractionation associated with gypsum precipitation (Raab and Spiro, 1991) is ignored here, and thus δ_0^S also describes the isotope geochemistry of F_{gyp}. The burial of biomass associated organic sulphur, although significant in modern and ancient anoxic marine environments (Bauer et al., 2022), is accompanied by very little sulphur isotope fractionation (Anderson and Pratt 1995; Werne et al., 2003). Bauer et al. (2022) provide few constraints, with the authors simply invoking it as needed. As previously stated, our samples from the Staithes S-20 borehole contain very little organic material, preventing us from providing any constraints ourselves. The burial of biomass associated organic sulphur is thus considered, in the context of the model, to be isotopically indistinguishable from the burial of evaporites. In addition, the isotopic composition of sulphurised organic matter is comparable to sedimentary pyrite burial (although slightly more ^{34}S enriched) (Anderson and Pratt, 1995), and is important within anoxic water masses of modern and ancient marine environments (Raven et al., 2019; Bauer et al., 2022). However, due to the scarcity of organic material within the evaporites sampled from the Staithes S-20 borehole, no

additional constraints are available to separate the two. Therefore, we have not included the sulphurisation of organic matter in our modelling procedure, as it would have limited to no impact on the output results. Although we encourage further research into this. Δ_S is the isotopic offset between seawater sulphate and sedimentary pyrite, induced during microbial sulphate reduction (MSR). The fractionation factor associated with MSR is far more significant than the fractionation during gypsum burial, and is thus set to values appropriate for the redox-state of the ocean (see Table S1). $\delta^{\mathrm{S}}_{\mathrm{W}}$ represents the sulphur isotopic composition of the riverine input flux. Derived from the chemical weathering of material in the terrestrial reservoir, the isotopic signal is mixed between sulphur sourced from the weathering of evaporites and the oxidative weathering of sedimentary sulphides. Here we use a modern value of 4.8 ‰ (Burke et al., 2018) (Table S1), as we have no means for accurately estimating a value specific to the Triassic.

It was necessary for the model to estimate the change in the sulphur isotope geochemistry of the ocean reservoir for a given period of time without assuming steady-state conditions (Kurtz et al., 2003; Gill et al., 2011). To achieve this, Equation S3 was substituted into Equation S4 to derive Equation S5 as follows:

$$\frac{d\delta_0^S}{dt} = \frac{F_W^S(\delta_W^S - \delta_0^S) - F_{py}\Delta_S}{M_0^S} \quad [S5]$$

Where F_{gyp} has been omitted from Equation S5 for the reasons discussed above. Although Equation S5 can be solved for steady state, it does not necessarily assume such a condition. One assumption it does make, however, is homogeneity in the $\delta^{34}S$ of ocean sulphur at any one point in time (Kurtz et al., 2003).

Conditions of steady state ensure that there is no instantaneous change in the isotopic composition and mass of the sulphate reservoir in response to variations in the sulphur input flux, as the latter is balanced by complementary changes to the output fluxes of sulphur (Kurtz et al., 2003). However, due to the relatively long residence time of sulphur in the ocean (>10 Myrs) (Paytan et al., 2012), an assumption of steady-state is not appropriate when modelling the sulphur cycle over short periods of time, equal to, or less than 10 Myrs (Kurtz et al., 2003). This is significant, as some components of the sulphur isotope curve are characterised by rapid isotopic variability, with durations less than the residence time of marine sulphur. Thus, it was necessary for us to derive Equation S5 that does not necessarily assume steady state. This ensures that the model allows for adjustments in the mass and isotopic composition of the sulphur reservoir in response to changes in the input and output fluxes of sulphur (Kurtz et al., 2003). Equation S5 can be rearranged to Equation S6, which models the pyrite burial flux over a given period without assuming conditions of steady state:

$$F_{py} = \frac{F_W^S(\delta_W^S - \delta_0^S) - \frac{d\delta_0^S}{dt} M_0^S}{\Delta_S} \quad [S6]$$

Modelled rates of pyrite burial are subject to uncertainty because of the assumptions made during the modelling procedure, including variability in the degree of isotopic fractionation and the continental weathering flux, both of which can influence the $\delta^{34}S$ of seawater sulphate. In addition, conditions of rapid isotopic change where steady state cannot be assumed, act to contribute to further uncertainty (Kurtz et al., 2003). To address this, it was necessary to complete a range of sensitivity tests to

better constrain the true cause of the biogeochemical instability characterising our isotope record.

Changes in the degree of isotopic fractionation ($\Delta^{34}S$) during processes such as microbial sulphate reduction (MSR) can occur and are constrained by a number of environmental and physiological factors (Canfield et al., 2010; Fike et al., 2015; Pasquier et al., 2017; Bryant et al., 2018; Rennie et al., 2018; Pasquier et al., 2021). In theory, if such changes did occur, this would influence the interpretation of our sulphur isotope record. Habicht et al. (2002) demonstrated that the fractionation factor for MSR is sensitive to ocean sulphate concentrations and reported very low $\Delta^{34}S$ values. However, this is likely only the case under conditions of very low sulphate (<200 µM) characteristic of the Archean ocean and is thus not likely to have had an impact on the isotopic variability of the Permian-Triassic $\delta^{34}S_{evap}$ record. We conducted a sensitivity test that enabled us to calculate the degree to which $\Delta^{34}S$ would have to vary to reasonably attribute the observed variability in our $\delta^{34}S_{evap}$ record to changes in $\Delta^{34}S$ alone. Figure S4 demonstrates that the Permian–Triassic $\delta^{34}S$ record would require an unrealistic degree of variability for $\Delta^{34}S$. Thus, we can say with relative confidence that $\Delta^{34}S$ did not exert a substantial influence on the $\delta^{34}S$ of Permian–Triassic seawater sulphate.

It is of course possible that changes in $\Delta^{34}S$, although alone not likely capable of inciting the variability observed in our $\delta^{34}S_{evap}$ record, may have been a contributing factor along with changes in the magnitude and isotopic composition of sulphur input fluxes, such as weathering and pyrite burial. We conducted additional sensitivity tests to assess modelled pyrite burial flux to the value set for $\Delta^{34}S$. For the Early Triassic positive $\delta^{34}S_{evap}$ excursion, increasing $\Delta^{34}S$ subdued the modelled pyrite burial flux

predicted to have incited this excursion. Similarly, if the $\Delta^{34}S$ value is shifted to account for a reduction in the magnitude of isotopic fractionation during the time interval associated with the negative $\delta^{34}S_{evap}$ excursion, the magnitude of the predicted decrease in pyrite burial/increase in pyrite weathering is marginally subdued (Fig. 3 of main text). The implications of this are discussed further in the main text. We also applied this sensitivity test to the positive $\delta^{34}S_{evap}$ excursion near the Norian/Rhaetian boundary. For a range of $\Delta^{34}S$ values between -35 ‰ and -50 ‰: if the magnitude of fractionation is increased (i.e., $\Delta^{34}S$ becomes more negative), the predicted increase in pyrite burial necessary to account for the positive excursion is lessened (Fig. S5). This suggests that although changes in $\Delta^{34}S$ may have contributed to driving the observed $\delta^{34}S_{evap}$ variability, accompanying changes in the rates of pyrite burial and weathering were likely required to account for the full extent of the isotopic variability of seawater sulphate during this time interval.

The sulphur isotopic composition of the riverine input flux (δ_W^S) is constrained by the relative contributions from the terrestrial weathering of sedimentary pyrite and gypsum, which is largely unknown for any point in the geologic past (Kurtz et al., 2003). Due to the fractionation factor for the formation of pyrite, if all other parameters are held constant, a reduction in the sulphur weathering flux would yield an associated increase in the $\delta^{34}S$ of marine sulphate, assuming no coincident change in the pyrite burial flux (Kurtz et al., 2003). Therefore, under such conditions, an increase in the riverine input flux (F_W^S) would likely incite an isotopic enrichment of seawater sulphate. In this way, changes in the magnitude and isotopic composition of sulphate entering the ocean reservoir are capable of driving variability in the $\delta^{34}S$ of seawater sulphate (Fike et al., 2015).

To assess whether the magnitude of the riverine sulphur input flux could have exerted a dominant control over the variability present in the Permian–Triassic $\delta^{34}S_{evap}$ record, we rearranged Equation S4 to solve for F_W^S and held the pyrite burial flux constant. Figure S6 shows that for the weathering flux to have a dominant control over the variability in the $\delta^{34}S_{evap}$ record during the Permian/Triassic boundary (PTB) and earliest Triassic, a preceding reduction in F_W^S to -1.94 Tmol/yr at 252 Ma would be necessary. A reduction in weathering is in conflict with the available proxy data, which suggests a substantial increase in continental weathering rates during the latest Permian and Early Triassic (Korte et al., 2003; Sun et al., 2018). Considering this, and that negative weathering rates are mathematically equivalent to pyrite burial, the model outputs confirm that the weathering flux alone could not have incited the variability observed across the PTB and Early Triassic $\delta^{34}S_{evap}$ record. In contrast, the sensitivity test suggests weathering rates would need to rise to ~2.93 Tmol/yr at ~248 Ma to account for the negative $\delta^{34}S_{evap}$ excursion observed at the Olenekian/Anisian boundary (OAB). This is only marginally higher than the modern riverine sulphur flux derived from pyrite and sulphate weathering of ~2.8 Tmol/yr (Burke et al., 2018). Although we propose multiple possible mechanisms for the negative $\delta^{34}S_{evap}$ excursion at the OAB, this sensitivity test suggests an increase in sulphur weathering could have contributed to the variability in the sulphur isotopic composition of seawater sulphate across this time interval.

During the model runs, the riverine input flux (F_W^S) set to a chosen value. In this case we set the F_W^S to 1.5 Tmol/yr (Kump and Garrels, 1986; Kurtz et al., 2003; Gill et al., 2011; Owens et al., 2013). Research on the modern sulphur cycle presents an estimate for the modern value for F_W^S of ~2.8 Tmol/yr when anthropogenic contributions are not considered (Burke et al., 2018). An alternative estimate for F_W^S of 3.5 Tmol/yr was used

by Rennie et al. (2018) when modelling the Cenozoic carbon and sulphur cycles. We thus considered it necessary to test for the sensitivity of our model to the value given to the riverine input flux. Raising the value to either 2.8 or 3.5 Tmol/yr changes the magnitude of the variability in pyrite burial necessary to account for the variability exhibited by the $\delta^{34}S_{evap}$ record (Fig. S7). Despite this, the trends in the record of inferred pyrite burial rates remain relatively unchanged, and thus although their magnitude is different, the number of pyrite burial events are not altered. This ensured that our overall interpretations are not impacted by a change in the value of F_W^S within the tested range.

To explore the sensitivity of the model outputs to ocean sulphate concentrations, the model was run assuming different values for the concentration of sulphate (Fig. S8). Three model runs were conducted for this test, the first assumed sulphate concentrations set to the values displayed in Table S1 and Fig. S9 (Fig. S8a), the second assumed a constant sulphate concentration of 12.5 mM (Fig. S8b) estimated for the Middle Triassic (Bernasconi et al., 2017), and third assumed a value of 28 mM (Fig. S8c), the modern concentration of seawater sulphate. As expected, the pyrite burial flux exhibits greater variability when sulphate concentrations are fixed at the Middle Triassic and modern values. A larger sulphate reservoir is less susceptible to perturbations, and thus larger changes in pyrite burial are required to incite the variability observed in the $\delta^{34}S_{evap}$ record.

Supplementary figures

Figure S1: *Cored material from Staithes S-20. The sharp unconformity can be seen separating the dark brown, laminated arenaceous sandstone of the Sherwood Sandstone Group, and the overlying gypsiferous silt-mudstone of the Mercia Mudstone Group (see arrow for way-up indicator).*

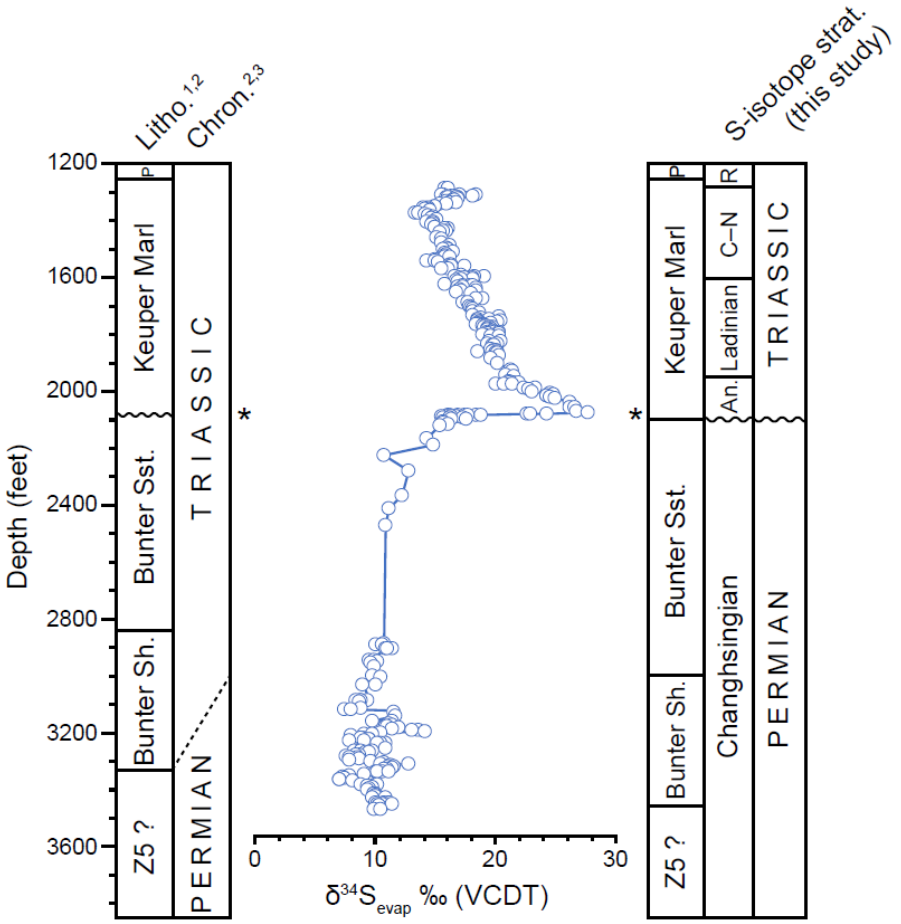

Figure S2: *Staithes S-20 borehole $\delta^{34}S_{evap}$ record. References (1 = Woods, 1973; 2 = Jeans, 1995; 3 = Warrington, 2019, pers. comm.).*

** = palynology sample assigned an earliest Anisian age (Warrington 2019, pers. comm.).*

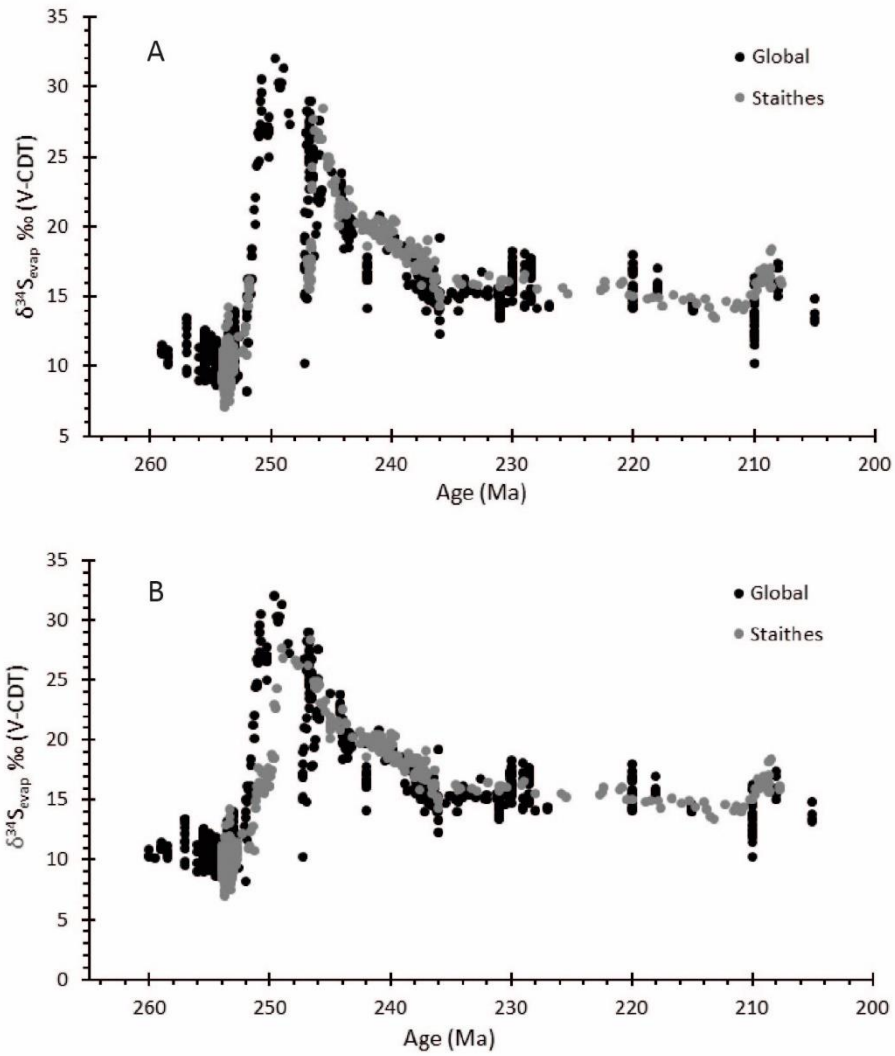

Figure S3: *Comparison between the age model with a major time gap (A) and a minor time gap (B) based upon their correlation with the global composite* $\delta^{34}S_{evap}$ *curve.*

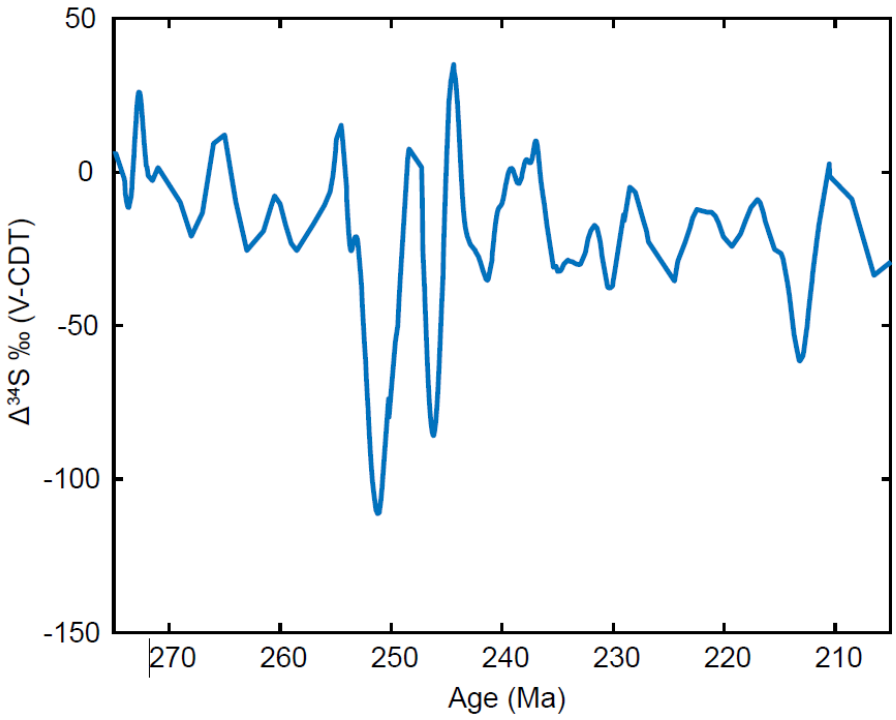

Figure S4: *Modelled changes in $\Delta^{34}S$ required to incite the observed variability in the Permian–Triassic $\delta^{34}S$ record.*

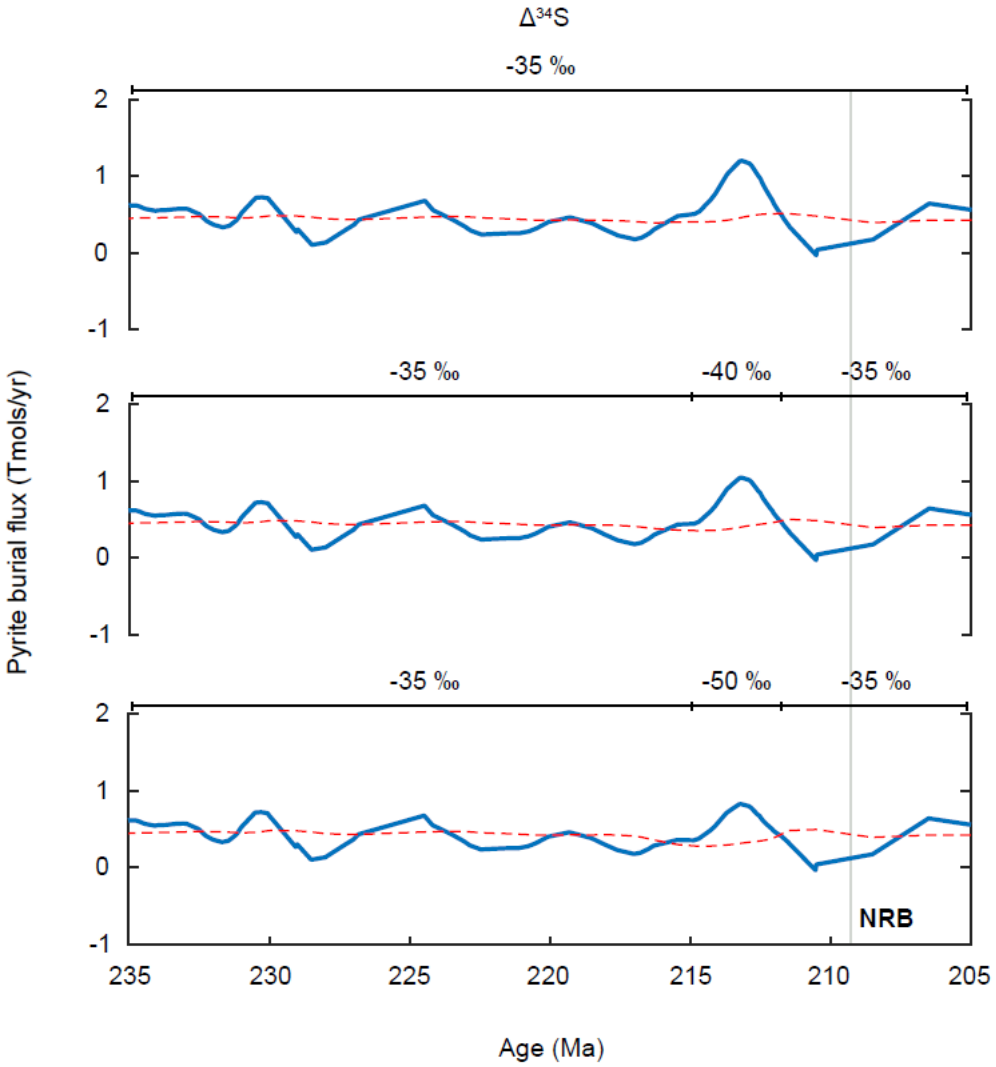

Figure S5: *Sensitivity of the modelled pyrite burial flux to changes in the fractionation factor for the chemical reduction of sulphate to sulphide ($\Delta^{34}S$) during the Late Triassic. The bar above each model output displays the value set for $\Delta^{34}S$ at different intervals of time. The only parameter changed between each model run is $\Delta^{34}S$. The grey line marks the position of the Norian/Rhaetian boundary (NRB).*

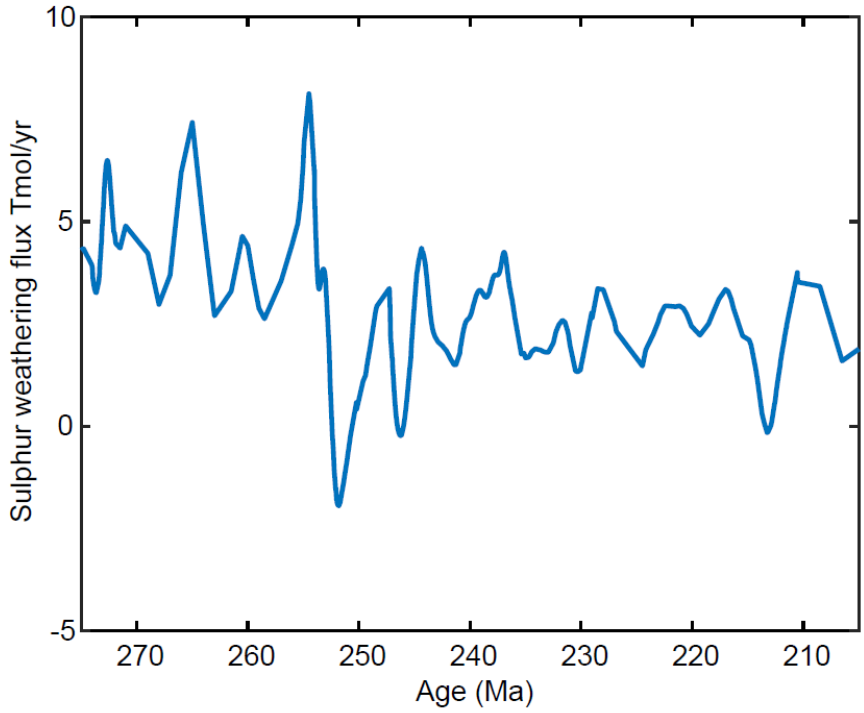

Figure S6: *Modelled changes in the riverine sulphur weathering flux required to incite the observed variability in the Permian–Triassic $\delta^{34}S$ record.*

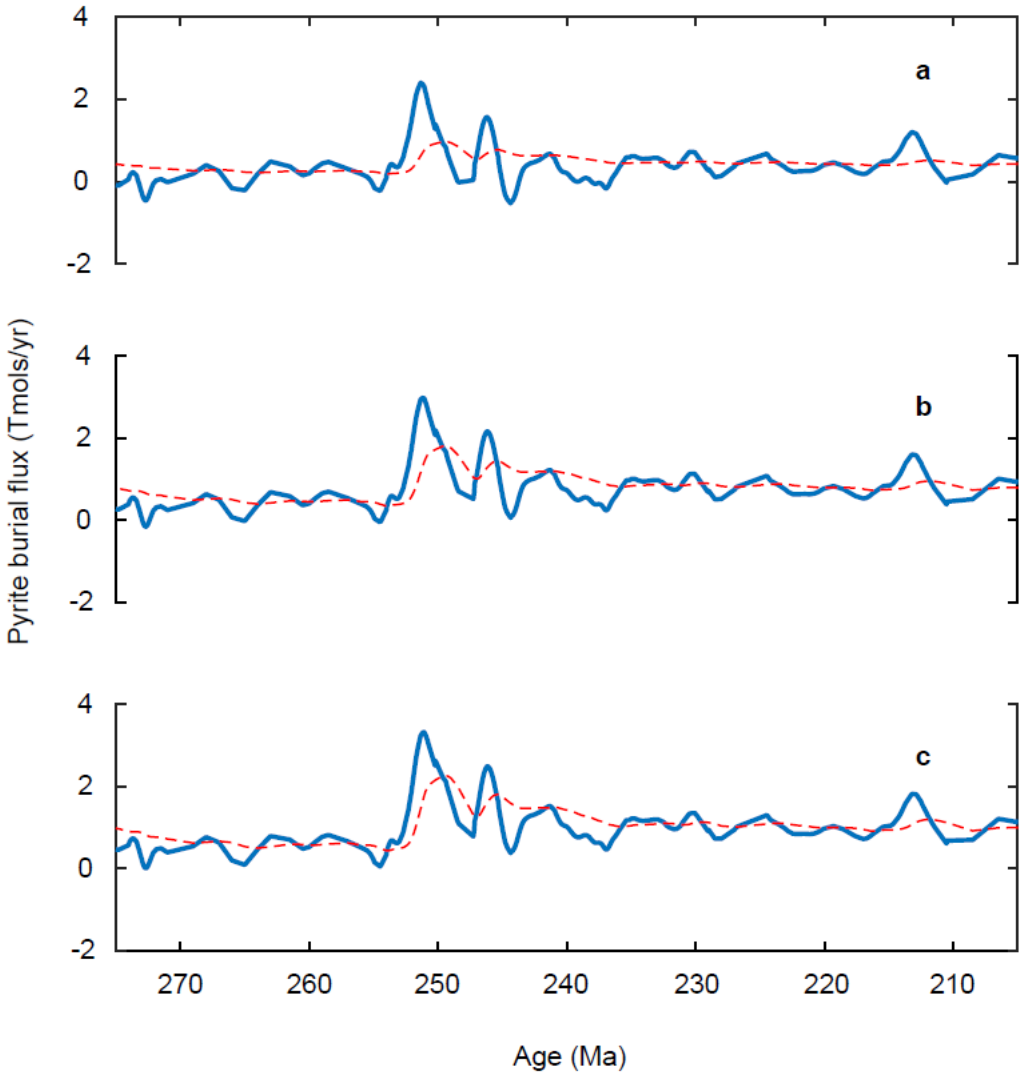

Figure S7: *The sensitivity of the modelled pyrite burial flux to the value set for the weathering input flux (FWS). (a) displays the model output when FWS is set to 1.5 Tmol/yr (Kump and Garrels, 1986; Kurtz et al., 2003; Gill et al., 2011; Owens et al., 2013), and is the pyrite burial record used in the main text. (b) shows the inferred pyrite burial flux when FWS is set to the value estimated for the modern sulphur cycle of 2.8 Tmol/yr (Burke et al., 2018), and (c) displays the model output when FWS is set to 3.5 Tmol/yr (Rennie et al., 2018).*

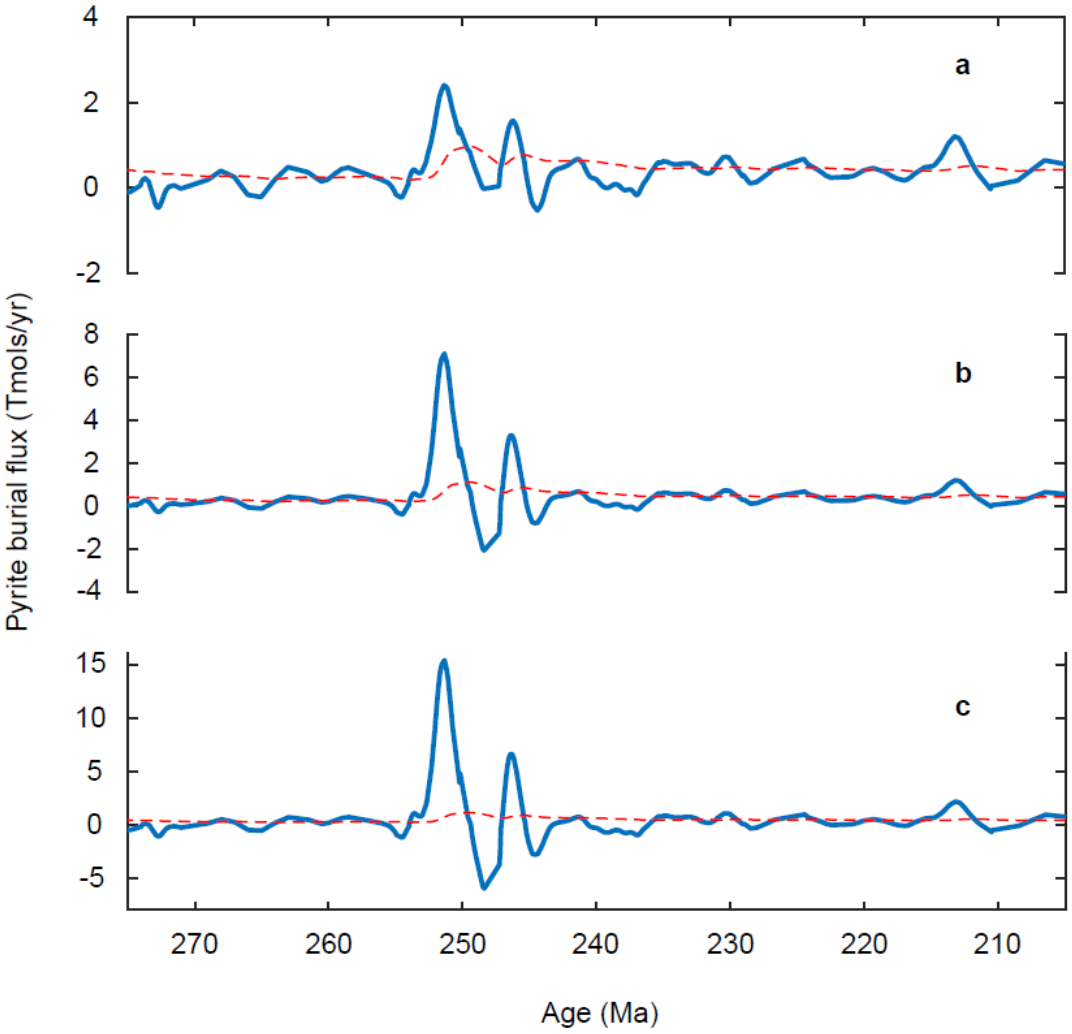

Figure S8: *The sensitivity of the modelled pyrite burial flux to seawater sulphate concentration. The model was run assuming the sulphate concentrations (a) displayed in Table S1. A second model run (b) assumed the sulphate concentration was fixed at the value estimated for the Middle Triassic of 12.5 mM (Bernasconi et al., 2017), and a third (c) assumed the modern concentration of 28 mM. No other parameters were changed between model runs.*

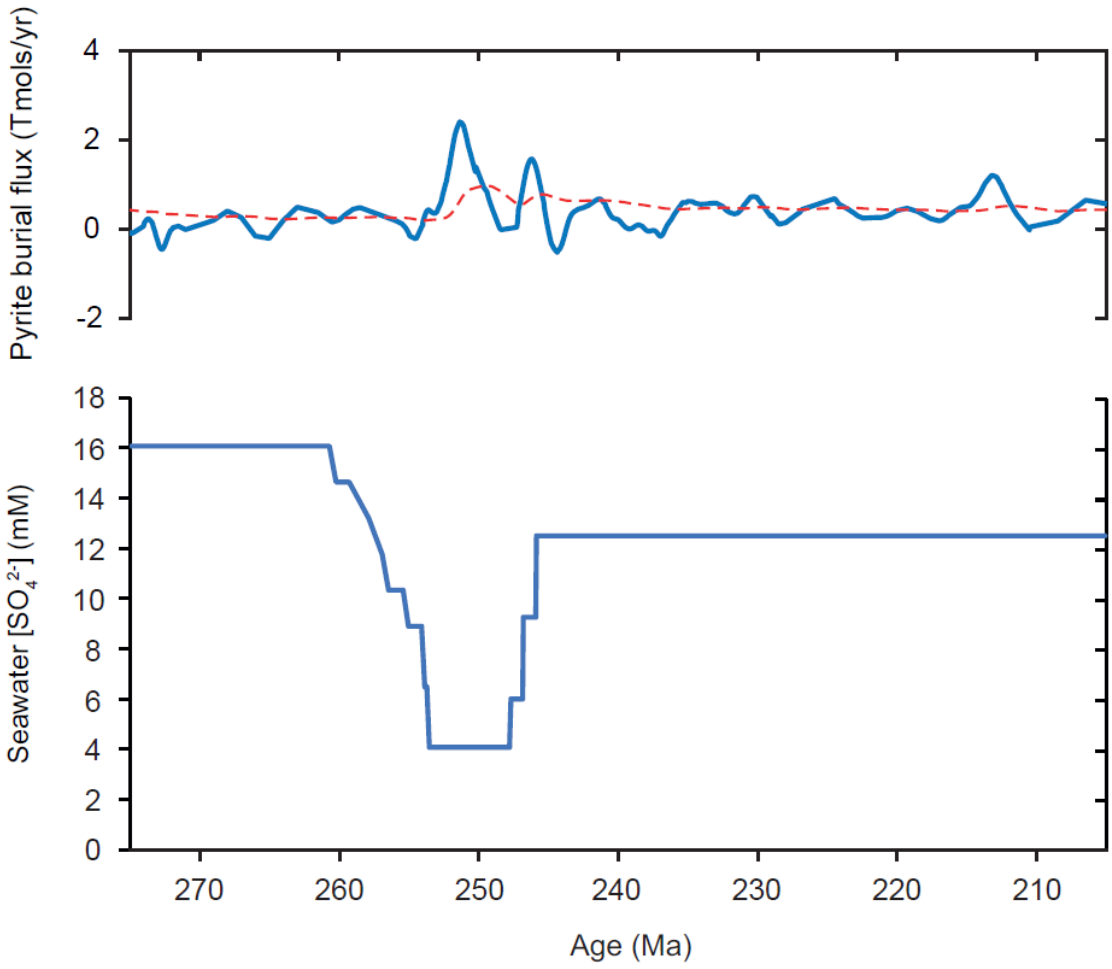

Figure S9: *The pyrite burial flux predicted for the late Permian–Triassic plotted alongside seawater sulphate concentrations used during the modelling procedure. Unfortunately, high-resolution modelling only exists for the Early Triassic (Bernasconi et al., 2017; Stebbins et al., 2019). Horita et al. (2002) analysed fluid inclusions in halite to derive estimates for seawater sulphate concentrations for the late Permian. Few estimates exist for the Middle and Late Triassic, however Bernasconi et al. (2017) provide estimates for the early Middle Triassic. See Table S1 for the specific values used for seawater sulphate concentrations.*

Supplementary tables

Parameter	Values applied	Source
M_O^S	Late Permian: 16 mM SO_4^{2-} (275–254 Ma) 8 mM SO_4^{2-} (254–252.5 Ma) PTB through Early Triassic (252.5–246.3 Ma): 2–6 mM SO_4^{2-} Early Middle Triassic (Early Anisian) (246.3–244 Ma): 6–9.3 mM SO_4^{2-} Middle through Late Triassic (244–201 Ma): 10–15 mM SO_4^{2-}	Horita et al. (2002) Bernasconi et al. (2017) Bernasconi et al. (2017)
F_W^S	$1.5x10^{18}$mol m.yr.	Kurtz et al. (2003)
δ_W^S	4.8 ‰	Burke et al. (2018)
Δ_S	-35 ‰ -40 ‰ for anoxia	Gill et al. (2011) Owens et al. (2013)
F_{gyp}	$0.5x10^{18}$ mol Myr	Gill et al. (2011)
F_{py}	$1.0x10^{18}$ mol Myr	Gill et al. (2011)

Table S1: *Values for parameters used in the sulphur isotope box model.*

References

Ambrose, K., Hough, E., Smith, N.J.P., Warrington, G., 2014. Lithostratigraphy of the Sherwood Sandstone Group of England, Wales and south-west Scotland. *British Geological Survey Research Report*, RR/14/01

Anderson, T.F., Pratt, L.M., 1995. Isotopic evidence for the origin of organic sulfur and elemental sulfur in marine sediments. In: Vairavamurphy, M.A., Schoonen, M.A.A., (eds) *Geochemical transformations of sedimentary sulfur, ACS symposium series*, vol., 612, pp., 378-396

Ault.W.U, Kulp.J.L, 1959. Isotopic geochemistry of sulfur, *Geochimica et Cosmochimica Acta*, vol 16(4), pp. 201-235

Bachmann, G.H., Geluk, M.C., Warrington, G., Becker-Roman, A., Beutler, G., Hagdorn, H., Hounslow, M.W., Nitsch, E., Röhling, H.-G., Simon, T., Szulc, A., 2010. Triassic. In:

Doornenbal, J.C., Stevenson, A.G. (eds) *Petroleum Geological Atlas of the Southern Permian Basin Area*. EAGE Publications b.v. (Houten), pp., 149-173

Baure, K.W., Bottini, C., Katsev, S., Jellinek, M., Francois, R., Erba, E., Crowe, S.E., 2022. Ferruginous oceans during OAE1a and collapse of the marine sulfate pool. *Earth and Planetary Science Letters*, vol., 578, pp., 117324

Bernasconi, S.M., Meier, I., Wohlwend, S., Brack, P., Hochuli, P.A., Blasi, H., Wortmann, U.G., Ramseyer, K., 2017. An evaportite-based high-resolution sulfur isotope record of Late Permian and Triassic seawater sulfate, *Geochimica et Cosmochimica Acta*, vol. 204, pp.331-349

Bojar.A.V, Halas.S, Bojar.H.P, Trembaczowski.A, 2016. Late Permian to Triassic isotope composition of sulfates in the Eastern Alps: palaeogeographic implications, *Geological Magazine*, vol 155(4), pp.1-14

Bourquin, S., Bercovici, A., López-Gómez, J., Diez, J.B., Broutin, J., Ronchi, A., Durand, M., Arché, A., Linol, B., Amour, F., 2011. The Permian-Triassic transition and the onset of Mesozoic sedimentation at the northwestern peri-Tethyan domain scale: Palaeogeographic maps and geodynamic implications. *Palaeogeography, Palaeoclimatology, Palaeoecology*, vol., 299, pp., 265-280

Brookfield, M.E., 2008. Palaeoenvironments and palaeotectonics of the arid to hyperarid intracontinental latest Permian-Late Triassic Solway Basin (U.K.). *Sedimentary Geology*, vol., 210, pp., 27-47

Bryant, R.N., Jones, C., Raven, M.R., Gomes, M.L., Berelson, W.M., Bradley, A.S., Fike, D.A., 2018. Sulfur isotope analysis of microcrystalline iron sulfides using secondary ion mass spectrometry imaging: Extracting local paleo-environmental information from modern and ancient sediments. *Rapid Communications in Mass Spectrometry*, vol., 33, pp., 491-502

Burke, A., Present, T.M., Paris, G., Rae, E.C.M., Sandilands, B.H., Gaillardet, J., Peucker-Ehrenbrink, B., Fischer, W.W., McClelland, J.W., Spencer, R.G.B., Voss, B.M., Adkins, J.F., 2018. Sulfur isotopes in rivers: Insights into global weathering budgets, pyrite oxidation, and the modern sulfur cycle. *Earth and Planetary Science Letters*, vol., 496, pp., 168-177

Butcher.G.S, Kendall.A.C, Boyce.A.J, Millar.I.L, Andrews.J.E, Dennis.P.F. 2012. Age determination of the Lower Watrous red-beds of the Williston Basin, Saskatchewan, Canada, *Bulletin of Canadian Petroleum Geology*, vol 60(4), pp.227-238

Carrillo, E., Rosell, L., Ortí, F., 2014. Multiepisodic evaporite sedimentation as an indicator of palaeogeographic evolution in foreland basins (South-eastern Pyrenean basin, Early-Middle Eocene). *Sedimentology*, vol., 61, pp., 2086-2112

Canfield, D.E., Farquhar, J., Zerkle, A.L., 2010. High isotope fractionations during sulfate reduction in a low-sulfate euxinic ocean analog. *Geology*, vol., 38, pp., 415-418

Claypool.G.E, Holser.W.T, Kaplan.I.R, Sakai.H, Zak.I, 1980. The age curves of sulfur and oxygen isotopes in marine sulfate and their mutual interpretation, *Chemical Geology*, vol 28, pp.199-260

Clement.G.P, Holser.W.T, 1988. Geochemistry of Moroccan evaporites in the setting of the North Atlantic Rift, *Journal of African Earth Sciences*, vol 7(2), pp.375-383

Clemmensen.L, Holser.W.T, Winter.D, 1985. Stable isotope study through the Permian-Triassic boundary in East Greenland, *Bulletin of the Geological Society of Denmark*, vol 33, pp.253-260

Cohen, K.M., Finney, S.M., Gibbard, P.L., Fan, J.X., 2013. The ICS International Chronostratigraphic Chart. *Episodes 36*, 199-204.

Crockford, P.W., Kunzmann, M., Bekker, A., Hayles, J., Bao, H., Halverson, G.P., Peng, Y., Bui, T.H., Cox, G.M., Gibson, T.M., Wöndle, S., Rainbird, R., Lepland, A., Swanson-Hysell, N.L., Master, S., Sreenivas, B., Kuznetsov, A., Krupenik, V., Wing, B.A., 2019. Claypool continued: Extending the isotopic record of sedimentary sulfate, *Chemical Geology*, vol. 513, pp.200-225

Davis, J.B., Kirkland, D.W., 1979. Bioepigenetic sulphur deposits. *Economic Geology*, vol. 74, pp.462-468

Denison.R.E, Kirkland.D.W, Evans.R, 1998. Using strontium isotopes to determine the age and origin of gypsum and anhydrite beds, *The journal of Geology*, vol 106, pp.1-17

Dill.H.G, Bechtel.A, Berner.Z, Botz.R, Kus.J, Heunisch.C, Abu Hamad.A.M.B, 2012. The evaporite-coal transition: Chemical, mineralogical and organic composition of the Later Triassic Abu Ruweis Formation, NW Jordan – Reference type of the "Arabian Keuper", *Chemical Geology*, vol 298, pp.20-40

Erkan.E, 1989. Die Sulfatlagerstätten der postvariszischen Transgressionsserie in den Ostalpen, *Nachrichten der Deutschen Geologischen Gesellschaft*, vol 41, pp.90-91

Feely, H.W., Kulp, J.L., 1957. Origin of Gulf Coast salt-dome sulphur deposits. *AAPG Bulletin*, vol. 41(8), pp.1802-1853

Fike, D.A., Bradley, A.S., Rose, C.V., 2015. Rethinking the ancient sulfur cycle. *Annual Review of Earth and Planetary Sciences*, vol., 43, pp., 593-622

Galamay.A.R, Meng.F, Bukowski.K, Ni.P, Shanina.S.N, Ignatovich.O.O, 2016. The sulphur and oxygen isotopic composition of anhydrite from the Upper Pechora Basin (Russia): new data in the context of the evolution of the sulphur isotopic record of Permian evaporites, *Geological Quarterly*, vol 60(4), pp.990-999

Gallois, R.W., 2009. The lithostratigraphy of the Penarth Group (Late Triassic) of the Severn Estuary area. *Geoscience in South-West England*, vol. 12, pp.71-84

García-Veigas.J, Cendón.D.I, Pueyo.J.J, Peryt.T.M, 2011. Zechstein saline brines in Poland, evidence of overturned anoxic ocean during the late Permian mass extinction event, *Chemical Geology*, vol 290, pp.189-201

García-Veigas.J, Cendón.D.I, Rosell.L, Ortí.F, Ruiz.J.T, Martín.J.M, Sanz.E, 2013. Salt deposition and brine evolution in the Granada Basin (Late Tortonian, SE Spain), *Palaeogeography, Palaeoclimatology, Palaeoecology*, vol 369, pp.452-465

Geluk, M., McKie, T., Kilhams, B., 2018. An introduction to the Triassic: current insights into the regional setting and energy resource potential of NW Europe. In: Kilhams, B., Kukla, P.A., Mazur, S., McKie, T., Mijnlieff, H.F., van Ojik, K. (eds) *Mesozoic Resource Potential in the Southern Permian Basin*. Geological Society, London, Special Publications, vol., 469, pp., 139-147

Gibert.L, Ortí.F, Rosell.L, 2007. Plio-Pleistocene lacustrine evaporites of the Baza Basin (Betic Chain, SE Spain), *Sedimentary Geology*, vol 200, pp.89-116

Gill, B.C., Lyons, T.W., Saltzman, M.R., 2007. Parallel, high-resolution carbon and sulfur isotope records of the evolving Paleozoic marine sulfur reservoir. *Palaeogeography, Palaeoclimatology, Palaeoecology*, vol. 256, pp.156-173

Gill, B.C., Lyons, T.W., Young, S.A., Kump, L.R., Knoll, A.H., Saltzman, M.R., 2011. Geochemical evidence for widespread euxinia in the Later Cambrian ocean. *Nature*, vol. 469, pp.80-83

Götzinger.M.A, Pak.E, 1983. Zur schwefelisotopen-verteilung in sulfid- und sulfatmineralen triadischer Gesteine der Kalkalpen, Österreich, *Mitteilungen der Gesellschaft der Geologie- und Bergbaustudenten Österreichs*, vol 29, pp.191-198

Gündoğan.I, Helvaci.E, Sözbilir.H, 2008. Gypsiferous carbonates at Honaz Dağı (Denizli): First documentation of Triassic gypsum in western Turkey and its tectonic significance, *Journal of Asian Earth Sciences*, vol 32, pp.49-65

Habicht, K.S., Gade, M., Thamdrup, B., Berg, P., Canfield, D.E., 2002. Calibration of sulfate levels in the Archean ocean. *Science*, vol., 298, pp., 2372-2374

Hardie, L.A., 1967. The gypsum-anhydrite equilibrium at one atmosphere pressure. *The American Mineralogist*, vol., 52, pp., 171-200

Holser.W.T, Clement.G.P, Jansa.L.F, Wade.J.A, 1988. Evaporite deposits of the North Atlantic Rift. In: Manspeizer.W. (ed) *Triassic-Jurassic rifting: continental breakup and the origin of the Atlantic Ocean and passive margins: Developments in Geotectonics Parts A and B*. Elsevier, Amsterdam, pp.525-556

Holser, W.T., Kaplan, I.R., 1966. Isotope geochemistry of sedimentary sulfates, *Chemical Geology*, vol. 1, pp.93-135

Holser.W.T, Magaritz.M, 1985. The Late Permian carbon isotope anomaly in the Bellephoron Basin, Carnic and Dolomite Alps, *Jahrbuch der Geologischen Bundesanstalt*, vol 128(1), pp.75-82

Horita, J., Zimmermann, H., Holland, H.D., 2002. Chemical evolution of seawater during the Phanerozoic: Implications for the record of marine evaporites. *Geochimica et Cosmochimica Acta*, vol., 66(21), pp., 3733-3756

Hounslow, M.W., McKie, T., Ruffell, A.H., 2012. Permian to Late Triassic post-orogenic collapse and rifting, arid deserts, evaporating seas and mass extinctions. In: Woodcock, N.H., Strachan, R.A (eds) *The Geological History of Britain and Ireland*, 2nd revised edn, Wiley, Chichester, pp.301-321

Hounslow, M., Ruffell, A.H., 2006. Triassic: Seasonal rivers, dusty deserts and saline lakes. In: Rawson, P.F., Brenchley, P. (eds) *The Geology of England and Wales*, Geological Society of London, pp., 295-325

Hovorka.S.D, Knauth.L.P, Fisher.R.S, Gao.G, 1993. Marine to nonmarine facies transition in Permian evaporites of the Palo Duro Basin, Texas: Geochemical response, *Geological Society of America Bulletin*, vol 105, pp.1119-1134

Howard.A.S., Warrington.G., Ambrose.K., Rees.J.G., 2008. A formational framework for the Mercia Mudstone Group (Triassic) of England and Wales. *British Geological Survey Research Report*, RR/08/004

Hryniv.S.P, Peryt.T.M, 2003. Sulfate cavity filling in the Lower Werra Anhydrite (Zechstein, Permian), Zdrada Area, Northern Poland: Evidence for early diagenetic evaporite paleokarst formed under sedimentary cover, *Journal of Sedimentary Research*, vol 73(3), pp.451-461

Huerta.P, Armenteros.I, Recio.C, Blanco.J.A, 2010. Palaeogroundwater evolution in playa-lake environments: Sedimentary facies and stable isotope record (Palaeogene, Almazán basin, Spain), *Palaeogeography, Palaeoclimatology, Palaeoecology*, vol 286, pp.135-148

Jeans, C.V., 1995. Clay mineral stratigraphy in Paleozoic and Mesozoic red bed facies onshore and onshore UK. In: Dunay, R.E., Hailwood, E.A., (ed) *Non-biostratigraphical methods of dating and correlation*, Geological Society Special Publication No., 89, pp., 31-55

Johnson, D.L., Present, T.M., Li, M., Shen, Y., Adkins, J.F., 2021. Carbonate associated sulfate (CAS) $\delta^{34}S$ heterogeneity across the End-Permian Mass Extinction in South China. *Earth and Planetary Science Letters*, vol., 574, pp., 117172

Kovalevych.V, Peryt.T.M, Beer.W, Geluk.M, Halas.S, 2002. Geochemistry of Early Triassic seawater as indicated by study of the Röt halite in the Netherlands, Germany, and Poland, *Chemical Geology*, vol 182(2-4), pp.549-563

Kramm.U, Wedepohl.K.H, 1991. The isotopic composition of strontium and sulfur in seawater of Late Permian (Zechstein) age, *Chemical Geology*, vol 90, pp.253-262

Kump, L.R., Garrels, R.M., 1986. Modeling atmospheric O_2 in the global sedimentary redox cycle. *American Journal of Science*, vol., 286, pp., 337-360

Kurtz, A.C., Kump, L.R., Arthur, M.A., Zachos, J.C., Paytan, A., 2003. Early Cenozoic decoupling of the global carbon and sulfur cycles. *Paleoceanography*, vol. 18(4)

Lepetit.P, Aehnelt.M, Viereck.L, Strauss.H, Abratis.M, Fritsch.S, Malz.A, Kukowski,N, Totsche.K.U, 2019. Intraformational fluid flow in the Thuringian Syncline (Germany) – Evidence from stable isotope data in vein mineralization of Upper Permian and Mesozoic sediments, *Chemical Geology*, vol 523, pp.133-153

Leslie.A.B, Harwood.G.M, Kendall.A.C, 1997. Geochemical variations within a laminated evaporite deposit: evidence for brine composition during formation of the Permian Castile Formation, Texas and New Mexico, USA, *Sedimentary Geology*, vol 110, pp.223-235

Lott, G.K., Warrington, G., 1988. A review of the latest Triassic succession in the U.K. sector of the Southern North Sea Basin. *Proceedings of the Yorkshire Geological Society*, vol., 47(2), pp., 139-147

Marenco.P.J, Corsetti.F.A, Kaufman.A.J, Bottjer.D.J, 2008. Environmental and diagenetic variations in carbonate associated sulfate: An investigation of CAS in the Lower Triassic of the western USA, *Geochimica et Cosmochimica Acta*, vol 72, pp.1570-1582

McKie, T., 2017. Paleogeographic evolution of latest Permian and Triassic salt basins in Northwest Europe. In: Soto, J.I., Flinch, J.F., Tari, G. (eds) *Permo-Triassic salt provinces of Europe, North Africa and the Atlantic Margins, tectonics and hydrocarbon potential*, pp., 159-173

McKie, T., Williams, B., 2009. Triassic palaeogeography and fluvial dispersal across the northwest European Basins. *Geological Journal*, vol., 44, pp., 711-741

Medici, G., West, L.J., Mountjoy, N.P., 2019. Sedimentary flow heterogeneities in the Triassic U.K. Sherwood Sandstone Group: Insights for hydrocarbon exploration. *Geological Journal*, vol., 54(3), pp., 1361-1378

Murray, R.C., 1964. Origin and diagenesis of gypsum and anhydrite. *Journal of Sedimentary Petrology*, vol., 34, pp., 512-523

Naylor.H, Turner.P, Vaughan.D.J, Boyce.A.J, Fallick.A.E, 1989. Genetic studies of red bed mineralization in the Triassic of the Cheshire Basin, northwest England, *Journal of the Geological Society, London*, vol 146, pp.685-699

Newell. A.J., 2018. Rifts, rivers and climate recovery: A new model for the Triassic of England. *Proceedings of the Geologists' association*, vol., 129, pp., 352-371

Niedermayr.G, Beran.A, Branstätter.F, 1989. Diagenetic type magnesites in the Permo-Scythian rocks of the Eastern Alps, Austria. In: Möller.P (ed) *Magnesite Geology, Mineralogy, Geochemistry, Formation of Mg-Carbonates*, pp.35-59. Monograph Series on Mineral Deposits. Berlin, Stuttgart: Gebrüder Bornträger.

Nielsen, H., 1978. Sulfur isotopes in nature. In: Wedepohl.K.K (ed) *Handbook of Geochemistry*. Sect. 16-B. Springer, Berlin

Nielsen.H, Ricke.W, 1964. Schwefel-Isotopenverhältnisse von Evaporiten aus Deutschland; Ein Beitrag zur Kenntnis von $\delta^{34}S$ im Meerwasser-Sulfat, *Geochimica et Cosmochimica Acta*, vol 28, pp.577-591

Ogg, J.G., Ogg, G.M., Gradstein, F.M., 2016. *A concise geologic timescale 2016*. Amsterdam: Elsevier

Ortí.F, Guimerà..J, Götz.A.E, 2020. Middle-Upper Triassic stratigraphy and structure of the Alt Palància (eastern Iberian Chain): A multidisciplinary approach, *Geologica Acta*, vol. 18, pp.1-25

Ortí.F, Pérez-López.A, García-Veigas.J, Rosell.L, Cendón.D.I, Pérez-Valera.F, 2014. Sulfate isotope compositions ($\delta^{34}S$, $\delta^{18}O$) and strontium isotopic ratios ($^{87}Sr/^{86}Sr$) of Triassic evaporites in the Betic Cordillera (SE Spain), *Revista de la Sociedad Geológica de España*, vol 27(1), pp.79-89

Ortí, F., Pérez-López, A., Pérez-Valera, F., Benedicto, C., 2022. Isotope composition ($\delta^{34}S$, $\delta^{18}O$) of the Middle-Early Jurassic sulfates in eastern Iberia. *Sedimentary Geology*, p.106104

Ortí.F., Salvany.J.M., Rosell.L., Castelltort.X., Inglès.M., Playà.E., 2018. Middle Triassic evaporite sedimentation in the Catalan Basin: Implications for the paleogeographic evolution in the NE Iberian platform. *Sedimentary Geology*, vol. 374, pp.158-178

Owens, J.D., Gill, B.C., Jenkyns, H.C., Bates, S.M., Severmann, S., Kuypers, M.M.M., Woodfine, R.G., Lyons, T.M., 2013. Sulfur isotopes track the global extent and dynamics of euxinia during Cretaceous Oceanic Anoxic Event 2. *Proceedings of the National Academy of Sciences*, vol., 110(46), pp., 18407-18412

Pak.E, 1978. Schwefelisotopenuntersuchungen am Institut für Radiumforschung und Kernphysik II, *Anzeiger der Akademie der Wissenschaften Mathematisch-Naturwissenschaftliche Klasse*, pp.6-22

Pak.E, Schauberger.O, 1981. Die geologische Datierung der ostalpinen Salzlagerstätten mittels Schwefelisotopenuntersuchungen, *Verhandlungen der Geologischen Bundesanstalt*, pp.185-192

Pankina.R.G, Maksimov.S.P, Kalinko.M.K, Monakhov.I.B, Guriyeva.S.M, 1975. Sulfur isotopic composition in the Phanerozoic evaporites of Bulgaria, *Geochemistry International*, vol 12(6), pp.79-83

Parrish, J.T., 1993. Climate of the supercontinent Pangea. *The Journal of Geology*, vol., 101(2), pp., 215-233

Pasquier, V., Bryant, R.N., Fike, D.A., Halevy, I., 2021. Strong local, not global, controls on pyrite sulfur isotopes. *Science Advances*, vol., 7, pp., eabb7403

Pasqiuer, V., Sansjofre, P., Rabineau, M., Revillon, S., Houghton, J., Fike, D.A., 2017. Pyrite sulfur isotopes reveal glacial-interglacial environmental changes. *Proceedings of the National Academy of Sciences*, vol., 114, pp., 5941-5945

Paytan, A., Gray, E.T., Ma, Z., Erhardt, A., Faul, K., 2012. Application of sulphur isotopes for stratigraphic correlation. *Isotopes in Environmental and Health Studies*, vol., 48(1), pp., 195-206

Peacock, D.C.P., 2004. The post-Variscan development of the British Isles within a regional transfer zone influenced by orogenesis. *Journal of Structural Geology*, vol., 26(12), pp., 2225-2231

Pérez-López, A., Benedicto, C., Ortí, F., 2021. Middle Triassic carbonates of Eastern Iberia (Western Tethyan Realm): A shallow platform model. *Sedimentary Geology*, vol., 420, pp., 105904

Peryt.T.M, Halas.S, Hryniv.S.P, 2010. Sulphur and oxygen isotope signatures of late Permian Zechstein anhydrites, West Poland: seawater evolution and diagenetic constraints, *Geological Quarterly*, vol 54(4), pp.387-400

Posey.H.H, Fisher.R.S, 1989. A sulfur and strontium isotopic investigation of Lower Permian anhydrite, Palo Duro Basin, Texas, U.S.A., *Applied Geochemistry*, vol 4, pp.395-407

Present, T.M., Adkins, J.F., Fischer, W.W., 2020. Variability in sulfur isotope records of Phanerozoic seawater sulfate, *Geophysical Research Letters*, vol., 47(18), pp., 1-17

Qing.H, Nickel.E, Marsh.A, Gerla.G, Yang.C, 2005. Geochemistry of anhydrites at the IEA Weyburn site: implications for assessing the effectiveness of sealing rocks, *Greenhouse Gas Control Technologies*, vol 2, pp.1981-1982

Raab, M., Spiro, B., 1991. Sulfur isotopic variations during seawater evaporation with fractional crystallization, *Chemical Geology*, vol., 86, pp., 323-333

Raven, M.R., Fike, D.A., Bradley, A.S., Gomes, M.L., Owens, J.D., Webb, S.A., 2019. Paired organic matter and pyrite $\delta^{34}S$ records reveal mechanisms of carbon, sulfur, and iron cycle disruption during Ocean Anoxic Event 2. *Earth and Planetary Science Letters*, vol., 512, pp., 27-38

Rennie, V.C.F., Paris, G., Sessions, A.L., Abramovich, S., Turchyn, A.V., Adkins, J.F., 2018. Cenozoic record of $\delta^{34}S$ in foraminiferal calcite implies an early Eocene shift to deep-ocean sulfide burial. *Nature Geoscience*, vol., 11, pp., 761-765

Richardson, J.A., Keating, C., Lepland, A., Hints, O., Bradley, A.S., Fike, D.A., 2019. Silurian records of carbon and sulphur cycling from Estonia: The importance of depositional environments on isotopic trends. *Earth and Planetary Science Letters*, vol., 512, pp., 71-82

Rick.B, 1990. Sulphur and oxygen isotopic evolution of Swiss Gipskeuper (Upper Triassic), *Chemical Geology: Isotope Geoscience Section*, vol 80(3), pp.243-250

Sarg.J.F, 1981. Petrology of the carbonate-evaporite facies transition of the Seven Rivers Formation (Guadalupian, Permian), southeast New Mexico, *Journal of Sedimentary Petrology*, vol 51(1), pp.73-95

Schobben, M., Stebbins, A., Algeo, T.J., Strauss, H., Leda, L., Haas, J., Struck, U., Korn, D., Korte, C., 2017. Volatile earliest Triassic sulphur cycle: A consequence of persistent low seawater sulfate concentrations and a high sulfur cycle turnover. *Palaeogeography, Palaeoclimatology, Palaeoecology*, vol., 468, pp., 74-85

Schreiber, B.C., Tabakh, M.E., 2000. Deposition and early alteration of evaporites. *Sedimentology*, vol., 47, pp., 215-238

Shen, L., Wang, L., Liu, C., Zhao, Y., 2021. Sr, S, and O isotope compositions of evaporites in the Lanping-Simao Basin, China. *Minerals*, vol., 11(2), pp., 1-20

Smith, D.B., 1989. The late Permian palaeogeography of north-east England. *Proceedings of the Yorkshire Geological Society*, vol., 47(4), pp., 285-312

Solomon.M, Rafter.T.A, Dunham.K.C, 1971. Sulphur and oxygen isotope studies in the northern Pannines in relation to ore genesis, *Transactions of the Institution of Mining and Metallurgy Section B, 80B*, pp.259-275

Spötl.C, Pak.E, 1996. A strontium and sulfur isotopic study of Permo-Triassic evaporites in the Northern Calcareous Alps, Austria, *Chemical Geology*, vol 131, pp.219-234

Stebbins, A., Algeo, T.J., Olsen, C., Sano, H., Rowe, H., Hannigan, R., 2019. Sulfur-isotope evidence for recovery of seawater sulfate concentrations from a PTB minimum by the Smithian-Spathian transition. *Earth-Science Reviews*, vol., 195, pp., 83-95

Stemmerik.L, Piasecki.S, 2004. Isotopic evidence for the age of the Røde Ø Conglomerate, inner Scoresby Sund, East Greenland, *Bulletin of the Geological Society of Denmark*, vol 51, pp.137-140

Stemmerik.L, Rouse.J.E, Spiro.B, 1988. S-isotope studies of shallow water, laminated gypsum and associated evaporites, Upper Permian, East Greenland, *Sedimentary Geology*, vol 58, pp.37-46

Strehl.V.E, Niedermayr.G, Scheriau-Niedermayr.E, Pak.E, 1980. Die Gipsvorkommen an der Südseite des Dobratsch (Villacher Alpe), Kärnten, *Carinthia II*, pp.77-89

Sun, H., Xiao, Y., Gao, Y., Zhang, G., Casey, J.F., Xhen, Y., 2018. Rapid enhancement of chemical weathering recorded by extreme light seawater lithium isotopes at the Permian-Triassic boundary. *Proceedings of the National Academy of Sciences*, vol., 115(15), pp., 3782-3787

Thode, H.G., Monster, J., 1965. Sulfur-isotope geochemistry of petroleum, evaporites, and ancient seas. In: Young, A., Galley, J.E. (ed) *Fluids in subsurface environments AAPG Memoir 4*, pp., 367-377. Tulsa, OK: American Association of Petroleum Geologists.

Thode.H.G, Monster.J, 1970. Sulfur isotope abundances and genetic relations of oil accumulations in the Middle East Basin, *AAPG Bulletin*, vol 54(4), pp.627-637

Tucker, M.E., 1991. Sequence stratigraphy of carbonate-evaporite basins: models and applications to the Upper Permian (Zechstein) of northeast England and adjoining North Sea. *Journal of the Geological Society*, London, vol., 148, pp., 1019-1036

Van Driessche, A.E.S., Canals, A., Ossorio, M., Reyes, R.C., García-Ruiz, J.M., 2016. Unraveling the sulfate sources of (giant) gypsum crystals using gypsum isotope fractionation factors, *The Journal of Geology*, vol., 124, pp., 235-245

Vredenburgh.L.D, Cheney.E.S, 1971. Sulfur and carbon isotopic investigation of petroleum, Wind River Basin, Wyoming, *AAPG Bulletin*, vol 55(11), pp.1954-1975

Warren, J.K., 2010. Evaporites through time: Tectonic, climatic and eustatic controls in marine and nonmarine deposits. *Earth-Science Reviews*, vol., 93(3-4), pp., 217-268

Warrington, G., Ivimey-Cook, H.C., 1992. Triassic. In: Cope, J.C.W., Ingham, J.K., Rawson, P.F., (eds) *Atlas of palaeogeography and lithofacies*. Geological Society, London, Memoirs, vol., 13(1), pp., 97-106

Werne, J.P., Lyons, T.W., Hallander, D.J., Formolo, M.J., Sinninghe Damsté, J.S., 2003. Reduced sulfur in euxinic sediments of the Cariaco Basin: sulfur isotope constraints on organic sufur formation. *Chemical Geology*, vol., 195, pp., 159-179

Wignall, P.B., Bond, D.P.G., 2008. The end-Triassic and Early Jurassic mass extinction records in the British Isles. *Proceedings of the Geologists' Association*, vol., 119, pp., 73-84

Woods, P.J.E., 1973. Potash exploration in Yorkshire: Boulby Mine pilot borehole. *Transactions (Section B) Institution of Mining and Metallurgy*, vol., 82, pp., 99-106

Worden, R.H., Smalley, P.C., Fallick, A.E., 1997. Sulfur cycle in buried evaporites. *Geology*, vol., 25, pp., 643-646

Yeremenko, N.A., Pankina, R.G., 1972. Variations of $\delta^{34}S$ in sulfates of recent and ancient marine basins of the Soviet Union. *Geochemistry International*, vol., 10, pp., 45-54

Appendix 2

Supplementary information for:

Biogeochemical changes within a hypersaline sabkha of the late Permian Eden Shales, UK: Stable isotopes and organic geochemistry

Jack Salisbury*, Vincent Grossi, Eva E. Stüeken, Balkis Eddhif, Arnauld Vinçon-Laugier, Ross Collin, Tom McKie, Darren R. Gröcke

* = corresponding author: jack.salisbury@durham.ac.uk

Methods

Carbon and oxygen isotope analysis of carbonate

The bulk sediment stable carbon and oxygen isotopic composition of the carbonate fraction were determined at LGL-TPE (Université Claude Bernard Lyon 1) using a dual-inlet GV Isoprime® mass spectrometer coupled to a Multiprep autosampler. Between 2 and 9 mg of untreated bulk sediment were placed in Labco vials and reacted with anhydrous oversaturated phosphoric acid at 90 °C for 20 minutes. Carbon and oxygen isotope ratios were reported in standard delta (δ) notation in per mil (‰) relative to Vienna Pee Dee Belemnite (VPDB). The $\delta^{13}C$ and $\delta^{18}O$ data were adjusted against the international reference material NIST NBS 18 and an internal Carrara Marble reference material. Since 2019, overall reproducibility of the in-house standard Carrara Marble is ±0.077 ‰ for $\delta^{13}C$ (2 SE, *n* = 595) and ±0.101 ‰ for $\delta^{18}O$ (2 SE, *n* = 1356). For NIST NBS 18, the reproducibility is ±0.103 ‰ for $\delta^{13}C$ (2 SE, *n* = 595) and ±0.158 ‰ for $\delta^{18}O$ (2 SE, *n* = 595), with mean $\delta^{13}C$ and $\delta^{18}O$ values of -5.014 ‰ and -23.200 ‰ (VPDB).

Results

$\delta^{13}C_{carb}$ and $\delta^{18}O_{carb}$ records

The $\delta^{13}C_{carb}$ data exhibit an initial negative excursion at the base of A bed, reducing from -1.19 ‰ at 98.35 m depth to -7.55 ‰ at 94.70 m. Subsequently, the $\delta^{13}C_{carb}$ profile remains relatively stable between depths of 93.69 m and 71.88 m, oscillating within a $\delta^{13}C_{carb}$ range of -8.11 ‰ to -5.59 ‰, before the $\delta^{13}C_{carb}$ profile increases to -3.48 ‰ at 69.77 m (Fig. S1). Across beds B and C, the $\delta^{13}C_{carb}$ data exhibit an initial negative excursion from -1.35 ‰ at 48.82 m to -4.52 ‰ at 48.46 m, after which the $\delta^{13}C_{carb}$ profile

displays an abrupt increasing trend to a maximum value of +2.02 ‰ at 40.58 m, before abruptly reducing to -4.67 ‰ at 35.38m (Figure S1). The $\delta^{18}O_{carb}$ profile within A bed oscillate between -6.01 ‰ and +0.01 ‰, with a gradual increasing trend from -3.41 ‰ at 81.40 m to +0.01 ‰ at 69.77 m. Across beds B and C, the $\delta^{18}O_{carb}$ data exhibit substantial variability (Fig. S1), with an initial negative excursion from -1.88 ‰ at 48.82 m to -10.18 ‰ at 47.89 m, before abruptly increasing to +2.82 ‰ at 35.38 m.

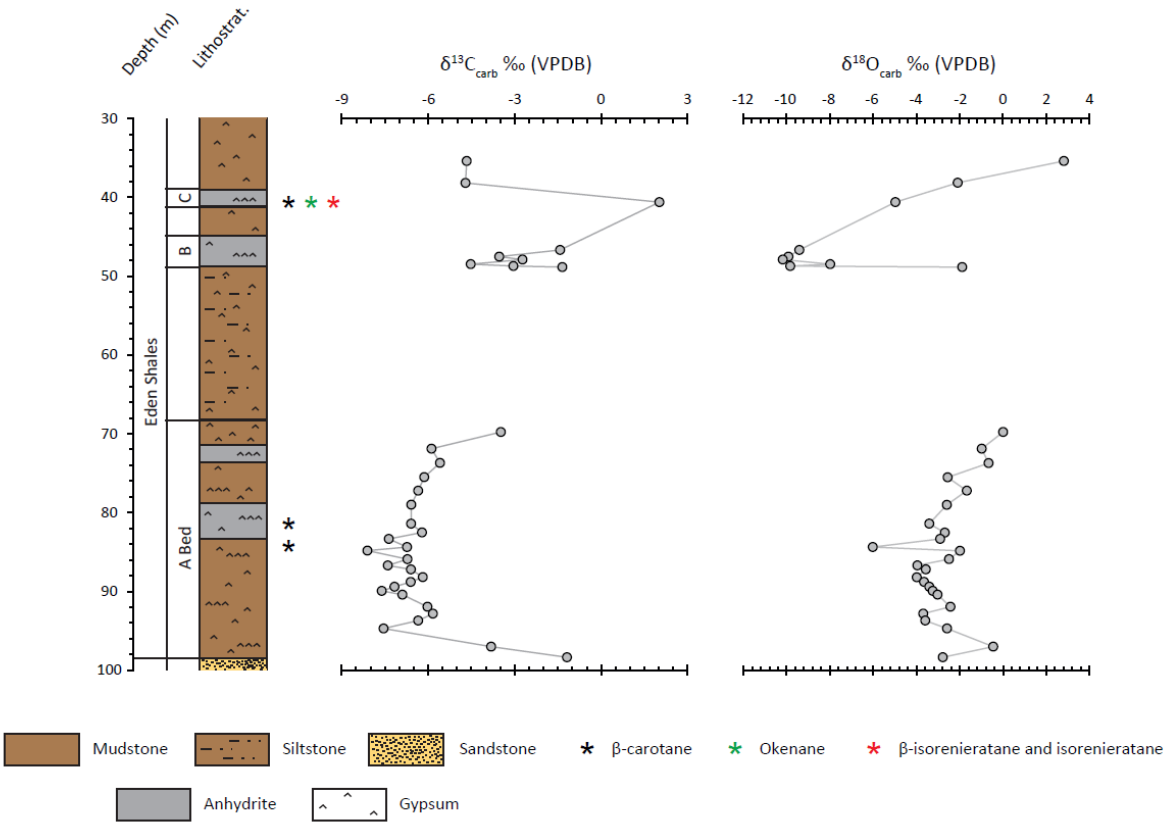

Figure S10: *$\delta^{13}C_{carb}$ and $\delta^{18}O_{carb}$ records plotted stratigraphically. These data are included within the supplementary rather than the main body of the manuscript due to concerns over the potential for diagenetic overprinting of the isotopic data.*

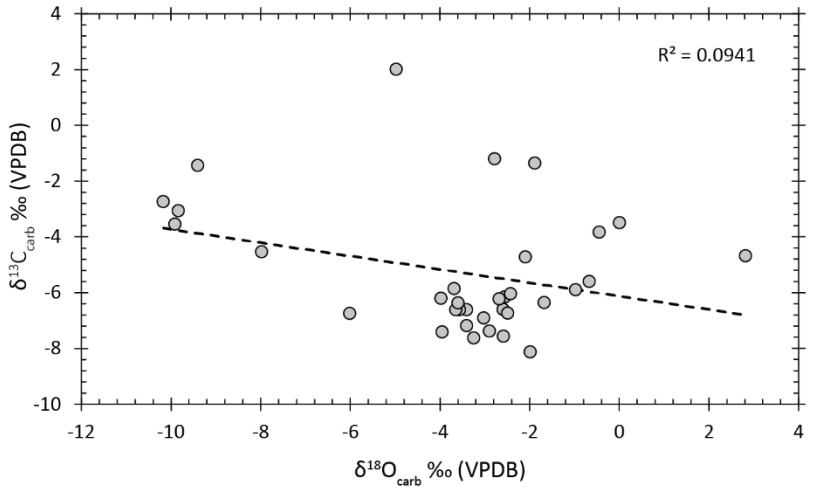
R² = 0.0941
δ13Ccarb ‰ (VPDB)
δ18Ocarb ‰ (VPDB)

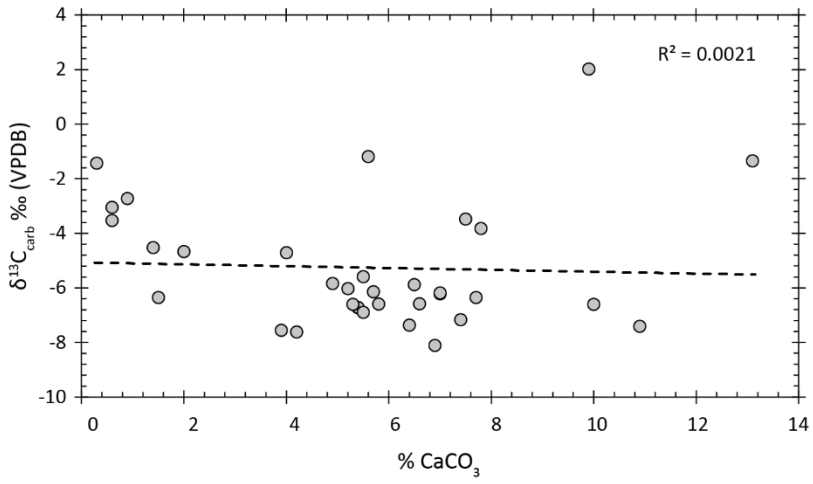
R² = 0.0021
δ13Ccarb ‰ (VPDB)
% CaCO3

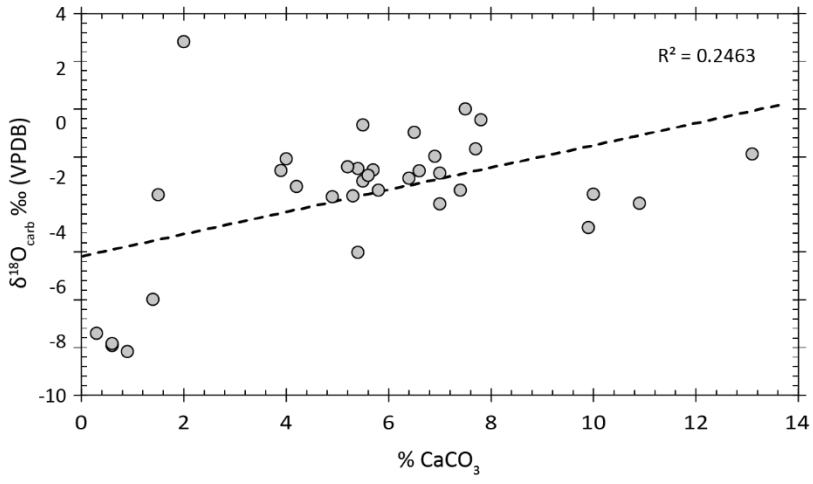
R² = 0.2463
δ18Ocarb ‰ (VPDB)
% CaCO3

Figure S11

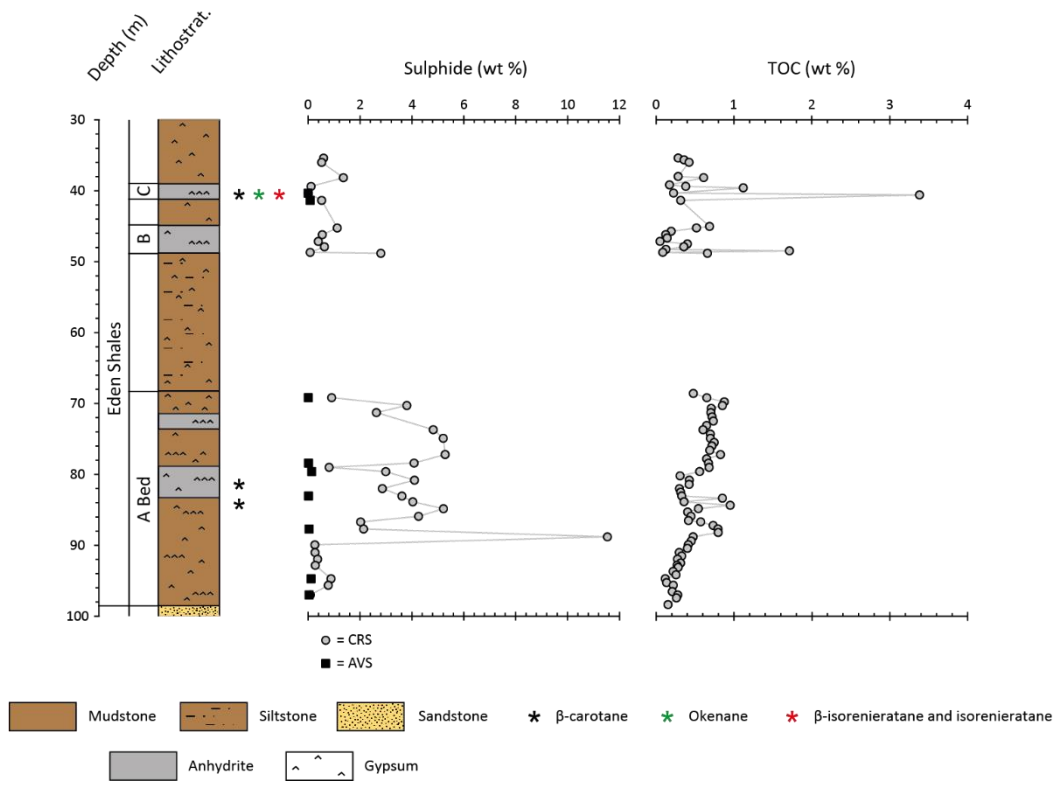

Figure S12: *(left) Sulphide content (wt %), (right) total organic carbon (TOC) content (wt %). Note that here we are reporting the TOC of the decalcified residues.*

Appendix 3

Preliminary $\delta^{34}S_{evap}$ from the Dp Morsleben 52a/95 drillcore, Germany.

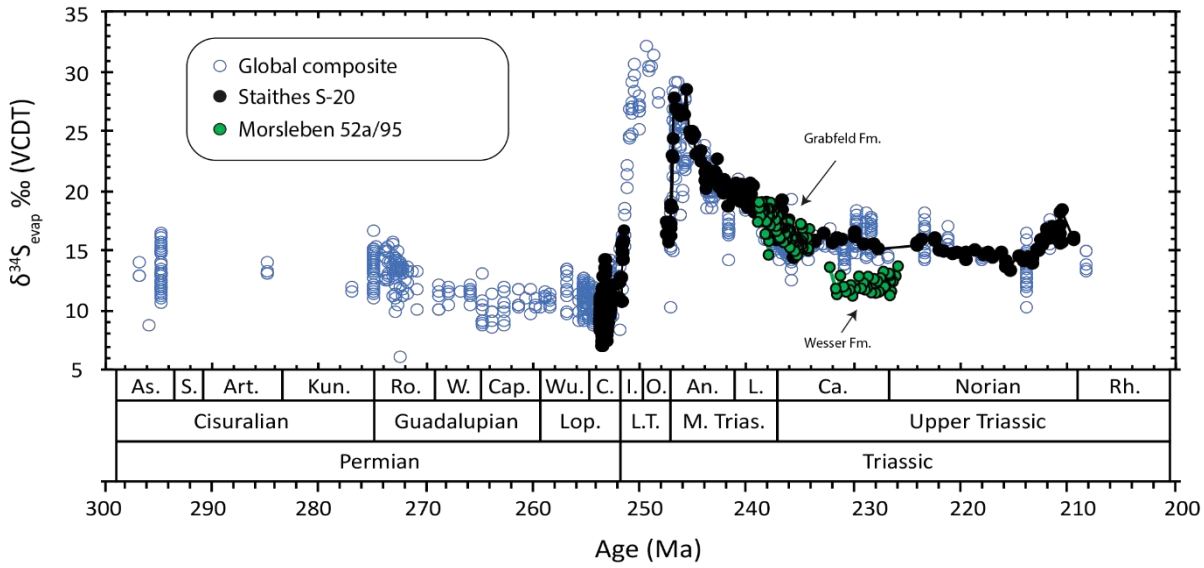

Figure S14: *Correlation scheme proposed for Dp Morsleben 52a/95 (Germany), Staithes S-20 (NE England) and the global composite $\delta^{34}S_{evap}$ age curve. The $\delta^{34}S_{evap}$ data from the Grabfeld Formation appear to correlate well with both Staithes S-20 and the global composite. However, data from the overlying Wesser Formation are offset, possibly reflecting diagenetic overprinting or inputs of terrestrial sulphate.*

Appendix 4

Preliminary $\delta^{34}S_{evap}$ and $\delta^{13}C_{org}$ data from the Lecera Formation (Triassic-Jurassic boundary).

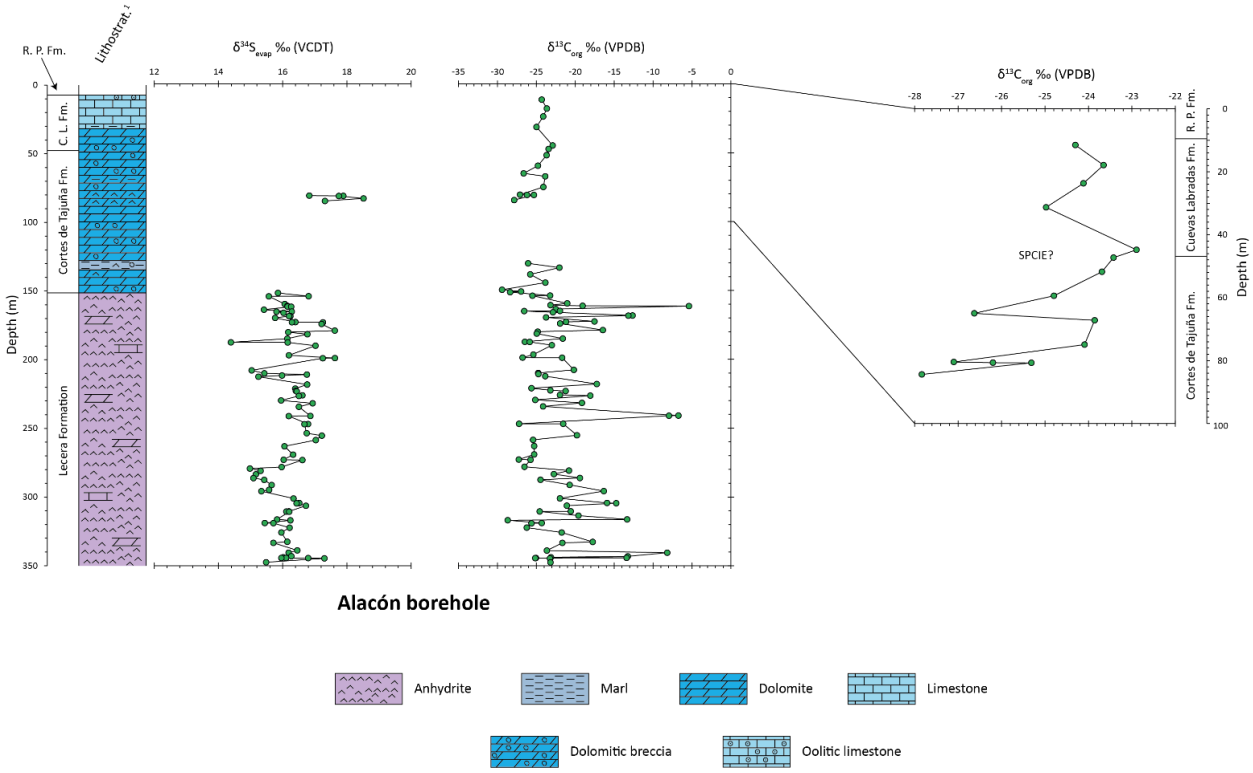

Figure S14: *The $\delta^{34}S_{evap}$ and $\delta^{13}C_{org}$ profiles for the Lecera Formation, Alacón Borehole, Spain. The $\delta^{34}S_{evap}$ data exhibit relative stability, in a pparent conflict with the published $\delta^{34}S_{CAS}$ records of He et al. (2020) and Tang et al. (2023). To the right, the top 100m of the $\delta^{13}C_{org}$ record is expanded to better display the variability observed in the carbonaceous facies. The lithostratigraphy is based upon (1) Bordonaba, A.P. (2003) Evolución sedimentaria del Jurásico Inferior (Hettangiense-Pliensbachiense) en el sector centro- oriental de la Cordillera Ibérica. Dpto. Ciencias de la Tierra, Universidad de Zaragoza, pp. 417. Abbreviations: C. L. Fm. - Cuevas Labradas Formation, R. P. Fm. - Rio Palomar Formation, SPCIE - Sinemurian Positive Carbon Isotope Excursion.*